Nonlinear Stochastic Vibration Analysis for Energy Harvesting and Other Applications

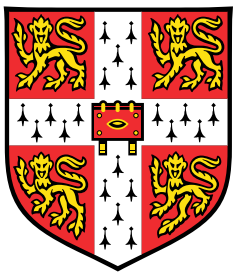

David Hawes

Supervisor: Prof. Robin Langley

Advisor: Prof. Jim Woodhouse

Department of Engineering
University of Cambridge

This dissertation is submitted for the degree of
Doctor of Philosophy

St Edmund's College December 2016

To mum, dad and Grace.

Declaration

I hereby declare that except where specific reference is made to the work of others, the contents of this dissertation are original and have not been submitted in whole or in part for consideration for any other degree or qualification in this, or any other university. This dissertation is my own work and contains nothing which is the outcome of work done in collaboration with others, except as specified in the text and Acknowledgements. Professor Langley supervised the entirety of the thesis and provided guidance at every stage. The work presented herein is my own, although Professor Langley played an integral part. This dissertation contains fewer than 65,000 words including appendices, bibliography, footnotes, tables and equations and has fewer than 150 figures.

David Hawes
December 2016

Acknowledgements

First and foremost, I would like to acknowledge the funding from the EPSRC Doctoral Training Award whose support provided enjoyable flexibility to explore the areas that interested me most. Secondly, I would like to thank Robin for his continual support, guidance, patience and not least his considerable intellect capable of dealing swiftly with problems that I had spent days stuck on. Thank you also to Grace, mum, dad and my house-mates at Russell Court for helping me through it all.

Abstract

With the rapid development of electronic technology, the power consumption of electronic devices has decreased significantly. Consequently, there is substantial interest in harvesting energy from ambient sources, such as vibration, in order to power small-scale wireless devices. To design optimal vibration harvesting systems it is important to determine the maximum power obtainable from a given vibration source.

Initially, white noise base excitation of a general nonlinear energy harvester model is considered. The power input from white noise is known to be proportional both to the total oscillating mass of the system and the magnitude of the noise spectral density, regardless of the internal mechanics of the system. This power is split between undesirable mechanical damping and useful electrical dissipation, where the form of the stiffness profile and device parameters determine the relative proportion of energy dissipated by each mechanism. An upper bound on the electrical power is derived and used to guide towards optimal harvesting devices, revealing that low stiffness systems exhibit maximum performance.

Many engineering applications will exhibit more complicated spectra than the flat spectrum of white noise. Expanding upon the white noise analysis, a method to investigate the power dissipation of nonlinear oscillators under non-white excitation is developed by extending the Wiener series. The relatively simple first term of the series, together with the excitation spectrum, is found to completely define the power dissipated. An important property of this first term, namely that the integral over its frequency domain representation is proportional to the oscillating mass, is derived and validated both numerically and experimentally, using a base excited cantilever beam with a nonlinear restoring force produced by magnets.

Another form of excitation prevalent in many mechanical systems is a combination of deterministic and broadband random vibration. Lastly, the Duffing oscillator is used to illustrate the behaviour of a nonlinear system under this form of excitation, where the response is observed to spread around the attractor that would be seen if purely deterministic excitation was present. The ability of global weighted residual methods to produce the complex responses typical of nonlinear oscillators is assessed and found to be accurate for systems with weak nonlinearity.

Table of contents

List of figures

List of tables

Chapter 1

Introduction and Literature Review

1.1 Introduction

Ambient energy exists in many forms: electromagnetic, solar, kinetic, thermal and wind amongst others. Energy harvesting is the concept of converting this ambient energy into electrical energy to power small electronic devices. The advantages of using ambient energy are significant; removing the need for battery replacement or large quantities of wiring and providing a power source in remote or inaccessible locations. The use of kinetic energy in the form of vibrations has been of considerable interest due to the availability of vibrational energy in structural, machinery, human and transport applications. One of the main applications of vibration energy harvesting is to power sensors or a network of sensors in order to monitor a complete system, although many other applications such as wearable electronics are also common.

The fundamental question of vibration energy harvesting is: what electro-mechanical system can extract maximum electrical energy (in a usable form) given the characteristics of a base vibration? In general, the system will be in the form of an oscillating mass with a chosen restoring force and an electrical transduction mechanism converting motion into electricity. Whilst a simple concept, a number of complexities quickly arise when the nature of realistic ambient vibrations are considered. Possible sources of vibration include turbines, aircraft, buildings and human movement, each of which will have different amplitudes and frequency content. Often the ambient vibration will include one or more dominant frequencies that could change with time, for example when a turbine changes its revolution speed; or the excitation could be narrowband, for example when broadband background noise is filtered through an approximately linear oscillator like a wing or building; or the excitation might be broadband noise or a combination of harmonic and broadband noise. For each different type of excitation, the optimal energy harvesting system may vary.

Initially, harmonic excitation was most commonly examined in the literature, leading to the design of linear resonant harvesters. However, these devices have a small operating frequency range, so are not suitable for applications where the excitation frequency is uncertain or may vary with time. To address this, nonlinear restoring forces were included to attempt to widen the bandwidth of a harvester. More recently, harvesters designed for random, particularly white noise, excitation have been investigated and the possible performance enhancements of nonlinear systems have been explored.

The desire for maximum power conversion in energy harvesting has driven demand for improved understanding of stochastically excited nonlinear systems. A clear limitation (not confined to energy harvesting) is the necessity to analyse nonlinear systems with a range of excitation inputs. With this in mind, this thesis aims to advance understanding and develop techniques for vibration analysis of nonlinear systems focusing on the following topics:

1. Calculation of the maximum power available to harvest from white noise base excitation.

2. A methodology for calculating the power input to a nonlinear oscillator excited by non-white noise.

3. Modelling approaches for nonlinear systems excited by a combination of deterministic and white noise excitation.

Since white noise is the most mathematically simple form of stochastic excitation, this thesis starts in Chapter 2 with the first item listed above by investigating the power dissipated in oscillators excited by white noise. A broad range of systems are analysed and a theoretical upper bound on power available for a general energy harvesting device is derived before discussing strategies for optimal power transfer.

Whilst white noise is a realistic approximation in some circumstances, many systems do not vibrate with a flat, or white, spectrum. Chapter 3 therefore investigates power dissipated by systems with non-white noise spectra by extending the Wiener series to encompass a general non-white input. A property of the series that helps calculate the power dissipated is then derived and examined numerically in Chapter 3 before being validated experimentally in Chapter 4.

Another common source of excitation that does not fall into the categories discussed in Chapters 2, 3 or 4 is a combination of deterministic and random noise. Chapter 5 investigates the effect of this form of excitation on nonlinear systems and discusses the suitability of global weighted residual approaches for modelling the response.

An outline of the content of the thesis is illustrated in Table 1.1 where the three main forms of excitation discussed above are shown to be applied first to a general, possibly multi-

degree-of-freedom (MDOF), oscillator before investigation of a sub-class of the general oscillator: a common energy harvester model. In general, the flow of the chapters is dictated by the type of excitation, starting with the simplest, white noise, and moving on to analyse the more complex non-white and harmonic plus white excitation. Within the investigation of each type of excitation, theory for all, or at least a wide variety of, nonlinear systems is developed and then assessed by using energy harvesting as an application. Chapter 4, however, is an exception as it contains the experimental validation of Chapter 3. Finally, the thesis finishes with Chapter 6 which documents the conclusions and suggestions for further work.

	White Noise	**Non-white Noise**	**Harmonic + White Noise**
General Oscillator	Chapter 2 and [47]	Chapters 3 and 4	Chapter 5
Energy Harvester	Chapter 2	Chapter 3	Chapters 2 and 5

Table 1.1 Outline of the content of the thesis displaying which chapter contains information on each type of excitation and the system it is applied to.

In order to provide a foundation for the work of Chapters 2-5 and reference previous work, the remainder of this chapter provides an introduction to the appropriate engineering areas, some of the prevalent methods and a detailed review of the relevant literature. Due to the different approaches and applications of each chapter, this work spans a wide range of the academic literature. As such, the literature review is split into four sections: an introductory discussion of standard methods in nonlinear and stochastic vibration theory, a review of the energy harvesting literature, a discussion of the Wiener series approach to nonlinear systems and finally a survey of methods for studying combined deterministic and randomly forced oscillators.

1.2 Introduction to Nonlinear and Stochastic Vibration Theory

1.2.1 Stochastic Vibration Theory

Random, or stochastic, vibrations occur in a wide range of engineering applications therefore theoretical understanding is necessary in order to model the systems and account for issues such as fatigue, the likelihood of failure and power dissipated by damping. Random vibrations take a variety of forms, but are generally split into two categories pertaining to their frequency

content: narrowband, having a dominant frequency band, and wideband, including all relevant frequencies to a similar extent. For randomly forced linear systems, the input can be simply related to the output and a number of the basic principles involved are discussed below. A useful text book on random vibration is [68], which can be referred to for further detail.

A critical tool for stochastic analysis is the probability density function (PDF), which provides information about how likely a random variable is to take any given value. A lot of information about a system can be retrieved from its PDF, including the likelihood of the response exceeding a specified value and the mean squared value of the response.

Another important tool is the correlation function, which assesses how related two random processes are at different times. A special type, the autocorrelation function, which is the ensemble average of the multiplication of the same random process at two different times, is a mathematically useful tool for examining the frequency content of a random process. If the Fourier transform of the autocorrelation function is taken the spectrum of the random process is found, which provides information about the frequencies present in the process. Additionally, it can be shown that the area under the spectrum gives the mean squared value of the random process, which provides a useful measure of the extent of variation of the process. The spectrum is of particular use for a linear system when relating a random input to the output, as it can be shown that the square of the magnitude of the system's frequency response acts like a filter on the input spectrum to provide the output spectrum. From this the mean squared value of the response can be found via integration over its spectrum.

1.2.2 Nonlinear Vibration Theory

Perfectly linear systems are unusual in practice although linear theory is often found to provide accurate results for many weakly nonlinear systems. When stronger nonlinearity is encountered, a number of approximate analytical and geometrical techniques exist for describing deterministic nonlinear vibrations. Often the simplest and most reliable solutions arise from time integration of an equation of motion, but this is computationally intensive so some of the more sophisticated techniques are briefly described below.

For weakly nonlinear systems, the method of perturbation seeks to find the dominant linear response and then use it to assess how the nonlinearity affects this response. Another useful technique is using harmonic balance, where, depending on the accuracy required, the output is assumed to be comprised of a chosen number of harmonics. This assumed output can be substituted into the equations of motion and the magnitude of each harmonic can be found if any additional harmonics generated are assumed to be negligible. When only the forcing frequency is used this method is called the describing function. A useful textbook describing these techniques is [92].

An illustrative geometric method that conveys a lot of information about a system is to plot the system response in the phase plane, plotting velocity against displacement. Stable and unstable equilibrium points and limit cycles can be found analytically to generate a picture of how a system behaves. Additionally, bifurcation analysis can be employed to understand how a system response transforms as a parameter changes.

1.2.3 Nonlinear Stochastic Vibration Theory

A lack of widely applicable nonlinear methods for solving deterministic problems suggests that when random and nonlinear vibration is combined, theories will be more complicated still. Nevertheless, various methods exist with a useful and conceptually intuitive method being equivalent linearisation described in [74]. The principle of equivalent linearisation is to represent a nonlinear system with an equivalent linear system by choosing the linear system properties that minimise the difference between the two systems. The benefit of this approach is that once the equivalent linear system has been found, linear vibration theory can be applied.

Another useful tool capable of handling stiffness nonlinearities is the Fokker-Planck equation, for which a derivation and applications are discussed in [51]. This is a partial differential equation that governs the PDF of a system forced by white noise. Some analytical solutions to the equation are known, in particular, the form of the PDF of an oscillator with nonlinear stiffness, linear damping and stationary white noise forcing can be found. A number of numerical methods also exist to solve the equation including a finite element solution by Langley [46], a cell method by Bontempi [6] and the path integral method by Wehner [87]. These methods are discussed further in Section 1.5.

For randomly forced nonlinear systems, often the statistical moments, the ensemble average of some exponent of a random variable [51], are required and can be found by manipulating the equations of motion. However, unlike in the linear case, these relationships cannot be solved as each moment depends on a higher moment, which in turn depends on a higher moment creating an infinite hierarchy of coupled equations. In order to find a solution for the desired moment, the series of moment equations must be truncated in some manner. There are a number of ways of achieving this in the literature. The simplest method, which can be shown to be the same as equivalent linearisation, is Gaussian closure, where the response PDF is assumed Gaussian and the moments are calculated using this PDF. More complex closure techniques also exist, with a notable one being that of [11] in which a more complex PDF, a truncated Gram-Charlier expansion (discussed further in Section 1.5), containing unknown coefficients is hypothesised. The moment equations provide the

information to find the unknown coefficients therefore an approximation of the PDF can be found.

Two methods commonly used in nonlinear system identification are the Volterra and Wiener series. Both of which expand a random nonlinear response into a series and are discussed in greater detail in Section 1.4

1.3 Energy Harvesting

Vibration energy harvesting is the concept of converting ambient vibrational energy into electrical energy to power small-scale electronic systems. The potential applications are limited by the power available in any given environment with many discussed in [2], but by far the most prevalent is to power wireless sensor networks.

In general, harvesters consist of an oscillatory mechanical system and a transduction mechanism that produces electrical energy from the motion. Three prominent transduction methods exist: piezoelectric, electromagnetic and electrostatic each illustrated in Figure 1.1. For a piezoelectric cantilever harvester the excitation causes deflection of the beam, which strains piezoelectric films on the cantilever generating a current. An electromagnetic harvester generally consists of an oscillating magnet, possibly at the tip of a cantilever and a coil through which the magnet oscillates such that a current is induced when the cantilever vibrates. Electrostatic energy harvesters usually involve capacitor plates with different voltages, where a current is induced as the distance between the plates varies due to motion and work is done against the electrostatic force.

A number of reviews of the energy harvesting literature exist, with a comprehensive, and highly cited one being [4] which states the equations of motion of a harvester and power equations under harmonic forcing. The three main transduction mechanisms outlined above are described in detail and the relevant advantages and disadvantages of each are discussed. It is concluded that piezoelectric transduction is the simplest and is well suited to miniaturisation to the MEMs scale; electromagnetic is a well-established technique, but miniaturisation can be difficult; meanwhile electrostatic transduction is well understood, but requires an initial polarising voltage or charge that can be a problem. The paper also contains tables comparing various devices of different research groups, although no metric is used to allow easy comparison of very differently sized devices from 1nW at 60mm^3 to 7mW at 9cm^3.

To improve comparison of devices, a useful review [62] discusses and applies various performance metrics, including some discussion on which transduction mechanisms work best in which environments. Two useful metrics discussed are harvester effectiveness, E_H,

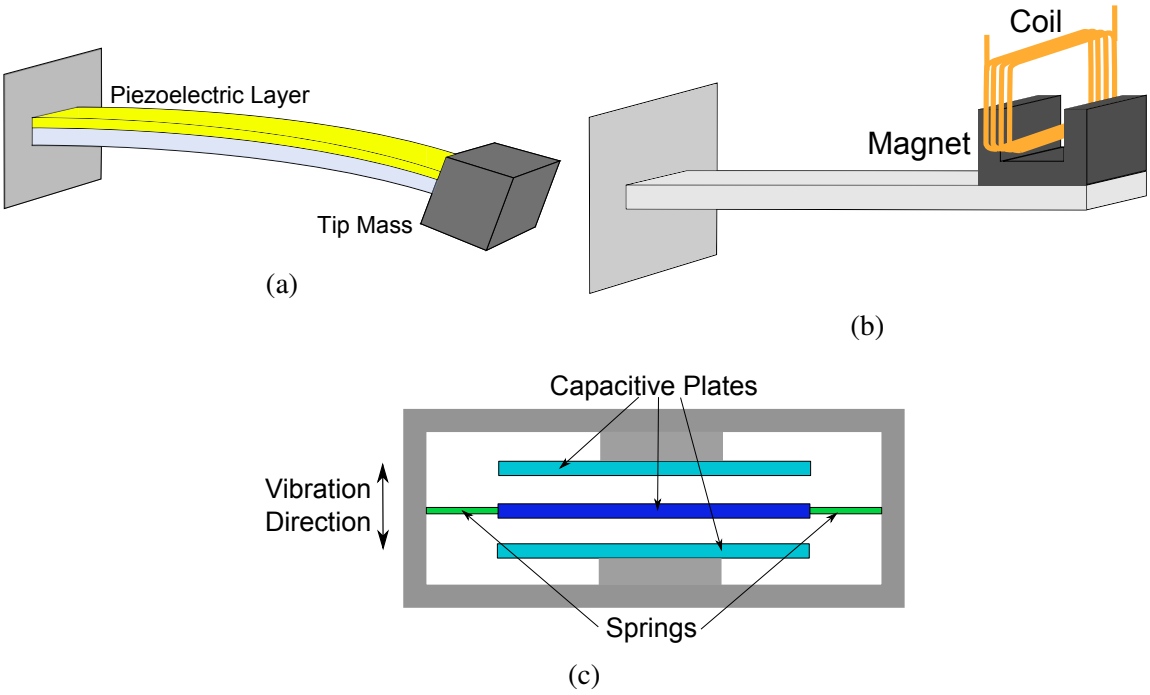

Fig. 1.1 Illustrations of common a) piezoelectric, b) electromagnetic and c) electrostatic energy harvester designs.

the ratio of useful power output to maximum possible output where the latter is known for harmonic forcing and volume figure of merit, FOM_v, similar to E_H, but maximum possible output is changed to a benchmark value for a cubic device with given density to compare devices as a function of their overall size. Harvesters from a number of research groups are plotted against these metrics to allow for comparison of devices. It should be noted that no metric fully accounts for all important features of a design and the most useful metric may depend on the specific application and excitation, particularly when in reality devices may work away from their optimal point. The paper comments that although the bandwidth of devices is rarely available in the literature, it would be useful to incorporate into metrics, since off-resonant behaviour is often a concern.

A short pragmatic analysis of which portable applications are capable of being powered by energy harvesters is also presented. The theoretical maximum power harvested for harmonic forcing at realistic human frequencies is found in terms of the size of a device. An estimate is made of the size of device needed to power four different applications: a sensor node, wristwatch, mobile phone and laptop. It is shown that a sensor node and wristwatch are capable of being powered by a sensibly sized device, whereas a mobile phone or laptop will need an ideal harvester almost as big as itself and forced continuously at 10Hz to supply

enough power. A comparison is made to battery performance, taking a lithium-ion battery of 1kJ/cm^3 capacity, if charged once per year provides approximately 30μW/cm^3, which is comfortably within the theoretical maximum power density of a resonant energy harvester.

As seen in the harvester comparisons in [62], even in 2008 a large number of devices have been designed and tested. To give an idea of the research field, two useful papers showing a systematic investigation of two straightforward, small-scale harvester designs are selected for discussion here. In [75] a simple piezoelectric harvester is designed to remain within a volume of 1cm^3 and different geometries are assessed within this constraint. A detailed theoretical analysis of the device is provided, including the electronics and properties of the piezoelectric layers. Theory and experiment are compared and shown to be in reasonable agreement.

A number of design considerations to optimise the output power are described including maximising the oscillating mass and modifying the geometry. The 1cm^3 device produces 375μW with vibrations of 2.5m/s^2 magnitude at 120Hz. The paper shows that a transmitting device that transmits intermittently can be powered by the harvester if it is used to charge a capacitor, which is discharged when the power is needed for transmission. No comparisons to other devices are given, possibly due to there being few others to compare to at the time of publication, so while this device is proved to be useful, it is difficult to show it is the best method.

The electromagnetic harvester of [3] was designed with a specific application in mind; harvesting from an air compressor unit. The harvester has a fixed coil and oscillating magnets attached to the tip of a cantilever beam. A heavy tungsten mass is placed on the tip as it is shown that power is proportional to the mass of the oscillator. Each component is assessed with a variety of analysis techniques, such as finite element modelling, in order to optimise them for practical use and for the excitation of the given application.

The experimental device is assessed and found to match the theoretical predictions that 30% of the input energy would be converted into useful electrical energy. The details and performance characteristics are well documented; the 0.15cm^3 device produces a power of 46μW in a resistive load of 4kΩ from 0.59m/s^2 acceleration at resonance of 52Hz. This is compared to a number of other devices using the normalised power density metric, which is the power output divided by acceleration level squared and volume. This harvester performs significantly better than the competing devices (including the device of [75] discussed above) by this metric, although it also mentions that bandwidth information would be useful to include in a metric.

Theoretical analysis of harvesters subject to harmonic excitation is common (see for example [3, 20, 21, 71]), with linear systems being generally well understood within standard

linear theory. However, a notable paper [80] investigates the optimal relationship in a linear harvester between the mechanical and electrical damping and concludes that, similar to electrical impedance matching, maximum power is transferred to the electrical circuit when the damping ratios are the same. Papers analysing nonlinear systems often use the methods described in Section 1.2.2, particularly to find the frequency response of the Duffing oscillator.

Many harvesters, including the ones of [75] and [3] discussed above, are approximately linear and are designed to resonate at a specific forcing frequency. If, however, the forcing frequency were to shift, the devices would no longer resonate and could have a significantly lower power output. This concern has created demand for harvesters with a wider bandwidth and a number of ideas have been suggested to accomplish this. A review of the methods available to increase bandwidth can be found in [99], with prominent ones being periodic or continuous tuning of the resonant frequency to match the excitation frequency, using an array of different frequency resonators so that one is always resonant or most significantly using nonlinear systems.

In general Duffing oscillators have been sought as they can be easy to design and if the higher energy orbit of a backbone curve could be exploited, the power output could be high. It is difficult to find a consensus in the literature that nonlinear harvesters of this type are superior to linear ones, largely due to the bandwidth being difficult to define for nonlinear devices and the trade-off between maximum power and bandwidth being subjective and application specific.

A nonlinear harvester design of particular interest is that of the double potential well, or bistable, harvester, an example of which is shown in Figure 1.2 where magnets are used to create two equilibrium positions for a beam. Two reviews of bistable devices are [32] and [70], where it is discussed that the premise of the bistable device is that it exhibits high energy orbits transitioning between the two potential wells. It is not completely clear whether the presence of low energy orbits is abundant enough to detract from the benefit of the high energy ones in situations where noise intermittently knocks the response from one to the other.

A particular benefit of the bistable harvesters is their frequency response, which is generally of a higher amplitude over a larger frequency range than linear and other nonlinear counterparts. Additionally, bistable devices often display some softening behaviour meaning that as the oscillation amplitude increases, the frequency decreases. Improved performance at low frequencies is therefore often observed and is of particular benefit in energy harvesting since the general trend is that the frequency of ambient vibrations is lower than those at which it is easy to create a device. There are no strong or overwhelming conclusions that

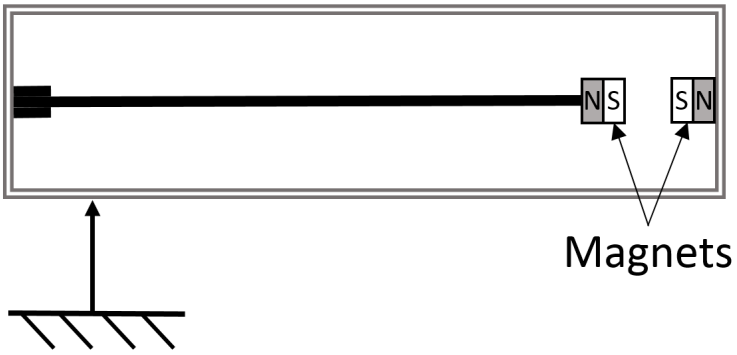

Fig. 1.2 Bistable energy harvester where magnets create two equilibrium positions.

bistable devices are certainly better than monostable ones for harmonic forcing, again largely due to the lack of useful metrics as discussed further in [70]. Nor is it obvious why a device with a potential barrier should generate a higher velocity and therefore power response than one without such an impedance. It is, however, clear that the widened and lowered frequency response is of significant benefit.

1.3.1 An Example: Powering a Tyre Pressure Measuring Sensor

The papers discussed above along with many others found in the literature take a possible working environment, simplify it to a sinusoidal source and try to replicate it in the laboratory. A useful paper and practical discussion that fits an energy harvester to a real application and assesses its suitability is undertaken in [85]. The application investigated is assessing how an energy harvester performs when powering a tyre pressure sensor embedded within a car tyre. The importance of correct tyre pressure to efficiency and safety is briefly discussed and the evolution of pressure monitoring methods, from external pressure monitoring to in-tyre battery powered sensors (requiring battery replacement) are mentioned. The harvester selected is a simple piezoelectric MEMS harvester with packaging approximately the size of a coin. Little emphasis is put on the design of the harvester, the majority of the analysis is directed towards its suitability for the application.

The harvester receives either mainly noise or mainly shock excitation depending on whether it is placed on the wheel rim or inner surface of the tyre respectively. It is found that on a tyre surface mounted harvester the shock produced as the tyre patch that the harvester is mounted on hits the road with every tyre revolution is enough to power the sensor. For example at a driving speed of 70kph an average power of 30μW is produced, which is sufficient to power a standard tyre pressure measuring system that requires an average power

of 7μW. A critical concern, however, is the reliability of such a harvester since the shock values can be extremely high, approximately 120g at a car speed of 60kph. An additional problem not discussed in the paper is what would happen when the car is not at a sufficient speed for energy harvesting. It seems likely that a battery would need to be charged by the energy harvester, which then powers the pressure monitoring circuitry. Nonetheless, energy harvesting seems to be an extremely useful potential power source for such applications.

1.3.2 Random Excitation

As suggested above, quantification of realistic excitation profiles is of concern for the application of energy harvesters. The majority of initial research in the field focussed on harmonic excitation leading to lightly damped resonant devices that neglect the presence of noise despite its occurrence in all realistic applications and the possibility that it could contain a significant proportion of energy to be harvested. Over the past few years a large body of work has been undertaken to investigate harvester performance to random excitation and, similar to harmonic harvesters, nonlinear designs such as the Duffing oscillator are of considerable interest due to potential performance benefits.

Theory based on stochastic excitation has lagged behind harmonic theory, but has been more prominent recently. One of the most notable discoveries is that for white noise base acceleration, it can be shown that the power harvested is proportional to the oscillating mass and the noise intensity and independent of the system used to dissipate it. This result has been partially shown or derived for simple or specific systems in a number of ways [13, 25, 28, 77], but by far the most general and complete proof is that of [47], extended in [48]. Here it is shown that for an arbitrary degree of freedom system with general nonlinearity dependent on displacement and velocity and excited by stationary white noise acceleration, the power, P, dissipated is

$$P = \frac{\pi S_0 M_{Tot}}{2} \tag{1.1}$$

where S_0 is the spectrum of the base acceleration and M_{Tot} is the total mass of the oscillator. This is derived using a variety of methods; using an equivalent linearisation argument, using the Fokker-Planck equation and by manipulating the equations of motion directly. Additionally, it is shown that if a general electrical circuit is coupled to the mechanical system, the energy dissipated by the mechanical damping plus the energy converted to electricity will be equal to the power in Eq. (1.1).

The work of [47] is extended in [48] to account for a more general range of systems. This includes systems that are constrained to remove a degree of freedom and are shown to dissipate less power than that of Eq. (1.1) and also time varying systems for which

results must be averaged over time as well as over an ensemble. Non-stationary systems are discussed further in Chapter 2 and the effect of constraining a system is illustrated in Chapter 3. Additionally [48] shows that for a wide class of systems, those that exhibit detailed balance, the power calculated using Eq. (1.1) will be greater than or equal to the power dissipated under non-white excitation where the peak of the spectrum is taken as S_0. The power from white noise excitation can therefore be thought of as an upper bound for these types of systems.

As with harmonic excitation, the bistable device is again of particular interest in the literature for stochastic vibrations [9, 10, 14, 32, 37, 56, 60, 70, 97]. The two reviews discussed above for harmonic forcing, [32] and [70], both discuss stochastically forced bistable devices, but [32] suggests that they are not well understood and more work should be done. A practical paper that presents simply the benefits of bistability experimentally is [10] where power benefits are shown with an optimal potential well shape. Cottone usefully plots how the power dissipated varies as the a geometry parameter responsible for the level of bistability varies for three different levels of noise and shows that there is an optimally bistable configuration.

Similar to harmonic forcing of bistable devices and consistent with observed results, a conceptual argument for why increased power is displayed is generally accepted: increased power is observed when inter-well dynamics are present. Again, it is not particularly well understood why the addition of a potential barrier assists a larger velocity and therefore power response and additionally, no clear sudden increase in power is observed when inter-well dynamics occurs, it is generally a smoother increase. Bistable harvesters are investigated further in Chapter 2 via a new approach that clarifies why benefits of the design are observed.

Since it seems that inter-well dynamics of a bistable oscillator produces additional power, an interesting idea to encourage inter-well crossover is that of [58], known as stochastic resonance. This involves periodically modulating the shape of the potential to encourage the response to continuously escape into the other potential well. An increase in output power using this method has been shown in [50, 58, 65, 98]. However, unfortunately in the primary paper, [58], the forcing used has a variety of harmonic components, so is difficult to conclude from and compare to other devices. The potential benefits of stochastic resonance for energy harvesting are not thought to be great and are discussed further in [48] and Chapter 2.

To supplement the experimental investigations there are a number of supporting theoretical papers attempting to understand the underlying physics of energy harvesters under random excitation in order to exploit it. Many studies into optimal systems for harvesting white noise excitations have been undertaken, for example [13–15, 25, 28, 36, 37, 55, 100], often with a particular focus on the potential of nonlinear systems to improve power trans-

fer. In general, the best system depends on the electrical circuit used; if only a dissipative electrical component is used, the power can be simply found and is independent of stiffness nonlinearity in keeping with [47]. However, if a circuit including a capacitor or inductor more representative of piezoelectric or electromagnetic harvesting respectively is used, it is found that the stiffness potential will affect the power output, with a bistable potential with inter-well dynamics proving effective. This is consistent with the experimental results of [10] and is discussed in more detail in Chapter 2.

Approaches for assessing harvester performance under white noise excitation vary, but a useful one for calculating the power dissipated is to find the PDF of the response. The Fokker-Planck equation governs the PDF so has been used to provide the response statistics of a nonlinear harvester, with a simple electrical circuit [13, 14] and for a more complex circuit in [15, 55]. With the simple circuit, the equations of motion can be reduced to use a known solution to the Fokker-Planck equation, whereas with the more complex circuit, more sophisticated solution techniques are required. In [15], the Fokker-Planck equation is manipulated to generate moment equations which are closed using the cumulant neglect closure technique and then solved numerically. Alternatively, [55] uses a Galerkin approach to iterate the form of the response PDF.

The response of harvesters to coloured, or filtered white noise, excitation, thought to be more realistic than white noise in some applications, has been calculated for nonlinear oscillators with a simple resistive circuit in [13, 14] and for a linear oscillator with a more complicated circuit in [61]. In [13, 14] coloured noise is applied by filtering white noise and creating extra variables in the Fokker-Planck equation which is then solved either by solution of the coupled moment equations [13] or using a decoupling procedure to provide a simpler approximate Fokker-Planck equation then an iterative procedure to find the PDF [14]. However, for a linear system, [61] solves for the second statistical moments, finding terms cross-correlated with the noise terms using Laplace transforms. Once again, [14] concludes that stiffness nonlinearities hinder power extraction if there is one potential well, but an optimal double potential well shape can be found where the response displays inter-well dynamics that increase power output. [61] found that a linear oscillator should be designed with low natural frequency and capacitor charging time in order to extract the most energy.

For non-white noise, the power output depends more strongly on the type of noise and system investigated, but since the majority of cases have linear damping and so satisfy detailed balance, the power from white noise can be thought of as an upper bound on the power available according to [48]. Additionally, a number of experimental investigations into harvesting under non-white noise have been conducted [9, 10, 33, 57, 60, 69] and also tend to favour bistable systems.

In theoretical papers, noise is assumed to be of a mathematically simple form such as white or coloured noise. Whether these assumptions are realistic is discussed in a productive review paper [26] which assesses the current capability of nonlinear harvesters to realistic noise profiles from human motion and bridge vibrations. Time histories of these vibrations were fed into some common harvester models and the performance was observed. In particular the effects of the deliberate nonlinearities were discussed and found to generally not be as beneficial as hoped with the theoretical noise input leading to the conclusion that more careful consideration of the excitation profile is required.

A particularly pragmatic and useful paper that investigates realistic excitation profiles is [72]. Rantz suggests a number of common issues with the qualification of vibration sources such as over-simplification, particularly for mathematical convenience, or selecting a small sample of possible sources. A large database of vibration data from 333 sources is broken down into subclasses according to the source type such as vehicle sources and vibration type such as filtered noise sources. Of particular interest to this thesis, of the 333 sources, 12% were designated as white noise and 17% as filtered noise (predominantly from structural sources). A very approximate, but nonetheless useful estimate is made that 23% of the sources would be best harvested with a linear resonant device and 53% with a cubic stiffness. Whilst it is clear from [26] and [72] that realistic input excitation must be accounted for, this does not diminish the value of starting theoretical investigations using approximations and assumptions to provide a mathematically simple system in order to explore the underlying dynamics.

1.3.3 Upper Bounds on Power

In general, with the exception of linear harmonic harvesting for which theory is straightforward, the approach to energy harvesting is to select an excitation profile and optimise a chosen type of device to this input. However, the maximum power it is possible to harvest, or put differently, the maximum power available in a given excitation, is rarely known therefore both the selection of the type of system and the optimisation procedure is unguided and it can be difficult to assess the performance of the resulting design. A useful approach where possible is to calculate the upper bound on power attainable for a given excitation in order to provide a target for a designer to aim towards. Additionally, the calculation of an upper bound can illuminate what type of devices will come closest to it, provide a useful metric to compare different devices against and allow a preliminary estimation of the harvester size necessary in a given operating environment for a given power requirement.

A simple bound on power from white noise excitation is provided by Eq. (1.1) as discussed above and according to [48] it can also provide an upper bound under non-white

random excitation for systems that exhibit detailed balance. For white noise inputs a tighter upper bound more specifically for electrical power dissipation is derived in [29] where a typical harvester circuit is coupled to the mechanical oscillator and it is found that a low frequency device increases the power bound. Additionally, the performance of linear and nonlinear harvesters against these bounds is compared and nonlinear devices are shown to provide no improvement over linear ones.

An alternative method, employed in [30, 38, 39], for a power bound from a general force input is to analyse input energy under various constraints (such as a maximum allowable displacement) in order to devise a strategy for maximum power transfer. In general this involves time-integration of the power input by the base subtracted by the power lost to mechanical damping and calculating the velocity response that will maximise this value. This is effective for deterministic or relatively consistent vibrations, but less capable of handling random excitation. Additionally, unphysical or difficult to realise responses are often found to provide the optimal velocity profile, although [39, 40] suggest a type of system capable of performing well. Differently, in [42] a performance metric that includes the size of the device is suggested in order to compare different systems under stochastic excitation. However, the maximum power must be calculated for any system in order to apply the metric therefore its use as a general power bound is limited.

There is a comparably large body of literature related to the electronics of energy harvesting as to the vibrations, but this is not considered in this thesis as its focus is on mechanical vibrations. Popular, simple electrical circuits for energy harvesting will be used in this report and are discussed further in Chapter 2.

1.4 Wiener Series

For energy harvesting applications it is the power dissipated by a randomly excited system that is of interest. An interesting and useful method for analysing nonlinear vibrations from Gaussian white noise is using a Wiener series approach, which can be easily applied to find the power input from random excitation. First developed by Norbert Wiener [91] as an adaptation of the Volterra series, the Wiener series is an orthogonal series expansion of a random response. It is a commonly used tool for nonlinear system identification, particularly for physiological systems [53, 84, 90].

A thorough description and explanation of both Volterra and Wiener theory and their applications can be found in [76], from which a short introduction to the elements of the theory relevant to this thesis is presented below.

The Volterra series describes the output, $y(t)$, of a nonlinear system with any input, $x(t)$, as a series of terms called Volterra functionals as follows

$$y(t) = \sum_{n=0}^{\infty} \mathbf{H}_n[x(t)] \tag{1.2}$$

where $\mathbf{H}_n[x(t)]$ is the nth order Volterra functional defined as

$$\mathbf{H}_n[x(t)] = \int_{-\infty}^{\infty} \ldots \int_{-\infty}^{\infty} h_n(\tau_1, \ldots, \tau_n) x(t-\tau_1) \ldots x(t-\tau_n) d\tau_1 \ldots d\tau_n. \tag{1.3}$$

The first order functional therefore looks like a convolution integral and is the only term required to completely define a linear system. However, for a nonlinear response the higher order functionals relate the input at a number of different times to the output. The $h_n(\tau_1, \ldots, \tau_n)$ functions are called kernels and are zero if any argument is less than zero since they are causal. These kernels must be calculated in order to provide the Volterra functionals and thus define the system.

Methods for calculating the Volterra functionals will not be discussed here except to say that difficulty in isolating contributions from, and therefore measuring, just one kernel are a major disadvantage of this technique. A second critical drawback is that the series will not always converge. For a white noise input, both of these issues can be alleviated via rearrangement into an orthogonal series: the Wiener series. Similar to the Volterra series, the Wiener series describes the nonlinear response as a sum of functionals called G-functionals as follows

$$y(t) = \sum_{n=0}^{\infty} \mathbf{G}_n[k_n; x(t)]. \tag{1.4}$$

Differently in the Wiener series case, each G-functional is comprised of a series of Volterra functionals now denoted $\mathbf{K}_{p(n)}[x(t)]$ where p is the order of the Volterra functional and n is the order of the G-functional that it belongs to such that

$$\mathbf{G}_n[k_n; x(t)] = \sum_{j=0}^{n} \mathbf{K}_{j(n)}[x(t)]. \tag{1.5}$$

The Volterra functionals $\mathbf{K}_{j(n)}[x(t)]$ are chosen such that the G-functionals satisfy the orthogonality condition

$$\mathrm{E}[\mathbf{H}_p[x(t)]\mathbf{G}_n[k_n; x(t)]] = 0 \qquad \text{for} \quad p < n \tag{1.6}$$

where $\mathrm{E}[Z]$ represents the ensemble average of a random variable Z and $\mathbf{H}_p[x(t)]$ is any pth order Volterra functional. Under this condition alternate Volterra kernels in a G-functional

series are zero and the first three and the nth G-functional for a white noise input of autocorrelation $R_{xx}(\tau) = \pi S_0 \delta(\tau)$ are

$$\mathbf{G}_0[k_0;x(t)] = k_0 \tag{1.7}$$

$$\mathbf{G}_1[k_1;x(t)] = \int_{-\infty}^{\infty} k_1(\tau_1)x(t-\tau_1)d\tau_1 \tag{1.8}$$

$$\mathbf{G}_2[k_2;x(t)] = \int_{-\infty}^{\infty}\int_{-\infty}^{\infty} k_2(\tau_1,\tau_2)x(t-\tau_1)x(t-\tau_2)d\tau_1 d\tau_2 - \pi S_0 \int_{-\infty}^{\infty} k_2(\tau_1,\tau_1)d\tau_1 \tag{1.9}$$

$$\begin{aligned}\mathbf{G}_n[k_n;x(t)] = \sum_{m=0}^{\text{floor}[n/2]} &\int_{-\infty}^{\infty}\ldots\int_{-\infty}^{\infty} \frac{(-1)^m n!(\pi S_0)^m}{(n-2m)!m!2^m}\times \\ &\int_{-\infty}^{\infty}\ldots\int_{-\infty}^{\infty} k_n(\tau_1,\tau_1,\ldots,\tau_m,\tau_m,\sigma_1,\ldots,\sigma_{n-2m})d\tau_1\ldots d\tau_m\times \\ &x(t-\sigma_1)\ldots x(t-\sigma_{n-2m})d\sigma_1\ldots d\sigma_{n-2m}.\end{aligned} \tag{1.10}$$

The function $k_n(\tau_1,\ldots,\tau_n)$ is called the nth order Wiener kernel and is to be found in order to describe the system under investigation. The kernels in the lower order Volterra functionals within a G-functional, $\mathbf{K}_{j(n)}[x(t)]$ when $j < n$, can be calculated from the nth order kernel and are therefore called derived kernels. For the Wiener series, by extending Eq. (1.6), any two G-functionals of different order are orthogonal meaning that the contribution from any functional and therefore kernel can be isolated and measured.

In this thesis, since it can completely define the power dissipation of a system, only the first kernel is of interest, so the method for its calculation is described below. For discussion and calculation of higher order kernels see [76], although the zeroth order kernel is clearly the time average of the output.

The input $x(t)$ at a time delay τ, $x(t-\tau)$, can be thought of as a first order time delay Volterra functional

$$\mathbf{D}_1[x(t)] = \int_{-\infty}^{\infty} \delta(\tau_1-\tau)x(t-\tau_1)d\tau_1 \tag{1.11}$$

$$= x(t-\tau). \tag{1.12}$$

Multiplying the output $y(t)$ by this time delayed input and taking the ensemble average gives

$$\begin{aligned}
\mathrm{E}[y(t)x(t-\tau)] =& \mathrm{E}\left[\mathbf{D}_1[x(t)]\sum_{n=0}^{\infty}\mathbf{G}_n[k_n;x(t)]\right] && (1.13)\\
=& \mathrm{E}[\mathbf{D}_1[x(t)]\mathbf{G}_0[k_0;x(t)]] + \mathrm{E}[\mathbf{D}_1[x(t)]\mathbf{G}_1[k_1;x(t)]] && (1.14)\\
=& \mathrm{E}[k_0 x(t-\tau)] + \mathrm{E}\left[\int_{-\infty}^{\infty} k_1(\tau_1)x(t-\tau_1)x(t-\tau)d\tau_1\right] && (1.15)\\
=& \pi S_0 k_1(\tau) && (1.16)
\end{aligned}$$

where $k_0 = 0$ for a zero mean output and the orthogonality condition of Eq. (1.6) has been employed. The first Wiener kernel can therefore be found simply from the cross-correlation between the input and the output. The kernel can also be considered in the frequency domain, denoted $K_1(\omega)$, as the Fourier transform of the time domain kernel thus transforming Eq. (1.16) yields

$$S_{yx}(\omega) = \pi S_0 K_1(\omega). \tag{1.17}$$

One disadvantage of the Wiener series is that it is valid only for a white noise input, although in [49] and summarised in [76] a method for extending to non-white inputs is discussed. A signal created from filtered white noise is taken as the input and is reverse filtered into a white signal before being input to a nonlinear system. The Wiener theory discussed above can then be applied using the white noise input and the reverse filter included to amend the results. In Chapter 3, the Wiener series is extended to non-white noise using a different derivation, but with the same result.

1.5 Combined Deterministic and Random Forcing

When analysing real engineering applications mathematically, many vibration problems are approximated as systems that are either harmonically or randomly excited. However, in many cases broadband noise with a series of harmonics is exhibited or deliberately generated such as the response of a helicopter [34], vibration of turbine blades under turbulent flow [59] and stochastic resonance [88].

More recently, this form of excitation is of interest in the field of energy harvesting, where devices are tuned to operate within a narrow frequency band and their robustness to disturbances from noise must be assessed [31]. Some energy harvesting papers have also performed experiments using this type of forcing [12, 23], although these are not discussed here since it is the vibration theory that is of interest.

Although still an idealisation, excitation modelled as a sinusoid superimposed onto broadband noise can more closely resemble the realistic case and should therefore more accurately model the system dynamics than approximating the excitation as simply harmonic or broadband noise. A number of techniques have been used to model nonlinear responses to this form of excitation and range from approximate analytical to numerical methods.

The analytical attempts to solve this problem are, naturally, approximations and are mentioned in passing here since they are not the focus of this work. In general they involve a combination of deterministic and stochastic nonlinear techniques to generate and solve coupled harmonic and noise equations [1, 7, 27, 67, 74, 86].

A useful and simple method is to manipulate the equivalent linearisation process to generate two coupled ODEs, one for mean terms and one for noise terms as shown in [74] and discussed further in Chapter 5. Anh et al [1] have published a similar method, but where the mean terms differential equations are solved using averaging instead of numerically like in [74] and the equations are uncoupled by using time-averaged terms. These methods have shown reasonable accuracy and generate rapid solutions. Nevertheless, the results are limited by the approximations made in order to generate solvable equations. If further accuracy is desired, numerical approaches are required.

In general, numerical methods for solving nonlinear problems with harmonic and broadband noise can be thought of as an extension of methods that solve the non-stationary Fokker-Planck equation. The finite difference [6, 45], finite element [45, 46, 79], path integration [87, 94, 93, 66] (described in Appendix A) and cell [6, 82] method are all applicable to non-stationary problems and have been used to investigate this form of excitation. Unfortunately, these techniques are computationally intensive, so are expected to be relatively slow to solve although no data has been found for comparison.

Of particular interest in Chapter 5 are global weighted residual solutions which have been applied to random vibration problems although few have been applied to random combined with harmonic vibration. These involve proposing the form of the probability density function with unknown coefficients and substituting it into the Fokker-Planck equation. Since the PDF will generally not satisfy this equation, a residual error will occur which can be minimised by being multiplied by a suitable weighting function and integrated over the entire state-space. A number of weighted integrals can be taken to generate a simple set of equations that are solved to find the coefficients that govern the shape of the PDF. In these solutions, the results depend on selection of a suitable proposed PDF that can reasonably approximate the true PDF and selection of suitable weighting functions that project the solution onto the relevant regions of state space.

A proposed PDF in the form of a sum of Gaussian distributions with state variables of varying exponent as weighting functions has been investigated [18], but found to have limited accuracy for responses far from Gaussian. In [17, 19] an exponential function containing polynomials of the state variables has been used as the PDF with state variables of varying exponent multiplied by a Gaussian distribution used as weighting functions. The sensitivity to the standard deviation used in the Gaussian weighting function is shown in [17] to be important and a method for selecting sensible weight functions has been devised and shown to work well.

In [5, 89] a Gram-Charlier type A series has been used as the proposed PDF and Hermite polynomials are used as weighting functions such that their orthogonality can be exploited to enable rapid solution. The Gram-Charlier type A series is limited in that it permits negative probabilities and only near to Gaussian responses so the Gram-Charlier type C series which accounts for polynomial qualities of the logarithm of the PDF has been used in [63] producing strong results. A similar method has been applied successfully to harmonic and noise excitation of a first order system in [95].

Another improvement on the Gram-Charlier type A method of [5, 89] is to use a more realistic distribution multiplying the polynomial series than the Gaussian of a Gram-Charlier type A series. This could come from equivalent linearisation, a known analytical solution of a similar Fokker Planck equation [54] or stochastic averaging to find the PDF of the peak responses [41, 78, 86]. A set of orthogonal polynomials can then be created and solved for this distribution. These methods have shown good accuracy and work well for higher order systems.

A method that has produced good results in the physics literature is the method of matrix continued fractions [43, 73]. It is similar to the weighted residual methods discussed above, but instead of solving coupled algebraic or differential equations for the stationary or non-stationary cases respectively, it solves for the PDF coefficients by noting that the equations from the weighted residuals can be formed into a tri-diagonal recurrence relation and therefore solved using matrix continued fractions.

The relative advantages and disadvantages of each of these methods is discussed in the relevant papers, but which one to choose will generally depend on two criteria: accuracy and computational efficiency. In Chapter 5 the global weighted residual methods of [5, 63, 89] will be extended to be applied to this form of excitation and compared to other methods in terms of the two criteria.

Chapter 2

Harvesting Power Bounds for White Noise Excitation

2.1 Introduction

Many mechanical systems to which an energy harvester can be attached vibrate randomly and with a spectrum covering a broad range of frequencies. When this is the case or when the bandwidth of an oscillator is considerably lower than that of its excitation, white noise is a reliable approximation of the spectrum. According to the characterisation and database used in [72], assuming white noise excitation could be reasonable for approximately 12% of vibration sources. It is therefore important to calculate the maximum power available from white noise and what type of system can achieve it.

The simple result of Eq. (1.1) from [47] is a convenient starting point as it shows that for any vibratory system under white noise excitation the power dissipated will be proportional to the oscillating mass and the magnitude of the spectrum. However, an energy harvester will consist of a mechanical oscillator coupled to an electrical circuit therefore power dissipation will be split between desirable electrical damping and undesirable mechanical damping. The work of this chapter is to calculate the maximum possible electrical power achievable for a given level of mechanical damping with a standard, but general, energy harvesting circuit.

Eq. (1.1) is useful because it provides an exact expression for the power dissipated for almost all possible oscillators. However, when an electrical circuit is coupled to the mechanical system, an exact expression for electrical power is only achievable for a limited number of systems and so it is difficult to determine the optimal design. An approach encompassing a wider range of possible systems is to calculate the upper bound on electrical power rather than an exact expression. Whilst generally unachievable an upper bound can

provide a good estimate of the maximum power available and illuminate the types of systems capable of attaining it.

It is probable that in some applications white noise co-exists with deterministic excitation or in the case of stochastic resonance [58], harmonic forcing is deliberately introduced. As discussed in [48], time-averages are required in addition to ensemble averages in order to calculate the power dissipated and the impact of the deterministic components on power dissipation is assessed in Section 2.3.

The aim of this chapter is to derive an upper bound on the power available to harvest from white noise excitation. This will allow for easy comparison between the diverse range of energy harvesters and illuminate what characteristics in a harvesting system are required to provide maximum power. In what follows, Section 2.2 derives the power bound and compares it to numerical simulations of a number of popular devices before Section 2.2.2 discusses desirable characteristics of optimal harvesters. The impact of nonlinear damping on the power bounds is discussed in Section 2.2.3 before the effect of introducing deterministic excitation to harvesters excited by white noise is explored in Section 2.3.

2.2 Upper Bounds on Power Harvested

In an effort to keep the upper bound applicable to as broad a range of harvesters as possible, an oscillator with general stiffness and electrical properties is investigated whilst still consisting of a coupled mechanical and electrical system. The analysis is concerned with a single-degree-of-freedom (SDOF) energy harvester as shown in Figure 2.1 which consists of a mass, m, that is connected to a vibratory surface via a linear damper of rate b and a nonlinear spring with restoring force $g(x)$, where x represents the displacement of the mass in relation to the vibrating base. An electrical circuit is coupled to the mass consisting of a capacitor of capacitance C and a nonlinear resistor such that the governing equations are

$$m\ddot{x} + b\dot{x} + g(x) + \theta V = -m\ddot{\xi}(t) \tag{2.1}$$

$$C\dot{V} + \frac{f(V)}{\gamma} = \theta\dot{x} \tag{2.2}$$

where θ is the electrical coupling coefficient, V and $f(V)/\gamma$ are the voltage over and current through the nonlinear resistor respectively and γ is the nonlinear equivalent of resistance used in order to scale the nonlinear resistance function $f(V)$. $\ddot{\xi}(t)$ represents the white noise base acceleration with auto-correlation function at a time lag τ of $\pi S_0\delta(\tau)$ where S_0 is the single-sided spectral density and $\delta(\tau)$ is the delta function.

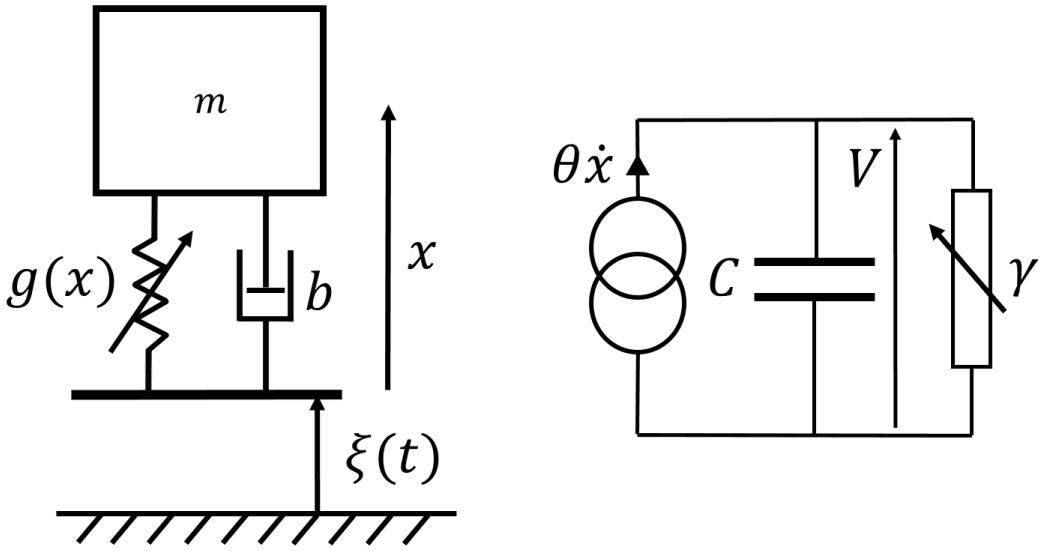

Fig. 2.1 Model of the energy harvester system with the mechanical oscillator and electrical harvesting circuit.

The harvester includes both a nonlinear spring and nonlinear resistor in order to encompass a broad range of possible harvesting devices. The capacitor in the circuit is typical of piezoelectric energy harvesting systems due to the properties of piezoelectric materials [22]. However, this system could also represent an electromagnetic harvester where voltage is exchanged for current and the capacitance becomes the coil inductance of the electromagnet [16]. The nonlinear resistor must be purely dissipative therefore $\text{sign}[f(V)] = \text{sign}[V]$. Eq. (2.2) will not account for all possible circuits as the nonlinearity of the resistor cannot represent effects from time derivatives or integrals of voltage due to components such as additional capacitors or inductors. Nevertheless, it will encompass a wider range of circuitry than the commonly assumed linear resistor and will help to assess whether nonlinear resistance profiles provide improved harvesting performance.

General nonlinear mechanical damping is not included as it prohibits the derivation of the following upper bound. Inclusion of nonlinear damping to the harvesting system and its effect on the power bound is discussed in Section 2.2.3, although in practice damping will generally be minimised so the impact on the maximum power attainable will most likely be small.

It is known from Eq. (1.1) that the power input to the system governed by Eqs. (2.1) and (2.2) is equal to $\pi S_0 m/2$ regardless of the specific system properties. This input power will be split between the desired electrical power, P_E, and the undesired mechanical damping, P_M,

as follows

$$\frac{\pi S_0 m}{2} = P_M + P_E \tag{2.3}$$

where

$$P_M = b\mathrm{E}\left[\dot{x}^2\right] \tag{2.4}$$

$$P_E = \theta \mathrm{E}\left[\dot{x}V\right]. \tag{2.5}$$

An alternative expression for the electrical power, P_E, can be obtained by multiplying Eq. (2.2) by V and taking the ensemble average of the resulting equation. Noting that $\mathrm{E}\left[V\dot{V}\right] = 0$ because the system response is stationary then yields

$$P_E = \frac{\mathrm{E}\left[Vf(V)\right]}{\gamma}. \tag{2.6}$$

Two upper bounds on the electrical power harvested, P_{EU1} and P_{EU2}, will now be calculated by manipulation of the equations of motion. Both upper bounds are required since one bound is found to limit electrical power dissipation for small γ and the other for large γ. However, at an optimal intermediate value of γ where the two bounds are equal, the maximum upper bound on electrical power is found.

The first bound, P_{EU1}, can be found from calculating the mean square velocity by squaring Eq. (2.2) and taking the ensemble average to yield

$$\mathrm{E}\left[\dot{x}^2\right] = \frac{1}{\theta^2}\mathrm{E}\left[\left(C\dot{V} + \frac{f(V)}{\gamma}\right)^2\right] \tag{2.7}$$

$$= \frac{C^2}{\theta^2}\mathrm{E}\left[\dot{V}^2\right] + \frac{2C}{\theta^2\gamma}\mathrm{E}\left[\dot{V}f(V)\right] + \frac{1}{\theta^2\gamma^2}\mathrm{E}\left[f(V)^2\right]. \tag{2.8}$$

The term $\mathrm{E}\left[\dot{V}f(V)\right]$ that appears in this equation is zero, since the response is stationary meaning that $\mathrm{E}\left[\dot{V}f(V)\right] = \frac{d}{dt}\mathrm{E}\left[r(V)\right] = 0$ where $r(V) = \int f(V)dV$.

Eqs. (2.3), (2.4), (2.6) and (2.8) can be combined to produce

$$\frac{\pi S_0 m}{2} = \frac{bC^2}{\theta^2}\mathrm{E}\left[\dot{V}^2\right] + \frac{b}{\theta^2\gamma^2}\mathrm{E}\left[f(V)^2\right] + \frac{1}{\gamma}\mathrm{E}\left[Vf(V)\right]. \tag{2.9}$$

From Eq. (2.6) the last term on the right hand side represents electrical power dissipation, for which an upper bound, P_{EU1}, is sought. Since minimisation of $\mathrm{E}\left[\dot{V}^2\right]$ will maximise electrical power, an upper bound on electrical power can be found by making the conservative assumption that $\mathrm{E}\left[\dot{V}^2\right] = 0$ (which also highlights that when designing a device for maximum

electrical power, $\mathrm{E}\left[\dot{V}^2\right]$ must be minimised). This leads to the bound

$$P_{EU1} = \frac{\pi S_0 m}{2} - \frac{b}{\theta^2 \gamma^2}\mathrm{E}\left[f(V)^2\right]. \tag{2.10}$$

A second upper bound on the electrical power, P_{EU2}, can be found by multiplying Eq. (2.1) by x and taking the ensemble average to give

$$m\mathrm{E}\left[x\ddot{x}\right] + b\mathrm{E}\left[x\dot{x}\right] + \mathrm{E}\left[xg(x)\right] + \theta\mathrm{E}\left[xV\right] = -m\mathrm{E}\left[x\ddot{\xi}\right]. \tag{2.11}$$

Since the response is stationary, by taking the time derivative of $\mathrm{E}\left[x\dot{x}\right]$ and $\mathrm{E}\left[x^2\right]$ it is found that $\mathrm{E}\left[x\ddot{x}\right] = -\mathrm{E}\left[\dot{x}^2\right]$ and $\mathrm{E}\left[x\dot{x}\right] = 0$. Additionally, $\mathrm{E}\left[x\ddot{\xi}\right] = 0$ since the displacement response at any time cannot be correlated to the excitation at that time for white noise or alternatively, the excitation does not instantaneously affect the displacement. The term $\mathrm{E}\left[xV\right]$ can be assessed by taking the ensemble average of the time integral form of Eq. (2.2) multiplied by V to yield

$$C\mathrm{E}\left[V^2\right] + \frac{1}{\gamma}\mathrm{E}\left[V\int f(V)dt\right] = \theta\mathrm{E}\left[xV\right]. \tag{2.12}$$

The stationary response means that $\frac{d}{dt}\mathrm{E}\left[\int V dt \int f(V)dt\right] = 0$ and therefore $\mathrm{E}\left[V\int f(V)dt\right] = -\mathrm{E}\left[\int V dt f(V)\right]$. If $g(x)$ and $f(V)$ are odd functions, the system is symmetric meaning that the joint probability density function (JPDF) of voltage and its integral, $p(\int V dt, V)$, is even in both $\int V dt$ and V and therefore $\mathrm{E}\left[V\int f(V)dt\right] = -\mathrm{E}\left[\int V dt f(V)\right] = 0$. In order to proceed with the upper bound for the electrical power, the restriction that $g(x)$ and $f(V)$ are odd functions must be applied although it is possible that even without this restriction, the term $\mathrm{E}\left[V\int f(V)dt\right]$ is still equal to zero. Numerical studies have been conducted to assess asymmetric functions and similarly provide $\mathrm{E}\left[V\int f(V)dt\right] = 0$, but it is difficult to say whether this will be generally true for all asymmetries.

Eqs. (2.11) and (2.12) can be combined to yield

$$-m\mathrm{E}\left[\dot{x}^2\right] + \mathrm{E}\left[xg(x)\right] + C\mathrm{E}\left[V^2\right] = 0 \tag{2.13}$$

where it can be noted that the removal of the electrical term produces the Virial theorem which equates the average value of two times the kinetic energy with the average force multiplied by displacement [24]. Eqs. (2.3), (2.4) and (2.6) can be combined with Eq. (2.13) giving

$$\frac{\pi S_0 m}{2} = \frac{b}{m}\left(\mathrm{E}\left[xg(x)\right] + C\mathrm{E}\left[V^2\right]\right) + \frac{1}{\gamma}\mathrm{E}\left[Vf(V)\right]. \tag{2.14}$$

Similar to Eq. (2.9), the rightmost term represents electrical power and so the second upper bound on the electrical power, P_{EU2}, is found when the terms $\mathrm{E}\left[xg(x)\right]$ and $\mathrm{E}\left[V^2\right]$ are minimised. The term $\mathrm{E}\left[V^2\right]$ is closely related to the electrical power term via the voltage PDF thus is not easy to minimise without minimising power whereas a minimum for the term $\mathrm{E}\left[xg(x)\right]$ can be found. It is clear that for a monostable system, with the origin at the equilibrium point, $xg(x)$ can only be positive therefore $\mathrm{E}\left[xg(x)\right] > 0$. However, for a system with more than one equilibrium position negative regions of $xg(x)$ occur on either one or both sides of an unstable equilibrium point giving the possibility of negative $\mathrm{E}\left[xg(x)\right]$. A simple argument for the positivity of this term can be made by considering equivalent linearisation [8] whereby the nonlinear system is represented by a linear system of stiffness k_{eq} that minimises the mean square error between the nonlinear and equivalent linear systems. In this case $k_{eq} = \mathrm{E}\left[xg(x)\right]/\mathrm{E}\left[x^2\right]$ and since a positive stiffness must best fit the stable system, $\mathrm{E}\left[xg(x)\right] \geq 0$ thus a minimum of $\mathrm{E}\left[xg(x)\right] = 0$ can be used in Eq. (2.14) to provide the upper bound for the electrical power.

It cannot be proven using the equations of motion Eqs. (2.1) and (2.2) that $\mathrm{E}\left[xg(x)\right] \geq 0$ since a counter-example can be found where resistance is infinite ($\gamma = \infty$) so the capacitor acts in the mechanical circuit like an extra spring. In this case the spring of the capacitor could stabilise the system about an unstable equilibrium position with a region of negative $xg(x)$, and therefore produce $\mathrm{E}\left[xg(x)\right] < 0$. However, under realistic conditions with finite resistance when $\gamma \neq \infty$ the capacitor is in parallel with a dissipative term so the system cannot be stabilised about an unstable equilibrium position therefore the equivalent linearisation argument above holds meaning that $\mathrm{E}\left[xg(x)\right] \geq 0$. This leads to the bound

$$P_{EU2} = \frac{\pi S_0 m}{2} - \frac{bC}{m}\mathrm{E}\left[V^2\right]. \tag{2.15}$$

In summary two equations have been derived, Eqs. (2.10) and (2.15), that provide two upper bounds for the electrical power: P_{EU1} and P_{EU2} respectively. In both of these equations the upper bound will depend on the statistics of the random voltage variable and therefore its PDF. Each equation can be written in terms of voltage moments by using Eq. (2.6) to substitute for the power term. An optimal voltage PDF will exist for each equation that maximises $\mathrm{E}\left[Vf(V)\right]/\mathrm{E}\left[f(V)^2\right]$ or $\mathrm{E}\left[Vf(V)\right]/\mathrm{E}\left[V^2\right]$ for Eq. (2.10) or (2.15) respectively in order to maximise P_{EU1} or P_{EU2} and provide the upper bound.

The aim of this section is to find the maximum power achievable and it is clear from the bounds in Eqs. (2.10) and (2.15) that this will occur when m and θ are maximised and b

and C are minimised. However, the optimal value of γ is less apparent. From a superficial analysis of the two bound equations at low and high γ, it is apparent that P_{EU1} increases with γ from zero to $\pi S_0 m/2$ whereas P_{EU2} decreases with γ from $\pi S_0 m/2$ to zero. If both of the power bounds can be shown to vary monotonically with γ, the maximum upper bound on electrical power, P_{Max}, will be achieved when the two bounds cross such that $P_{EU1} = P_{EU2}$ with corresponding optimal γ value, γ_{opt}. Whether or not P_{EU1} and P_{EU2} increase or decrease monotonically is investigated in what follows.

Monotonically Varying Bounds

Starting with the simpler of the two bounds, Eq. (2.15); calling $\mathrm{E}\left[V^2\right] = \sigma^2$ and writing $\mathrm{E}[Vf(V)]$ as a function of σ^2 such that

$$\mathrm{E}[Vf(V)] = \alpha(\sigma^2). \tag{2.16}$$

Using Eq. (2.16) the change in either upper bound, P_{EU1} or P_{EU2}, with respect to γ is found by differentiation of Eq. (2.6) by γ yielding

$$\frac{\partial P_{EU1/2}}{\partial \gamma} = -\frac{\alpha(\sigma^2)}{\gamma^2} + \frac{1}{\gamma}\frac{\partial \sigma^2}{\partial \gamma}\frac{\partial \alpha(\sigma^2)}{\partial \sigma^2} \tag{2.17}$$

and similarly differentiation of the right hand side of Eq. (2.15) provides

$$\frac{\partial P_{EU2}}{\partial \gamma} = -\frac{bC}{m}\frac{\partial \sigma^2}{\partial \gamma}. \tag{2.18}$$

Equating Eqs. (2.17) and (2.18) gives the value of $\frac{\partial \sigma^2}{\partial \gamma}$ which can be substituted back into Eq. (2.18) to provide the change in the bound with γ

$$\frac{\partial P_{EU2}}{\partial \gamma} = -\frac{bC\alpha(\sigma^2)}{m\gamma^2}\frac{1}{\frac{1}{\gamma}\frac{\partial \alpha(\sigma^2)}{\partial \sigma^2} + \frac{bC}{m}}. \tag{2.19}$$

The value of $\frac{\partial \alpha(\sigma^2)}{\partial \sigma^2}$ will always be positive because an increase in $\mathrm{E}\left[V^2\right]$ will always provide an increase in $\mathrm{E}[Vf(V)]$ therefore the right hand side of Eq. (2.19) will be negative and so P_{EU2} will decrease monotonically with γ.

A similar analysis for P_{EU1} does not prove that P_{EU1} increases monotonically with γ from zero to $\pi S_0 m/2$ for all possible functions $f(V)$ and voltage PDF shapes. However, a criterion can be derived that provides a quick check for whether a given electrical nonlinearity and voltage PDF will provide a monotonic bound. Starting again by defining a function to relate

the mean square value of $f(V)$ to the mean square voltage

$$\mathrm{E}\left[f^2(V)\right] = \beta(\sigma^2). \tag{2.20}$$

Differentiation of Eq. (2.10) with respect to γ and substitution of Eq. (2.20) yields

$$\frac{\partial P_{EU1}}{\partial \gamma} = \frac{2b}{\theta^2\gamma^3}\beta(\sigma^2) - \frac{b}{\theta^2\gamma^2}\frac{\partial \sigma^2}{\partial \gamma}\frac{\partial \beta(\sigma^2)}{\partial \sigma^2}. \tag{2.21}$$

Again, $\frac{\partial \sigma^2}{\partial \gamma}$ can be found by equating Eqs. (2.17) and (2.21) then substituted into Eq. (2.17) to yield

$$\frac{\partial P_{EU1}}{\partial \gamma} = \frac{b}{\gamma^3\theta^2}\frac{1}{\alpha' + \frac{b}{\theta^2\gamma}\beta'}\left(2\beta\alpha' - \alpha\beta'\right) \tag{2.22}$$

where α' and β' represent differentiation with respect to σ^2 and are both positive since the moments of $Vf(V)$ and $f^2(V)$ will both increase as σ^2 increases. The increase in P_{EU1} with γ will be monotonic if

$$2\beta\alpha' - \alpha\beta' > 0. \tag{2.23}$$

Noting that the left hand side of Eq. (2.23) can be rearranged as

$$2\beta\alpha' - \alpha\beta' = \alpha\beta\frac{\partial}{\partial \sigma^2}\left(\ln\left(\frac{\alpha^2}{\beta}\right)\right) \tag{2.24}$$

the inequality will be satisfied if α^2/β, or $\mathrm{E}\left[Vf(V)\right]^2/\mathrm{E}\left[f^2(V)\right]$, always increases as the mean square voltage, σ^2, increases. Whilst it seems likely that this is the case because the numerator is of higher order in V than the denominator, there is no obvious proof and so the condition of Eq. (2.23) is investigated further by proposing a PDF of the form $Kp(KV)$. A small increase in K, δK will provide a small decrease in σ^2, $\delta\sigma^2$, such that $\frac{\partial K}{\partial \sigma^2} < 0$. Using this PDF in Eq. (2.23) yields

$$2\int f^2(V)Kp(KV)dV\frac{\partial K}{\partial \sigma^2}\frac{\partial}{\partial K}\left(\int Vf(V)Kp(KV)dV\right) - \int Vf(V)Kp(KV)dV\frac{\partial K}{\partial \sigma^2}\frac{\partial}{\partial K}\left(\int f^2(V)Kp(KV)dV\right) > 0. \tag{2.25}$$

Removing the $\frac{\partial K}{\partial \sigma^2}$ terms inverts the inequality and making the substituting $\hat{V} = KV$ provides

$$2\int f^2\left(\frac{\hat{V}}{K}\right)p(\hat{V})d\hat{V}\frac{\partial}{\partial K}\left(\int \frac{\hat{V}}{K}f\left(\frac{\hat{V}}{K}\right)p(\hat{V})d\hat{V}\right) - \int \frac{\hat{V}}{K}f\left(\frac{\hat{V}}{K}\right)p(\hat{V})d\hat{V}\frac{\partial}{\partial K}\left(\int f^2\left(\frac{\hat{V}}{K}\right)p(\hat{V})d\hat{V}\right) < 0. \quad (2.26)$$

Performing the differentiations inside the integrals yields the criterion for monotonically increasing P_{EU1}

$$\mathrm{E}\left[Vf(V)f'(V)\right]\mathrm{E}\left[Vf(V)\right] - \mathrm{E}\left[f^2(V)\right]\left(\mathrm{E}\left[Vf(V)\right] + \mathrm{E}\left[V^2f'(V)\right]\right) < 0 \quad (2.27)$$

where $f'(V) = df/dV$. To prove that P_{EU1} always increases monotonically with γ, the criterion of Eq. (2.27) would have to be met for all possible electrical nonlinearities, $f(V)$, and all possible voltage PDFs, $p(V)$. This would require proving exhaustively and so is not investigated here, although two useful cases are shown: when $\mathrm{E}\left[h(V)\right] = h(V_K)$, for any symmetric function $h(V)$ where V_K is an arbitrary positive voltage, and for any power law electrical nonlinearity, $f(V) = AV^n$.

The former case is of interest because this PDF maximises P_{EU1} so provides the upper bound as discussed later. The left hand side of Eq. (2.27) becomes $-f^3(V_K)V_K$ which is less than zero so the bound is monotonic for this PDF. For the case where $f(V) = AV^n$, the left hand side of Eq. (2.27) becomes $-A^3\mathrm{E}\left[V^{n+1}\right]\mathrm{E}\left[V^{2n}\right]$ which is less than zero so the bound is monotonic for this electrical nonlinearity. Whether or not the criterion of Eq. (2.27) is met for other nonlinear functions, $f(V)$, could be assessed computationally by proposing a general form of voltage PDF such as

$$p(V) = B\exp\left(\sum_{n=1}^{N} a_n V^{2n}\right) \quad (2.28)$$

and using an optimisation solver to maximise the left hand side of Eq. (2.27) to see if it can go above zero.

For the remainder of this chapter P_{EU1} will be assumed to monotonically increase with γ. Whilst this seems a reasonable assumption from the criteria of Eq. (2.27) any electrical nonlinearity used by a designer should be assessed against the criterion to ensure that this assumption is valid.

Since P_{EU1} limits the power at small values of γ and P_{EU2} limits the power at large values and the power bounds vary monotonically with γ, the maximum upper bound on electrical power, P_{Max}, will be achieved when $P_{EU1} = P_{EU2}$ with corresponding optimal

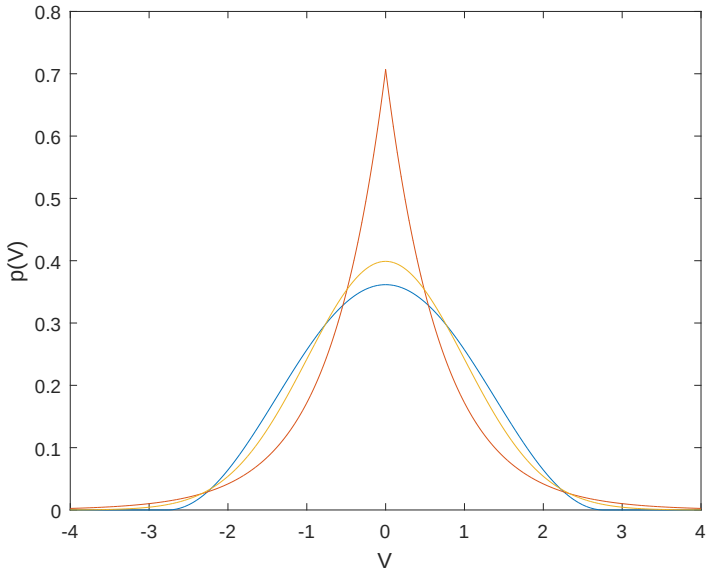

Fig. 2.2 Probability density functions of a platykurtic (blue), leptokurtic (red) and Gaussian (yellow) system all with the same mean square value.

γ value, γ_{opt}. At this point the voltage PDF must be the same for both P_{EU1} and P_{EU2}, although it is not obvious what PDF will maximise power; it could be one that maximises P_{EU1} and so $\mathrm{E}\left[Vf(V)\right]/\mathrm{E}\left[f(V)^2\right]$ or one that maximises P_{EU2} and so $\mathrm{E}\left[Vf(V)\right]/\mathrm{E}\left[V^2\right]$ or a different distribution. To illustrate this, suppose $f(V) = V^3$ meaning that maximisation of P_{EU1} requires maximum $\mathrm{E}\left[V^4\right]/\mathrm{E}\left[V^6\right]$ therefore a platykurtic voltage distribution with low tail probability. Conversely to maximise P_{EU2} requires maximisation of $\mathrm{E}\left[V^4\right]/\mathrm{E}\left[V^2\right]$ therefore a leptokurtic voltage distribution with high tail probability. Whether the maximum power point where $P_{EU1} = P_{EU2}$ is greater for a platykurtic or leptokurtic distribution is not clear and will be found for the general nonlinearity, $f(V)$, in what follows. Examples of a platykurtic and a leptokurtic distribution are compared with a Gaussian distribution all with the same mean square value in Figure 2.2.

For the maximum upper bound on electrical power $P_{EU1} = P_{EU2} = P_{Max}$ so Eqs. (2.10) and (2.15) are equated to provide optimal γ,

$$\gamma_{opt} = \sqrt{\frac{m}{C\theta^2}\frac{\mathrm{E}\left[f(V)^2\right]}{\mathrm{E}\left[V^2\right]}} \tag{2.29}$$

and therefore using Eq. (2.6)

$$P_{Max} = \frac{\mathrm{E}[Vf(V)]}{\gamma_{opt}} \tag{2.30}$$

$$= \sqrt{\frac{C\theta^2}{m}\frac{\mathrm{E}[V^2]}{\mathrm{E}[f(V)^2]}}\mathrm{E}[Vf(V)]\,. \tag{2.31}$$

Eq. (2.31) can be rearranged to give $\mathrm{E}\left[V^2\right]$ in terms of P_{Max} and the voltage moments

$$\mathrm{E}\left[V^2\right] = P_{Max}\sqrt{\frac{m}{C\theta^2}}\frac{\sqrt{\mathrm{E}[f(V)^2]\,\mathrm{E}[V^2]}}{\mathrm{E}[Vf(V)]} \tag{2.32}$$

which can be substituted into Eq. (2.15) with $P_{EU2} = P_{Max}$ yielding

$$\frac{\pi S_0 m}{2} = P_{Max}\left(\frac{b}{\theta}\sqrt{\frac{C}{m}}\frac{\sqrt{\mathrm{E}[f(V)^2]\,\mathrm{E}[V^2]}}{\mathrm{E}[Vf(V)]} + 1\right). \tag{2.33}$$

Clearly the voltage PDF that minimises $\sqrt{\mathrm{E}[f(V)^2]\,\mathrm{E}[V^2]}/\mathrm{E}[Vf(V)]$ provides the maximum value of P_{Max}. The minimum of this term is demonstrated to be unity as follows. The positive definite integral below provides an initial inequality

$$\int_{-\infty}^{\infty}\int_{-\infty}^{\infty}\left[V_2 f(V_1) - V_1 f(V_2)\right]^2 p(V_1)p(V_2)dV_1dV_2 \geq 0 \tag{2.34}$$

that can be rearranged to yield

$$\int_{-\infty}^{\infty}\int_{-\infty}^{\infty}\left[V_2^2 f(V_1)^2 + V_1^2 f(V_2)^2 - 2V_1V_2 f(V_1)f(V_2)\right]\times \tag{2.35}$$

$$p(V_1)p(V_2)dV_1dV_2 \geq 0 \tag{2.36}$$

$$2\mathrm{E}\left[V^2\right]\mathrm{E}\left[f(V)^2\right] - 2\mathrm{E}[Vf(V)]^2 \geq 0 \tag{2.37}$$

$$\mathrm{E}\left[V^2\right]\mathrm{E}\left[f(V)^2\right] \geq \mathrm{E}[Vf(V)]^2 \tag{2.38}$$

$$\frac{\sqrt{\mathrm{E}[f(V)^2]\,\mathrm{E}[V^2]}}{\mathrm{E}[Vf(V)]} \geq 1. \tag{2.39}$$

The PDF, $p(V)$, that provides the limiting case of the inequality is the most extreme platykurtic distribution taking the form of two delta functions at $\pm V_k$

$$p(V) = \frac{1}{2}\delta(V - V_k) + \frac{1}{2}\delta(V + V_k) \tag{2.40}$$

where V_K is an arbitrary positive voltage. Any moments required in Eq. (2.39) are even functions of V since $f(V)$ is an odd function therefore with the PDF of Eq. (2.40) and any even function, $h(V)$, the ensemble average of $h(V)$ is

$$\mathrm{E}[h(V)] = \int_{-\infty}^{\infty} h(V)p(V)dV = h(V_k) \tag{2.41}$$

and so

$$\frac{\sqrt{\mathrm{E}[f(V)^2]\,\mathrm{E}[V^2]}}{\mathrm{E}[Vf(V)]} = 1. \tag{2.42}$$

Alternatively, a linear resistor, where $f(V) = V$, provides this result regardless of the voltage PDF. Substituting this maximum power case from Eq. (2.42) into Eq. (2.33) provides an upper bound on power available to harvest

$$P_{Max} = \frac{\theta\sqrt{m}}{b\sqrt{C}+\theta\sqrt{m}}\frac{\pi S_0 m}{2}. \tag{2.43}$$

2.2.1 Numerical Examples

Two examples will now be used to illustrate the upper bound of Eq. (2.43) and compare a number of common harvester designs to it.

Example 1: Linear resistance, nonlinear stiffness

A frequently analysed energy harvester in the literature [9, 16, 22] is one with a linear resistance, R. Putting $\gamma = R$ and $f(V) = V$ in Eq. (2.2) yields

$$C\dot{V} + \frac{V}{R} = \theta\dot{x}. \tag{2.44}$$

Using this equation of motion with Eq. (2.1) and noting $\mathrm{E}\left[f(V)^2\right] = \mathrm{E}[Vf(V)] = \mathrm{E}\left[V^2\right]$ in Eqs. (2.10) and (2.15) the bounds become

$$P_{EU1} = \frac{R\theta^2}{b+R\theta^2}\frac{\pi S_0 m}{2} \tag{2.45}$$

$$P_{EU2} = \frac{m}{m+bCR}\frac{\pi S_0 m}{2}. \tag{2.46}$$

These two bounds are equal and provide the maximum of Eq. (2.43) when $R = \sqrt{m/C\theta^2}$. Interpreting the expressions of Eqs. (2.45) and (2.46) physically reveals that the first shows

the system is like a potential divider between mechanical damping and equivalent electrical damping, $R\theta^2$, from the resistor. As the electrical damping increases, more of the input power, $\pi S_0 m/2$, is dissipated electrically rather than mechanically. The second bound is less apparent, but shows that if the time constant, CR, of the electrical circuit is too large then less energy will be able to flow into the electrical circuit so less power will be dissipated in it.

In order to assess how prominent devices compare to the power bounds, a number of popular stiffness profiles have been simulated to calculate their power under white noise excitation. From linear vibration theory, the optimal linear device can be found analytically as one with zero stiffness, $g(x) = 0$, and this is compared to a Duffing oscillator, $g(x) = 100x + 2 \times 10^9 x^3$, a bistable device tuned to produce maximum power at optimal resistance, $g(x) = -40x + 3 \times 10^9 x^3$, and a device with linear stiffness $g(x) = 10x$, but with end stops restricting motion of a mass. The comparison is presented in Figure 2.3 where power is plotted against resistance and all simulations are found to lie beneath the power bounds of Eqs. (2.43), (2.45) and (2.46). Parameter values representative of a small energy harvester are used with $m = 1 \times 10^{-3}$kg, $b = 5 \times 10^{-3}$kg/s, $\theta = 1 \times 10^{-4}$N/V, $S_0 = (2 \times 10^{-3}/\pi)\,\mathrm{m}^2/\mathrm{s}^3$ and $C = 1 \times 10^{-9}$F. It has been difficult to attain all parameters required from the literature, particularly for the electrical coupling coefficient, therefore the values selected are guided both by the literature and values that provide realistic numerical simulation results.

The zero stiffness harvester is seen to perform best, closely following the bounds for most resistances. All other devices have a lower peak power and do not get as close to the bounds with the bistable device being second best. It is interesting to note that the zero stiffness device closely follows the upper bounds for low and high resistance and therefore the assumptions made to derive the bounds, namely that $\mathrm{E}\left[\dot{V}^2\right] = 0$ and $\mathrm{E}\left[xg(x)\right] = 0$, are realistic in these regions.

Example 2: Cubic resistance asymmetric nonlinear stiffness

In some circumstances nonlinear electrical components can be used to attempt to improve power dissipation or maintain performance whilst improving another characteristic such as reducing the displacement of the device. To illustrate this, three systems were simulated: a zero stiffness $g(x) = 0$, a symmetric bistable $g(x) = -40x + 6 \times 10^{10} x^3$ and an asymmetric bistable system $g(x) = -40x + 10^6 x^2 + 6 \times 10^{10} x^3$, all coupled to a cubic nonlinear resistance where $f(V) = V^3$. All other parameters were the same as in Example 1.

Applying this nonlinear resistance to the bounds of Eqs. (2.10) and (2.15) reveals that for maximum power according to Eq. (2.10) the most extreme platykurtic distribution of Eq. (2.40) is desired and so Eq. (2.10) can be solved for V_k and therefore P_{EU1}. Conversely, the upper bound on power from Eq. (2.15) requires the most extreme leptokurtic distribution for

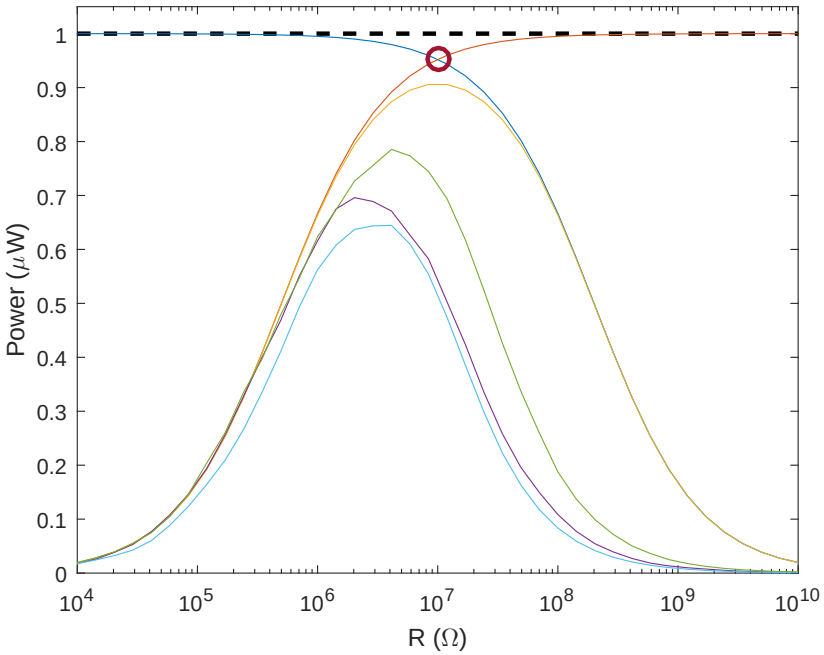

Fig. 2.3 Comparison of a number of harvesting systems to the power bounds with linear electrical resistance. $\pi S_0 m/2$ (black dashes), Eq. (2.45) (red), Eq. (2.46) (dark blue), Eq. (2.43) (red circle), zero stiffness (yellow), Duffing (purple), bistable (green) and end stops (light blue).

which there is no upper bound. To illustrate the curve of Eq. (2.15), a conservative estimate using a Laplace distribution of voltage (as seen in Figure 2.2) where $\mathrm{E}\left[V^4\right]/\mathrm{E}\left[V^2\right]^2 = 6$ has been used. However, this is no longer an upper bound curve since more power could be dissipated if a voltage distribution of higher kurtosis could be attained.

The power bounds and the power harvested from the selected devices are plotted against γ in Figure 2.4. Again, the systems are seen to perform within the power bound of Eq. (2.10) and below the conservative estimate of Eq. (2.15) when using a Laplace distribution for voltage. Consequently, no system is found to surpass the maximum available power of Eq. (2.43). Again, the zero stiffness device performs best, but not as close to the bounds as for linear resistance. Additionally, the asymmetric bistable system is included in the plot to illustrate that whilst the bounds do not apply to asymmetric systems, it is improbable that asymmetry will significantly improve performance.

The curve from Eq. (2.15) is also plotted with the voltage distribution of Eq. (2.40) to show that under this condition, the two lines of Eq. (2.10) and (2.15) cross at the maximum power point of Eq. (2.43) shown by the dashed purple line. Clearly the zero stiffness oscillator has a more leptokurtic voltage distribution for high γ therefore provides more power than when the voltage distribution of Eq. (2.40) is used. Nevertheless, the Laplace distribution seems to be a good upper bound estimate.

2.2.2 Optimal Harvester Design

A summary of the assumptions used to achieve the power bound of Eq. (2.43) is useful since if a device can be designed for which these assumptions can be reached then maximum power will be attained. Firstly the assumption that $\mathrm{E}\left[\dot{V}^2\right] = 0$ should be examined alongside the requirement to maximise the power $\mathrm{E}[Vf(V)]$. Together, these suggest that a low frequency voltage response is desired; a result that is unsurprising considering the electrical circuit acts like a low-pass filter. This agrees well with [29] where a low frequency response also provides an increased power bound.

Secondly, the assumption $\mathrm{E}[xg(x)] = 0$ should be aimed for although how to achieve it is not obvious. When no electrical coupling is present $\mathrm{E}[xg(x)] = \pi S_0 m^2/2b$ regardless of $g(x)$ therefore the optimal stiffness profile is one that decreases $\mathrm{E}[xg(x)]$ most significantly when electrical coupling is applied. For a monostable system $xg(x)$ increases with $|x|$, therefore minimising $\mathrm{E}[xg(x)]$ is equivalent to requiring the electrical circuit to decrease the amplitude of the motion as much as possible. From the equivalent linearisation argument made earlier this is also true for a multi-stable system. In keeping with the minimisation of $\mathrm{E}\left[\dot{V}^2\right]$ and since the impedance of the capacitor is high at low frequencies, the circuit will reduce the displacement most for a low frequency response.

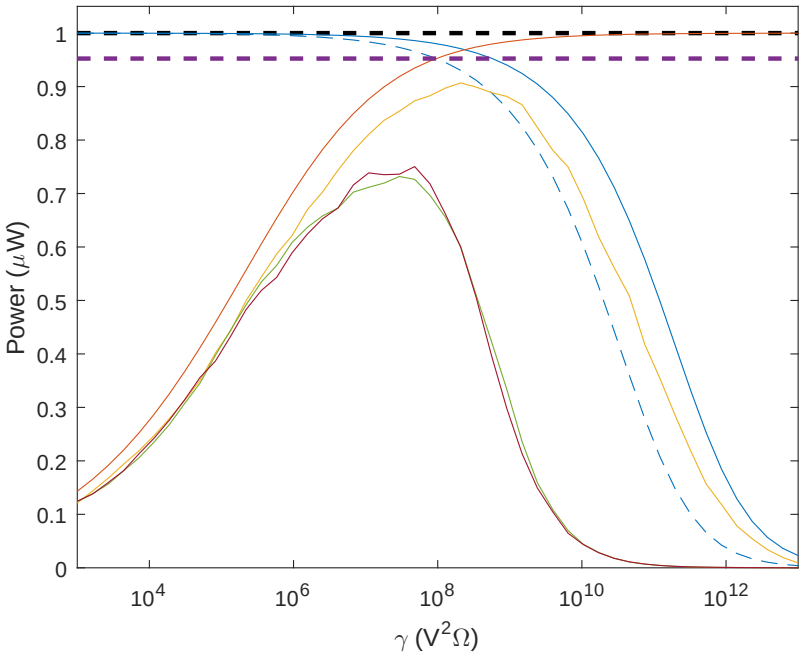

Fig. 2.4 Comparison of a number of harvesting systems to the power bounds with cubic electrical resistance. $\pi S_0 m/2$ (black dashes), Eq. (2.10) (red), Eq. (2.15) with Laplace distribution where $\mathrm{E}\left[V^4\right]/\mathrm{E}\left[V^2\right]^2 = 6$ (solid dark blue), Eq. (2.15) with distribution of Eq. (2.40) where $\mathrm{E}\left[V^4\right]/\mathrm{E}\left[V^2\right]^2 = 1$ (dashed dark blue), zero stiffness (yellow), bistable (green), asymmetric bistable (maroon) and Eq. (2.43) purple dashes.

Additionally, when a nonlinear resistor is used, the voltage PDF of Eq. (2.40) is required to achieve the maximum power of Eq. (2.43). This is clearly unrealistic although it emphasises that the most platykurtic voltage distribution achievable is desired. This could be sought through a combination of stiffness and electrical nonlinearities; however, for the case of linear resistance the maximum power is not dependent on the voltage distribution therefore linear electronics may be a useful method for bypassing this requirement.

In terms of optimal system parameters, Eq. (2.43) shows that maximising the oscillating mass and electrical coupling and removal of both mechanical damping and the piezoelectric capacitance (or coil inductance in an electromagnetic harvester) will increase the maximum power available. The majority of these parameters will be restricted by design or material constraints, therefore it is essential to select the optimal resistance (or nonlinear equivalent).

In summary, the most important property for a harvester aiming to approach the upper bound on power is a low frequency response. This ensures both $\mathrm{E}\left[\dot{V}^2\right]$ and $\mathrm{E}\left[xg(x)\right]$ are low and provided the resistance is linear, the voltage distribution is unimportant. A low frequency response will typically be enabled by a low stiffness device, hence the zero stiffness system in Figures 2.3 and 2.4 performs close to the bound. If a lower frequency device could be devised, it is assumed that its performance could be improved further.

In practice, zero stiffness is not possible since it would require infinite displacement, although low stiffness devices with finite displacement are achievable. A bistable device is a good example where, if well tuned for inter-well dynamics, the majority of the oscillations will occur within a displacement range of relatively low potential, or a low stiffness region, yet it still has a high stiffness at large displacement to restrict motion.

A useful property of this power bound is that it encompasses both linear and nonlinear stiffness profiles and can therefore provide some insight into the pertinent question of whether nonlinear devices perform better than linear ones. Whilst no device will be able to surpass the bound, it is not known whether a nonlinearity can enable a device to come closest to the bound. Given the requirement of a low stiffness device it seems a zero stiffness (linear) device is optimal, but not possible due to practical considerations. A nonlinear device like a bistable one therefore becomes attractive as it provides low stiffness for maximum power, but also restricts displacement and is physically realisable.

In the examples above, the nonlinear resistance has not provided an increase in maximum power (achieved with zero stiffness) since with the linear and cubic resistances the maximum power was found to be $0.91\mu W$ for both. It may be possible that other electrical nonlinearities improve performance, although since power close to the bound can be achieved by simply using a linear resistance unless there is a practical reason to use a nonlinear resistance, the improvement may not be worth the increased complexity.

2.2.3 Nonlinear Damping

An interesting idea to reduce the displacement and therefore size of a harvester whilst maintaining strong performance is to introduce nonlinear damping [83]. An upper bound on electrical power dissipation for a system with nonlinear damping similar to those of Eqs. (2.10) and (2.15) can be derived provided the electrical resistance is linear, but only for a prescribed rather than a general damping nonlinearity. As such, the method will be described below for a linear plus cubic damping nonlinearity as in [83], although it would need modifying accordingly for a different damping profile.

Eq. (2.1) can be modified to become

$$m\ddot{x} + b\dot{x} + a\dot{x}^3 + g(x) + \theta V = -m\ddot{\xi}(t) \tag{2.47}$$

and the electrical terms in Eq. (2.2) can be taken as $f(V) = V$ and $\gamma = R$. The mechanical power dissipation will be different from the linear case of Eq. (2.4) and becomes

$$P_M = b\mathrm{E}\left[\dot{x}^2\right] + a\mathrm{E}\left[\dot{x}^4\right] \tag{2.48}$$

which can be calculated by substituting in $\dot{x}$ from Eq. (2.2) to yield

$$P_M = \frac{bC^2}{\theta^2}\mathrm{E}\left[\dot{V}^2\right] + \frac{b}{\theta^2R^2}\mathrm{E}\left[V^2\right] + \frac{aC^4}{\theta^4}\mathrm{E}\left[\dot{V}^4\right] + \frac{a}{\theta^4R^4}\mathrm{E}\left[V^4\right] + \frac{6aC^2}{\theta^4R^2}\mathrm{E}\left[\dot{V}^2V^2\right]. \tag{2.49}$$

Similar to Eq. (2.12), $\mathrm{E}\left[V\dot{V}^3\right] = 0$ because the joint PDF for V and $\dot{V}$ is even in both of its arguments for the symmetric system. As before, this may also be true for an asymmetric system, but cannot be shown to be generally true.

For an upper bound on electrical power, $\mathrm{E}\left[V^2\right]/R$, the mechanical power must be minimised therefore lower bounds for the $\mathrm{E}\left[V^4\right]$, $\mathrm{E}\left[\dot{V}^2\right]$, $\mathrm{E}\left[\dot{V}^4\right]$ and $\mathrm{E}\left[\dot{V}^2V^2\right]$ terms are of interest. $\mathrm{E}\left[V^4\right]$ and $\mathrm{E}\left[\dot{V}^4\right]$ can be minimised with respect to $\mathrm{E}\left[V^2\right]$ and $\mathrm{E}\left[\dot{V}^2\right]$ by using the extreme platykurtic distribution of Eq. (2.40) to give $\mathrm{E}\left[V^4\right] = \mathrm{E}\left[V^2\right]^2$ and $\mathrm{E}\left[\dot{V}^4\right] = \mathrm{E}\left[\dot{V}^2\right]^2$.

No tighter bound than $\mathrm{E}\left[\dot{V}^2V^2\right] \geq 0$ can be found for this term, although $\mathrm{E}\left[\dot{V}^2\right]$ and therefore $\mathrm{E}\left[\dot{V}^4\right]$ can be shown to have a bound greater than zero as follows. Eq. (2.13) is still true for the nonlinear damping case of Eq. (2.47) because $\mathrm{E}\left[x\dot{x}^3\right] = 0$ again due to the joint PDF of displacement and velocity being even in both of its arguments for the symmetric system. Combining Eqs. (2.13) and (2.8), the $\mathrm{E}\left[\dot{x}^2\right]$ term can be removed to yield

$$\mathrm{E}\left[\dot{V}^2\right] \geq \left(\frac{\theta^2}{Cm} - \frac{1}{C^2R^2}\right)\mathrm{E}\left[V^2\right] \tag{2.50}$$

where as in Section 2.2 the lower bound of $\mathrm{E}\left[xg(x)\right] \geq 0$ has been employed.

When $\theta^2 CR^2 > m$ then Eq. (2.50) gives a tighter lower bound on $\mathrm{E}\left[\dot{V}^2\right]$. Combining Eqs. (2.3), (2.6), (2.49) and (2.50) therefore yields the upper bound on electrical power, P_{EUND}, for a nonlinearly damped harvester

$$\frac{\pi S_0 m}{2} = \begin{cases} \left(1+\frac{b}{\theta^2 R}\right) P_{EUND} + \frac{a}{\theta^4 R^2} P_{EUND}^2 & \text{for} \quad \theta^2 CR^2 \leq m, \\ \left(1+\frac{bRC}{m}\right) P_{EUND} + \left(\frac{aR^2C^2}{m^2} + 2\frac{a}{\theta^4 R^2} - 2\frac{aC}{\theta^2 m}\right) P_{EUND}^2 & \text{for} \quad \theta^2 CR^2 > m. \end{cases} \tag{2.51}$$

These polynomials must be solved to calculate P_{EUND}.

Numerical Example

Plotting the bound against resistance along with a number of common stiffness profiles illustrates its similarity to the bounds from linear damping. The electrical power dissipated by the same systems as Figure 2.3 with the same parameters and cubic damping coefficient $a = 100\text{kg s/m}^2$ is plotted against resistance and the bound of Eq. (2.51) in Figure 2.5. The bound increases with resistance for $R < \sqrt{m/C\theta^2}$ and decreases otherwise, providing a maximum power bound at $R = \sqrt{m/C\theta^2} = 10^7\Omega$. Interestingly, this is the same as the optimal resistance for the linear damping case, although the upper bound on electrical power with linear plus cubic damping at this resistance is lower than the bound of Eq. (2.45) with only linear damping. The addition of cubic damping has therefore reduced the upper bound on power. The simulated systems perform below the bound with the zero stiffness device again achieving power closest to the maximum showing that the bound is realistic and this device is close to optimal.

A drawback of this approach for nonlinear damping upper bounds is that a new bound must be derived for every damping profile. Consequently, there is no derivable limit on electrical power for all cases in the same way Eq. (2.43) accounts for a general electrical nonlinearity and the performance of harvesters with different damping functions cannot readily be compared. The possibility of an innovative damping nonlinearity improving harvesting performance is therefore difficult to assess. Nevertheless, one simple conclusion can be drawn: any damping mechanism that minimises mechanical dissipation is preferable.

2.3 Time-varying Excitation and Stochastic Resonance

This chapter has so far been concerned with calculating the maximum power available to harvest from white noise excitation. As discussed in Section 1.3.2 white noise is a

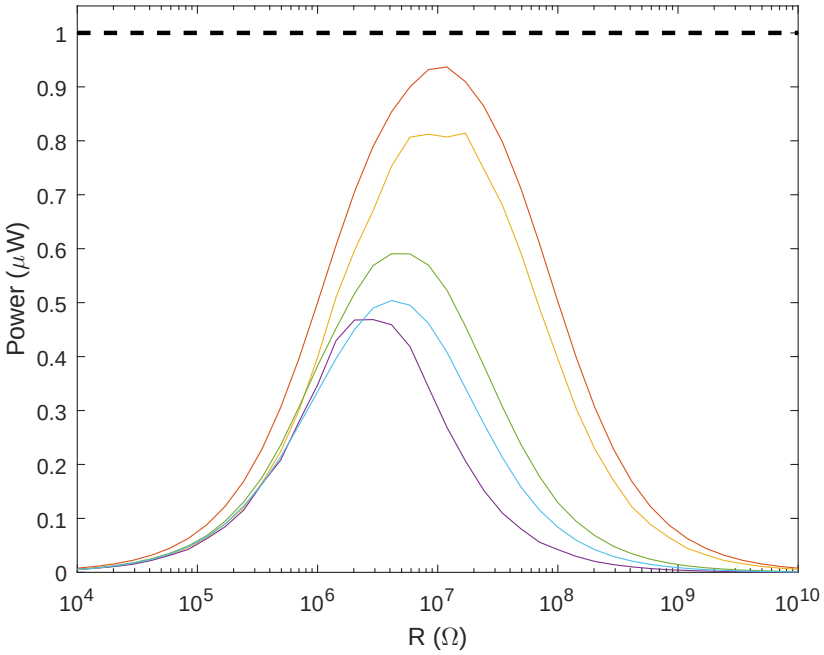

Fig. 2.5 Comparison of a number of harvesting systems to the power bounds with nonlinear damping and linear electrical resistance. $\pi S_0 m/2$ (black dashes), Eq. (2.51) (red), zero stiffness (yellow), Duffing (purple), bistable (green) and end stops (light blue).

mathematical representation of only a proportion of possible excitation. Whilst in some environments the vibration statistics will stay constant, in reality many signals containing white noise may well vary with time. This could be either fluctuations in magnitude or with a deterministic mean term such as combined harmonic and white noise excitation. In some cases a harmonic force is even deliberately introduced in addition to the noise to enhance harvesting performance using a phenomenon known as stochastic resonance.

By exploring the work of [48], this section will present a discussion of the potential impact on energy harvesting from deterministic excitation combined with white noise along with a review of stochastic resonance. Despite the likelihood of encountering such vibrations, little work has been published on random excitation with time-varying magnitude, presumably due to its complexity, and so it will not be discussed.

An abridged version of the derivation from [48] for the power dissipated under combined harmonic and white noise is presented below. The equation of motion for a multi-degree-of-freedom oscillator with general stiffness and damping nonlinearity and white noise base excitation is

$$\mathbf{M}(\mathbf{y})\ddot{\mathbf{y}} + \mathbf{g}(\mathbf{y},\dot{\mathbf{y}},t) = -\mathbf{f}(\mathbf{y})\ddot{b} \tag{2.52}$$

where $\mathbf{y}$ is a vector of generalised coordinates, $\mathbf{M}$ is the mass matrix, $\mathbf{g}(\mathbf{y},\dot{\mathbf{y}},t)$ is a general nonlinear function of the system displacements and velocities and time, $\mathbf{f}$ is a vector that relates base motion to each coordinate and $\ddot{b}$ is a white noise base acceleration with autocorrelation function $\mathrm{E}\left[\ddot{b}(t)\ddot{b}(t+\tau)\right] = \pi S_0 \delta(\tau)$. Any deterministic and parametric excitation terms are included within $\mathbf{g}(\mathbf{y},\dot{\mathbf{y}},t)$ which Langley states is periodic with period T, although this is only to simplify the remaining discussion and the constraint of periodicity need not be made.

The power input by white noise at any instant of any realisation can be calculated using

$$P = \dot{\mathbf{y}}^{\mathrm{T}}\mathbf{g}(\mathbf{y},\dot{\mathbf{y}},t). \tag{2.53}$$

However, in energy harvesting the average power is of interest and so Eq. (2.53) must be averaged over both an excitation cycle and the ensemble to yield

$$< \mathrm{E}[P] >= \frac{1}{T}\int_0^T \mathrm{E}\left[\dot{\mathbf{y}}^{\mathrm{T}}\mathbf{g}(\mathbf{y},\dot{\mathbf{y}},t)\right] dt \tag{2.54}$$

where $< Z >$ represents the time average over one period of the variable Z.

This power will be split between mechanical and electrical dissipation and can be calculated by first converting the equations of motion into a state-space representation

$$\mathbf{x} = \begin{pmatrix} \mathbf{y} \\ \dot{\mathbf{y}} \end{pmatrix} \tag{2.55}$$

such that

$$\dot{\mathbf{x}} = \begin{pmatrix} \dot{\mathbf{y}} \\ -\mathbf{M}^{-1}\mathbf{g}(\mathbf{x},t) \end{pmatrix} + \begin{pmatrix} \mathbf{0} \\ -\mathbf{M}^{-1}\mathbf{f}\ddot{b} \end{pmatrix} = \mathbf{F}(\mathbf{x},t) + \mathbf{G}\zeta(t) \tag{2.56}$$

where $\zeta(t)$ is a vector of uncorrelated white noise signals, each with unit spectral density, and

$$\mathbf{G} = \sqrt{\pi S_0}\left(\mathbf{0}_{2N\times 2N-1} \;\; (\mathbf{0}^{\mathrm{T}}_{1\times N} \;\; -\mathbf{f}^{\mathrm{T}}\mathbf{M}^{-1})^{\mathrm{T}}\right) \tag{2.57}$$

where N is the number of degrees of freedom.

The probability density function of the state vector, $p(\mathbf{x},t)$, of the system satisfies the Fokker-Planck equation

$$\frac{\partial p}{\partial t} = -\frac{\partial}{\partial x_i}\left[H_i p - \frac{1}{2}\frac{\partial}{\partial x_j}\left(D_{ij}p\right)\right] \tag{2.58}$$

where

$$H_i = F_i + \frac{1}{2}\frac{\partial G_{ij}}{\partial x_k}G_{kj} \tag{2.59}$$

$$D_{ij} = G_{ik}G_{jk} \tag{2.60}$$

and the summation convention is used. Due to the periodic nature of $\mathbf{g}(\mathbf{x},t)$, the PDF of $\mathbf{x}$ will also be periodic once steady-state is reached.

If the Fokker-Planck equation, Eq. (2.58) is multiplied by the kinetic energy $(1/2)M_{rs}\dot{y}_r\dot{y}_s$, integrated over state-space and averaged over one time-period of the harmonic excitation the average power dissipated is calculated using Eq. (2.54) as

$$< \mathrm{E}[P] >= \frac{1}{T}\int_0^T \mathrm{E}\left[\dot{\mathbf{y}}^{\mathrm{T}}\mathbf{g}(\mathbf{y},\dot{\mathbf{y}},t)\right]dt = \frac{\pi S_0}{2} < \mathrm{E}\left[\mathbf{f}^{\mathrm{T}}\mathbf{M}^{-1}\mathbf{f}\right] > . \tag{2.61}$$

The term $\mathrm{E}\left[\mathbf{f}^{\mathrm{T}}\mathbf{M}^{-1}\mathbf{f}\right]$ is discussed in detail in [48] and Section 3.4.1 where it is shown to be equal to the total oscillating mass unless a generalised coordinate is constrained in which case it becomes less than the mass. The significance of the result of Eq. (2.61) is that a white noise base excitation will provide the same input power regardless of any external or parametric forcing applied to the system.

Supposing a harmonic force, $F\cos(\omega t)$, acts on a degree of freedom of a harvester, y_1, in addition to white noise, the power dissipated, P_{Harm}, by the harmonic component is simply calculated as the time and ensemble average of the velocity of the relevant degree of freedom multiplied by the harmonic forcing, $P_{Harm} =< F\cos(\omega t)\mathrm{E}[\dot{y}_1] >$. Conveniently, this is the same calculation as would be made if the white noise were not present although the mean velocity term would differ somewhat due to the noise. It is likely that the ensemble average value of the velocity with white noise would be close to the value without noise (illustrated later in Figure 5.2) and so superposition of power calculated by a system with only white noise added to power dissipated by a system with only harmonic forcing present would be a reasonable estimate of total power dissipation in a system with combined noise and harmonic inputs.

A similar non-stationary case to the example described above that has received attention in energy harvesting literature is the case of stochastic resonance [50, 58, 65, 81, 96, 98]. This involves attempting to promote inter-well dynamics of a bistable harvester subject to white noise base acceleration by periodically modulating its potential well with a parametric force. An example equation of motion governing such a system taken from [58] is

$$\ddot{x} + b\dot{x} - \mu(1 - \eta\cos(\omega t))x + x^3 = \ddot{\xi}(t) \tag{2.62}$$

where the harmonic term $\eta\cos(\omega t)$ is a parametric forcing introduced to modulate the linear stiffness such that the potential barrier between the two wells varies with time. The parameters μ, η and ω can be selected using the Kramers rate, which uses the probability of crossover from one well to the other to find the expected rate of crossovers.

The consequence of Eq. (2.61) for stochastic resonance is immediately apparent from the power flow, where the power from white noise, P_{Noise}, is fixed and equal to the power dissipated, P_{Diss}, minus the power input for the parametric excitation, P_{In}, (equal to $-\mu\eta\cos(\omega t)\mathrm{E}[\dot{x}x]$ in the case of Eq. (2.62)), such that

$$P_{Diss} = P_{Noise} + P_{In}. \tag{2.63}$$

Since the power in from the noise is fixed (equal to $\pi S_0/2$ for Eq. (2.62)), it is clear that no additional excitation can improve net power harvested since P_{In} must be subtracted from the dissipated power. Nevertheless, in an energy harvesting system power is split between undesirable mechanical and desirable electrical dissipation therefore it is possible that the power would be split more profitably by a system under stochastic resonance than one not. What harvester design to compare the stochastic resonance case to is an important question

since significant performance improvements from stochastic resonance are published, but are often an improvement when parametric excitation is added to a poorly tuned device.

Importantly, an upper bound on power harvested is provided by Eq. (2.61) that cannot be surpassed regardless of the electromechanical system. The previous power bound of Eq. (2.43) is no longer valid as the system was assumed to be stationary a number of times in its derivation. Supposing, when coupled to a complementary electrical system, that stochastic resonance can provide enhanced harvested power, a number of practical questions must be addressed. Importantly, whether or not adding mass to the device in the form of the parametric forcing equipment is more profitable than simply increasing the oscillating mass. Additionally, it must be assessed whether the external forcing circuit is worth the extra cost and complexity and how it will be powered. Lastly, if the noise varies slowly over time, the device may become mis-tuned and not exhibit any benefits of stochastic resonance for periods of time.

2.4 Conclusions

A new upper bound on harvested power has been derived for a single-degree-of-freedom harvester under white noise base excitation with a general stiffness nonlinearity and coupled to a nonlinear electrical circuit. Whilst this bound makes assumptions that are not physically realisable, these assumptions were used to examine the type of system that can come close to the bounds and produce maximum power. It was found that due to the low-pass nature of the circuitry, minimising the mechanical stiffness maximised the electrical power produced. A zero linear stiffness device is therefore seen to come closest to the bounds, although it is difficult to achieve in practice due to its large displacement response. A bistable system that possesses a low stiffness region, but with stronger restoring forces at large displacements is therefore thought to be a good design for approaching the power bound although it must be tuned to the level of excitation.

Further work extending the power bound to other excitation conditions such as non-white excitation and more general electrical circuitry would improve applicability. Despite this, as it stands the upper bound is thought to be useful because for linearly damped (and therefore the majority of systems to a reasonable approximation) white noise is an upper bound on any non-white noise with the same peak spectrum [48]. Additionally, the use of a purely resistive electrical component (excluding the unavoidable piezoelectric capacitor or electromagnetic inductance) to model the circuit dynamics will likely provide an upper bound on power since more complex circuitry will include greater parasitic losses.

An example of the method to derive a bound for nonlinear damping has been described and seen to provide similar bounds to linear damping, although it is not extendible to all damping profiles. Nevertheless, mechanical damping will often be small compared to electrical damping so higher fidelity damping modelling will be unlikely to make a large difference to the bound.

When designing devices for harvesting energy from broadband random vibrations the bound of Eq. (2.43) can be used to compare devices against each other and also as a measure of harvester efficiency. Additionally, a quick estimate of the power available to harvest in a given operating environment can be made in order to estimate the required harvester specification and thus the feasibility of vibration harvesting for a specific application.

Finally, combining external or parametric excitation with white noise was found to have no effect on the power input from the noise which remains proportional to the oscillating mass and magnitude of the spectrum. Consequently, stochastic resonance and other deterministic excitation can only provide an improvement to a harvester without deterministic excitation by more effectively splitting the power dissipation between the electrical and mechanical mechanisms. In addition to the practical complications, this suggests that stochastic resonance is unlikely to become a realistic option.

Chapter 3

Power Dissipated under Non-white Noise Excitation

3.1 Introduction

Random vibrations arise in a wide variety of engineering structures and as such their properties can vary greatly. In particular, certain frequencies can be more dominant than others or the statistics of a random vibration could be more complex than the commonly assumed Gaussian form. In Chapter 2, the power dissipated by systems excited by Gaussian white noise vibrations was analysed and applied to a broad range of energy harvesting systems. Whilst white noise is a good approximation of the excitation when the bandwidth of the noise is significantly wider than that of the system, it is neither realistic since in theory it has infinite mean square velocity nor is it a reasonable approximation when the spectrum has non-uniform frequency content.

In this chapter, by extending the Wiener series approach, a general methodology is developed for calculating the power dissipated by a general nonlinear multi-degree-of-freedom oscillatory system excited by random Gaussian base motion of any spectrum. The Wiener series method, described in Section 1.4, has been developed to compute the output of a nonlinear system to a white noise input. One method for extending to non-white inputs is to take a filtered white noise signal and reverse filter it into a white signal before being input to a nonlinear system. The Wiener theory can then be applied using the white noise input with the reverse filter included to amend the results and yield an orthogonal series with a non-white input as described in [49, 76].

An alternative derivation of this series, herein called the extended Wiener series, is presented in this chapter by proving that the general nth order functional in the series satisfies

the relevant orthogonality condition. This approach eventually provides the same series as that of [49, 76], but the orthogonality of the *n*th order functional is proven mathematically as opposed to being stated in [49]. Crucially, this yields the structure of the functionals, which is required in the subsequent power analysis.

From the extended series a simple expression for the power dissipated can be derived in terms of the first extended Wiener kernel and the spectrum of the input. Additionally, a useful property of the first kernel is derived that helps to illustrate how power is dissipated and hence assists the design of a system where power is a consideration. In the case of energy harvesting, the theory guides towards the goal of maximising power, although it can also be applied to minimise power input from random excitation into a system as required by applications where vibration is undesirable. Additionally, whilst power is the primary concern of the theory, for a single-degree-of-freedom system with linear damping the mean square velocity of the response can also be calculated since it is proportional to the power dissipated.

In what follows the Wiener series will be extended to incorporate non-white excitation in Section 3.2 and then the method for calculating the kernels for the new series is described in Section 3.3. The derivation of a method for calculating power dissipation using the series is shown in Section 3.4 followed by validation of the theory via numerical simulations in Section 3.5. Finally, the methodology will be applied to energy harvesting from non-white noise vibrations in Section 3.7.

3.2 Extended Wiener Series for Non-white inputs

Similar to a Wiener series, a random output signal from a nonlinear process can be described as a sum of functionals

$$y(t) = \sum_{n=0}^{\infty} \mathbf{g}_n[k_n; x(t)] \tag{3.1}$$

where $x(t)$ is a Gaussian random input of any spectrum and the Wiener G-functionals, $\mathbf{G}_n[k_n; x(t)]$ have been replaced with a lower case $\mathbf{g}_n[k_n; x(t)]$ to represent that these are extended Wiener functionals for non-white noise. Each g-functional is defined as a sum of Volterra functionals, $\mathbf{K}_{j(n)}[x(t)]$, up to the order of the g-functional such that

$$\mathbf{g}_n[k_n; x(t)] = \sum_{j=0}^{n} \mathbf{K}_{j(n)}[x(t)] \tag{3.2}$$

where the Volterra functional $\mathbf{K}_{j(n)}[x(t)]$ takes the form

$$\mathbf{K}_{j(n)}[x(t)] = \int_{-\infty}^{\infty} ... \int_{-\infty}^{\infty} k_{j(n)}(\tau_1, ..., \tau_j) x(t-\tau_1) ... x(t-\tau_j) d\tau_1 ... d\tau_j. \tag{3.3}$$

The order of the Volterra functional is therefore j and $k_{j(n)}(\tau_1, ..., \tau_j)$ is called an extended Wiener kernel of order j and must be calculated. The (n) term in the subscript of both the functional and the kernel denotes that they both belong to the Volterra series of the nth order g-functional. When $j = n$ the nth order kernel $k_{n(n)}$ will be rewritten as k_n and is called the leading order kernel.

Two important features of the extended Wiener kernels are that they are causal such that

$$k_n(\tau_1, ..., \tau_n) = 0 \qquad \text{for any} \quad \tau_1 ... \tau_n < 0 \tag{3.4}$$

and they are symmetric such that for any permutation of the arguments, the output is the same, for example

$$k_3(\tau_1, \tau_2, \tau_3) = k_3(\tau_3, \tau_1, \tau_2) = k_3(\tau_2, \tau_1, \tau_3). \tag{3.5}$$

The relationship between the extended Wiener kernels in a g-functional can be found by enforcing the orthogonality condition

$$\mathrm{E}[\mathbf{H}_p[x(t)]\mathbf{g}_n[k_n; x(t)]] = 0 \qquad \text{for} \quad p < n \tag{3.6}$$

where $\mathbf{H}_p[x(t)]$ is any Volterra functional of order p;

$$\mathbf{H}_p[x(t)] = \int_{-\infty}^{\infty} ... \int_{-\infty}^{\infty} h_p(\lambda_1, ..., \lambda_p) x(t-\lambda_1) ... x(t-\lambda_p) d\lambda_1 ... d\lambda_p. \tag{3.7}$$

This condition is required to create an applicable orthogonal series, like the Wiener series, that converges and where the contribution from each g-functional can be isolated in order to calculate it.

An ansatz of the form of the extended Wiener kernels, and therefore the g-functionals, can be taken by modifying the Wiener series to remove the white noise assumption. Its orthogonality properties according to Eq. (3.6) can then be investigated. The first three and the nth g-functionals are modified from Eqs. (1.7)-(1.10) to become

$$\mathbf{g}_0[k_0; x(t)] = k_0 \tag{3.8}$$

$$\mathbf{g}_1[k_1; x(t)] = \int_{-\infty}^{\infty} k_1(\tau_1) x(t-\tau_1) d\tau_1 \tag{3.9}$$

$$\mathbf{g}_2[k_2;x(t)] = \int_{-\infty}^{\infty}\int_{-\infty}^{\infty} k_2(\tau_1,\tau_2)x(t-\tau_1)x(t-\tau_2)d\tau_1 d\tau_2 - \int_{-\infty}^{\infty}\int_{-\infty}^{\infty} k_2(\tau_1,\tau_2)R_{xx}(\tau_1-\tau_2)d\tau_1 d\tau_2 \quad (3.10)$$

$$\mathbf{g}_n[k_n;x(t)] = \sum_{m=0}^{\text{floor}[n/2]} \int_{-\infty}^{\infty}\dots\int_{-\infty}^{\infty} \frac{(-1)^m n!}{(n-2m)!m!2^m} \times \int_{-\infty}^{\infty}\dots\int_{-\infty}^{\infty} k_n(\tau_1,\dots,\tau_{2m},\sigma_1,\dots,\sigma_{n-2m}) \times R_{xx}(\tau_1-\tau_2)\dots R_{xx}(\tau_{2m-1}-\tau_{2m})d\tau_1\dots d\tau_{2m} \times x(t-\sigma_1)\dots x(t-\sigma_{n-2m})d\sigma_1\dots d\sigma_{n-2m} \quad (3.11)$$

where $R_{xx}(\tau)$ is the autocorrelation function of the input at a time lag τ, σ represents time lags that are integrated over and in the nth functional the sum now includes only alternate order Volterra functionals. Additionally with this form each extended Wiener kernel within a g-functional can be derived from the leading order kernel and the autocorrelation function of the input.

The orthogonality condition of Eq. (3.6) can now be assessed by combining it with Eq. (3.11) giving

$$\begin{aligned}\mathrm{E}\left[\mathbf{H}_p[x(t)]\mathbf{g}_n[k_n;x(t)]\right] = \int_{-\infty}^{\infty}\dots\int_{-\infty}^{\infty} h_p(\lambda_1,\dots,\lambda_p) \times \\ \sum_{m=0}^{\text{floor}[n/2]} \int_{-\infty}^{\infty}\dots\int_{-\infty}^{\infty} \frac{(-1)^m n!}{(n-2m)!m!2^m} \times \\ \int_{-\infty}^{\infty}\dots\int_{-\infty}^{\infty} k_n(\tau_1,\dots,\tau_{2m},\sigma_1,\dots,\sigma_{n-2m}) \times \\ R_{xx}(\tau_1-\tau_2)\dots R_{xx}(\tau_{2m-1}-\tau_{2m})d\tau_1\dots d\tau_{2m} \times \\ \mathrm{E}\left[x(t-\sigma_1)\dots x(t-\sigma_{n-2m})x(t-\lambda_1)\dots x(t-\lambda_p)\right] \\ d\sigma_1\dots d\sigma_{n-2m}d\lambda_1\dots d\lambda_p \end{aligned} \quad (3.12)$$

which will be shown to be equal to zero by extending the method of [76].

Inspecting the ensemble average term in Eq. (3.12), it can be rewritten as

$$\mathrm{E}\left[s_1\dots s_q l_1\dots l_p\right] \quad (3.13)$$

where $q = n-2m$, s_q represents $x(t-\sigma_q)$ and l_p represents $x(t-\lambda_p)$ and are Gaussian random variables. Using the Gaussian property [51], the ensemble average can be expanded

into a sum of products of ensemble averages of one or two variables. Since the input is assumed to be zero mean if $p+n$ is odd then the ensemble average in Eq. (3.12) becomes zero and the orthogonality condition is proven trivially. If $p+n$ is even then the ensemble average becomes a sum of products of autocorrelations of the input. For example

$$\begin{aligned}\mathrm{E}[s_1 s_2 l_1 l_2] &= \mathrm{E}[s_1 s_2]\mathrm{E}[l_1 l_2] + \mathrm{E}[s_1 l_1]\mathrm{E}[s_2 l_2] + \mathrm{E}[s_1 l_2]\mathrm{E}[l_1 s_2] \\ &= R_{xx}(\sigma_1 - \sigma_2)R_{xx}(\lambda_1 - \lambda_2) + R_{xx}(\sigma_1 - \lambda_1)R_{xx}(\sigma_2 - \lambda_2) + \\ &\qquad R_{xx}(\sigma_1 - \lambda_2)R_{xx}(\sigma_2 - \lambda_1). \end{aligned} \tag{3.14}$$

Due to the symmetry property of the kernel in Eq. (3.12) various terms in the sum of products of autocorrelations will provide the same result when integrated over both the τ and σ spaces. For example, the rightmost two terms in Eq. (3.14) will provide the same result from the integral because σ_1 and σ_2 are interchangeable whereas the first term will provide a different result. In fact, for a given value of m the same integral will be produced by any product of autocorrelations that has the same number of autocorrelations with arguments involving the difference between a σ and λ term such as $R_{xx}(\sigma_1 - \lambda_1)$. Call this number $N_{r|m}$ where r represents the number of arguments including both a σ and a λ term and m is the summation variable in Eq. (3.12). For example in Eq. (3.14) where m is not specified, $N_{0|m} = 1$ and $N_{2|m} = 2$.

$N_{r|m}$ must be found for the general case of Eq. (3.13) and can be calculated as follows. Firstly, the number of possible ways r s's can be chosen from q s's and r l's from p l's is $\binom{q}{r} = q!/(q-r)!r!$ and $\binom{p}{r} = p!/(p-r)!r!$ respectively. The number of ways these s's and l's can be arranged such that each s is paired with an l is $r!$. This leaves $q-r$ s's that can be paired in $(q-r)!/((q-r)/2)!2^{(q-r)/2}$ distinct ways and $p-r$ l's that can be paired in $(p-r)!/((p-r)/2)!2^{(p-r)/2}$ distinct ways. Therefore the total number, $N_{r|m}$, of ensemble averages with r terms including both an s and l is

$$\begin{aligned} N_{r|m} &= \frac{q!}{(q-r)!r!}\frac{p!}{(p-r)!r!}r!\frac{(q-r)!}{((q-r)/2)!2^{(q-r)/2}}\frac{(p-r)!}{((p-r)/2)!2^{(p-r)/2}} \\ &= \frac{q!p!}{r!((q-r)/2)!((p-r)/2)!2^{(q+p)/2-r}}. \end{aligned} \tag{3.15}$$

Note that $N_{r|m}$ depends on m since q depends on m as $q = n-2m$ and if q is odd (then p is odd) and r must be odd and if q is even (then p is even) and r must be even. Additionally, since the maximum number of σs and λs that can be taken out and paired is the minimum of

q or p, r must be less than or equal to the smaller of q and p so that

$$r \leq \begin{cases} q & q \leq p \\ p & q > p \end{cases}. \tag{3.16}$$

Combining Eqs. (3.12) and (3.15) using $q = n - 2m$ yields

$$\begin{aligned}
\mathrm{E}\left[\mathbf{H}_p[x(t)]\mathbf{g}_n[k_n;x(t)]\right] = &\int_{-\infty}^{\infty} \ldots \int_{-\infty}^{\infty} h_p(\lambda_1,\ldots,\lambda_p)\times \\
&\sum_{m=0}^{\mathrm{floor}[n/2]} \int_{-\infty}^{\infty} \ldots \int_{-\infty}^{\infty} \frac{(-1)^m n!}{(n-2m)!m!2^m}\times \\
&\int_{-\infty}^{\infty} \ldots \int_{-\infty}^{\infty} k_n(\tau_1,\ldots,\tau_{2m},\sigma_1,\ldots,\sigma_{n-2m})\times \\
&R_{xx}(\tau_1-\tau_2)\ldots R_{xx}(\tau_{2m-1}-\tau_{2m})d\tau_1\ldots d\tau_{2m}\times \\
&\sum_{r=0}^{\min[n-2m,p]} N_{r|m} R_{xx}(\sigma_{r+1}-\sigma_{r+2})\ldots R_{xx}(\sigma_{n-2m-1}-\sigma_{n-2m}) \\
&R_{xx}(\sigma_1-\lambda_1)\ldots R_{xx}(\sigma_r-\lambda_r)R_{xx}(\lambda_{r+1}-\lambda_{r+2})\ldots R_{xx}(\lambda_{p-1}-\lambda_p) \\
&d\sigma_1\ldots d\sigma_{n-2m}d\lambda_1\ldots d\lambda_p \\
= &\int_{-\infty}^{\infty} \ldots \int_{-\infty}^{\infty} h_p(\lambda_1,\ldots,\lambda_p)\times \\
&\sum_{m=0}^{\mathrm{floor}[n/2]} \sum_{r=0}^{\min[n-2m,p]} \frac{(-1)^m n!}{(n-2m)!m!2^m} N_{r|m}\times \\
&\int_{-\infty}^{\infty} \ldots \int_{-\infty}^{\infty} k_n(\tau_1,\ldots,\tau_{2m},\sigma_1,\ldots,\sigma_{n-2m})\times \\
&R_{xx}(\tau_1-\tau_2)\ldots R_{xx}(\tau_{2m-1}-\tau_{2m})d\tau_1\ldots d\tau_{2m}\times \\
&R_{xx}(\sigma_{r+1}-\sigma_{r+2})\ldots R_{xx}(\sigma_{n-2m-1}-\sigma_{n-2m}) \\
&R_{xx}(\sigma_1-\lambda_1)\ldots R_{xx}(\sigma_r-\lambda_r)R_{xx}(\lambda_{r+1}-\lambda_{r+2})\ldots R_{xx}(\lambda_{p-1}-\lambda_p) \\
&d\sigma_1\ldots d\sigma_{n-2m}d\lambda_1\ldots d\lambda_p.
\end{aligned} \tag{3.17}$$

To prove that the series is orthogonal, this equation must be equal to zero. For a given value of r, the sum over m will contain the integrals of the same value, having the same number of autocorrelations that have both a σ and a λ term in their argument. However, the upper limit of the sum over m must change according to the value of r selected since according to Eq. (3.16), $r \leq n-2m$ so for a given r, $m \leq (n-r)/2$. Therefore to show that Eq. (3.17) is equal

to zero and hence prove orthogonality, it must be shown that for any permissible value of r

$$\sum_{m=0}^{(n-r)/2} \frac{(-1)^m n!}{(n-2m)!m!2^m} N_{r|m} = 0. \tag{3.18}$$

Substituting Eq. (3.15) with $q = n-2m$ into Eq. (3.18) yields

$$\sum_{m=0}^{(n-r)/2} \frac{(-1)^m n!p!}{m!r!((n-2m-r)/2)!((p-r)/2)!2^{(n+p)/2-r}} = \frac{n!p!}{r!((p-r)/2)!2^{(n+p)/2-r}} \sum_{m=0}^{(n-r)/2} \frac{(-1)^m}{m!((n-2m-r)/2)!}. \tag{3.19}$$

Now to show the orthogonality condition, Eq. (3.6), we must show

$$\sum_{m=0}^{(n-r)/2} \frac{(-1)^m}{m!((n-2m-r)/2)!} = 0. \tag{3.20}$$

Renaming such that $M = (n-r)/2$ and rearranging yields

$$\begin{aligned} \sum_{m=0}^{M} \frac{(-1)^m}{m!(M-m)!} &= \frac{1}{M!} \sum_{m=0}^{M} \frac{M!(-1)^m}{m!(M-m)!} \\ &= \frac{1}{M!}(1-1)^M \\ &= 0 \end{aligned}$$

by taking a binomial expansion around the point -1. The orthogonality condition of Eq. (3.6) has therefore been proven for the nth g-functional of the form of Eq. (3.11) and so the Wiener series has been extended to non-white noise inputs.

3.3 Calculating Wiener kernels

One of the key characteristics that makes the Wiener series desirable is that the kernels can be determined simply using cross-correlation [76]. It is important therefore to assess whether the kernels from the extended series can also be simply calculated. The cross-correlation method described in [76] is a time domain method where the cross-correlation between input and output measurements either from experiments or simulations are calculated at various relative time lags in order to calculate the Wiener kernels. A simple rearrangement of the method can convert it into the frequency domain such that cross-correlations become cross-spectra.

The frequency domain approach is more applicable for the extended Wiener kernels since the time domain approach for white noise relies on the useful white noise property that the autocorrelation function is a delta function whereas the frequency approach does not.

The method to calculate the first three extended Wiener kernels is derived in this section following the same approach used for white noise in [76], but in the frequency instead of time domain. The approach for the higher order kernels will be the same, but is not shown here. Firstly, the multi-dimensional delay Volterra functional, $\mathbf{D}_n[x(t)]$ must be introduced as

$$\begin{aligned}\mathbf{D}_n[x(t)] &= x(t-\sigma_1)...x(t-\sigma_n)\\ &= \int_{-\infty}^{\infty}...\int_{-\infty}^{\infty}\delta(\tau_1-\sigma_1)...\delta(\tau_n-\sigma_n)x(t-\tau_1)...x(t-\tau_n)d\tau_1...d\tau_n\end{aligned} \tag{3.21}$$

and is used to take cross-correlations of the output with the input at various time lags given by the σs.

The zeroth kernel is simply calculated as the ensemble average of the response which is equivalent to taking the ensemble average of the extended Wiener series with a zeroth order Volterra kernel and using the orthogonality property, Eq. (3.6), such that

$$\begin{aligned}\mathrm{E}[y(t)] &= \mathrm{E}\left[\sum_{n=0}^{\infty}\mathbf{g}_n[k_n;x(t)]\right]\\ &= \mathbf{g}_0[k_0;x(t)]\\ &= k_0.\end{aligned} \tag{3.22}$$

The first kernel can be calculated by taking the ensemble average of the response multiplied by the first order delay Volterra functional

$$\begin{aligned}\mathrm{E}[y(t)x(t-\sigma)] &= \mathrm{E}\left[\sum_{n=0}^{\infty}\mathbf{g}_n[k_n;x(t)]\mathbf{D}_1[x(t)]\right]\\ &= k_0\mathrm{E}[x(t-\sigma)]+\int_{-\infty}^{\infty}k_1(\tau_1)\mathrm{E}[x(t-\tau_1)x(t-\sigma)]\,d\tau_1\\ &= \int_{-\infty}^{\infty}k_1(\tau_1)R_{xx}(\sigma-\tau_1)d\tau_1.\end{aligned} \tag{3.23}$$

In the case of a white noise input, the autocorrelation function is simply $R_{xx}(\sigma-\tau_1)=\pi S_0\delta(\sigma-\tau_1)$ and the cross-correlation of the input and output is equal to $\pi S_0 k_1(\tau)$. However, with a non-white input, the cross-correlation is less simple and Eq. (3.23) becomes less useful for calculating $k_1(\tau)$. Eq. (3.23) can be transformed to the frequency domain by taking the

Fourier transform of both sides of the equation giving

$$\begin{aligned}
\int_{-\infty}^{\infty} \mathrm{E}\left[y(t)x(t-\sigma)\right] \mathrm{e}^{-i\omega\sigma} d\sigma &= \int_{-\infty}^{\infty}\int_{-\infty}^{\infty} k_1(\tau_1) R_{xx}(\sigma-\tau_1)\mathrm{e}^{-i\omega\sigma} d\tau_1 d\sigma \\
S_{yx}(\omega) &= \int_{-\infty}^{\infty} k_1(\tau_1)\mathrm{e}^{-i\omega\tau_1} \int_{-\infty}^{\infty} R_{xx}(\sigma-\tau_1)\mathrm{e}^{-i\omega(\sigma-\tau_1)} d\sigma d\tau_1 \\
S_{yx}(\omega) &= \int_{-\infty}^{\infty} k_1(\tau_1)\mathrm{e}^{-i\omega\tau_1} d\tau_1 \int_{-\infty}^{\infty} R_{xx}(s)\mathrm{e}^{-i\omega s} ds \\
S_{yx}(\omega) &= K_1(\omega) S_{xx}(\omega) \\
\implies K_1(\omega) &= \frac{S_{yx}(\omega)}{S_{xx}(\omega)} \qquad (3.24)
\end{aligned}$$

where $s = \sigma - \tau_1$, $S_{yx}(\omega)$ is called the cross-spectrum between output and input and $K_1(\omega)$ and $S_{xx}(\omega)$ are Fourier transforms of $k_1(\tau)$ and $R_{xx}(\tau)$ such that

$$K_1(\omega) = \int_{-\infty}^{\infty} k_1(\tau)\mathrm{e}^{-i\omega\tau} d\tau \qquad (3.25)$$

$$k_1(\tau) = \frac{1}{2\pi}\int_{-\infty}^{\infty} K_1(\omega)\mathrm{e}^{i\omega\tau} d\omega \qquad (3.26)$$

$$S_{xx}(\omega) = \int_{-\infty}^{\infty} R_{xx}(\tau)\mathrm{e}^{-i\omega\tau} d\tau \qquad (3.27)$$

$$R_{xx}(\tau) = \frac{1}{2\pi}\int_{-\infty}^{\infty} S_{xx}(\omega)\mathrm{e}^{i\omega\tau} d\omega. \qquad (3.28)$$

The first extended Wiener kernel can therefore be calculated from Eq. (3.24) with known input spectrum and the cross-spectrum, S_{yx}, calculated from either experimental or numerical results. The kernel can then be found in the time domain using Eq. (3.26).

The second extended Wiener kernel can be calculated with the same approach. The ensemble average of the output multiplied by a second order delay Volterra functional is

calculated as

$$\begin{aligned}
\mathrm{E}\left[y(t)x(t-\sigma_1)x(t-\sigma_2)\right] &= \mathrm{E}\left[\sum_{n=0}^{\infty}\mathbf{g}_n[k_n;x(t)]\mathbf{D}_2[x(t)]\right] \\
&= k_0\mathrm{E}\left[x(t-\sigma_1)x(t-\sigma_2)\right]+ \\
&\quad \int_{-\infty}^{\infty}k_1(\tau_1)\mathrm{E}\left[x(t-\tau_1)x(t-\sigma_1)x(t-\sigma_2)\right]d\tau_1+ \\
&\quad \int_{-\infty}^{\infty}\int_{-\infty}^{\infty}k_2(\tau_1,\tau_2)\mathrm{E}\left[x(t-\tau_1)x(t-\tau_2)x(t-\sigma_1)x(t-\sigma_2)\right]d\tau_1 d\tau_2- \\
&\quad \int_{-\infty}^{\infty}\int_{-\infty}^{\infty}k_2(\tau_1,\tau_2)\mathrm{E}\left[x(t-\tau_1)x(t-\tau_2)\right]\mathrm{E}\left[x(t-\sigma_1)x(t-\sigma_2)\right]d\tau_1 d\tau_2 \\
&= k_0R_{xx}(\sigma_1-\sigma_2)+ \\
&\quad 2\int_{-\infty}^{\infty}\int_{-\infty}^{\infty}k_2(\tau_1,\tau_2)R_{xx}(\sigma_1-\tau_1)R_{xx}(\sigma_2-\tau_2)d\tau_1 d\tau_2. \quad (3.29)
\end{aligned}$$

where the symmetry property of the kernel discussed in Section 3.2 has been used and the ensemble average of an odd number of Gaussian excitations is equal to zero. Fourier transforms are taken over both time delays, σ_1 and σ_2 yielding

$$\begin{aligned}
&\int_{-\infty}^{\infty}\int_{-\infty}^{\infty}\mathrm{E}\left[y(t)x(t-\sigma_1)x(t-\sigma_2)\right]\mathrm{e}^{-i(\omega_1\sigma_1+\omega_2\sigma_2)}d\sigma_1 d\sigma_2 = \\
&\qquad k_0\int_{-\infty}^{\infty}\int_{-\infty}^{\infty}R_{xx}(\sigma_1-\sigma_2)\mathrm{e}^{-i(\omega_1\sigma_1+\omega_2\sigma_2)}d\sigma_1 d\sigma_2+ \\
&\qquad 2\int_{-\infty}^{\infty}\int_{-\infty}^{\infty}\int_{-\infty}^{\infty}\int_{-\infty}^{\infty}k_2(\tau_1,\tau_2)R_{xx}(\sigma_1-\tau_1)R_{xx}(\sigma_2-\tau_2)\times \\
&\qquad \mathrm{e}^{-i(\omega_1\sigma_1+\omega_2\sigma_2)}d\tau_1 d\tau_2 d\sigma_1 d\sigma_2 \\
S_{yxx}(\omega_1,\omega_2) &= k_0S_{xx2}(\omega_1,\omega_2)+2\int_{-\infty}^{\infty}\int_{-\infty}^{\infty}k_2(\tau_1,\tau_2)\mathrm{e}^{-i(\omega_1\tau_1+\omega_2\tau_2)}\times \\
&\qquad \int_{-\infty}^{\infty}\int_{-\infty}^{\infty}R_{xx}(\sigma_1-\tau_1)R_{xx}(\sigma_2-\tau_2)\times \\
&\qquad \mathrm{e}^{-i(\omega_1(\sigma_1-\tau_1)+\omega_2(\sigma_2-\tau_2))}d\tau_1 d\tau_2 d\sigma_1 d\sigma_2 \\
S_{yxx}(\omega_1,\omega_2) &= k_0S_{xx2}(\omega_1,\omega_2)+2\int_{-\infty}^{\infty}\int_{-\infty}^{\infty}k_2(\tau_1,\tau_2)\mathrm{e}^{-i(\omega_1\tau_1+\omega_2\tau_2)}d\tau_1 d\tau_2\times \\
&\qquad \int_{-\infty}^{\infty}R_{xx}(s_1)\mathrm{e}^{-i\omega_1 s_1}ds_1\int_{-\infty}^{\infty}R_{xx}(s_2)\mathrm{e}^{-i\omega_2 s_2}ds_2 \\
S_{yxx}(\omega_1,\omega_2) &= k_0S_{xx2}(\omega_1,\omega_2)+2K_2(\omega_1,\omega_2)S_{xx}(\omega_1)S_{xx}(\omega_2) \quad (3.30)
\end{aligned}$$

where $s_1=\sigma_1-\tau_1$ and $s_2=\sigma_2-\tau_2$, $S_{yxx}(\omega_1,\omega_2)$ is called the second order cross-spectrum between output and input, $S_{xx2}(\omega_1,\omega_2)$ is the second order input spectrum and the second

kernel is defined in the frequency domain as

$$K_2(\omega_1,\omega_2) = \int_{-\infty}^{\infty}\int_{-\infty}^{\infty} k_2(\tau_1,\tau_2)\mathrm{e}^{-i(\omega_1\tau_1+\omega_2\tau_2)}d\tau_1 d\tau_2. \tag{3.31}$$

The second order kernel can be calculated from Eq. (3.30) with the first and second order input spectrum being properties known from the given input characteristics, k_0 already calculated from Eq. (3.22) and the second order cross-spectrum calculated from either experimental or numerical data. To simplify Eq. (3.30) the first term involving k_0 on the right hand side can be removed using the method of [76] to modify the initial cross-correlation to account for this term such that

$$\int_{-\infty}^{\infty}\int_{-\infty}^{\infty} \mathrm{E}\left[(y(t)-\mathbf{g}_0[k_0;x(t)])\,x(t-\sigma_1)x(t-\sigma_2)\right]\mathrm{e}^{-i(\omega_1\sigma_1+\omega_2\sigma_2)}d\sigma_1 d\sigma_2 = 2K_2(\omega_1,\omega_2)S_{xx}(\omega_1)S_{xx}(\omega_2). \tag{3.32}$$

Subsequent kernels can be calculated in the same manner although a general calculation method for the nth kernel is not derived here since only the first kernel is of interest.

3.4 Power from the Extended Series

In energy harvesting applications, amongst others, the quantity of primary interest is the power dissipated by an oscillator. The theory from the previous section can be applied in order to provide a framework for calculating the power dissipated under random excitation with a general spectrum.

This section will analyse a general N-degree-of-freedom-system identical to that of [48] of the form

$$\mathbf{M}(\mathbf{y})\ddot{\mathbf{y}} + \mathbf{g}(\mathbf{y},\dot{\mathbf{y}},t) = -\mathbf{f}(\mathbf{y})\ddot{b}(t) \tag{3.33}$$

where $\mathbf{y}$ is a vector of the N generalised coordinates describing the system, $\mathbf{g}(\mathbf{y},\dot{\mathbf{y}},t)$ is a vector of length N that represents a general nonlinear dissipative and restoring force, $\ddot{b}(t)$ is a random base acceleration and $\mathbf{f}(\mathbf{y})$ is a forcing vector that relates the base motion to the force on the system. The rth term of this vector can be calculated as

$$f_r = \sum_j m_j\left(\frac{\partial \mathbf{u}_j}{\partial y_r}.\mathbf{n}\right) \tag{3.34}$$

where m_j is the jth mass, $\mathbf{n}$ is a unit vector in the direction of the base excitation in a Cartesian coordinate system, $\mathbf{u}_j$ is the location of the jth mass in the same Cartesian coordinate system and y_r is the rth generalised coordinate.

The power, P, input by the base excitation and therefore dissipated by this system can be calculated by summing the effective force on each mass multiplied by its velocity such that

$$\begin{aligned} P &= -\mathrm{E}\left[\dot{\mathbf{y}}^{\mathrm{T}}\mathbf{f}(\mathbf{y})\ddot{b}(t)\right] \\ &= \mathrm{E}\left[z(t)\xi(t)\right] \end{aligned} \tag{3.35}$$

where

$$\begin{aligned} z(t) &= \dot{\mathbf{y}}^{\mathrm{T}}\mathbf{f}(\mathbf{y}) \\ &= \mathbf{f}(\mathbf{y})^{\mathrm{T}}\dot{\mathbf{y}} \end{aligned} \tag{3.36}$$

and $\xi(t) = -\ddot{b}(t)$.

An extended Wiener series can be created for the random variable $z(t)$ with input $\xi(t)$

$$z(t) = \sum_{n=0}^{\infty} \mathbf{g}_n[k_n; \xi(t)] \tag{3.37}$$

and the power from Eq. (3.35) can be calculated with this Wiener series using Eq. (3.35)

$$P = \mathrm{E}\left[\sum_{n=0}^{\infty} \mathbf{g}_n[k_n; \xi(t)]\xi(t)\right]. \tag{3.38}$$

where it can be noted that the excitation $\xi(t)$ can be thought of as a first order Volterra functional

$$\xi(t) = \int_{-\infty}^{\infty} \xi(\tau)\delta(\tau - t)d\tau \tag{3.39}$$

and the orthogonality property of Eq. (3.6) can be used to remove any g-functionals of order greater than unity yielding

$$\begin{aligned} P &= \mathrm{E}\left[k_0\xi(t)\right] + \mathrm{E}\left[\int_{-\infty}^{\infty} k_1(\tau)\xi(t-\tau)d\tau\xi(t)\right] \\ &= \int_{-\infty}^{\infty} k_1(\tau)R_{\xi\xi}(\tau)d\tau. \end{aligned} \tag{3.40}$$

where $R_{\xi\xi}(\tau)$ is the autocorrelation of the excitation at time lag τ and the excitation has been assumed to have zero mean. This equation becomes more informative when converted into

the frequency domain where using Eq. (3.26) in Eq. (3.40) yields

$$\begin{aligned} P &= \int_{-\infty}^{\infty} \frac{1}{2\pi} \int_{-\infty}^{\infty} K_1(\omega) \mathrm{e}^{i\omega\tau} d\omega R_{\xi\xi}(\tau) d\tau \\ &= \frac{1}{2\pi} \int_{-\infty}^{\infty} K_1(\omega) \int_{-\infty}^{\infty} R_{\xi\xi}(\tau) \mathrm{e}^{i\omega\tau} d\tau d\omega \\ &= \frac{1}{2\pi} \int_{-\infty}^{\infty} K_1(\omega) S_{\xi\xi}(\omega) d\omega. \end{aligned} \tag{3.41}$$

where $S_{\xi\xi}(\omega) = \int_{-\infty}^{\infty} R_{\xi\xi}(\tau)\mathrm{e}^{i\omega\tau} d\tau$ is a slight variant on Eq. (3.27) and is true because $R_{\xi\xi}(\tau)$ is real and even.

Eq. (3.41) can be used to calculate the power where $K_1(\omega)$ can be calculated using Eq. (3.24) either from numerical or experimental data. In order to understand how power will be dissipated, the properties of the first kernel are investigated in the following sections.

3.4.1 Integral of the First Extended Wiener Kernel

In what follows, a useful property of the first kernel, namely

$$\frac{1}{2\pi} \int_{-\infty}^{\infty} K_1(\omega) d\omega = \frac{\mathrm{E}\left[\mathbf{f}^{\mathrm{T}} \mathbf{M}^{-1} \mathbf{f}\right]}{2}, \tag{3.42}$$

that influences understanding of power dissipation will be derived. By using Eq. (3.26), Eq. (3.42) can be rewritten as

$$k_1(0) = \frac{\mathrm{E}\left[\mathbf{f}^{\mathrm{T}} \mathbf{M}^{-1} \mathbf{f}\right]}{2} \tag{3.43}$$

and can be derived by thinking of the base excitation as a series of impulses of magnitudes given by $\xi(t)$. A small change in $z(t)$ due to an impulse $\xi(T)$ at time T, termed $z(t)|_{\xi(T)}$ to differentiate it from the change in z due to previous impulses, can be assessed both from physical reasoning and from the Wiener series.

Physically, the effect of an impulse will instantaneously only change the acceleration term, $\mathbf{M}(\mathbf{y})\ddot{\mathbf{y}}$, and have no effect on the nonlinear term $\mathbf{g}(\mathbf{y}, \dot{\mathbf{y}}, t)$ so from Eq. (3.33)

$$\lim_{\delta t \to 0} \mathbf{M}(\mathbf{y}) \frac{\delta \dot{\mathbf{y}}|_{\xi(T)}}{\delta t} = \mathbf{f}(\mathbf{y}) \xi(T) \tag{3.44}$$

where $\frac{\delta \dot{\mathbf{y}}|_{\xi(T)}}{\delta t}$ represents the accelerations of the generalised coordinates only due to the excitation at time T. This equation can be described physically as a unit impulse giving a unit change in momentum.

Rearranging Eq. (3.44), a small change in $\dot{\mathbf{y}}$, $\delta\dot{\mathbf{y}}|_{\xi(T)}$, from the excitation is therefore

$$\lim_{\delta t\to 0}\delta\dot{\mathbf{y}}|_{\xi(T)} = \mathbf{M}^{-1}\mathbf{f}\xi(T)\delta t. \tag{3.45}$$

The small time-step, δt, here is from a time just before the impulse, T^-, to a time just after the impulse, T^+, where $T^+ - T^- = \delta t$ and the magnitude of the impulse is $\xi(T)\delta t$.

The change in the velocity vector from excitation $\xi(T)$ at time T, $\delta\dot{\mathbf{y}}|_{\xi(T)}$ can also be calculated from the Wiener series. From Eq. (3.36) the change in the velocity vector provides a change in the $z(t)$ variable

$$\delta z|_{\xi(T)} = \mathbf{f}(\mathbf{y})^{\mathrm{T}}\delta\dot{\mathbf{y}}|_{\xi(T)} \tag{3.46}$$

where the Wiener series of Eq. (3.37) can be rewritten in a variational form

$$\delta z|_{\xi(T)} = \sum_{n=0}^{\infty}\Delta\mathbf{g}_n[k_n;\xi(T)]. \tag{3.47}$$

and the $\Delta\mathbf{g}_n$ terms represent the change in nth g-functional due to the excitation at time T, $\xi(T)$.

The zeroth order Δg-functional is simply

$$\Delta\mathbf{g}_0[k_0;\xi(T)] = 0 \tag{3.48}$$

since it does not depend on the excitation. The first order Δg-functional is

$$\Delta\mathbf{g}_1[k_1;\xi(T)] = \lim_{\delta t\to 0}\int_{-\delta t/2}^{\delta t/2} k_1(\tau)\xi(T-\tau)d\tau. \tag{3.49}$$

Since the instantaneous response to a single impulse of magnitude $\xi(T)\delta t$ is being assessed, the integral of Eq. (3.49) disappears and the first Δg-functional becomes

$$\Delta\mathbf{g}_1[k_1;\xi(T)] = \lim_{\delta t\to 0} k_1(0^+)\xi(T)\delta t \tag{3.50}$$

meaning that immediately after the impulse the first Δg-functional contributes $k_1(0^+)\xi(T)\delta t$ to the response where the argument 0^+ in $k_1(\tau)$ represents the time instantaneously after $\tau_1 = 0$. This is analogous to the impulse response of a linear system where immediately after an impulse, the response would be given by the value of the impulse response just after the impulse multiplied by the magnitude of the impulse. However, whilst in the linear case $k_1(\tau)$ would completely define the response to the impulse, in the nonlinear case the higher order functionals may also contribute to this value so must also be assessed.

The second order Δg-functional is

$$\begin{aligned}\Delta\mathbf{g}_2[k_2;\xi(T)] &= \lim_{\delta t\to 0}\int_{-\delta t/2}^{\delta t/2}\int_{-\infty}^{\infty} k_2(\tau_1,\tau_2)\xi(T-\tau_1)\xi(T-\tau_2)d\tau_1 d\tau_2 + \\ &\qquad \int_{-\infty}^{\infty}\int_{-\delta t/2}^{\delta t/2} k_2(\tau_1,\tau_2)\xi(T-\tau_1)\xi(T-\tau_2)d\tau_1 d\tau_2 - \\ &\qquad \int_{-\delta t/2}^{\delta t/2}\int_{-\delta t/2}^{\delta t/2} k_2(\tau_1,\tau_2)\xi(T-\tau_1)\xi(T-\tau_2)d\tau_1 d\tau_2 \\ &= \lim_{\delta t\to 0} 2\xi(T)\delta t\int_{-\infty}^{\infty} k_2(0^+,\tau_2)\xi(T-\tau_2)d\tau_2 + k_2(0^+,0^+)\xi(T)\xi(T)\delta t^2 \\ &= \lim_{\delta t\to 0} 2\xi(T)\delta t\int_{-\infty}^{\infty} k_2(0^+,\tau_2)\xi(T-\tau_2)d\tau_2 \end{aligned} \tag{3.51}$$

where the symmetry of the second kernel, $k_2(\tau_1,\tau_2) = k_2(\tau_2,\tau_1)$, has been used and the subtraction of the double integral between $-\delta t/2$ and $\delta t/2$ on the first line accounts for the counting of the $-\delta t/2 \le \tau_1 \le \delta t/2$, $-\delta t/2 \le \tau_2 \le \delta t/2$ region in both of the first two terms on the right hand side. The value of this integral clearly goes to zero as $\delta t \to 0$ since it is of order δt^2. For all higher order Δg-functionals, this region will also be negligible since its value will be of order δt^n where n is the order of the functional. For the same reason as the first functional, one argument of the second kernel is evaluated at $\tau_1 = 0^+$.

Similarly, the nth Δg-functional is

$$\begin{aligned}\Delta\mathbf{g}_n[k_n;\xi(T)] &= \lim_{\delta t\to 0}\sum_{m=0}^{\text{floor}[(n-1)/2]}(n-2m)\frac{(-1)^m n!}{(n-2m)!m!2^m}\int_{-\delta t/2}^{\delta t/2}\cdots\int_{-\infty}^{\infty}\times \\ &\qquad \int_{-\infty}^{\infty}\cdots\int_{-\infty}^{\infty} k_n(\tau_1,...,\tau_{2m},\sigma_1,...,\sigma_{n-2m})\times \\ &\qquad\quad R_{\xi\xi}(\tau_1-\tau_2)...R_{\xi\xi}(\tau_{2m-1}-\tau_{2m})d\tau_1...d\tau_{2m}\times \\ &\qquad\quad \xi(T-\sigma_1)...\xi(T-\sigma_{n-2m})d\sigma_1...d\sigma_{n-2m} \\ &= \lim_{\delta t\to 0}\sum_{m=0}^{\text{floor}[(n-1)/2]}\frac{(-1)^m n!}{(n-2m-1)!m!2^m}\xi(T)\delta t\int_{-\infty}^{\infty}\cdots\int_{-\infty}^{\infty}\times \\ &\qquad \int_{-\infty}^{\infty}\cdots\int_{-\infty}^{\infty} k_n(\tau_1,...,\tau_{2m},0^+,\sigma_2,...,\sigma_{n-2m})\times \\ &\qquad\quad R_{\xi\xi}(\tau_1-\tau_2)...R_{\xi\xi}(\tau_{2m-1}-\tau_{2m})d\tau_1...d\tau_{2m}\times \\ &\qquad\quad \xi(T-\sigma_2)...\xi(T-\sigma_{n-2m})d\sigma_2...d\sigma_{n-2m} \end{aligned} \tag{3.52}$$

where the limit of the summation is different from that of Eq. (3.11) because only terms that involve at least one excitation term can affect δz.

Combining Eqs. (3.45), (3.46), (3.47) and (3.52) yields

$$\begin{aligned}\lim_{\delta t\to 0}\mathbf{f}^{\mathrm{T}}\mathbf{M}^{-1}\mathbf{f}\xi(T)\delta t = \lim_{\delta t\to 0} k_1(0^+)\xi(T)\delta t + \\ 2\xi(T)\delta t\int_{-\infty}^{\infty} k_2(0^+,\tau_2)\xi(T-\tau_2)d\tau_2 + ... + \\ \sum_{m=0}^{\mathrm{floor}[(n-1)/2]}\frac{(-1)^m n!}{(n-2m-1)!m!2^m}\xi(T)\delta t\int_{-\infty}^{\infty}...\int_{-\infty}^{\infty}\times \\ \int_{-\infty}^{\infty}...\int_{-\infty}^{\infty}k_n(\tau_1,...,\tau_{2m},0^+,\sigma_2,...,\sigma_{n-2m})\times \\ R_{\xi\xi}(\tau_1-\tau_2)...R_{\xi\xi}(\tau_{2m-1}-\tau_{2m})d\tau_1...d\tau_{2m}\times \\ \xi(T-\sigma_2)...\xi(T-\sigma_{n-2m})d\sigma_2...d\sigma_{n-2m}. \qquad (3.53)\end{aligned}$$

To simplify further and isolate the $k_1(0^+)$ term, the $\xi(T)\delta t$ terms can be cancelled and the expected value taken (noting that depending on the system both **f** and **M(y)** can be random variables) giving

$$\begin{aligned}\mathrm{E}\left[\mathbf{f}^{\mathrm{T}}\mathbf{M}^{-1}\mathbf{f}\right] = & k_1(0^+) + 2\int_{-\infty}^{\infty} k_2(0^+,\tau_2)\mathrm{E}\left[\xi(T-\tau_2)\right]d\tau_2 + ... + \\ & \sum_{m=0}^{\mathrm{floor}[(n-1)/2]}\frac{(-1)^m n!}{(n-2m-1)!m!2^m}\int_{-\infty}^{\infty}...\int_{-\infty}^{\infty}\times \\ & \int_{-\infty}^{\infty}...\int_{-\infty}^{\infty}k_n(\tau_1,...,\tau_{2m},0^+,\sigma_2,...,\sigma_{n-2m})\times \\ & R_{\xi\xi}(\tau_1-\tau_2)...R_{\xi\xi}(\tau_{2m-1}-\tau_{2m})d\tau_1...d\tau_{2m}\times \\ & \mathrm{E}\left[\xi(T-\sigma_2)...\xi(T-\sigma_{n-2m})\right]d\sigma_2...d\sigma_{n-2m}. \qquad (3.54)\end{aligned}$$

It is clear that for any even n, the nth term will be zero since it will include an ensemble average of an odd number of zero mean excitation terms. The limit of the sum over m therefore becomes $(n-1)/2$ and the nth term can be investigated in a similar manner as Section 3.2.

The ensemble average containing $n-2m-1$ terms can be rewritten as a sum of products of autocorrelation functions. There are $(n-2m-1)!/((n-2m-1)/2)!2^{(n-2m-1)/2}$ distinct ways of pairing the terms so there will be this many terms in the sum and the integral over each term will be the same due to the symmetry property of the kernels. The nth term in Eq.

(3.54) therefore becomes

$$\sum_{m=0}^{(n-1)/2} \frac{(-1)^m n!}{(n-2m-1)!m!2^m} \frac{(n-2m-1)!}{((n-2m-1)/2)!2^{(n-2m-1)/2}} \times \int_{-\infty}^{\infty} ... \int_{-\infty}^{\infty} \int_{-\infty}^{\infty} ... \int_{-\infty}^{\infty} k_n(\tau_1, ..., \tau_{2m}, 0^+, \sigma_2, ..., \sigma_{n-2m}) \times R_{\xi\xi}(\tau_1 - \tau_2)...R_{\xi\xi}(\tau_{2m-1} - \tau_{2m}) \times R_{\xi\xi}(\sigma_2 - \sigma_3)...R_{\xi\xi}(\sigma_{n-2m-1} - \sigma_{n-2m}) d\tau_1 ... d\tau_{2m} d\sigma_2 ... d\sigma_{n-2m} \tag{3.55}$$

where the integral is the same for every value of m. Analysis of this term shows that it is equal to zero since the sum becomes

$$\begin{aligned} \sum_{m=0}^{(n-1)/2} \frac{(-1)^m n!}{m!((n-1)/2-m)!2^{(n-1)/2}} &= \frac{n!}{M!2^{(n-1)/2}} \sum_{m=0}^{M} \frac{M!(-1)^m}{m!(M-m)!} \\ &= \frac{n!}{M!2^{(n-1)/2}} (1-1)^M \\ &= 0 \end{aligned}$$

where $M = (n-1)/2$ and a binomial expansion around the point -1 has been used. Eq. (3.54) therefore becomes

$$k_1(0^+) = \mathrm{E}\left[\mathbf{f}^{\mathrm{T}} \mathbf{M}^{-1} \mathbf{f}\right]. \tag{3.56}$$

The value of the first kernel, $k_1(\tau)$, around the $\tau = 0$ point will now be explored. When $\tau = 0^-$, instantaneously before any excitation, the response must be zero because the system is causal so $k_1(0^-) = 0$. Combining with Eq. (3.56) suggests that at $\tau = 0$ the value of the kernel is halfway between $k_1(0)$ and $k_1(0^+)$, so $k_1(0) = \mathrm{E}\left[\mathbf{f}^{\mathrm{T}} \mathbf{M}^{-1} \mathbf{f}\right]/2$ as required by Eq. (3.43). This is equivalent to saying at $k_1(0)$, only half of the impulse from the excitation has occurred so the response is only half the magnitude. The importance of this point is observed when examining the relationship between the time and frequency domain kernels, $k_1(\tau)$ and $K_1(\omega)$ connected via Eqs. (3.25) and (3.26). The causality of $k_1(\tau)$ implies that the real and imaginary parts of the frequency domain kernel are even and odd respectively. When an inverse Fourier transform is taken of the frequency kernel, the real and imaginary parts generate even, $k_{1E}(\tau)$, and odd, $k_{1O}(\tau)$, time functions respectively. For $\tau < 0$ the two functions are equal and opposite, $k_{1E}(\tau < 0) = -k_{1O}(\tau < 0)$, so cancel to ensure a causal response whereas for $\tau > 0$ the two functions are equal, $k_{1E}(\tau > 0) = k_{1O}(\tau > 0)$, and add to generate the time kernel. However, when $\tau = 0$ the odd function must be zero, $k_{1O}(0) = 0$, but the even function has a finite value given by the integral over the real part of the frequency kernel. Assuming $k_{1E}(\tau)$ is smooth, this value will be $k_1(0^+)/2$. The factor of

two is therefore important for calculating power dissipation according to Eq. (3.41). This is similar to analysis of a point at a discontinuity in Fourier analysis where the calculated value at the discontinuity is the mean of the values to either side of it.

Although the triple product term $\mathrm{E}\left[\mathbf{f}^{\mathrm{T}}\mathbf{M}^{-1}\mathbf{f}\right]$ in Eq. (3.56) seems physically unintuitive, it has been discussed in detail in [48] where it has been shown that for a system with a total oscillating mass, M_{Tot},

$$\mathrm{E}\left[\mathbf{f}^{\mathrm{T}}\mathbf{M}^{-1}\mathbf{f}\right] \leq M_{Tot}. \tag{3.57}$$

In [48] Langley shows that if a system is constrained to reduce its number of degrees of freedom then $\mathrm{E}\left[\mathbf{f}^{\mathrm{T}}\mathbf{M}^{-1}\mathbf{f}\right] < M_{Tot}$. However, if there is no constraint on the system, the inequality of Eq. (3.57) becomes an equality so

$$\mathrm{E}\left[\mathbf{f}^{\mathrm{T}}\mathbf{M}^{-1}\mathbf{f}\right] = M_{Tot}. \tag{3.58}$$

An illustrative example is given where, quoting directly from the text, 'a planar inverted pendulum, consisting of a lumped mass m mounted on a massless rod of length L. The rotation of the pendulum from the vertical is θ and the elastic extension of the rod is r. The elastic stiffness of the rod is k_2 and a rotational spring of stiffness k_1 is attached to the base of the rod; dampers of rate c_2 and c_1 are attached in parallel with the springs.' The equations of motion for this system are

$$\begin{pmatrix} m(L+r)^2 & 0 \\ 0 & m \end{pmatrix} \begin{pmatrix} \ddot{\theta} \\ \ddot{r} \end{pmatrix} + \begin{pmatrix} 2m(L+r)\dot{r}\dot{\theta} + c_1\dot{\theta} + k_1\theta - mg(L+r)\sin\theta \\ -m(L+r)\dot{\theta}^2 + c_2\dot{r} + k_2 r + mg\cos\theta \end{pmatrix} = \begin{pmatrix} m(L+r)\sin\theta \\ -m\cos\theta \end{pmatrix} \ddot{b}(t) \tag{3.59}$$

where g is the acceleration due to gravity and $\ddot{b}(t)$ is the acceleration of the base of the rod in the vertical direction. Here, the mass matrix and force vector provide $\mathrm{E}\left[\mathbf{f}^{\mathrm{T}}\mathbf{M}^{-1}\mathbf{f}\right] = m$ since the mass is free to move anywhere on the plane. If, however, the system is constrained such that the rod becomes infinitely stiff, a single-degree-of-freedom system results with equation of motion

$$mL^2\ddot{\theta} + c_1\dot{\theta} + k_1\theta - mgL\sin\theta = mL\sin\theta\ddot{b}(t). \tag{3.60}$$

In this case $\mathrm{E}\left[\mathbf{f}^{\mathrm{T}}\mathbf{M}^{-1}\mathbf{f}\right] = m\mathrm{E}\left[\sin^2\theta\right]$ so the triple product is less than the total oscillating mass because motion has been constrained to one generalised coordinate, θ, and motion in the entire plane is not possible.

In practice the two systems of Eq. (3.59) and (3.60) could be expected to give almost identical responses when a very high rod stiffness is used in the unconstrained case. It seems

counter-intuitive therefore that the constrained system should provide such a different triple product and thus first Wiener kernel from Eq. (3.56) (which has consequences for power dissipation) from that of the unconstrained system. Langley provides physical reasoning for this effect arguing that any constrained system such as the one of Eq. (3.60) is in reality still an unconstrained system like Eq. (3.59), but with components or couplings of infinite stiffness that reduce the number of generalised coordinates.

For white noise excitation as used in [48], which covers all frequencies, the system must still include the infinite frequency components in order to account for all resonances and be a good model across the entire frequency range. According to Langley 'the use of [Eq. (3.60)] is equivalent to the assumption that the excitation does not extend to the second linear resonance, so that the system is essentially excited by band limited noise, leading to a lower result for the power input by the base excitation.'

The inverted pendulum systems of Eqs. (3.59) and (3.60) are simulated and used to illustrate this discussion in Section 3.5.2. The case of band-limited noise is interesting since the kernel is undefined for any frequency range that contains no excitation and this will be discussed separately in Section 3.6.

To summarise the results so far: the power dissipated by a general nonlinear oscillator, Eq. (3.33), under random excitation of a general spectrum, $S_{\ddot{\xi}\ddot{\xi}}(\omega)$, can be calculated using Eq. (3.41). To do this, the first Wiener kernel must be calculated from either simulations or experimentally using Eq. (3.24), but crucially for a designer of a system desiring a preliminary estimate of power dissipation, the first Wiener kernel has the property of Eq. (3.42) where the triple product term is simply equal to the oscillating mass provided the system is unconstrained.

It should be noted that this approach extends the results for white noise excitation of [47] and [48] to general random excitation. The white noise results are retrieved by using $S_{\ddot{\xi}\ddot{\xi}}(\omega) = \pi S_0$ where the factor of π remains in the spectrum since the Fourier transform formula used is Eq. (3.27) with an autocorrelation function $R_{bb}(\tau) = \pi S_0 \delta(\tau)$. This is substituted into Eq. (3.41) and combining with Eq. (3.42) and (3.57) the power dissipated by white noise is

$$P_{White} = \frac{\pi S_0 \mathrm{E}\left[\mathbf{f}^{\mathrm{T}}\mathbf{M}^{-1}\mathbf{f}\right]}{2} \leq \frac{\pi S_0 M_{Tot}}{2}. \tag{3.61}$$

The value of this approach for non-white noise, particularly when applied to energy harvesting, will be illustrated in the following sections. Additionally, for a system with linear damping, the approach is not limited to calculation of power, but also provides the mean square velocity of the response since this is proportional to power.

3.4.2 Properties of the First Extended Wiener Kernel

Two interesting properties of the first extended Wiener kernel are worth mentioning. Firstly, since the time domain kernel, $k_1(\tau)$, is real and causal, the frequency domain kernel, $K_1(\omega)$, is complex with an even real part and odd imaginary part. The imaginary part therefore does not contribute to the integral in Eqs. (3.41) or (3.42) so the equations can be modified such that the integrals are only performed over positive frequencies and the real part of the kernel giving

$$P = \frac{1}{\pi}\int_0^\infty \mathrm{Re}[K_1(\omega)]S_{\xi\xi}(\omega)d\omega \tag{3.62}$$

and

$$\frac{1}{\pi}\int_0^\infty \mathrm{Re}[K_1(\omega)]d\omega = \frac{\mathrm{E}\left[\mathbf{f}^{\mathrm{T}}\mathbf{M}^{-1}\mathbf{f}\right]}{2}. \tag{3.63}$$

The real part of the first kernel completely defines the power dissipated.

Secondly, the sign of the real part of the first kernel is of interest. For a passive system, clearly the power dissipated must be positive therefore the integral of Eq. (3.62) must be positive. However, it is an interesting question as to whether the real part of the first kernel should be positive for all frequencies. For a linear system, this must be the case since the frequency kernel is the frequency response and independent of the input spectrum so a negative kernel within any frequency range would mean the system would dissipate negative power if only driven by excitation in this range. Nevertheless, there is no reason why this should be true for every nonlinear oscillator and the question of whether the real part of the kernel is always positive remains an open one.

In [48] the sign of the kernel has implications for whether the power dissipated for a given system by white noise excitation of spectrum S_0 will always be greater than the power dissipated by that system under an excitation of non-white spectrum with a peak of magnitude S_0 and thus whether white noise can act as an upper bound on power available. Langley has proved in [48] that for any single-degree-of-freedom system with linear damping and general stiffness nonlinearity the kernel is always positive due to the system satisfying the 'detailed balance' condition [52]. The proof can be simply extended to the case of general random excitation thus the real part of the first extended Wiener kernel of a system with detailed balance is positive for all frequencies.

This argument can now also be made from Eq. (3.62) where if the real part of the first kernel is positive at all frequencies and S_{Max} is the maximum value of the spectrum then

$\mathrm{Re}[K_1(\omega)]S_{\xi\xi}(\omega) \leq \mathrm{Re}[K_1(\omega)]S_{Max}$ and thus

$$\begin{aligned} P &\leq \frac{1}{\pi}\int_0^\infty \mathrm{Re}[K_1(\omega)]S_{Max}d\omega \\ &\leq \frac{S_{Max}}{\pi}\int_0^\infty \mathrm{Re}[K_1(\omega)]d\omega \\ &\leq \frac{S_{Max}\mathrm{E}\left[\mathbf{f}^{\mathrm{T}}\mathbf{M}^{-1}\mathbf{f}\right]}{2} \\ &\leq \frac{S_{Max}M_{Tot}}{2} \end{aligned}$$

using Eqs. (3.57) and (3.63). This is comparable to the white noise result of Eq. (3.61) and shows that the power dissipated by white noise excitation provides an upper bound on the power available to harvest from excitation of any spectrum if the peak of the spectrum is taken as the white noise spectrum amplitude and the real part of the first kernel is positive for all frequencies. The upper bounds on power dissipation are discussed in more detail in Section 3.7.

It has not been possible to say more about the sign of the real part of the first kernel for more general oscillators although it may well be true that the kernel must be positive at all frequencies for any passive system. However, when the system is not passive it has been shown in [48] by considering a nonlinear system with time varying stiffness excited by white noise that the real part of the kernel can be negative within a small frequency range.

3.5 Numerical Validation

The theory developed in Section 3.4 will be illustrated using a number of example systems in this section. In particular the two results of Eqs. (3.62) and (3.63) will be examined along with the effect of nonlinearity and excitation spectrum on the first kernel.

Numerical time domain simulations are conducted where an ensemble of results is built up by exciting a nonlinear oscillator with a number of realisations of random noise of a chosen spectrum. The ode45 routine in MATLAB is used and the first extended Wiener kernel can be found using Eq. (3.24) where $S_{yx}(\omega)$ becomes $S_{z\xi}(\omega)$ and $S_{xx}(\omega)$ becomes $S_{\xi\xi}(\omega)$ with ξ being the negative of the base motion.

The cross-spectrum of random variables $x(t)$ and $y(t)$ can be calculated from the cross-correlation. Taking the cross-correlation and averaging both over the ensemble and over the time length, T, of the signal yields

$$R_{yx}(\tau) = \frac{1}{T}\int_0^T \mathrm{E}\left[y(t)x(t-\tau)\right]dt. \tag{3.64}$$

The cross-spectrum can be found by taking the Fourier transform of the cross-correlation giving

$$\begin{aligned} S_{yx}(\omega) &= \int_0^T \frac{1}{T}\int_0^T \mathrm{E}\left[y(t)x(t-\tau)\right]dt\mathrm{e}^{-i\omega\tau}d\tau \\ &= \frac{1}{T}\mathrm{E}\left[\int_0^T\int_0^T \mathrm{e}^{-i\omega t}y(t)x(t-\tau)\mathrm{e}^{-i\omega(\tau-t)}dtd\tau\right] \\ &= \frac{1}{T}\mathrm{E}\left[\int_0^T \mathrm{e}^{-i\omega t}y(t)dt\int_T^0 x(s)\mathrm{e}^{i\omega s}(-ds)\right] \\ &= \frac{1}{T}\mathrm{E}\left[\mathscr{F}(y)\mathscr{F}^*(x)\right] \end{aligned}$$

where $s = t-\tau$ and $\mathscr{F}$ represents the discrete Fourier transform.

3.5.1 Single-degree-of-freedom Systems

As a simple example of a nonlinear system, the base excited Duffing oscillator

$$m\ddot{y} + c\dot{y} + ky + \varepsilon y^3 = -m\ddot{b}(t) \tag{3.65}$$

serves as a useful model for displaying the key features of the first kernel. In this case $z = m\dot{y}$ and $\mathrm{E}\left[\mathbf{f}^{\mathrm{T}}\mathbf{M}^{-1}\mathbf{f}\right] = m$.

The first Wiener kernel is plotted in the time and frequency domains in Figure 3.1 for an oscillator with different values of the nonlinearity constant under white noise base excitation of spectrum $S_0 = 2\pi$W/kg. The parameters used are $m = 3$kg, $c = 0.4$kg/s and $k = 10$N/m and it can clearly be seen that the initial jump of the time domain kernel is of magnitude m and the integral of Eq. (3.63) is 1.52, 1.49 and 1.52kg for $\varepsilon = 0$, 0.1 and 0.3N/m^3 respectively. Additionally, as nonlinearity increases, the time domain first kernel decays more rapidly and the frequency domain kernel becomes lower and wider meaning that the kernel appears more damped with nonlinearity. This effect is due to the higher order kernels having greater influence at higher nonlinearity meaning more energy is distributed from the first kernel to the higher order ones thus increasing the energy loss, or damping, of the first kernel. The power dissipated can be calculated directly from the time domain results as 9.70, 9.23 and 9.60W and from Eq. (3.62) as $P = 9.55$, 9.36 and 9.55W for $\varepsilon = 0$, 0.1 and 0.3N/m^3 respectively showing that the simulations agree well with the theory and the white noise result of 9.42W from Eq. (3.61).

The base acceleration in the previous figure is white noise and so the result that the integral over the frequency domain first kernel must be constant has already been proven

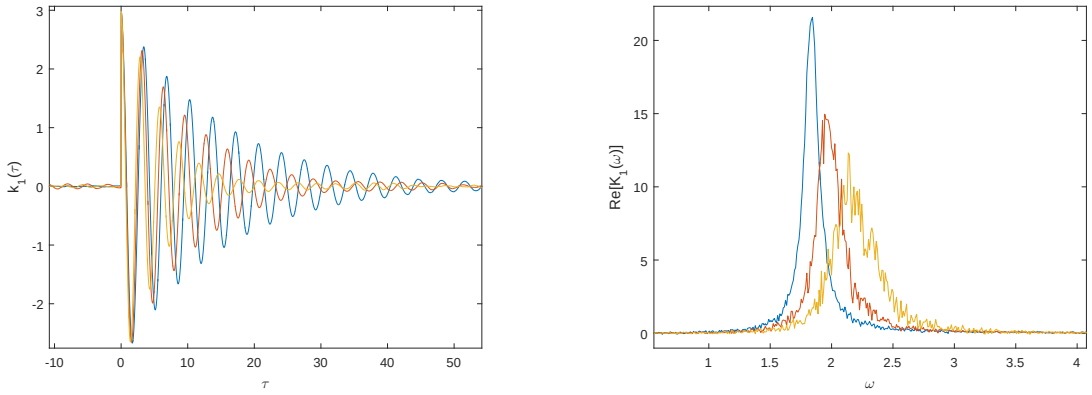

(a) (b)

Fig. 3.1 a) Time and b) frequency domain first Wiener kernels under white noise when $\varepsilon = 0$ (blue), $\varepsilon = 0.1$ (red) and $\varepsilon = 0.3\text{N/m}^3$ (yellow).

from a combination of Wiener theory and [47]. Next, a non-white excitation with spectrum

$$S_{\xi\xi}(\omega) = \frac{\pi S_0}{2} \frac{\omega_0^4}{\left(\omega_0^2 - \omega^2\right)^2 + 4\zeta_0^2\omega_0^2\omega^2} \tag{3.66}$$

is applied to three nonlinear oscillators: a monostable oscillator with $k = 0$, a bistable oscillator with $k = -200$ exhibiting inter-well dynamics and a bistable oscillator with $k = -300\text{N/m}$ largely vibrating in one potential well. The other parameters are $m = 3\text{kg}$, $c = 0.4\text{kg/s}$, $\varepsilon = 300\text{N/m}^3$, $\omega_0 = 16\text{rad/s}$, $\zeta_0 = 0.3$ and $S_0 = 0.3\text{W/kg}$. Since the narrowband signal's low spectrum at high frequencies amplifies errors in the first kernel, a very low level white noise has been applied in addition to the narrowband noise to provide a more significant spectrum at high frequencies. The effect of low or zero input spectrum at certain frequencies is discussed further in Section 3.6.

The time and real part of the frequency first kernels are displayed in Figure 3.2 where the addition of two potential wells is seen to strongly affect the kernels. The monostable case behaves with one strong resonance whereas the bistable cases contain two resonances, one at approximately the frequency of inter-well dynamics and one at approximately the frequency of single-well dynamics. In the case where the linear stiffness is more negative, a lower resonant peak is observed at the frequency of inter-well dynamics since the majority of motion is within one potential well. In the time domain, the responses are highly damped due to the strong nonlinearity and reflect the dominant frequencies present.

As before and expected by the theory, the initial jump of the time kernel is approximately of value m and the integral over the frequency kernel from Eq. (3.63) is 1.50, 1.43 and 1.52kg

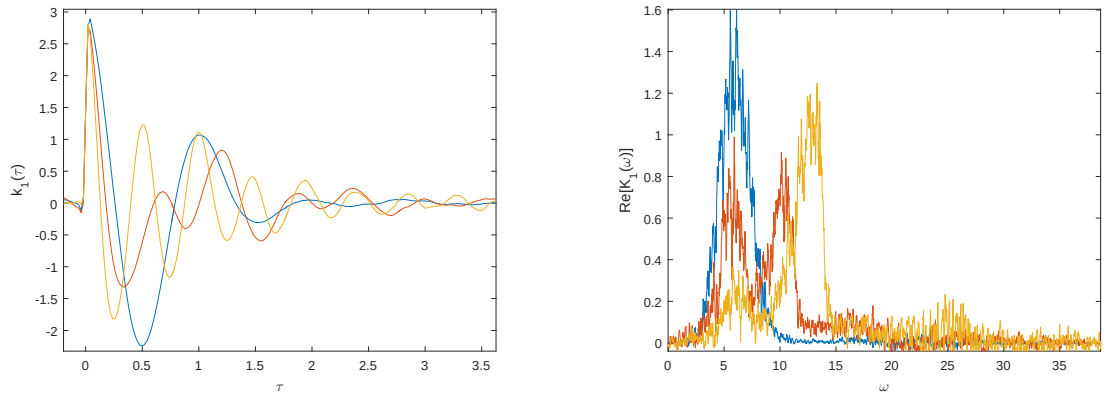

(a) (b)

Fig. 3.2 a) Time and b) frequency domain first extended Wiener kernels under narrowband noise when $k = 0$ (blue), $k = -200$ (red) and $k = -300$N/m (yellow).

for $k = 0$, $k = -200$ and $k = -300$N/m respectively. Additionally, the power dissipated can be calculated directly from the time domain results as 1.86, 2.33 and 3.25W and from Eq. (3.62) as $P = 1.85$, 2.32 and 3.24W for $k = 0$, $k = -200$ and $k = -300$N/m respectively again showing that the simulations agree well with the theory.

An interesting feature of both Figures 3.1 and 3.2 is that the noisiness of the kernel in the frequency domain seems correlated to level of nonlinearity in the system. Whilst the noise decreases with a greater ensemble, this feature suggests that compared to the linear case where the response is consistent regardless of input magnitude, a nonlinear oscillator requires more information to build up a complete description and thus extended Wiener series of the response because the response varies with input level. Additionally, due to the cubic stiffness of the Duffing oscillator, the first kernel often contains a noisier region at approximately three times the resonance frequency.

For a nonlinear system, the kernels depend on both the magnitude and spectrum of the excitation. For example, taking the oscillator of Figure 3.1 with $\varepsilon = 0.1\text{N/m}^3$, if the input magnitude was reduced, the output displacement would be smaller and therefore the stiffening nonlinearity would have less effect making the response lower frequency. Likewise, a large input excitation increases the response displacement, increasing the frequency and a similar plot to Figure 3.1 could be made.

It is also interesting to investigate the effect of different forms of input spectra although to provide a reasonable comparison the approximate magnitude of the input should be kept the same. Three input spectra; band-limited noise with a flat spectrum, low-pass noise of

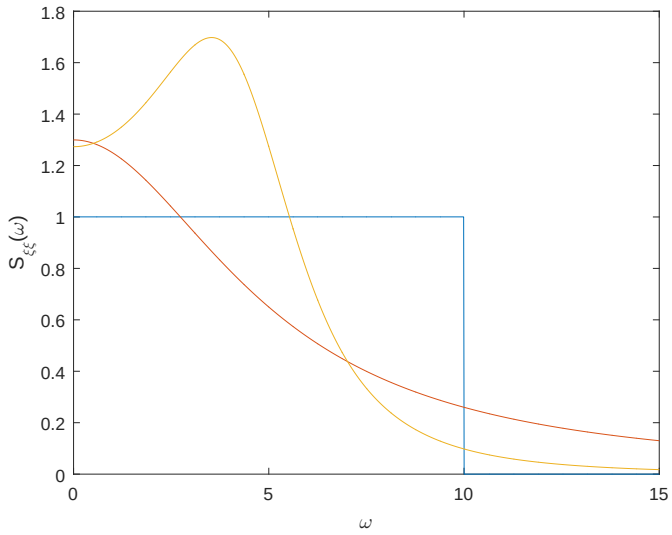

Fig. 3.3 Base acceleration spectra for band-limited (blue), low-pass (red) and narrowband (yellow) noise all with the same mean square acceleration.

spectrum given by

$$S_{\xi\xi}(\omega) = \frac{\pi S_0}{2} \frac{\omega_c^2}{\omega_c^2 + \omega^2} \tag{3.67}$$

and narrowband noise of Eq. (3.66) each chosen to have the same mean square acceleration (and therefore integral over the spectrum) are applied to a nonlinear oscillator. The band limited noise is chosen to have a spectrum of magnitude 1.00W/kg at frequencies between 0 and 10 rad/s and zero spectrum elsewhere, the low pass noise has $S_0 = 1.30$W/kg and $\omega_c = 5$rad/s and the narrowband noise has $S_0 = 1.27$W/kg, $\omega_0 = 5$rad/s and $\zeta_0 = 0.5$ and all three spectra are plotted in Figure 3.3.

The first kernel in the time and frequency domain is plotted in Figure 3.4 using $m = 3$kg, $c = 0.2$kg/s, $k = 10$N/m and $\varepsilon = 0.3$N/m^3. Subtle differences are seen between the kernels from band-limited and low-pass noise, with the low-pass noise having marginally higher frequency and damping. The kernel from the narrowband noise is more different still, with greater damping and a higher resonant frequency suggesting it oscillates over a greater, and therefore stiffer, displacement range. The integral over the kernel remains within 4% of the expected value of 1.5kg with 1.52, 1.52 and 1.56kg from the band-limited, low-pass and narrowband noise respectively.

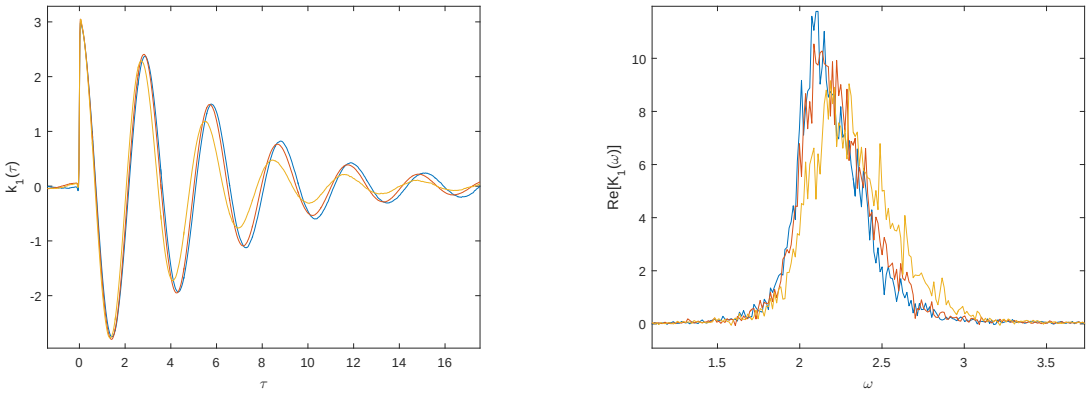

(a) (b)

Fig. 3.4 a) Time and b) frequency domain first Wiener kernels under band-limited (blue), low-pass (red) and narrowband (yellow) noise.

3.5.2 Multi-degree-of-freedom Systems

The numerical simulations show strong agreement with the theory for a SDOF oscillator so attention is now turned to two MDOF scenarios; two masses each defined by one generalised coordinate and a single mass able to move in two directions thus defined by two generalised coordinates. For the former case a two mass system of the form of Figure 3.5 is taken with equations of motion

$$\begin{pmatrix} m_1 & 0 \\ 0 & m_2 \end{pmatrix} \begin{pmatrix} \ddot{x} \\ \ddot{y} \end{pmatrix} + \begin{pmatrix} c_1+c_3 & -c_3 \\ -c_3 & c_2+c_3 \end{pmatrix} \begin{pmatrix} \dot{x} \\ \dot{y} \end{pmatrix} + \begin{pmatrix} k_1 x + \varepsilon x^3 + k_3(x-y) \\ k_2 + k_3(y-x) \end{pmatrix} = - \begin{pmatrix} m_1 \\ m_2 \end{pmatrix} \ddot{b}(t). \tag{3.68}$$

In this case the vector triple product $\mathrm{E}\left[\mathbf{f}^{\mathrm{T}}\mathbf{M}^{-1}\mathbf{f}\right] = m_1 + m_2$ so the integral over the kernel is compared to this amount. A system is analysed with parameter values of $m_1 = 1.5$kg, $m_2 = 0.7$kg, $c_1 = 0.4$kg/s, $c_2 = 0.2$kg/s, $c_3 = 0.05$kg/s, $k_1 = 15$N/m, $k_2 = 15$N/m, $k_3 = 5$N/m, $\varepsilon = 2000$N/m^3 and narrowband base acceleration with spectrum given by Eq. (3.66) where $\omega_0 = 6$rad/s, $\zeta_0 = 0.2$ and $S_0 = 2$W/kg and the time and real part of the frequency domain first kernels are plotted in Figure 3.6.

As might be expected since it contains a summation of the velocities of the two masses, the Wiener kernel contains two dominant frequencies: the resonant frequency of each mass. Interestingly, the first resonance has very little noise, whereas at frequencies above it the kernel is noisier presumably due to effects from the stiffening nonlinearity interacting with the second resonance. The integral over the frequency kernel is calculated as 1.09kg which is very close to the theoretically predicted result using Eq. (3.63) of $(m_1 + m_2)/2 = 1.1$kg and

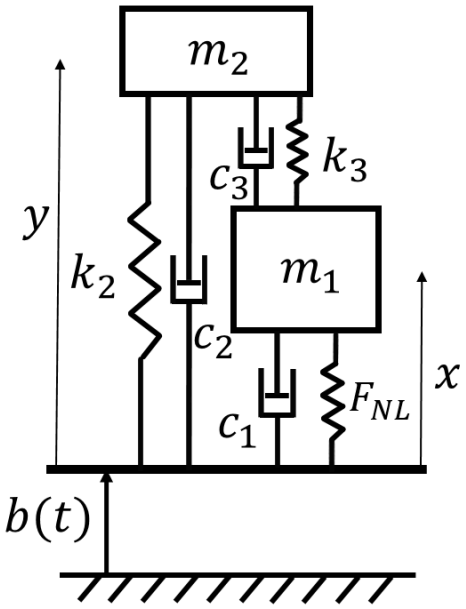

Fig. 3.5 Two degree-of-freedom system with two masses connected by a linear spring and one mass connected to the base via a nonlinear spring where $F_{NL} = k_1 x + \varepsilon x^3$.

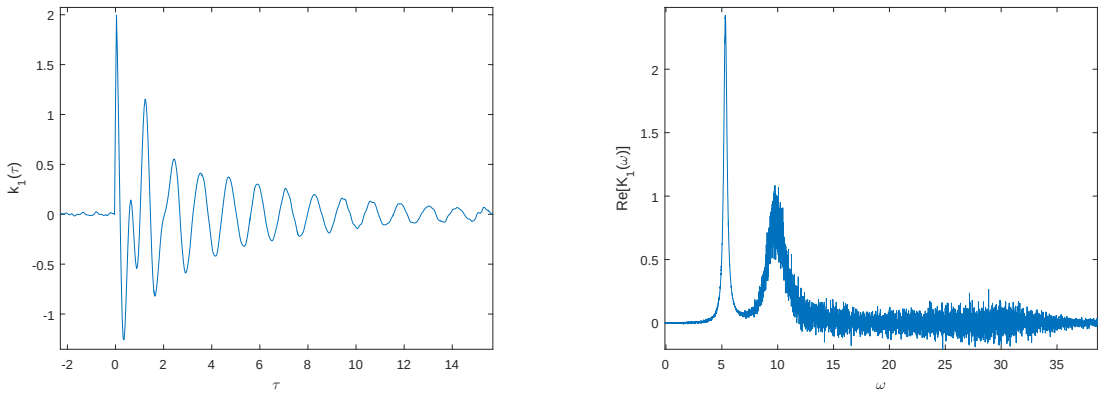

(a) (b)

Fig. 3.6 a) Time and b) frequency domain first Wiener kernels under narrowband noise for the 2 mass system of Figure 3.5.

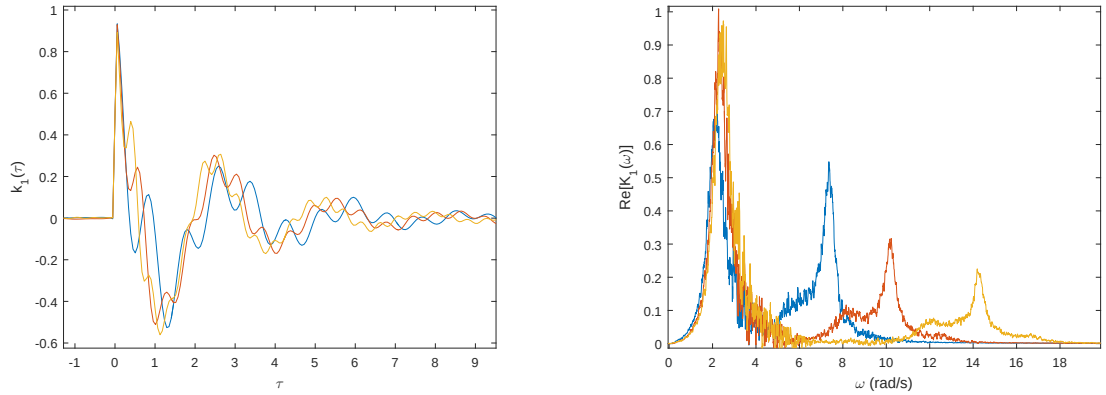

(a) (b)

Fig. 3.7 a) Time and b) frequency domain first Wiener kernels under narrowband noise for the inverted pendulum system of Eq. (3.59) with $k_2 = 50$ (blue), 100 (red) and 200N/m (yellow).

the power dissipated has been calculated directly from the simulations as 7.87W which is again very close to the power calculated from Eq. (3.62) of 7.89W.

The second MDOF case considered is the inverted pendulum described by Eq. (3.59) where $\mathrm{E}\left[\mathbf{f}^{\mathrm{T}}\mathbf{M}^{-1}\mathbf{f}\right] = m$. The first kernel is shown in Figure 3.7 for three different values of rod stiffness, $k_2 = 50$, 100 and 200N/m and other parameters $m = 1$kg, $L = 0.75$m, $c_1 = 0.1$kgm^2/s/rad, $c_2 = 0.5$kg/s, $k_1 = 5$Nm/rad, $g = 9.81$m/s^2 and narrowband base acceleration with spectrum given by Eq. (3.66) where $\omega_0 = 1$rad/s, $\zeta_0 = 0.5$ and $S_0 = 2$W/kg. As before the kernel has two dominant frequency components, approximately from oscillating in the θ direction at $\sqrt{k_1/L^2m} = 3.0$ rad/s and in the r direction at $\sqrt{k_2/m}$ rad/s. The power calculated directly from the simulations is 94, 81 and 76mW for $k_2 = 50$, 100 and 200N/m and again shows close resemblance to the power calculated from Eq. (3.62) as 95, 81 and 76mW. The integral over the frequency kernel is calculated as 0.49, 0.50, and 0.49kg which is very close to the theoretically predicted result using Eq. (3.63) of 0.5kg.

As the rod stiffness is increased, Figure 3.7 shows that the frequency of the second resonance increases and also the magnitude of the peak decreases. With greater rod stiffness, eventually the axial resonant frequency of the rod will be higher than the maximum frequency provided by the noise which is a computational limitation dictated by the minimum time-step used for the simulations and therefore the computation time of the simulations. From the discussions in Section 3.4.1 this is similar to the case where the axial displacement of the rod is constrained and the system becomes SDOF with equations of motion given by Eq. (3.60) and is discussed in the following section.

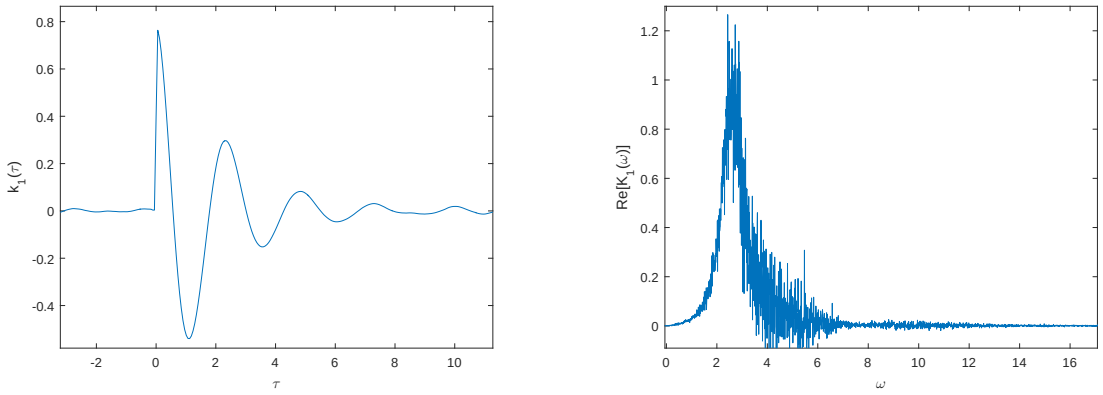

(a) (b)

Fig. 3.8 a) Time and b) frequency domain first Wiener kernels under narrowband noise for the SDOF inverted pendulum system in Eq. (3.60).

Power for Constrained Systems

For the constrained inverted pendulum system of Eq. (3.60) with an infinitely stiff rod the triple product and therefore the integral over the first kernel are no longer equal to the mass since $\mathrm{E}\left[\mathbf{f}^{\mathrm{T}}\mathbf{M}^{-1}\mathbf{f}\right] = m\mathrm{E}\left[\sin^2\theta\right]$. First, this result and its subsequent implications for power will be verified numerically and then the disparity between $\mathrm{E}\left[\mathbf{f}^{\mathrm{T}}\mathbf{M}^{-1}\mathbf{f}\right]$ for a two degree-of-freedom (2DOF) inverted pendulum with a stiff rod and the SDOF will be discussed.

An inverted pendulum with $m = 1\mathrm{kg}$, $L = 0.75\mathrm{m}$, $c_1 = 0.1\mathrm{kgm}^2/\mathrm{s/rad}$, $k_1 = 5\mathrm{Nm/rad}$ and $g = 9.81\mathrm{m/s}^2$ is excited by narrowband base acceleration with spectrum given by Eq. (3.67) where $\omega_0 = 1\mathrm{rad/s}$, $\zeta_0 = 0.5$ and $S_0 = 2\mathrm{W/kg}$ and the resulting first kernel is plotted in Figure 3.8. For this SDOF case, the response has one resonant frequency and due to the constraint of the infinite rod stiffness, the integral over the kernel in Eq. (3.63) is less than the mass, equalling 0.40kg which is close to the value of $\mathrm{E}\left[\mathbf{f}^{\mathrm{T}}\mathbf{M}^{-1}\mathbf{f}\right]$ calculated directly from simulations as 0.39kg and the decrease can be observed by a reduction in the initial jump of the time kernel from 1 to approximately 0.8 when compared to the unconstrained 2DOF case. The power dissipated by the damper calculated directly from the simulations is 70mW and from Eq. (3.62) is 70mW suggesting that the equation is still valid for the constrained case.

The transition from a two to a one degree of freedom system as rod stiffness is increased is interesting because of its impact on the integral over the first kernel and therefore triple product $\mathrm{E}\left[\mathbf{f}^{\mathrm{T}}\mathbf{M}^{-1}\mathbf{f}\right]$ and power dissipation. In theory for a finite, but very high, stiffness the system is always 2DOF since the first kernel is valid for frequencies higher than the axial resonant frequency of the rod. The inclusion of the second resonance in the kernel

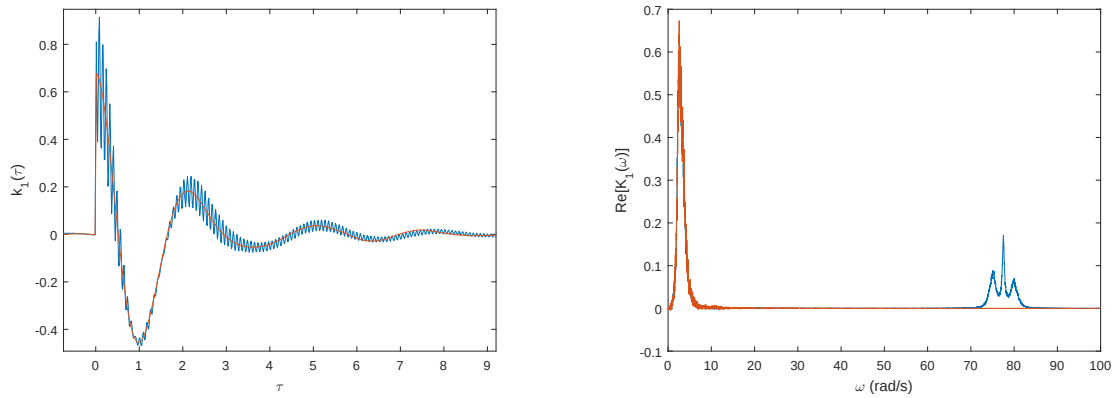

(a) (b)

Fig. 3.9 a) Time and b) frequency domain first Wiener kernels under band-limited noise for the 2DOF (blue) and SDOF (red) inverted pendulum systems where the maximum frequency in the simulations is greater than the second resonance of the 2DOF system.

adds to the integral over it and the triple product is equal to the mass. The difference in the kernels between the constrained SDOF and unconstrained 2DOF cases can be seen in Figure 3.9 where for the first resonance the kernels are almost identical, whereas the 2DOF contains the second resonance. The parameters selected are the same as in Figure 3.7, but with $k_2 = 6000$N/m providing an axial natural frequency of 77.5rad/s.

The result on the $\mathrm{E}\left[\mathbf{f}^{\mathrm{T}}\mathbf{M}^{-1}\mathbf{f}\right]$ term is apparent from the integral over the frequency domain kernel. For the 2DOF system the integral contains the second resonance and is 0.48kg, close to the expected theoretical value of $\mathrm{E}\left[\mathbf{f}^{\mathrm{T}}\mathbf{M}^{-1}\mathbf{f}\right]/2 = m/2 = 0.5$kg. Conversely, the integral over the frequency domain kernel for the SDOF system is $\mathrm{E}\left[\mathbf{f}^{\mathrm{T}}\mathbf{M}^{-1}\mathbf{f}\right]/2 = \mathrm{E}\left[m\sin^2(\theta)\right]/2 = 0.34$kg and is less than the 2DOF system because the second resonance is not included.

The consequence of modelling constrained systems carefully is illuminated when analysing the power dissipated by such systems. Applying band-limited noise with a flat spectrum of magnitude 2W/kg in the range 0-50rad/s and therefore not including the second resonance, the power dissipated by the SDOF and 2DOF systems respectively directly from simulations is 0.21 and 0.21W. This is very close to the values calculated using Eq. (3.62) of 0.21 and 0.23W. However, when white noise of magnitude 2W/kg is applied to the two systems the power dissipated by the SDOF and 2DOF systems respectively from simulations is very different: 0.22 and 0.29W. Here, the 2DOF has dissipated more power than the SDOF due to its second resonance. Whilst Eq. (3.62) can accurately calculate the power dissipated by constrained and unconstrained systems, failure to include all resonances of a system in the frequency range of interest will produce underestimates of the power.

In summary, the theory of Eqs. (3.62) and (3.63) has been validated within the bounds of reasonable noise error provided the frequency range used includes all significant frequency responses of the system. Where this is not the case, either the maximum frequency content of the simulations should be increased or a constraint should be added to the system such that the higher resonance is removed and $\mathrm{E}\left[\mathbf{f}^{\mathrm{T}}\mathbf{M}^{-1}\mathbf{f}\right]$ is no longer equal to M_{Tot}.

3.6 Band-limited Noise

Since the calculation of the first extended Wiener kernel involves dividing by the base acceleration spectrum according to Eq. (3.24), it is important to investigate the properties of the kernel for band-limited noise where there is zero input base acceleration at certain frequencies. In a sense all of the previous simulations have been for band-limited noise in that the time step has been finite therefore there has been a maximum frequency. However, in these cases, with the deliberate exception of Section 3.5.2 no significant dynamics occurs at higher frequencies than those included in the simulations. Of interest here, are cases where there is no input spectrum at frequencies of normally large response.

Looking initially at the linear case is useful since the first kernel is known to be the frequency response and all higher order kernels are equal to zero. For the kernel to successfully provide the output from a band-limited input, it is only required at frequencies where there is non-zero input spectrum. The value of the kernel at other frequencies has no impact on the output and hence can be undefined. However, if it is left undefined or set to an arbitrary value the result of Eq. (3.63) becomes false and suggests that a band-limited input invalidates the derivation. Physically, the derivation is based on a unit impulse imparting unit momentum to the system (instantaneously all momentum goes to the first kernel which dissipates it to the others) and this would remain true even with a band-limited input. If this is the case, the value of the kernel at frequencies of zero input will be prescribed even though it neither impacts the output nor is there a way to calculate it.

To illustrate this, a linear system of the form of Eq. (3.65) with $\varepsilon = 0$ has frequency response, $H(\omega)$, and therefore first kernel given by

$$K_1(\omega) = mH(\omega) = \frac{m^2\omega i}{k - m\omega^2 + c\omega i} \tag{3.69}$$

and is excited by band-limited noise with a flat spectrum of magnitude S_0 in the range $3 \leq \omega \leq 7$ and zero at all other frequencies. The real part of the first kernel in the frequency domain is plotted from simulations and Eq. (3.69) in Figure 3.10 with $m = 1.0$kg, $c = 0.5$kg/s, $k = 10$N/m and $S_0 = 2$W/kg. The time domain kernel is not plotted since the noise from

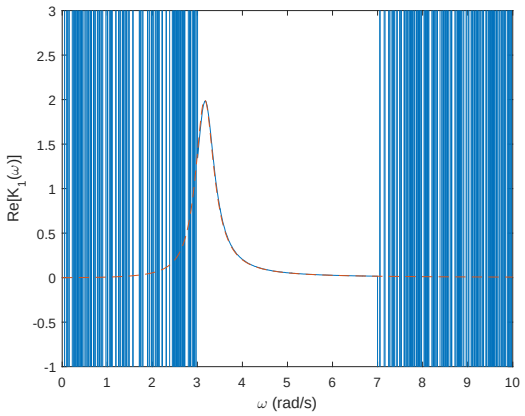

Fig. 3.10 Real part of the frequency domain first kernel of a linear system under band-limited noise calculated from simulations (blue) and Eq. (3.69) (red).

the frequencies outside those in the input spectrum is so high that in the time domain the kernel is almost entirely noise. At frequencies within the range of input spectrum the kernel is equal to the frequency response although elsewhere it is extremely noisy, presumably due to numerical noise from the discrete Fourier transform of z being divided by a very small number. It may be that an infinite ensemble would reduce the noise to the frequency response, but it is not possible to achieve. Clearly the noise in the kernel creates two problems when compared to the theory; it is non-causal and the integral over it does not equal $m/2$ as required by Eq. (3.63).

For the nonlinear case with $\varepsilon = 10\text{N/m}^3$, the first kernel is displayed in Figure 3.11 where similar to the linear case, the response is well defined in the range of frequencies where input is present, but is extremely noisy elsewhere. As before, clearly the integral over the kernel does not equal $m/2$ as required by Eq. (3.63) due to the noise. However, the power can still be calculated using Eq. (3.62) as 1.38W since the kernel is multiplied by the input spectrum and is equal to the power of 1.38W calculated directly from the simulations.

The highly non-causal kernels due to the noise from the simulations for both the linear and nonlinear cases suggest that for a causal kernel some knowledge of its value at frequencies where the input spectrum is zero is required. A possible way to find information about the kernel at other frequencies is to include very low level noise at these frequencies; enough to provide division by a non-zero quantity in Eq. (3.24), but not enough to affect the dynamics of the system at frequencies where the input is high. For the nonlinear case analysed above the first kernel is shown in Figure 3.12 when band-limited noise is applied, but the low amplitude range of the spectrum is zero, $S_0/20$ and $S_0/100$. The kernel for the case containing regions

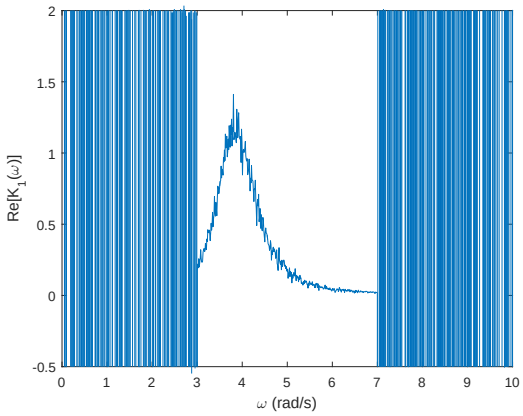

Fig. 3.11 Real part of the frequency domain first kernel of a nonlinear system under band-limited noise calculated from simulations.

of zero spectrum is only plotted in the frequency range where non-zero input occurs and is not plotted in the time domain due to its noise.

The addition of the low amplitude regions of the input spectrum provides kernels with lower noise at frequencies with low input than when zero input was used, although in these regions the higher the input spectrum, the lower the noisiness of the kernel. The small additional input spectrum does not have a noticeable effect on the kernel within the frequency range of high amplitude excitation suggesting that the first kernel can be reliably calculated for band-limited noise by using a low level rather than zero input spectrum. Additionally, the kernel remains unchanged as the low level noise tends towards zero suggesting that even for the case of zero spectrum the kernel is defined over all frequencies, even though it cannot be calculated at all frequencies. This would substantiate the result of Eq. (3.63), which is supported by the simulations providing an integral over the kernel of 0.50 and 0.51kg for the $S_0/20$ and $S_0/100$ cases respectively, very close to the theoretically predicted values of $m/2 = 0.5$kg.

3.7 Maximising Power Dissipation and Power Bounds

In energy harvesting applications maximum power dissipation is desired and the means of accomplishing it by using the theory of Section 3.4 is discussed in this section. When designing a harvester, it will be optimised for the spectrum of its operating environment, although this could change with time either varying in amplitude or frequency content. The

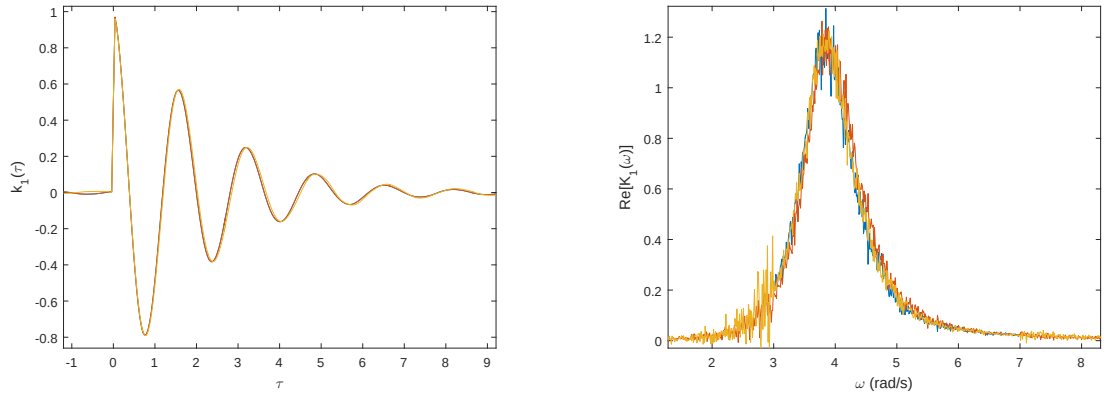

(a) (b)

Fig. 3.12 a) Time and b) frequency domain first Wiener kernels under band-limited noise with the low amplitude range of the spectrum set to 0 (blue), $S_0/20$ (red) and $S_0/100$ (yellow).

method of Section 3.4 does not account for time variations although it is still useful to provide guidance in non-stationary environments.

Firstly, it is clear that for maximum power the integral of the real part of the first extended Wiener kernel should be maximised. According to Eqs. (3.63) and (3.57) and the discussion in Section 3.4.1 this requires an unconstrained system meaning that the inequality of Eq. (3.57) becomes an equality and the total oscillating mass must be maximised.

With the integral over the first kernel being $\pi M_{Tot}/2$, the power can be found by multiplying the kernel by the excitation spectrum and integrating as shown in Eq. (3.62). Assuming initially that the real part of the first kernel must be positive at all frequencies the power will be maximised if all of the kernel is concentrated at the frequency at the peak of the spectrum. An upper bound on the power dissipated is therefore given by using the optimal real part of the kernel

$$\mathrm{Re}[K_{1\,Opt}(\omega)] = \frac{\pi M_{Tot}}{2}\delta(\omega-\omega_{Max}) + \frac{\pi M_{Tot}}{2}\delta(\omega+\omega_{Max}) \tag{3.70}$$

where ω_{Max} is the frequency at which the spectrum is a maximum. Calling $S_{\xi\xi Max} = S_{\xi\xi}(\omega_{Max})$ the maximum power, P_{Max}, can be found using Eq. (3.62) as

$$\begin{aligned} P_{Max} &= \frac{1}{\pi}\int_0^\infty \frac{\pi M_{Tot}}{2}\delta(\omega-\omega_{Max})S_{\xi\xi}(\omega)d\omega \\ &= \frac{M_{Tot}S_{\xi\xi Max}}{2}. \end{aligned} \tag{3.71}$$

Interestingly, this is the same as the maximum power available from white noise found in Eq. (3.61) if $S_{\xi\xi Max} = \pi S_0$. This is unsurprising since a system with an extremely narrow first kernel, approximated as a delta function in Eq. (3.70), is completely unaffected by noise

at frequencies away from its peak. The noise that does affect it is seen as a flat spectrum of magnitude $S_{\xi\xi Max}$ therefore a white noise input would give the same response and thus power as the non-white spectrum.

The optimal first kernel of Eq. (3.70) could be thought to be completely unrealistic since its frequency response is infinitely thin. However, if the bandwidth of the oscillator is significantly smaller than that of the noise the result will be the same. A linear oscillator given by Eq. (3.65) with $\varepsilon = 0$ has the first kernel of the form of Eq. (3.69) and will have the narrowest peak when damping, c, is minimum and the power will be maximised when $\sqrt{k/m} = \omega_{Max}$.

It is likely that this minimally damped linear oscillator with its natural frequency at the spectrum maximum is the optimal system for power dissipation since adding nonlinearity to a system has been shown to increase the damping of $k_1(\tau)$ and therefore increase the width of $K_1(\omega)$ as observed in Figure 3.1. The increase in the damping of the kernel with nonlinearity arises due to the influence of the higher order kernels becoming stronger. As proved in Section 3.4 all of the power from a given impulse of base excitation instantaneously appears in the first kernel, but is subsequently distributed from the first kernel to the higher order ones. However, the optimality of the linear system has not been shown formally so a nonlinear system may exist that somehow attains a narrower frequency response than the optimal linear one and therefore dissipates more power.

Whilst in theory a first kernel significantly narrower than the excitation spectrum seems preferable it may not be desirable in practice if the input spectrum is time-varying or uncertain since if the excitation changes slightly from the optimised frequency, a very low power response will result. This problem is a well known one in harvesting from harmonic excitation where a minimally damped linear system is known to be optimal at a fixed excitation frequency, but the narrow bandwidth generates little power if the excitation frequency varies slightly [99]. Much attention has been directed towards nonlinear harvesters to widen the bandwidth of a system whilst retaining high amplitude responses [99, 71]. A similar approach may be applied here, although the design of a harvester will be complicated since the first kernel will change with the spectrum of the excitation applied. Despite this, the first kernel from one input spectrum may well be a good approximation of the kernel from a slightly modified input spectrum.

If the assumption of a positive real part of the first kernel is removed the above analysis is invalid. The maximum power dissipated is no longer given by Eq. (3.71), but is unbounded since a system may exist where at frequencies with high excitation spectrum the kernel could be high, and at frequencies where the spectrum is low the kernel could be negative. The total integral over the kernel would still be given by Eq. (3.63) therefore the power could be

greater than that given by Eq. (3.71). For example the real part of a first kernel could take the form

$$\begin{aligned}\mathrm{Re}[K_1(\omega)] =& a\frac{\pi M_{Tot}}{2}\delta(\omega-\omega_{Max})+a\frac{\pi M_{Tot}}{2}\delta(\omega+\omega_{Max})\\ &-b\frac{\pi M_{Tot}}{2}\delta(\omega-\omega_{Low})-b\frac{\pi M_{Tot}}{2}\delta(\omega+\omega_{Low})\end{aligned} \tag{3.72}$$

where as before ω_{Max} represents the frequency of maximum spectrum, ω_{Low} represents a frequency where the spectrum is low, $a \gg 1$ and $a-b=1$. In this case in Eq. (3.62), the integral over the delta functions at ω_{Max} will contribute to the power significantly more than the delta functions at ω_{Low} if $S_{\xi\xi}(\omega_{Max}) \gg S_{\xi\xi}(\omega_{Low})$ meaning

$$P \approx a\pi S_{\xi\xi}(\omega_{Max})M_{Tot}/2 \tag{3.73}$$

and the power is therefore unbounded. However, the possibility of negative kernel seems unlikely for passive systems as discussed in [48] and Section 3.4.2.

The above discussion is based on a single-degree-of-freedom harvester; whether a multi-degree-of-freedom system can improve power dissipation is worth considering. Additional degrees-of-freedom could be added either with more dimensions or more masses. The important result for maximising power is to concentrate the first kernel at the peak frequency of the input spectrum. However, increasing the degrees of freedom will increase the number of resonances and so not permit the kernel to be concentrated around one frequency. A MDOF system will therefore not be able to dissipate as much power as an optimal SDOF system.

3.7.1 Linear Harvester with Filtered Noise

The discussion from the previous section can be illustrated analytically using a linear harvester. Since the system is linear the method used does not require the extended Wiener approach, although it can still be seen as an application of the theory of this chapter because the frequency response of a linear oscillator is equal to the first extended Wiener kernel. The aim of this example is not to validate the theory, but to illustrate the complexity of analysing even a simple harvester in order to show how the simplicity of the method of power calculation from Eqs. (3.62) and (3.63) is helpful to provide a conceptual understanding of how power is dissipated.

Taking a linear oscillator of the non-dimensional form

$$\ddot{y}+2\zeta\omega_n\dot{y}+\omega_n^2 y=\xi \tag{3.74}$$

and therefore first kernel and frequency response, $H(\omega)$, between base acceleration, ξ, and response velocity, $\dot{y}$, is

$$K_1(\omega) = H(\omega) = \frac{\omega i}{\omega_n^2 - \omega^2 + 2\zeta\omega_n\omega i}. \tag{3.75}$$

When excited by filtered noise with spectrum given by Eq. (3.66) the power dissipated can be calculated from Eq. (3.41) using complex analysis as follows

$$\begin{aligned} P &= \frac{1}{2\pi}\frac{\pi S_0}{2}\omega_0^4 \int_{-\infty}^{\infty} \frac{i\omega}{\omega_n^2 - \omega^2 + 2\zeta\omega_n\omega i} \frac{1}{\left(\omega_0^2 - \omega^2\right)^2 + 4\zeta_0^2\omega_0^2\omega^2} d\omega \\ &= \frac{S_0\omega_0^4}{4} \int_{-\infty}^{\infty} \frac{i\omega}{-(\omega-\beta)(\omega+\beta^*)} \frac{1}{(\omega-\alpha)(\omega-\alpha^*)(\omega+\alpha)(\omega+\alpha^*)} d\omega \end{aligned} \tag{3.76}$$

where $\beta = \omega_n\sqrt{1-\zeta^2} + i\omega_n\zeta$ and $\alpha = \omega_0\sqrt{1-\zeta_0^2} + i\omega_0\zeta_0$. Integrating clockwise over a contour in the complex plane along the real axis and with infinite radius in the negative imaginary region gives two residues from the poles at α^* and $-\alpha$ yielding

$$\begin{aligned} P &= -2\pi i \frac{S_0\omega_0^4}{4} \left[\frac{i\alpha^*}{-(\alpha^*-\beta)(\alpha^*+\beta^*)(\alpha^*-\alpha)(\alpha^*+\alpha)2\alpha^*} + \right. \\ &\qquad \left. \frac{-i\alpha}{-(-\alpha-\beta)(-\alpha+\beta^*)(-2\alpha)(-\alpha-\alpha^*)(-\alpha+\alpha^*)} \right] \\ &= -\frac{\pi S_0\omega_0^4}{4(\alpha^*-\alpha)(\alpha^*+\alpha)} \left[\frac{1}{(\alpha^*-\beta)(\alpha^*+\beta^*)} - \frac{1}{(-\alpha-\beta)(-\alpha+\beta^*)} \right] \\ &= -\frac{\pi S_0\omega_0^4}{4\times(-2i\omega_0\zeta_0)\times 2\omega_0\sqrt{1-\zeta_0^2}} \frac{(\alpha+\beta)(\alpha-\beta^*) - (\alpha^*-\beta)(\alpha^*+\beta^*)}{(\alpha^*-\beta)(\alpha^*-\beta)^*(\alpha+\beta)(\alpha+\beta)^*} \\ &= \frac{\pi S_0\omega_0^2}{16i\zeta_0\sqrt{1-\zeta_0^2}} \frac{\alpha^2 - (\alpha^2)^* + \alpha\beta - (\alpha\beta)^* - \alpha\beta^* + (\alpha\beta^*)^*}{|(\alpha^*-\beta)(\alpha+\beta)|^2} \\ &= \frac{\pi S_0\omega_0^2}{16i\zeta_0\sqrt{1-\zeta_0^2}} \frac{2i\mathrm{Im}[\alpha^2] + 2i\mathrm{Im}[\alpha\beta] - 2i\mathrm{Im}[\alpha\beta^*]}{||\alpha|^2 + \beta(\alpha^*-\alpha) - \beta^2|^2}. \end{aligned} \tag{3.77}$$

The numerator and denominator of the right hand term can be calculated in turn as follows

$$\begin{aligned}\mathrm{Im}[\alpha^2]+\mathrm{Im}[\alpha\beta]-\mathrm{Im}[\alpha\beta^*] =& 2\omega_0^2\zeta_0\sqrt{1-\zeta_0^2}+\omega_0\omega_n\zeta\sqrt{1-\zeta_0^2}+\\ & \omega_n\omega_0\zeta_0\sqrt{1-\zeta^2}+\omega_0\omega_n\zeta\sqrt{1-\zeta_0^2}-\\ & \omega_n\omega_0\zeta_0\sqrt{1-\zeta^2}\\ =& 2\omega_0^2\zeta_0\sqrt{1-\zeta_0^2}+2\omega_0\omega_n\zeta\sqrt{1-\zeta_0^2}\\ =& 2\omega_0\sqrt{1-\zeta_0^2}(\omega_0\zeta_0+\omega_n\zeta)\end{aligned} \tag{3.78}$$

$$\begin{aligned}||\alpha|^2+\beta(\alpha^*-\alpha)-\beta^2|^2 &= |\omega_0^2+2\omega_0\zeta_0\omega_n\zeta-\omega_n^2+2\omega_n^2\zeta^2-2i\omega_n\sqrt{1-\zeta^2}(\omega_0\zeta_0+\omega_n\zeta)|^2\\ &= \omega_0^4+\omega_n^4-2\omega_0^2\omega_n^2+4\omega_0^3\zeta_0\omega_n\zeta+4\omega_0^2\omega_n^2\zeta^2+4\omega_n^2\omega_0^2\zeta_0^2+4\omega_n^3\zeta\omega_0\zeta_0\\ &= (\omega_0^2-\omega_n^2)^2+4\omega_0\omega_n\left(\zeta\zeta_0(\omega_0^2+\omega_n^2)+\omega_0\omega_n(\zeta^2+\zeta_0^2)\right).\end{aligned} \tag{3.79}$$

Combining Eqs. (3.77)-(3.79) provides the power dissipated

$$P=\frac{\pi S_0\omega_0^3}{4\zeta_0}\frac{\omega_0\zeta_0+\omega_n\zeta}{(\omega_0^2-\omega_n^2)^2+4\omega_0\omega_n\left(\zeta\zeta_0(\omega_0^2+\omega_n^2)+\omega_0\omega_n(\zeta^2+\zeta_0^2)\right)}. \tag{3.80}$$

which can be written in terms of non-dimensional ratios $\Omega=\omega_n/\omega_0$ and $Z=\zeta/\zeta_0$ as

$$P=\frac{\pi S_0}{4}\frac{1+\Omega Z}{(1-\Omega^2)^2+4\Omega\zeta_0^2\left(Z(1+\Omega^2)+\Omega(Z^2+1)\right)}. \tag{3.81}$$

For energy harvesting, the excitation parameters ζ_0 and ω_0 are set by the operating environment and the harvester parameters must be chosen to maximise power. As discussed in Section 3.7, maximum power is dissipated when $\zeta\to 0$ and ω_n is at the peak excitation frequency. This is because the integral of the mechanical frequency response is the same for any ω_n and ζ, so maximum power is found when all the kernel is concentrated at the peak excitation frequency. This could be shown by differentiating Eq. (3.81) with respect to Ω and Z although the analysis becomes complicated since only positive values of Ω and Z are permitted.

In the simplest energy harvesting case, the damping is split into unwanted mechanical damping, ζ_m, and desirable electrical damping, ζ_e, so the damping ratio becomes $\zeta=\zeta_m+\zeta_e$. Clearly, the mechanical damping should be minimised, but will always arise to some extent due to air or material damping and as such will need to be designed around. In order to yield

maximum power, the optimal electrical damping and natural frequency is required for given mechanical damping and noise parameters.

The electrical power, P_E, dissipated is

$$P_E = \frac{Z_e}{Z_e + Z_m} P \tag{3.82}$$

where $Z_e = \zeta_e/\zeta_0$ and $Z_m = \zeta_m/\zeta_0$. It is possible by differentiation to find the values of Ω and Z_e that yield maximum electrical power for any given Z_m and noise parameters. However, the algebra becomes complicated so it is simpler to investigate conceptually and through limiting cases.

For maximum electrical power, both terms in Eq. (3.82) would ideally be maximised. However, they compete against each other since the power in to the system, P, is maximised if the total damping is minimised whereas to convert the majority of this input power into electrical power, electrical damping must be maximised compared to mechanical damping. The optimal strategy will depend on the specific noise and mechanical damping parameters.

Figure 3.13a shows the electrical power dissipated plotted against Ω and Z_e when $\zeta_0 = 0.2$, $Z_m = 0.6$ and $S_0 = 4/\pi$W/kg and Figure 3.13b shows the breakdown of the terms in Eq. (3.82) taken at the Ω value that provides maximum P_E at a given value of Z_e. The decrease of the total power input with increasing Z_e in Figure 3.13b shows that the widening of the frequency response with Z_e means the response is not concentrated at the maximum of the input spectrum thus total input power is decreased. However, the red line representing P_E shows electrical power is low for low Z_e despite input power being high because the majority of the input power is dissipated mechanically. As electrical damping increases, the total input power decreases, but the electrical power increases because the proportion of input power dissipated electrically increases. At an optimal amount of electrical damping, approximately $Z_e = 1$, the balance between the decreasing input power and increasing proportion of power dissipated electrically is optimal to provide maximum electrical power dissipation as shown by the peak in Figure 3.13a.

For the locations marked A, B and C on Figure 3.13 the excitation spectrum and the first kernel from Eq. (3.75) with and without the electrical damping are plotted in Figure 3.14. This illustrates the frequency response that maximises electrical power at various values of Z_e. Since total power is given by the area under the spectrum multiplied by the kernel, the figures display the necessity to obtain the right balance between keeping a narrow kernel around the peak of the input spectrum and widening the first kernel by adding electrical damping to increase electrical compared to mechanical power.

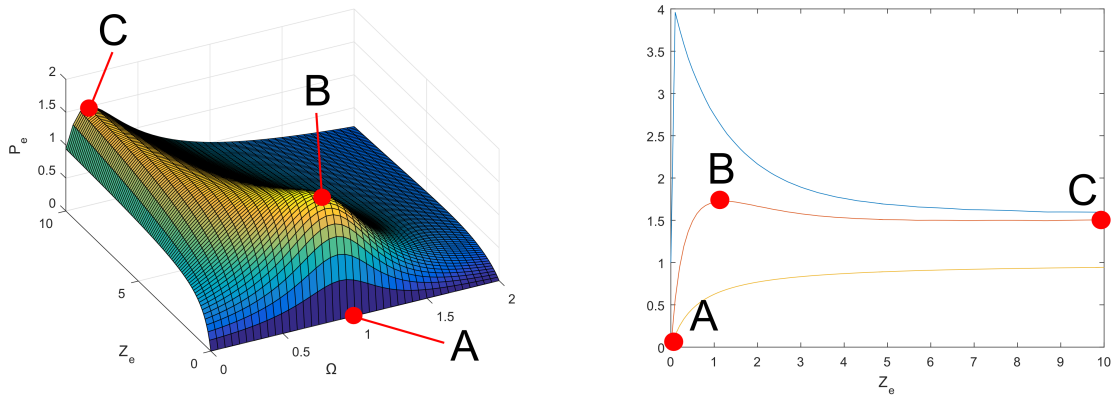

(a) (b)

Fig. 3.13 a) Electrical power dissipated by a linear oscillator under narrowband excitation plotted against Ω and Z_e and b) total power, P, (blue), electrical power, P_E, (red) and fraction $Z_e/Z_m + Z_e$ (yellow) all taken at the value of Ω with that gives maximum electrical power for the given value of Z_e.

Values of ζ_0 and Z_m have been selected here to illustrate the main characteristics of electrical power dissipation; however, if different values were chosen, the power dissipation may not follow the same pattern. The complexity of this section for this simple linear harvester suggests detailed analysis for a more complicated harvester, such as one coupled to an electrical circuit, or a nonlinear design under non-white noise would be complicated. The simplicity of the result of Eq. (3.62) to provide a rough estimate of power and guide design is therefore attractive due to the complexity of more detailed analysis.

3.7.2 Application to the Power Bounds of Chapter 2

Since detailed analysis of even a simple energy harvester becomes complicated for non-white base acceleration, the use of upper bounds on power as used in Chapter 2 with white base acceleration is potentially useful in order to comment on performance for a wide range of harvesters rather than specific ones. As discussed in Section 3.7 the maximum power input from any excitation spectrum is given by the white noise result of Eq. (1.1) and hence the results of Chapter 2 still provide upper bounds on power. Nevertheless, a harvester designer will be optimising a system for a specific excitation spectrum and must design around mechanical damping constraints such as air and material damping. If a minimum damping value is taken, a new maximum power input, P_{InMax}, could in theory be found by optimising the first extended Wiener kernel with the constraint of a minimum damping value. In many cases of narrowband input spectra, the maximum power would be given by

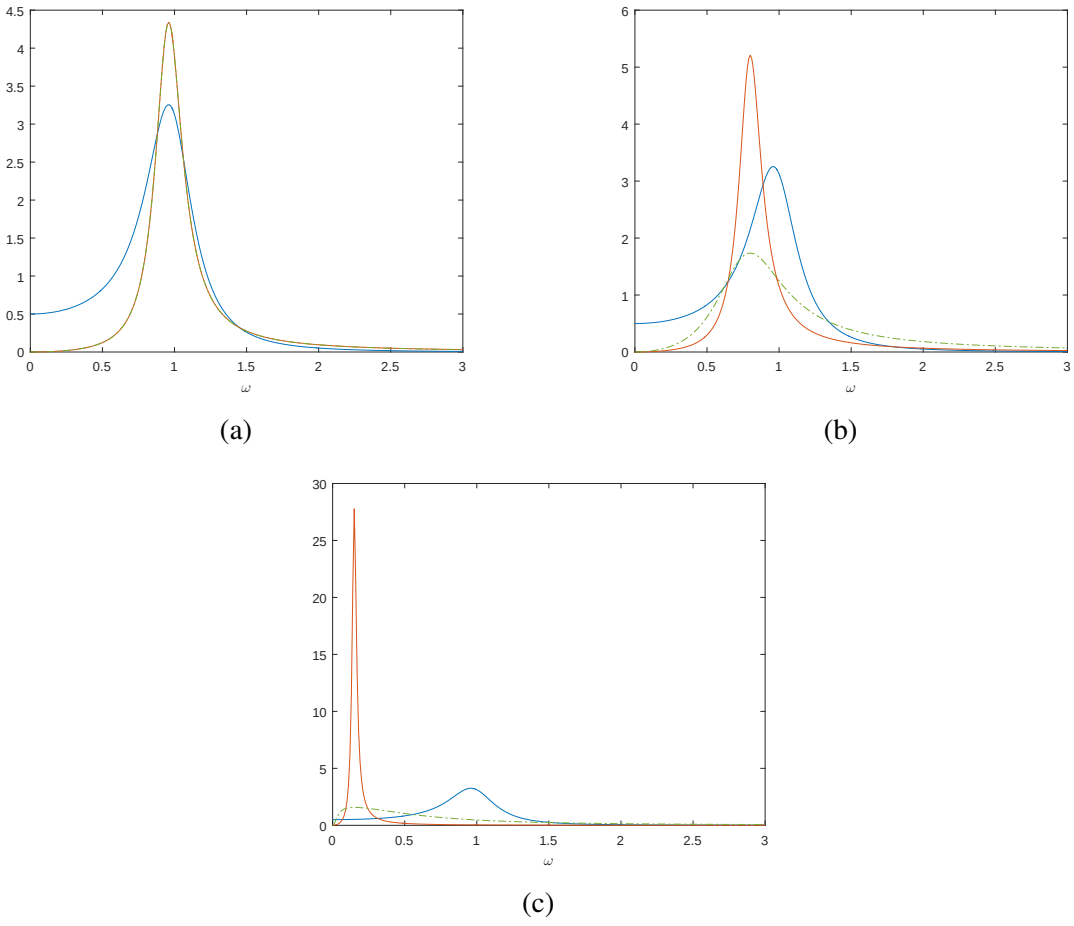

Fig. 3.14 Plots of the excitation spectrum (blue) and the real part of the first kernel with (red) and without (green dashed) electrical damping with parameters from positions a) A, b) B and c) C in Figure 3.13.

a linear system with minimum damping and frequency tuned to the peak of the excitation spectrum since any increase in damping will widen the peak of the frequency kernel and reduce input power. However, with a more complex input spectrum a different first kernel from the minimally damped linear one may dissipate more power. This maximum input power can then replace the $\pi S_0 m/2$ terms in the power bounds of Eqs. (2.10), (2.15) and (2.43) in order to scale them down to be tighter bounds for the case of non-white noise.

In Chapter 2, for white noise, low frequency devices were found to harvest most electrical power since the harvesting circuit acts like a low-pass filter. However, with narrowband noise spectra, maximum input power will be achieved when the natural frequency of the device is close to that of the excitation spectrum. If the noise is of a higher frequency than the cut-off of the electrical low-pass filter, the two requirements are conflicting and so it is interesting to investigate how the two might compete with an example. Taking the linear electrical resistance case used in Figure 2.3, but with a narrowband excitation spectrum of the same peak magnitude as the white noise given by Eq. (3.66) with parameters $S_0 = 2.52 \times 10^{-5}$W/kg, $\omega_0 = 400$rad/s and $\zeta_0 = 0.1$ a strong estimate of the maximum power input is given by the linear case, with minimum damping $b = 5 \times 10^{-3}$kg/s and optimised linear stiffness to give $P_{InMax} = 0.94\mu$W compared to the $\pi S_0 m/2 = 1\mu$W from white noise. Whilst this has not been proven to be the maximum power input so cannot strictly provide an upper bound, it provides a useful estimate in order that the bounds are tighter and therefore more attainable and informative.

Figure 3.15 displays the bounds for a white noise excitation spectrum along with the estimated bounds using P_{InMax} from narrowband excitation and simulations of the formerly optimal zero stiffness harvester, a linear stiffness harvester with $k = 157$N/m giving the resonance at the peak of the excitation spectrum and a nonlinear harvester with $k = 100$N/m and cubic nonlinearity $\varepsilon = 30 \times 10^9$N/m^3. All simulations are found to lie well within the bounds, but in contrast to the results for white noise excitation, the zero stiffness oscillator now performs very poorly. The harvesters with stiffnesses providing frequency responses closer to the peak excitation spectrum frequency perform strongly as the power into the system is high and outweighs the disadvantages that the high frequency response has in distributing power between electrical and mechanical dissipation due to the low pass filter nature of the electrical circuit. Conversely, in the zero stiffness case only a small amount of power is input into the low frequency response due to the mismatch in its natural frequency and that of the spectrum even though the input power is efficiently dissipated electrically rather than mechanically.

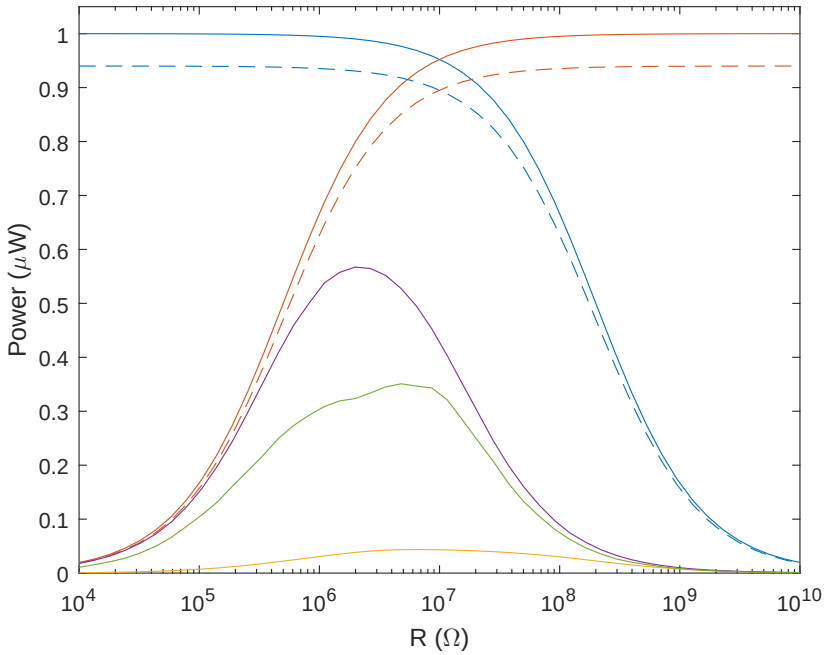

Fig. 3.15 Power bounds from Eq. (2.45) (blue) and (2.46) (red) where dashed lines represent tighter bounds using P_{InMax} instead of $\pi S_0 m/2$ and power dissipated from simulations with zero stiffness harvester (yellow), linear stiffness $k = 157$N/m (purple) and nonlinear stiffness with $k = 100$N/m and $\varepsilon = 30 \times 10^9$N/m^3 (green).

3.8 Conclusions

A methodology has been presented for calculating the power dissipated by nonlinear MDOF systems under general random base excitation. The Wiener series approach has been extended to incorporate a Gaussian random input with general spectrum and the power dissipated is shown to be dependent only on the first kernel and the spectrum of the input according to Eq. (3.62). Calculation of the first kernel can be made either via simulations or from experimental data and it is shown to have the property that the integral over the frequency domain kernel is proportional to the total oscillating mass, Eq. (3.63), for an unconstrained system.

The combination of Eqs. (3.62) and (3.63) provides a simple conceptual understanding of power flow in nonlinear randomly excited systems. The first extended Wiener kernel displays peaks around the resonances of the system therefore for applications where power input to the system is to be minimised, the resonances of the system should be designed to be at a frequency where the input spectrum is low. Conversely, for energy harvesting applications, power input to the system will be maximised when the resonances of the harvester are at frequencies where the input spectrum is high. For the case of white noise base excitation, Eqs. (3.62) and (3.63) show that regardless of the system characteristics and therefore the first Wiener kernel, the power dissipated is simply proportional to the magnitude of the spectrum and the total oscillating mass according to Eq. (3.61) for an unconstrained system. This is the same result as [47, 48] and therefore provides an alternative derivation to those previously presented.

Whilst these conclusions are conceptually obvious, the existence of Eqs. (3.62) and (3.63) provide a rigorous mathematical framework for calculating power and also allow upper and lower bounds to be found for power dissipation under a given excitation spectrum. Interestingly, the results of this chapter provide the same conclusion as [48]; provided the real part of the first extended Wiener kernel is positive at all frequencies, an upper bound on power dissipated under non-white excitation can be given simply by the white noise result of Eq. (3.61) where πS_0 is the peak value of the non-white spectrum.

The triple product term, $\mathrm{E}\left[\mathbf{f}^{\mathrm{T}}\mathbf{M}^{-1}\mathbf{f}\right]$, of Eq. (3.63) has been investigated and shown to be equal to the total oscillating mass if the system is unconstrained and less than the mass when the system is constrained such that there are fewer generalised coordinates than the equivalent unconstrained system. The effect of adding a constraint can be thought of as removing a resonance from the first kernel. The total available power will therefore decrease because the integral over the kernel decreases.

A critical assumption of the theory is that the base motion is independent of the oscillating system, or no feedback is provided from the system to the base. In reality this will not be

true, but may be a valid assumption under some conditions. The impact of the assumption is assessed experimentally in the following chapter.

Numerical simulations of various illustrative systems have been used to investigate the theory. An average percentage error of 1.5% when comparing numerical simulations to the value predicted by Eq. (3.63) shows strong support of the theory with the exception of the band-limited noise case for reasons discussed in Section 3.6. With numerical results reinforcing the theory, it is also useful to validate it experimentally to ensure its practical application is viable and this is explored in the following chapter.

Chapter 4

Experimental Validation of the Extended Wiener Series Approach

4.1 Introduction

The extension of the Wiener series to encompass non-white excitation using the method of Chapter 3 has, to the author's knowledge, not been done before. In addition, the result of Eq. (3.42) that has implications on the power dissipated of a system is original and worth further investigation. As such, experimental validation is profitable to supplement the compelling numerical validation of Chapter 3 and also to assess the applicability of the theory in reality.

The key result in question is that the integral over frequency of the first extended Wiener kernel in the frequency domain, $K_1(\omega)$, is proportional to the triple product $\mathrm{E}\left[\mathbf{f}^{\mathrm{T}}\mathbf{M}^{-1}\mathbf{f}\right]$ according to Eq. (3.42). This is equivalent to the initial jump of the kernel in the time domain, $k_1(\tau)$, being equal to $\mathrm{E}\left[\mathbf{f}^{\mathrm{T}}\mathbf{M}^{-1}\mathbf{f}\right]$ according to Eq. (3.56). The conceptual argument for this result is that any input excitation can be thought of as a series of impulses, with each impulse instantaneously imparting a total change in momentum and therefore velocity on the system that is proportional to the magnitude of the impulse and inversely proportional to the triple product $\mathrm{E}\left[\mathbf{f}^{\mathrm{T}}\mathbf{M}^{-1}\mathbf{f}\right]$. The orthogonal form of the extended Wiener series means that all of the power from any impulse is found instantaneously only in the first kernel thus its initial jump is equal to $\mathrm{E}\left[\mathbf{f}^{\mathrm{T}}\mathbf{M}^{-1}\mathbf{f}\right]$.

In this chapter a simple experiment designed to validate this result is described and the resulting first kernels are presented for a variety of configurations. Ideally, a base-excited SDOF nonlinear oscillator would be built, but due to practical considerations a cantilever beam with a tip mass and magnets providing a nonlinear restoring force is used. The MDOF

nature of the beam is noticeable in the first kernel, but seems to have little impact on the integral over the first kernel.

The consequence of the result of Eq. (3.42) is that it provides insight into how power is dissipated in a system according to Eq. (3.62). Due to practical limitations, this is not investigated experimentally, nor is the orthogonality of the Wiener series, although orthogonality is implicitly validated providing Eq. (3.42) is shown to be true.

The remainder of this chapter contains a description of the experimental apparatus and data processing methods in Section 4.2 followed by analysis and discussion of first extended Wiener kernels from the experiment in a variety of nonlinear configurations in Section 4.3. Finally, the validity of the experimental approach for nonlinear systems is examined in Section 4.4 before conclusions are documented in Section 4.5.

4.2 Experimental Apparatus

A simple experiment capable of validating the result of Eq. (3.42) is desired. Primary requirements are to build a SDOF system with random base excitation and nonlinearity sufficiently strong to validate the theory along with, if possible, being easily modifiable in order to analyse a variety of conditions. Ideally, a system with the equation of motion

$$m\ddot{y} + f(\dot{y}) + g(y) = -m\ddot{b} \tag{4.1}$$

would be designed where m is the oscillating mass and $\ddot{b}$ is the base acceleration. Since the aim of the experiment is to validate Eq. (3.42) rather than compare simulations from a model to experimental results, the exact forms of the damping, $f(\dot{y})$, and stiffness, $g(y)$, are not critical provided the system is observably nonlinear.

Figure 4.1 displays the experimental apparatus that consists of a cantilever beam with a lumped tip mass with the base of the beam clamped to a sliding base that is shaken by an electromagnetic shaker. Neodymium cylinder and disc magnets are used to generate a nonlinear restoring force on the tip mass in addition to the approximately linear restoring force of the beam. Clearly a cantilever beam is not a SDOF system, although with a tip mass the second resonance will be at a significantly higher frequency than the first such that the second mode will have little effect on the first extended Wiener kernel. The MDOF nature of the beam will be discussed in more detail in Section 4.3.

The experiment has been designed to be easily modifiable to ensure it can validate Eq. (3.42) for a range of parameter values and stiffness and damping profiles in Eq. (4.1). The tip mass can be varied and easily moved along the beam and beams of various thickness can

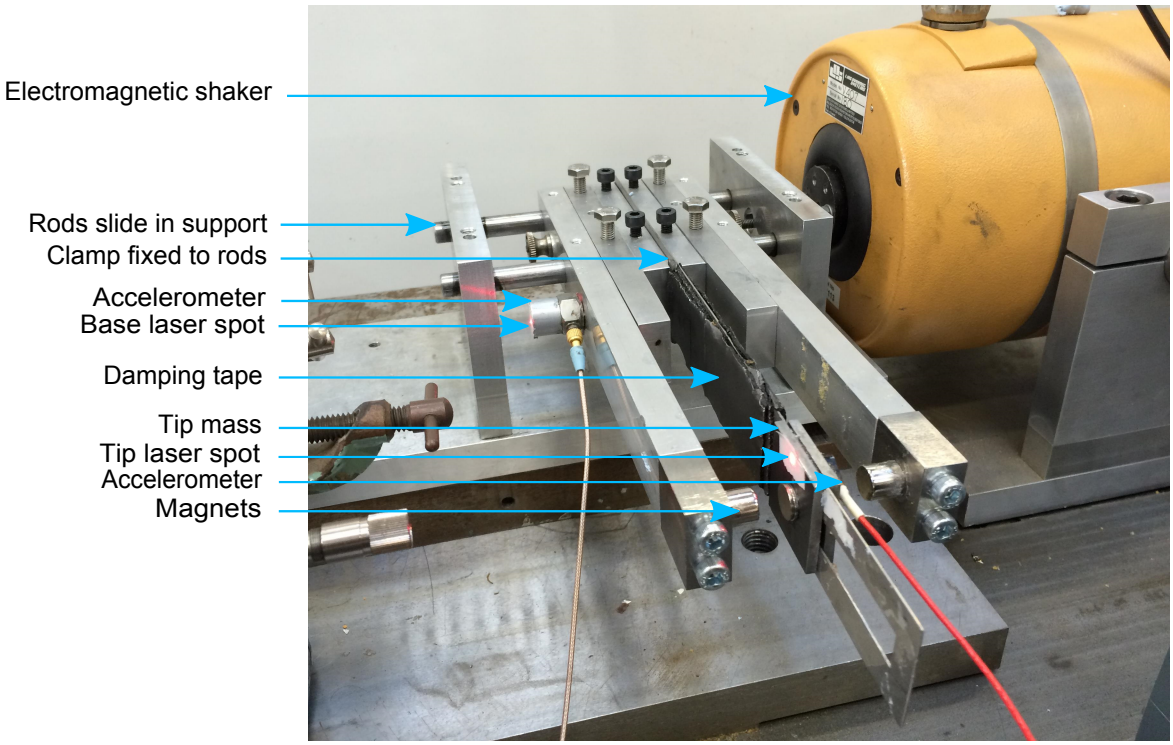

Fig. 4.1 Experimental apparatus.

be used to modify the linear stiffness of the system. The number of magnets can be varied to change the strength of the nonlinearity, with no magnets providing a linear system and one configuration even capable of producing a bistable system. Additionally, the damping can be modified with the use of damping tape stuck along the length of the beam along with other mechanisms such as increasing air damping by attaching paper to the beam to increase drag and friction damping where rough paper is held in light contact with the beam such that the beam rubs on the paper as it oscillates.

4.2.1 Instrumentation

The experiment requires a single input, the force for the electromagnetic shaker, and two outputs, the base acceleration and the tip mass velocity relative to the base. A computer with a National Instruments data-logging card was used to generate and measure the relevant signals along with the required instrumentation as displayed in the schematic of Figure 4.2. The electromagnetic forcing signal was first low-pass filtered with a cut-off frequency of 6283rad/s to remove unwanted high frequency noise and spikes before being amplified to provide sufficient power for the shaker.

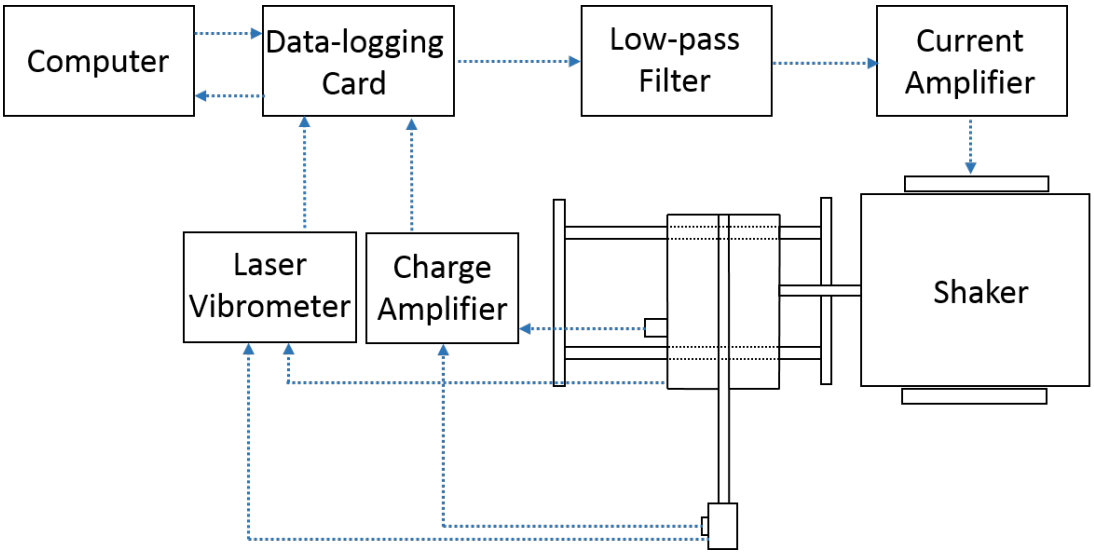

Fig. 4.2 Schematic of the instrumentation used in the experiment.

The base acceleration was measured using an accelerometer and two methods were used to measure the tip velocity: an accelerometer and a laser vibrometer. The tip accelerometer used was small in order that it had minimal effect on the system and was placed on the tip mass such that the relative tip velocity can be calculated by time-integration of the relative acceleration which is found by subtracting the base from the tip acceleration. Both accelerometers were calibrated using a laser vibrometer. The velocity calculated from the accelerometer data was poor at low frequencies, but strong at high frequencies due to integration, therefore the relative tip velocity was also measured using a laser vibrometer which has stronger performance at low frequencies, but too much noise at high frequencies. This is discussed further in Section 4.2.3.

4.2.2 Excitation

A base force signal can be specified computationally and transmitted to the shaker. However, due to the dynamics of the shaker, base and tip, the true spectrum of the base acceleration is very different from the one intended and is highly dependent on the configuration of the oscillating mass. An example is shown in Figure 4.3 where the input spectrum from the computational signal is compared with spectrum from the actual base acceleration and the computational spectrum has been scaled to compare to the base excitation.

A number of differences are observed, in particular at low frequencies the experimental spectrum is low because the coil that drives the magnet in the electromagnetic shaker is ineffective at these frequencies. Additionally a sharp dip followed by a slight peak is seen at

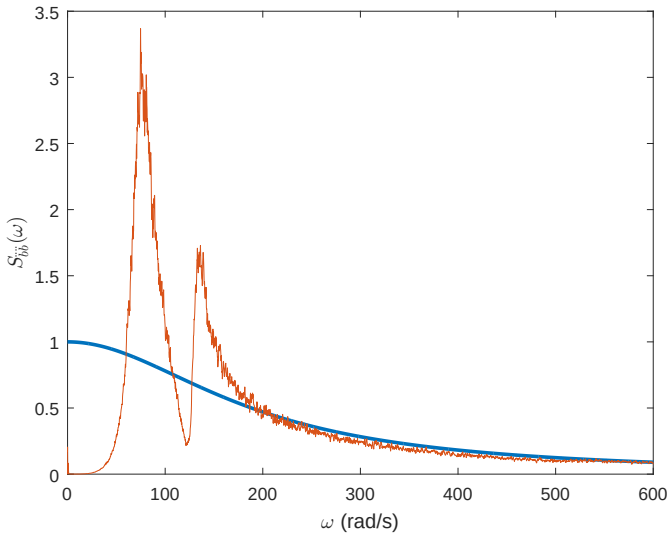

Fig. 4.3 Comparison of the spectrum specified by the computer (blue) to the true base acceleration spectrum (red).

around 120rad/s in the experimental spectrum because this is the natural frequency of the tip mass and the system acts as a vibration isolator meaning the base acceleration is low. At high frequencies the curves are more similar although do not exhibit exactly the same roll-off.

The differences arise because the system is not simply a base-excited mass and the beam vibration feeds back to the base and shaker. A more detailed model for the system including the base is discussed further in Section 4.4. It may be possible to devise a more elaborate spectrum with the computer in order to produce the desired true base acceleration spectrum, although the exact form of the excitation spectrum is not important to validate the theory since a first kernel can be calculated for any input spectrum. To provide a measure of the excitation amplitude in what follows, the maximum value of the spectrum input by the computer will be taken and called S_{Max}.

4.2.3 Data Processing

Since the experimental system is unconstrained and can be approximately modelled by the equation of motion of Eq. (4.1), the triple product, $\mathrm{E}\left[\mathbf{f}^{\mathrm{T}}\mathbf{M}^{-1}\mathbf{f}\right]$, is equal to the oscillating mass. The value of this mass will be difficult to calculate as some of the beam mass must be included. It is therefore preferable to modify the output of the extended Wiener series from what would be $z = m\dot{y}$ according to Eq. (3.36) to $z = \dot{y}$. The result is that the integral over the kernel in Eq. (3.42) is no longer equal to $m/2$, but 1/2. This is easier to validate since no

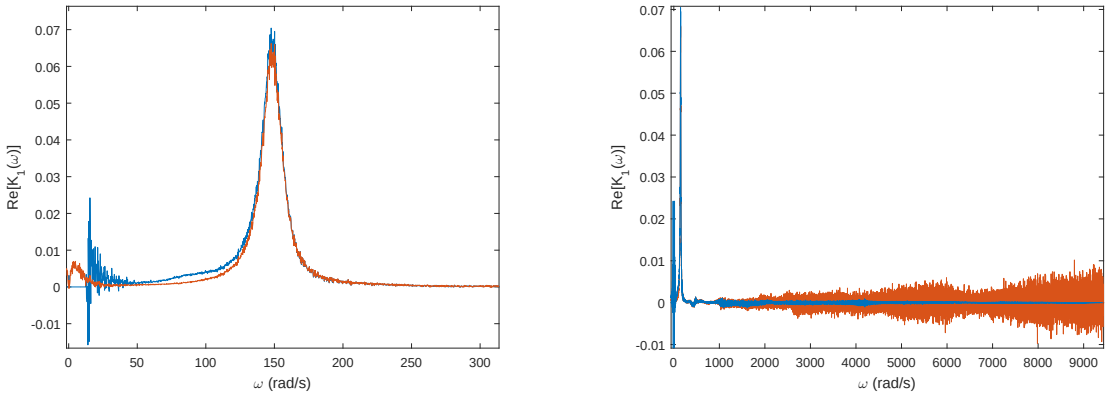

(a) (b)

Fig. 4.4 Real part of the first extended Wiener kernel of sample experimental data from accelerometer (blue) and laser vibrometer (red) data a) around resonance and b) across the entire frequency domain. Only accelerometer data above 12.6rad/s is included.

estimate of the oscillating mass is required, but is still validating the important property of the first kernel since its magnitude has just been divided by its mass.

A physical description of this process can be given by arguing that any base acceleration impulse over a small time, δt, to a base excited oscillating mass is equivalent to an impulse, I, on the mass where $I = -m\ddot{b}\delta t$ with oscillating mass m and acceleration $\ddot{b}$. This impulse provides a change in momentum equal to the impulse and therefore a change in velocity, $\Delta\dot{x}$, equal to $\Delta\dot{x} = I/m = -\ddot{b}\delta t$. The change in the velocity is therefore independent of the mass.

In order to show the quality of the raw data, a sample real part of the first extended Wiener kernel is shown in the frequency domain in Figure 4.4 using both accelerometer and laser vibrometer data. The sampling rate for this and all subsequent results is 18800rad/s as this comfortably encompasses the frequencies of interest and will also provide a small time-step to allow close examination of the first kernel in the $\tau = 0$ region. The experiment is conducted by applying a 30s realisation of a given noise spectrum to the beam started at rest. This process is repeated a number of times, in this case 40 times, to provide an ensemble of data that can be averaged. Whilst the kernel shows approximately the desired characteristics around the resonance, noise is high elsewhere therefore a number of improvements made by processing the data are discussed below.

Inspection of the time signal from the laser vibrometer shows occasional sharp spikes in the velocity data as seen in Figure 4.5. These can be removed using a median filter that replaces every point in a signal by the median of that point and a specified number of

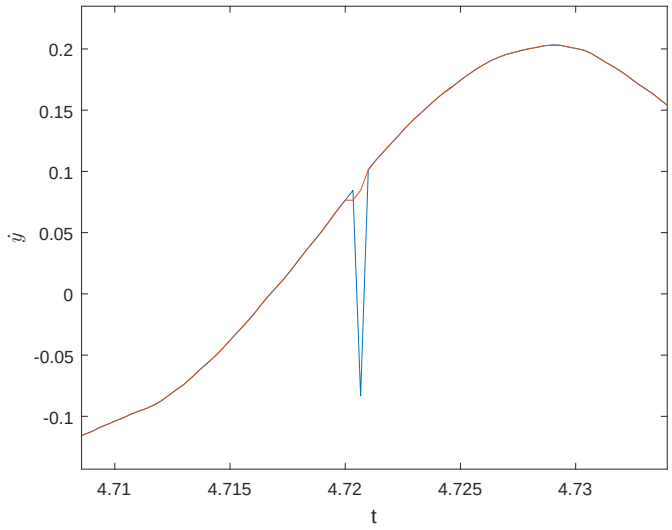

Fig. 4.5 Comparison of unfiltered (blue) and median filtered (red) velocity signal from laser vibrometer.

neighbouring points. Whilst it is clear that the spike is not completely removed, a significant improvement has been made.

Additionally, noise in the frequency domain can be decreased both by using a larger ensemble and by smoothing the data with a five-point moving average filter. Since the accelerometer data is strong at high frequencies, but weak at low frequencies and vice-versa for the laser vibrometer, the best results are achieved by combining the best regions of the two. The kernel calculated using the laser vibrometer is used up to 346rad/s and accelerometer data for frequencies after that.

The very low frequency part of the first kernel from the laser vibrometer also contains noise and drift. This is largely due to the low excitation spectrum at these frequencies, as seen in Figure 4.3, magnifying noise when dividing by the spectrum to calculate the kernel. One cause is the abrupt end of each realisation causing a small low frequency drift if the signal does not end close to zero. The effect can be reduced by tapering the ends of the time signals such that they fall smoothly to zero and this is shown to be effective in Figure 4.6.

4.3 Results

In what follows, the first extended Wiener kernel is investigated for a variety of different systems using the same method as numerical simulations in Section 3.5. One big difference between experimental and numerical results is that different systems cannot be compared with

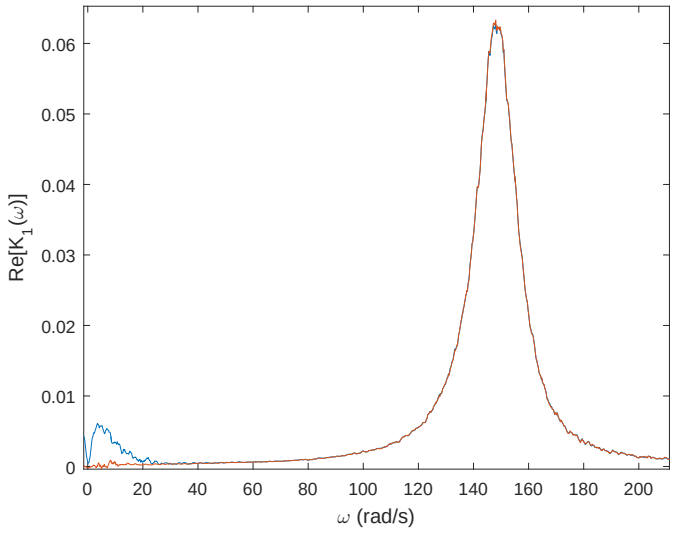

Fig. 4.6 Comparison of first kernel without (blue) and with (red) tapered time signals.

the same base acceleration spectrum because the system configuration affects the spectrum. A useful way of varying a system is to vary the magnitude of the excitation in order to affect the magnitude of the tip motion between the magnets. With a low amplitude base motion, the tip motion is also low meaning its range of movement within the nonlinear magnetic force is low. Across any small displacement, the nonlinear force could be reasonably approximated by a linear force so the system is close to linear. However, when the base and therefore tip motion are large, the tip moves through a large region of nonlinear magnetic force and so the nonlinearity of the response is increased.

4.3.1 Stiffening Nonlinearity

The experiment was set up in the configuration of Figure 4.1 where the magnets provide a stiffening nonlinearity. This characteristic is exposed by observing its 'backbone curve'; a measure of how the frequency of oscillation varies with its amplitude. Calculation of the curve is made by releasing the tip from a large deflection and finding the time between peaks and amplitudes of the subsequent decay. The amplitude is plotted against frequency of oscillation in Figure 4.7 where each dot represents the frequency of one time period and the peak velocity within that period. A number of impulses are used to build up a full picture of the curve. The stiffening nonlinearity is evident in that as the amplitude decreases, the natural frequency decreases, with the change in frequency over the amplitude range being approximately 2.5 Hz.

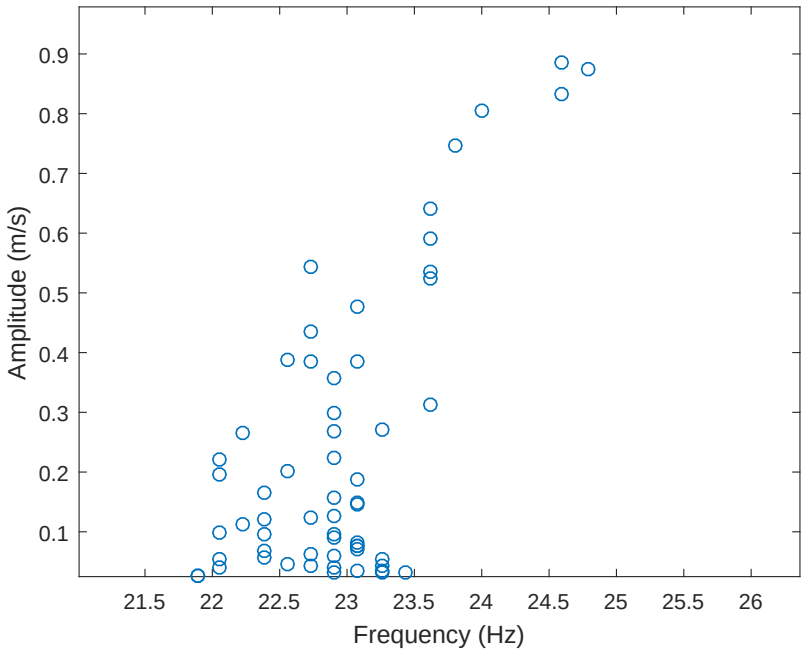

Fig. 4.7 Backbone curve of the stiffening experimental system.

The first extended Wiener kernel is displayed for this configuration with three different excitation magnitudes in Figure 4.8. Very similar to the numerical results of Figure 3.1 where the stiffness parameter is increased, the kernels show the natural frequency and the damping of the first kernel increasing with excitation amplitude. As discussed above, the similarity is to be expected because increasing the excitation increases the nonlinearity. Another similarity with the numerical results is that the more nonlinear the response, the higher the noisiness of the frequency kernel.

The critical result to verify is that the area under the real part of the frequency kernel is according to Eq. (3.42) or equivalently that $k_1(0) = \mathrm{E}\left[\mathbf{f}^{\mathrm{T}}\mathbf{M}^{-1}\mathbf{f}\right]/2$ according to Eq. (3.43) where in the case of the experiment, $\mathrm{E}\left[\mathbf{f}^{\mathrm{T}}\mathbf{M}^{-1}\mathbf{f}\right] = 1$. Due to experimental noise, it is worth also evaluating the value of the time kernel at $\tau = 0^+$ where $k_1(0^+) = 1$ from Eq. (3.56). A close-up plot of the time kernel around $\tau = 0$ is shown in Figure 4.9 and the values of $k_1(0)$ are 0.50, 0.50 and 0.50 and $k_1(0^+)$ are 0.99, 0.99 and 0.98 for $S_{Max} = 0.005$, 0.02 and 0.5 respectively.

A notable feature that differs from the numerical results is the occurrence of high frequency peaks other than the dominant resonant response. This is visible both in the time domain kernel and in Figure 4.10 that shows the real part of the first kernel at frequencies higher than resonance for the three excitation values. Figure 4.10a shows two features; one

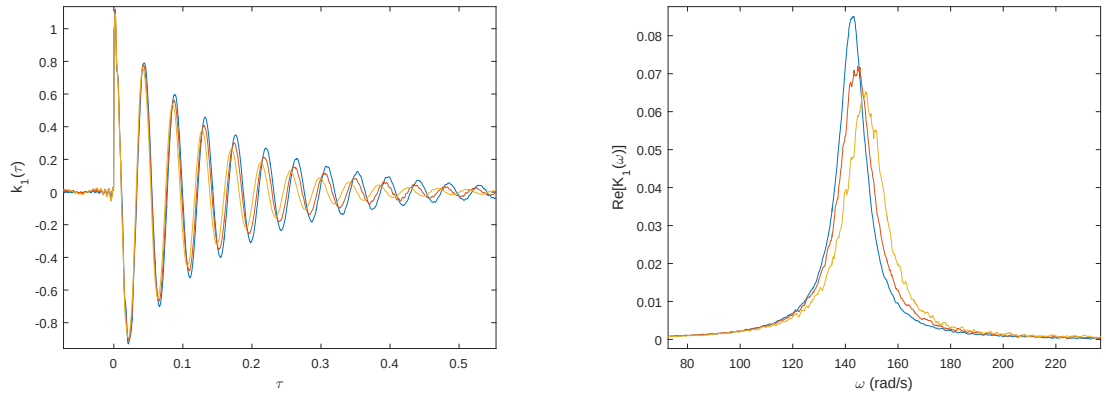

(a) (b)

Fig. 4.8 a) Time and b) frequency first kernels from the experiment set up as a stiffening spring with increasing excitation magnitude: $S_{Max} = 0.005$ (blue), $S_{Max} = 0.02$ (red) and $S_{Max} = 0.5$ (yellow).

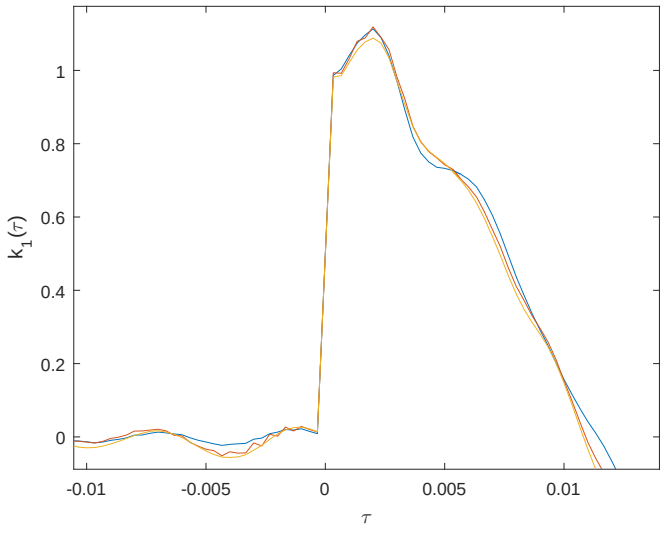

Fig. 4.9 Time first kernels around $\tau = 0$ with increasing excitation magnitude: $S_{Max} = 0.005$ (blue), $S_{Max} = 0.02$ (red) and $S_{Max} = 0.5$ (yellow).

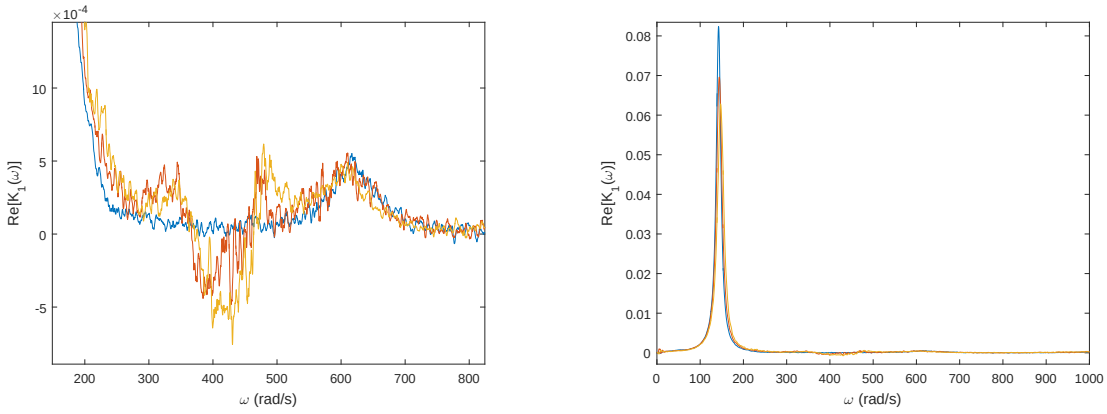

(a) (b)

Fig. 4.10 Real part of the frequency first kernels at higher frequencies than the resonance with increasing excitation magnitude: $S_{Max} = 0.005$ (blue), $S_{Max} = 0.02$ (red) and $S_{Max} = 0.5$ (yellow). a) Close-up around the second resonance and b) comparison of the first and second resonances.

at approximately 400rad/s and the other around 620rad/s. Since all three curves contain the peak at 620rad/s, it must be the second resonant frequency of the beam. However, only the two kernels from higher excitation contain the dip around 400rad/s with the higher excitation showing a larger dip suggesting it is a feature caused by the nonlinearity of the system increasing. This is reinforced by observing that the dip is at approximately three times the dominant frequency; a characteristic typical of nonlinear oscillators because any symmetric stiffness profile that can be approximately modelled by a polynomial will contain a linear term and most likely a second order cubic term. The cubic term, like a Duffing oscillator transfers energy from the linear resonant frequency to three times that frequency. The precise reason for this nonlinear feature is unknown, although it is clear from Figure 4.10b that its contribution to the integral over the kernel is negligible compared to that of the dominant frequency.

Whilst the structure is not a single-degree-of-freedom system, it does behave as one within a reasonable error bound sufficiently to validate Eq. (3.42) since, as shown in Figure 4.10b, the integral over the real part of the kernel is affected very little by the presence of the second resonance. Taking the case with $S_{Max} = 0.005$ the integral in the region $0 \leq \omega < 400$ which excludes the second resonance is 1.65 whereas the integral in the region $0 \leq \omega < 800$ including it is 1.70, a 3% difference. However, this does not account for the possibility that the presence of the second resonance could affect the first resonance such that Eq. (3.42) would still be true regardless of the size of the second resonance. The frequency spacing

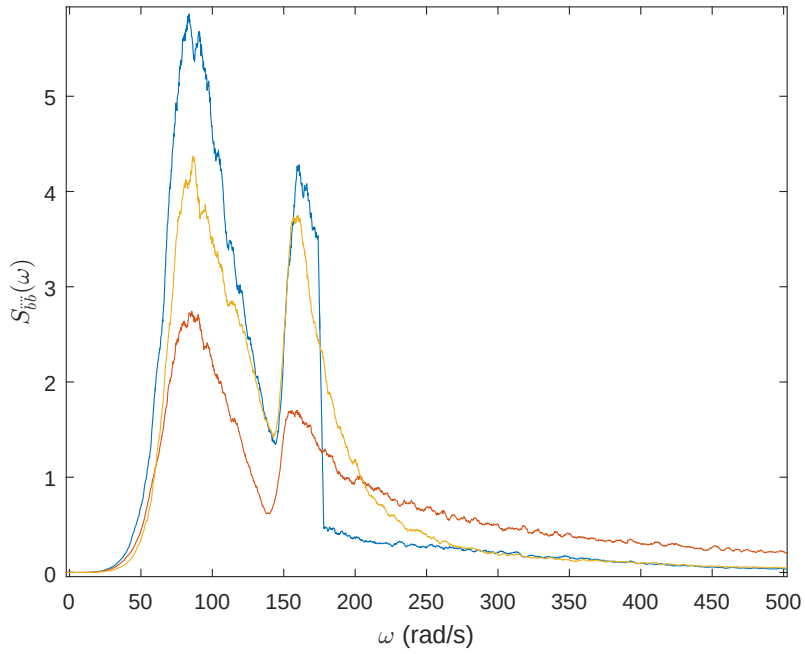

Fig. 4.11 Base acceleration spectra from three different inputs: band-limited (blue), low-pass (red) and narrowband (yellow).

between the first and second resonance and the size of it could be modified by changing the size of the tip mass or its location along the beam, although since the results are strong and the second resonance has little effect, this is not investigated further.

The form of the input spectrum supplied by the computer in Figure 4.8 was held constant, only the magnitude was varied. It is also interesting to investigate how the first extended Wiener kernel will change with various input spectra of approximately the same mean square acceleration. Three input spectra were selected: band-limited with constant spectrum up to 28Hz then zero after, low pass from Eq. (3.67) with $\omega_c = 25 \times 2\pi$ and narrowband from Eq. (3.66) with $\omega_c = 25 \times 2\pi$ and $\zeta_0 = 0.32$. These spectra were input to the electromagnetic shaker and the resulting base acceleration spectra due to the dynamics of the system are shown in Figure 4.11. The magnitude of each spectrum was selected such that the mean square base acceleration was approximately constant at 162, 159 and 161m^2/s^4 for the band-limited, low-pass and narrowband spectra respectively.

The real part of the first extended Wiener kernels from the three excitation spectra are displayed in Figure 4.12 where, similar to the numerical simulations of Figure 3.4, the kernels vary with spectra. The most notable difference between the kernels is the lower resonant frequency from the low-pass excitation most likely because the input spectrum

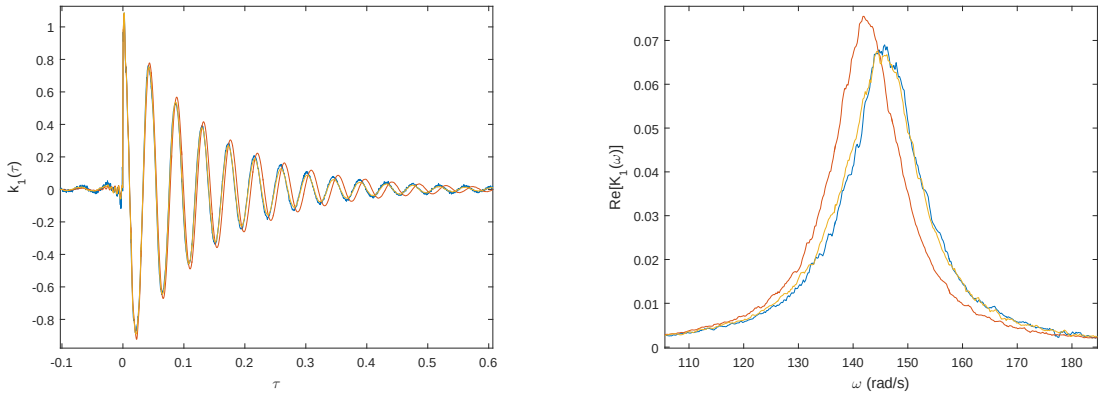

(a) (b)

Fig. 4.12 a) Time and b) frequency first kernels from the experiment set up as a stiffening spring with band-limited (blue), low-pass (red) and narrowband (yellow) excitation spectra.

is lower around the resonance of the system meaning that the response displacement, the stiffness and thus the frequency are all lower. Interestingly the kernels from band-limited and narrowband excitation are very similar, with the narrowband kernel being marginally more damped, possibly a sign of greater nonlinearity. The values of $k_1(0)$ are 0.47, 0.50 and 0.50 and $k_1(0^+)$ are 0.97, 0.98 and 0.98 for the band-limited, low-pass and narrowband spectra respectively, again providing strong support for the validity of Eqs. (3.43) and (3.56).

4.3.2 Asymmetric Nonlinearity

The symmetric system of the previous figures and discussion closely resembles the theory of Chapter 3, but it is also useful to ensure the validity of the theory for asymmetric systems. The experiment can easily be modified to provide an asymmetric potential by removing the magnets on one side of the beam and the real part of the first kernel is displayed in Figure 4.13 for two excitation magnitudes. Interestingly, the kernel from the larger excitation has a lower resonance suggesting the asymmetric system is softening instead of stiffening. Additionally, the kernels are more highly damped than the symmetric equivalent possibly because the asymmetric system is more highly nonlinear. The values of $k_1(0)$ are 0.50 and 0.51 and $k_1(0^+)$ are 0.99 and 1.0 for the low and high excitation respectively, again providing strong support for the validity of Eqs. (3.43) and (3.56).

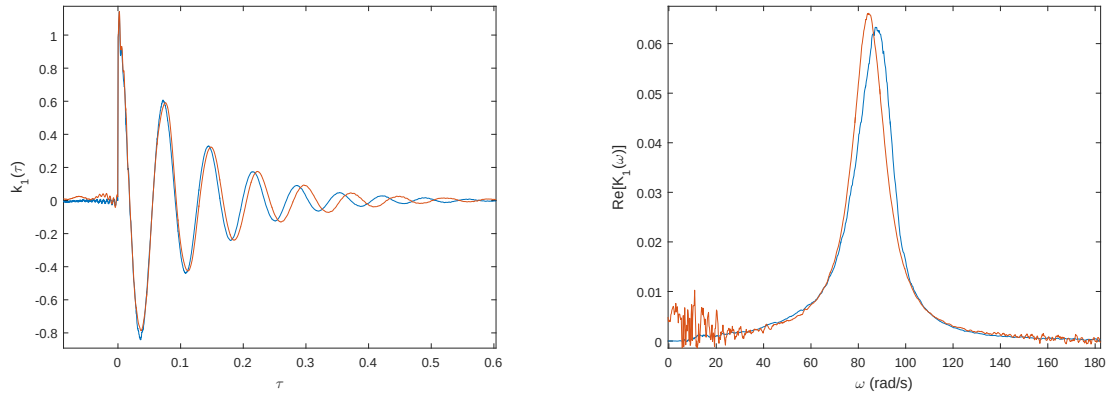

(a) (b)

Fig. 4.13 a) Time and b) frequency first kernels from the experiment set up with an asymmetric potential and $S_{Max} = 0.002$ (blue) and $S_{Max} = 0.2$ (red).

4.3.3 Bistable Nonlinearity

The nonlinear behaviour displayed by the stiffening and asymmetric systems above is evident, but not strong. A system with two equilibrium points is more distinctly nonlinear and is worth investigation both because of its interest in energy harvesting as well as to validate the theory for stronger nonlinearities. The experiment has been modified to create two potential wells as displayed in Figure 4.14 where the magnet on the beam is attracted to either one of the two magnets on the upper plate. At the tip of the cantilever, a piece of paper has been added to increase damping for reasons discussed in Section 4.4.

The backbone curve of the bistable experiment can be calculated using the same method as for the stiffening system and is displayed in Figure 4.15. At high amplitudes, inter-well crossover is observed and a high frequency that increases with amplitude is displayed. At lower amplitudes, below approximately 0.45m/s, the tip is trapped within one potential well and exhibits softening behaviour whereby the frequency decreases with amplitude. A clear pattern is evident, although there is some spread around it caused by the effect of higher harmonics and the two potential wells not being identical.

The first extended Wiener kernel is displayed in Figure 4.16 for three different excitation amplitudes; one providing almost all motion in a single potential well, one with intermittent crossover between wells and one with almost continuous crossover. The kernel shows softening behaviour and increased damping as the amplitude of the excitation is increased. The strongly nonlinear response when exhibiting inter-well dynamics is the cause of the

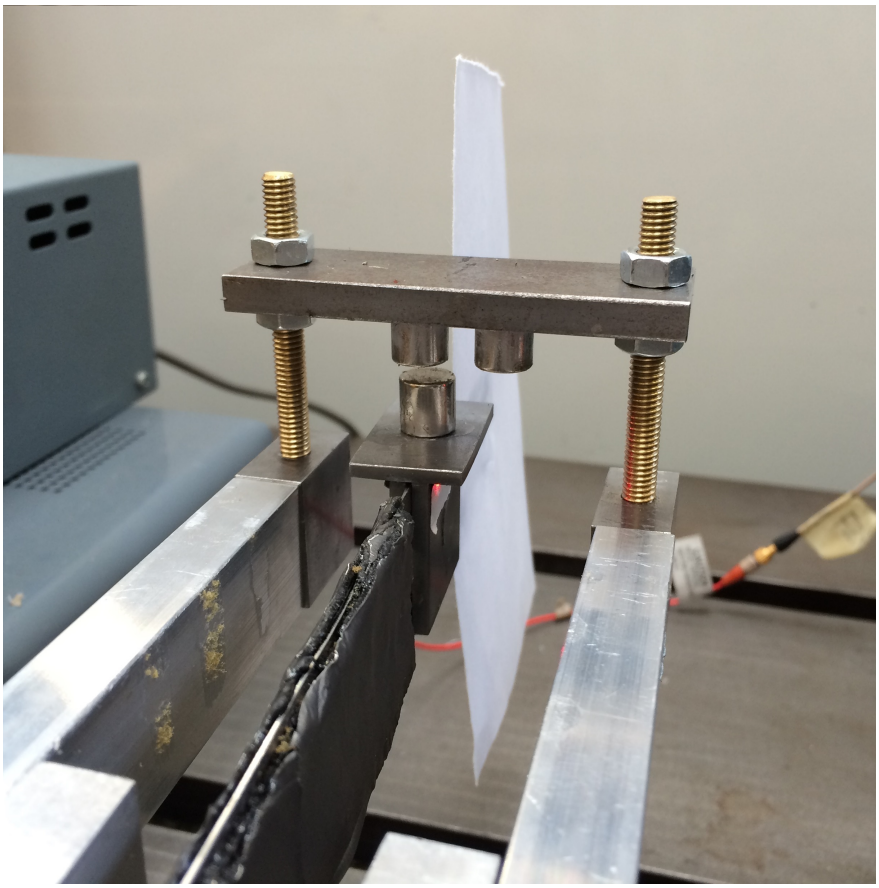

Fig. 4.14 Experimental apparatus in bistable configuration.

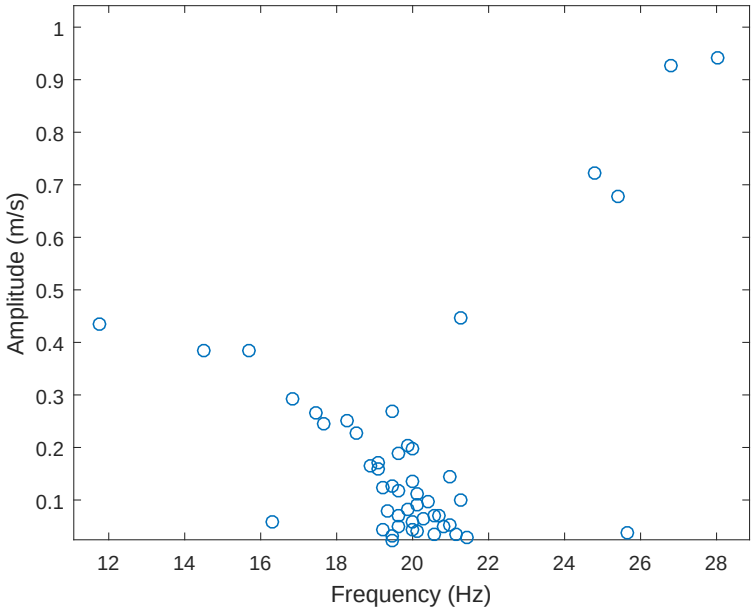

Fig. 4.15 Backbone curve of the bistable experimental system.

increased damping whereas when oscillating in one potential well, the kernel is closer to linear and possesses lower damping.

A critical feature that conflicts with theory is that when observed in the time domain in Figures 4.16a and b, the kernel possesses a small non-causal section particularly for the more strongly nonlinear responses with inter-well oscillations. Discussion of this important feature is left until Section 4.4 although its effect on the kernel around $\tau = 0$ and therefore Eq. (3.56) is of interest here. The values of $k_1(0^-)$, $k_1(0)$ and $k_1(0^+)$ for the three levels of excitation are presented in Table 4.1 along with the difference between each value, which according to theory should be 0.5. Whilst the non-causal part shifts the initial jump of the kernel at $\tau = 0$ downwards and therefore strongly effects the values of $k_1(0)$ and $k_1(0^+)$, the magnitude of the jump is still very close to unity.

Excitation	$k_1(0^-)$	$k_1(0)$	$k_1(0^+)$	$k_1(0)-k_1(0^-)$	$k_1(0^+)-k_1(0)$
$S_{Max} = 0.007$	-0.05	0.45	0.95	0.50	0.50
$S_{Max} = 0.02$	-0.14	0.37	0.87	0.51	0.50
$S_{Max} = 0.05$	-0.17	0.34	0.84	0.51	0.50

Table 4.1 Values of the first extended Wiener kernel around $\tau = 0$.

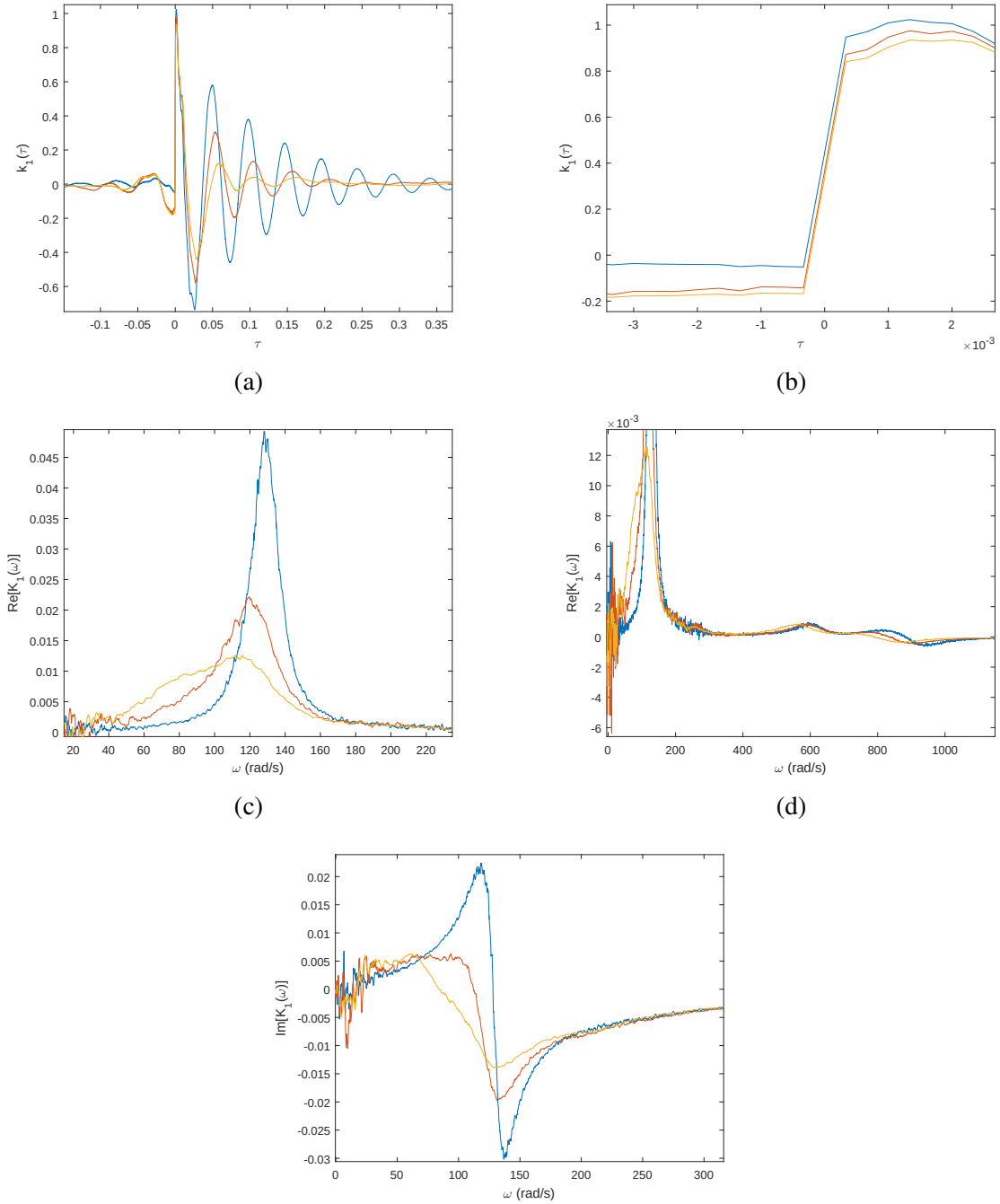

Fig. 4.16 First extended Wiener kernels for the bistable experimental set-up with $S_{Max} = 0.007$ (blue), $S_{Max} = 0.02$ (red) and $S_{Max} = 0.05$ (yellow). a) Time kernel, b) close-up of time kernel around $\tau = 0$ c) resonant peaks of real part of frequency kernel d) real part of frequency kernel over wide frequency range and e) imaginary part of the frequency kernel.

The imaginary part of the frequency kernel is responsible for the odd part of the time kernel and therefore the difference between $k_1(0^-)$ and $k_1(0^+)$ whereas the real part of the frequency kernel is responsible for the even part of the time kernel and therefore the value at precisely $k_1(0)$. From the results in Table 4.1 where the differences between $k_1(0^-)$, $k_1(0)$ and $k_1(0^+)$ are 0.5, it seems that the imaginary part of the frequency kernel abides by the theory of Eqs. (3.56) and therefore (3.42) whereas the real part does not. Despite this, the theory cannot be considered validated for this configuration and so the source of the non-causality is investigated further in Section 4.4.

The occurrence of low frequency noise is evident from Figures 4.16d and e. This most likely arises from the relatively low frequency of transitions from one well to another and has been mitigated by using a very large ensemble; 720 realisations of 10s each when $S_{Max} = 0.05$. The second and third resonance of the beam is also displayed in Figure 4.16d where relative to the fundamental resonance their magnitude seems to have grown when compared to the stiffening oscillator of Figure 4.10b. One possibility is that the torsional mode has become more prevalent due to both an increased moment of inertia of the tip mass about the beam centre-line and the torque generated by the magnetic forces. This may have a discernible effect on the validation of Eq. (3.42) although it is outweighed by the non-causality of the time kernel.

4.3.4 Gaussian Assumption

An important assumption in the theory of Chapter 3 is that the base acceleration is Gaussian. This is assessed in Figure 4.17 by calculating the probability density function of the base acceleration from the system of Figure 4.8 with $S_{Max} = 0.5$ and comparing it to a Gaussian distribution with the same mean square value. The experimental input is clearly not Gaussian, containing a sharper peak and shorter tails than the Gaussian distribution. However, the results of this section seem to validate the theory of Chapter 3 which assume a Gaussian input. This may be because the relatively small departure from a Gaussian distribution of the base excitation has a relatively small impact on the theory.

In Section 3.4.1 the Gaussian property of the excitation provides the orthogonality between the different order of g-functionals. It is this orthogonality that means the power input by any impulse of excitation is applied instantaneously only into the first kernel in Eq. (3.54). If the input is slightly non-Gaussian and assuming the kernels are still chosen in the form of Eq. (3.11), the orthogonality of the kernels will be only slightly affected. This means that the power in from each impulse of excitation will still largely be input to the first kernel and the result of Eq. (3.56) will not vary significantly although higher order kernels may also have small effects. Consequently, whilst theoretically invalid, the theory of Chapter 3 may

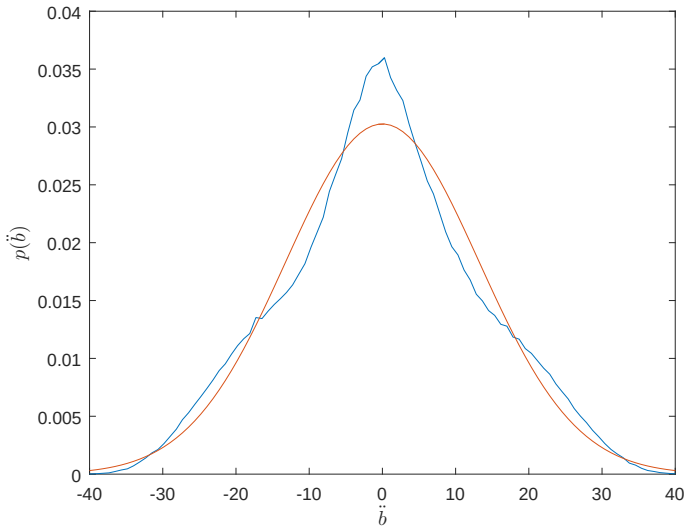

Fig. 4.17 Probability density function of experimental base acceleration (blue) compared to a Gaussian distribution (red).

still be applied to a system with an input close to Gaussian, but only to provide an estimate rather than exact calculation of the power dissipation.

In theory, the Wiener series could be extended further to non-white and non-Gaussian excitation although to provide an orthogonal series the functionals would no longer take the neat form of Eq. (3.11). The complexity of the series would most likely render it of little use and it may not be the case that the integral over the first kernel is proportional to $\mathrm{E}\left[\mathbf{f}^{\mathrm{T}}\mathbf{M}^{-1}\mathbf{f}\right]$ since the derivation will change.

4.3.5 Sources of Error

Excluding the bistable system, the results from the experiment for validating Eq. (3.43) are compelling with an average percentage error over all monostable configurations at both $k_1(0)$ and $k_1(0^+)$ of 1.3%. However, a number of sources of error and variations from the theory, such as the Gaussian assumption discussed above, still exist. Firstly, the data will most likely have both random and systematic errors. Random errors and fluctuations occur both from electrical noise in the instrumentation and from the random nature of the input with both decreasing satisfactorily with averaging. Systematic errors arise from both the automatic calibration of the laser vibrometer and the manual calibration of the accelerometers that relies on the laser vibrometer although these are thought to be small. Additionally, properties of

the system such as damping and sliding friction that may vary with time and room properties such as temperature may have an adverse impact on results.

A large potential source of deviation from the theory is due to the MDOF nature of the beam. Not only the extra resonances affecting the integral over the kernel, but the assumption that the beam acts as the single-degree-of-freedom oscillator of Eq. (4.1). From this the kernel has been adapted according to the discussion in Section 4.2.3 such that $k_1(0) = 0.5$ meaning that no estimate of the oscillating mass is required. The effect of this assumption, particularly if the tip mass is small compared with the beam may be that $k_1(0)$ should not be equal to 0.5, but something slightly higher or lower and therefore validation against this value could be unreliable. In reality, a more reasonable model of the system would be to split the beam into a number of elemental masses and a tip mass and treat the system as MDOF. In practice this is difficult since the velocity of every elemental mass and an estimate of the mass would be required, most likely adding considerable additional error. Alternatively, modal coordinates could be used to represent the beam response. Given the relatively small second resonance compared to the first, the first modal coordinate can be seen to dominate suggesting that the SDOF assumption is reasonable.

Given these sources of error, the very low percentage error of 1.3% from the experimental results strongly supports the theory of Eq. (3.42) and therefore can be said to have validated it for moderate nonlinearity. For the bistable case with stronger nonlinearity, the experiment becomes unsuitable as discussed in Section 4.4.

4.3.6 Power Calculation

Although Eqs. (3.43) and (3.63) have been verified within reasonable experimental error margins, their implication for power dissipation according to Eq. (3.62) has not been investigated experimentally due to the difficulty of obtaining power data. An overestimate of the power dissipated could be calculated from the power provided to the electromagnetic shaker although due to losses in the shaker and sliding mechanism this would be unreliable for calculating the power dissipated by the beam. The only alternative is to calculate power by multiplying the base force by the tip velocity as $\mathrm{E}\left[-m\ddot{b}\dot{y}\right]$ using Eq. (4.1). However, this is identically equal to using Eq. (3.62) and so is of little value.

4.4 Validity of the Experimental Approach

Strong experimental results are observed in Section 4.3 that validate the theory of Chapter 3 for moderate nonlinearity. However, within certain parameter ranges, typically low damping

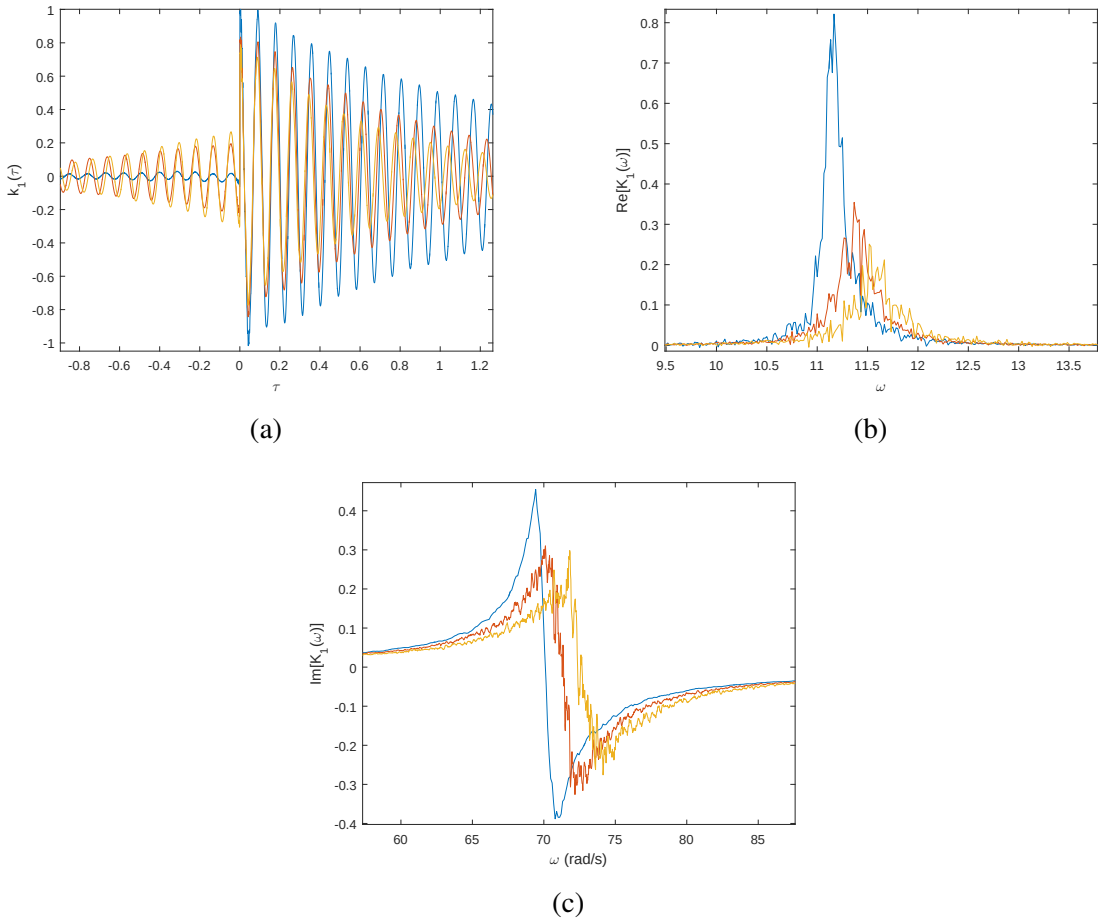

Fig. 4.18 a) Time, b) real and c) imaginary parts of frequency first kernels from the experiment with low damping and excitation magnitudes: $S_0 = 0.001$ (blue), $S_0 = 0.003$ (red) and $S_0 = 0.006$ (yellow).

and high nonlinearity, a non-causal time kernel has been observed as seen for the bistable system in Figure 4.16. The effect is displayed more distinctly in Figure 4.18 where a stiffening beam with lower damping than that of Section 4.3 is forced by three different magnitudes of excitation. The derivation of the kernels in Chapter 3 states that they are causal therefore the occurrence of a non-causal kernel may indicate a problem with the theory. This section investigates this phenomena and shows that it is due to an undesirable effect of the experimental design: that the base excitation is correlated to the tip response meaning that in reality the kernel calculated is not an extended Wiener kernel and can therefore be non-causal.

The experiment is designed to replicate a SDOF nonlinear oscillator with random base excitation. In reality however, the experimental system is not so simple and is better modelled

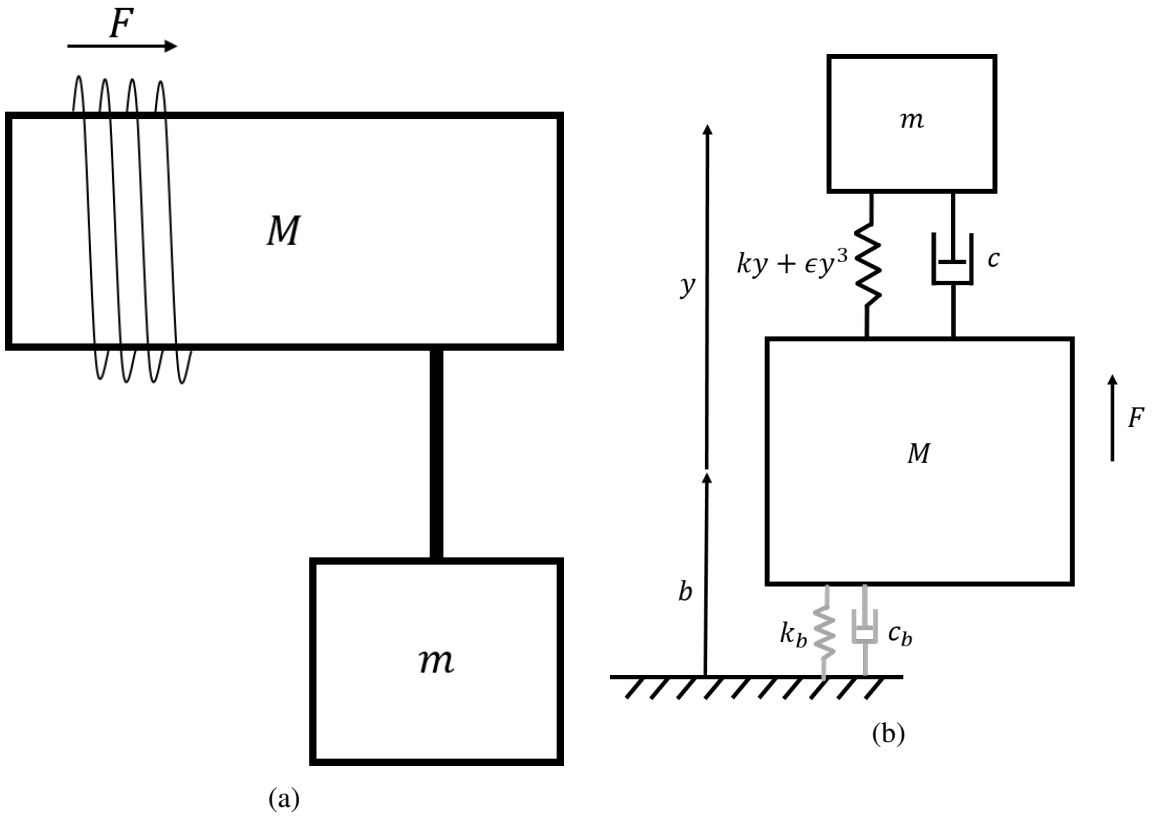

Fig. 4.19 System diagrams of the 2DOF experimental system.

as a 2DOF system with a forced base mass and excited tip mass as shown in Figure 4.19. Here, the base mass, M, represents both the electromagnet mass within the shaker and the mass that oscillates on the sliders and the external force represents the force from the current in the coil of the shaker.

The equations of motion for this system can be written, assuming a cubic nonlinearity, as

$$\begin{pmatrix} M & 0 \\ m & m \end{pmatrix} \begin{pmatrix} \ddot{b} \\ \ddot{y} \end{pmatrix} + \begin{pmatrix} c_b & -c \\ 0 & c \end{pmatrix} \begin{pmatrix} \dot{b} \\ \dot{y} \end{pmatrix} + \begin{pmatrix} k_b b - ky - \varepsilon y^3 \\ ky + \varepsilon y^3 \end{pmatrix} = \begin{pmatrix} F \\ 0 \end{pmatrix} \tag{4.2}$$

and can be solved numerically via time integration for a realisation of a force input, F, of a given spectrum. The base stiffness and damping, k_b and c_b, will be negligible in the experiment since they represent the restoring force and damping of the combined base and shaker mass, therefore in the majority of cases below they are set to zero. The system response can therefore have infinite mean square displacement, but this does not affect the first extended Wiener kernel between base acceleration and tip velocity so can be ignored.

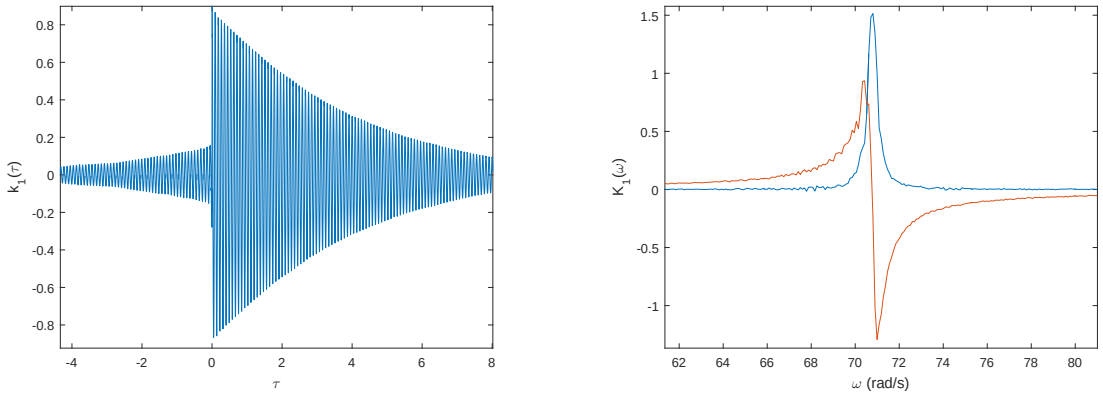

(a) (b)

Fig. 4.20 a) Time and b) real part (blue) and imaginary part (red) of the frequency first kernels for the linear 2DOF system.

This 2DOF system model has been seen to show a non-causal time kernel under two different conditions: linear springs with very low damping and nonlinear springs with low damping. Firstly, the linear problem is a numerical one, since clearly the first extended Wiener kernel is the impulse response as it is in the SDOF case and is therefore causal. A system with $M = 0.5$kg, $m = 0.01$kg, $c_b = 0$kg/s, $k_b = 0$N/m, $c = 3 \times 10^{-3}$kg/s, $k = 50$N/m, $\varepsilon = 0$N/m^3 is excited by a white noise input force of spectrum magnitude $F_0 = 1$N^2/s. 18 realisations of a time series of length 750 cycles of the natural frequency of the oscillator are averaged. The time and frequency first kernels are shown in Figure 4.20 where the acceleration of the mass M is taken as the input and the relative velocity of mass m to mass M as the output of the Wiener system.

The non-causal part of the time kernel is a problem since in the linear case the kernel should be the impulse response which must be causal. Additionally, in the frequency domain, the imaginary part of the kernel has a significantly smaller positive than negative part suggesting it is incorrect. The reason for the problems can be seen in the frequency domain by looking at how the first kernel is calculated from the cross-spectrum of $\dot{y}$ and $\ddot{b}$ and the base excitation spectrum, $S_{\ddot{b}\ddot{b}}$, according to Eq. (3.24). Figure 4.21 shows the three constitutive parts of Eq. (3.24) and shows that the system acts like a vibration absorber around the resonance of the mass m. The base excitation at this frequency is very small since most energy from the force is injected straight into the tip mass meaning that the kernel is calculated by dividing the cross-spectrum by a very small excitation spectrum at this frequency. Any small error in the cross-spectrum of excitation spectrum is magnified due to the division by a small number hence generating inaccuracies in the first kernel and consequently the non-causal part observed in Figure 4.20.

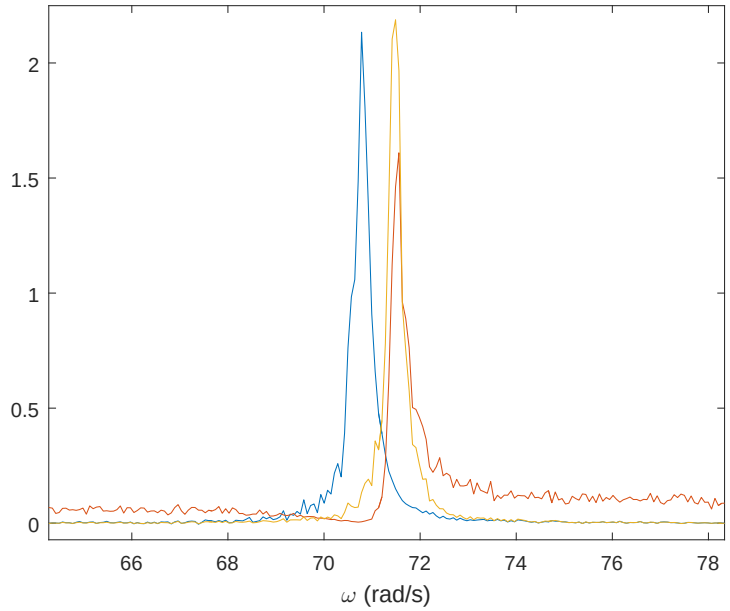

Fig. 4.21 First kernel (blue), base acceleration spectrum (red) and cross-spectrum between tip velocity and base acceleration (yellow) where curves are scaled to fit on plot.

This problem can be improved simply by increasing the size of the ensemble used to calculate the kernel, increasing the time of each realisation or smoothing the excitation spectrum by changing parameters such as increasing damping. Figure 4.22 shows the negative time part of the first kernel and how the non-causal part is reduced by a larger ensemble with greater realisation time and by a system with increased damping compared to the kernel of Figure 4.20.

Whilst this issue with a linear oscillator is important to consider, it does not appear to contribute to the experimental feature shown in Figure 4.18 since for the approximately linear response to low excitation, the kernel is almost causal. The increase in non-causality with excitation magnitude suggests it is a consequence of increasing nonlinearity. The first kernel must therefore be investigated using the 2DOF model of the experiment with nonlinear components.

Parameter values $M = 0.5$kg, $m = 0.01$kg, $c_b = 0$kg/s, $k_b = 0$N/m, $c = 0.02$kg/s, $k = 50$N/m and $\varepsilon = 1 \times 10^6$N/m^3 are chosen in order to model a similar configuration to that of Figure 4.18. The first kernel is shown for different excitation magnitudes in Figure 4.23 where it is seen that the experimental phenomena of a non-causal first kernel has been replicated by the simulations and thus is not merely an experimental peculiarity. The imaginary part of the frequency kernel is also displayed as it better illustrates the contrast between causal and

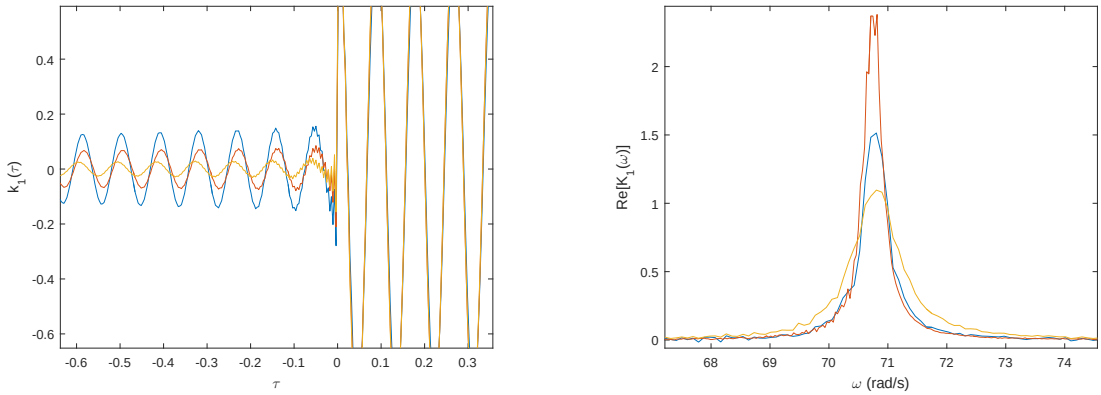

(a) (b)

Fig. 4.22 Comparison of a) negative section of time kernels and b) frequency kernels with simulations as described for Figure 4.20 (blue), increased ensemble size to 40 realisations each with length 2000 cycles of the natural frequency (red) and $c = 0.008$kg/s (yellow).

non-causal kernels via the difference between its maximum and minimum points. In general, more non-causal kernels have a lower maximum compared to its minimum.

It is important to address whether this phenomena undermines the theory of Chapter 3 which states in Eq. (3.4) that the kernels must be causal. A useful comparison to make is to compare the first kernel from three cases:

- Case 1: The full 2DOF model of Figure 4.19.
- Case 2: A SDOF oscillator with the same parameters and initial conditions as Case 1 and excited by the same base acceleration time history. In theory this should be identical to Case 1.
- Case 3: A SDOF oscillator with the same parameters as Case 1 and excited by Gaussian noise of the same spectrum as Case 1, but not the same time history.

The kernels for the three cases are plotted in Figure 4.24 for the same parameters as in Figure 4.23 with $F_0 = 5 \times 10^{-3}\text{N}^2\text{s}$. For each of the three cases the responses will be discussed and compared to each other, although it is important to note that when the system is linear, all three cases generate the same kernel: the impulse response.

Case 1: A non-causal kernel is observed for the nonlinear system.

Case 2: In theory, case 2 should be identical to case 1 but the negative time part of the kernels differ and case 2 is closer to being causal suggesting there is a difference between the methods. This is a numerical issue and is due to the slightly differing solution methods where within each time step, case 1 solves the 2DOF system therefore includes base dynamics within

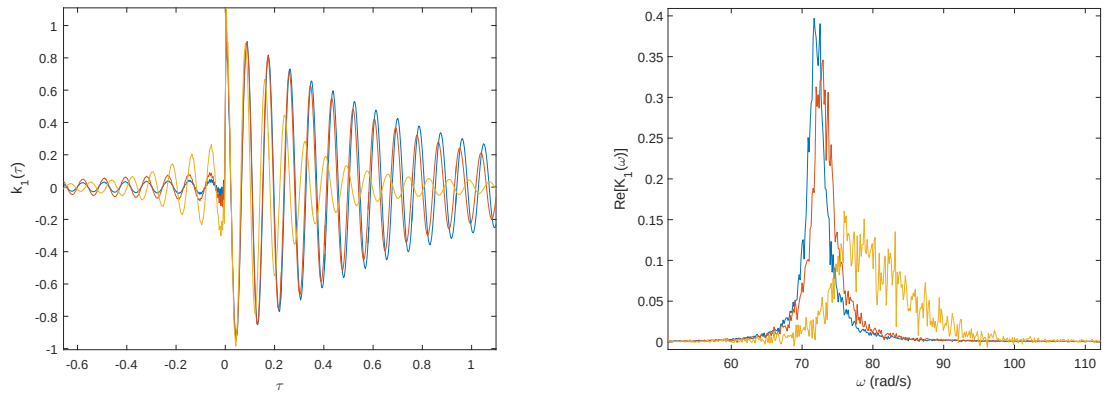

(a) (b)

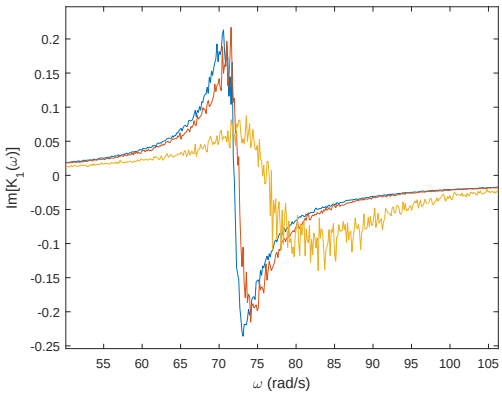

(c)

Fig. 4.23 a) Time, b) real and c) imaginary parts of frequency kernels with force input of magnitude $F_0 = 5 \times 10^{-4}\text{N}^2\text{s}$ (blue), $F_0 = 1 \times 10^{-3}\text{N}^2\text{s}$ (red) and $F_0 = 5 \times 10^{-3}\text{N}^2\text{s}$ (yellow).

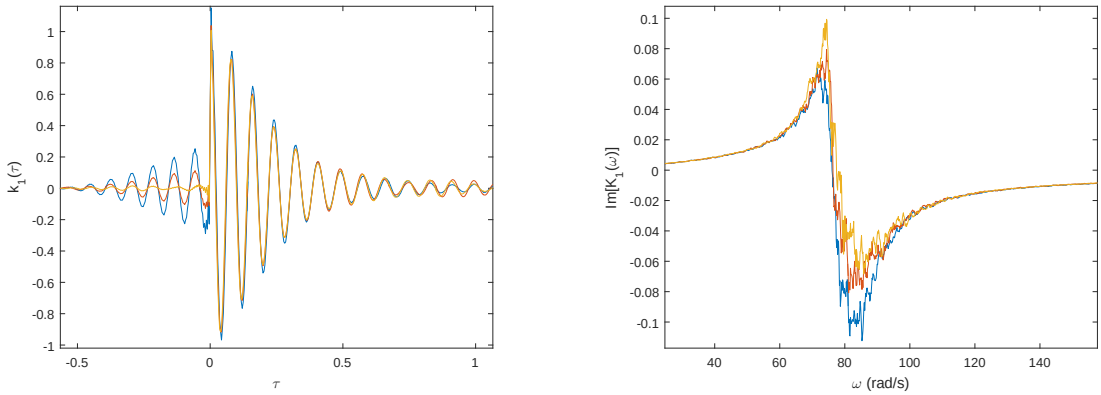

(a) (b)

Fig. 4.24 a) Time and b) frequency first kernels from case 1 (blue), case 2 (red) and case 3 (yellow) simulations.

a time step whereas the SDOF system of case 2 linearly interpolates the base acceleration between the values at the start and end of the time step.

Exploration of time histories illustrates the difference in the kernels from case 1 and 2. Despite the identical base acceleration and initial conditions the response for the two cases is seen to be very similar at some times and diverge to be very different at others. This is also true when the initial conditions for each case differ, but the excitation remains the same. The result of a less non-causal kernel in case 2 than case 1 suggests that at times where the velocity responses of case 1 and 2 are very similar, the kernel calculated is non-causal and at times when they are different, the kernel is causal. On average therefore, a less non-causal response than case 1 is observed.

Time histories have also been investigated for a linear system where the tip response in case 2 was found to match that of case 1 exactly. Even when different initial conditions between case 1 and 2 are applied the transients decay and the case 2 response converges to that of case 1 and the resulting kernel is causal.

The improved causality of case 2 due to times when the velocity response varies from case 1 suggests that the non-causality in the kernel is due to some specific complementarity between the base excitation and the tip response. The base excitation is affected by the tip motion and so tuned to the specific system attached to it. This hypothesis is validated by slightly mis-tuning the tip motion from that of the base by tweaking the linear stiffness. In this case, the tip motion from case 1 and 2 diverges completely and the kernel becomes causal.

Case 3: Importantly, case 3 that applies the given base acceleration spectrum provides a causal kernel.

Combining the results of the three cases suggests that since they all contain the same input spectrum, the difference between the first kernels must be due to the feedback from the tip affecting the base motion. For the 2DOF system, any given realisation of base excitation is therefore tuned to system attached to it and this complementarity affects the calculation of the first kernel.

It is tempting to suggest that since the spectra of case 1 and 3 are the same, the difference in the kernel is due to the excitation in case 1 being non-Gaussian and in case 3 being Gaussian. Case 3 has a base motion that is calculated from a summation of sinusoids of different frequency with random phase that is independent of the phase at any other frequency hence the input is Gaussian (by the central limit theorem [51]). In contrast, it could be argued that the difference in case 1 is that various frequencies within the spectrum could be correlated meaning that any time signal is not simply a summation of sinusoids of different frequency with independent random phase and as such is non-Gaussian.

This is not the case because, conceivably, the Wiener series could be extended to encompass non-white and non-Gaussian excitation. In this case the g-functionals would no longer have the form of Eq. (3.11) and the lower order Volterra functionals within a g-functional would no longer be derived from the leading order one. However, the first kernel would still be the same as the Gaussian case and would still be causal because the nonlinear system is causal. This suggests that the non-causal part of the first kernel for case 1 is not due to a subtly non-Gaussian input, but because the base and tip motion are tuned to each other by the feedback from the nonlinear spring. A comparison of the two PDFs of the base acceleration from the two methods in Figure 4.25 emphasises the Gaussian input where both are seen to be extremely similar.

The distinction between the two systems of cases 1 and 3 is therefore not due to the Gaussian nature of the input, but the influence the tip has on the base. The consequence of this effect will be explored via a number of illustrative plots before Section 4.4.1 provides a more mathematical justification for the non-causal kernels observed.

Observation of the phase difference at each frequency between the base acceleration and the tip velocity for the two systems demonstrates their differing dynamics. Taking the same parameters as Figure 4.24, the ensemble average of the sine of the difference in phase between base acceleration and tip velocity, $\mathrm{E}\left[\sin(\varepsilon_{\ddot{b}}(\omega)-\varepsilon_{\dot{y}}(\omega))\right]$, is plotted against frequency in Figure 4.26. To calculate this, the phase at any frequency from the base acceleration, $\varepsilon_{\ddot{b}}$, or tip velocity, $\varepsilon_{\dot{y}}$, can be found from a DFT of the time signal.

The difference in the phase at resonance between base acceleration and tip velocity for the 2DOF and SDOF cases indicates that the dynamics of the two systems are different. Although superposition of frequency responses is not valid for this nonlinear system, thinking

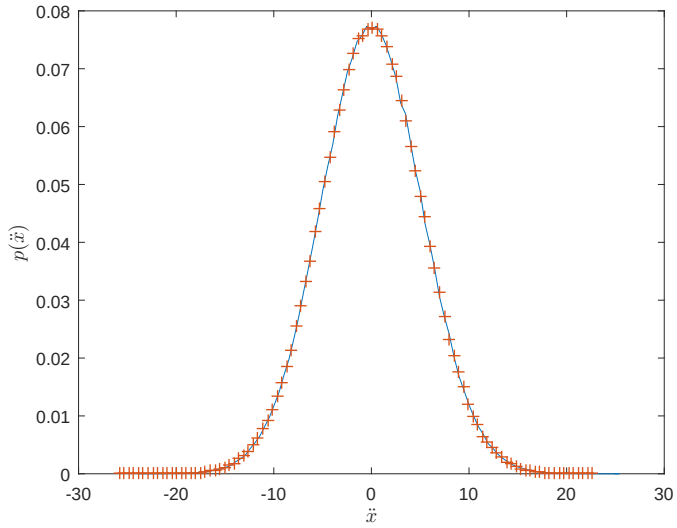

Fig. 4.25 Base acceleration PDF of 2DOF (blue line) and SDOF (red crosses) systems with the same spectra.

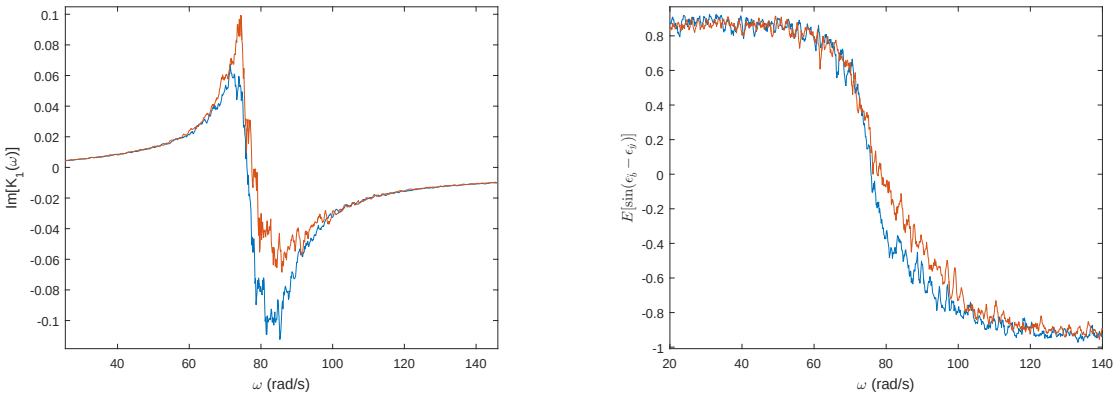

(a) (b)

Fig. 4.26 a) Imaginary parts of First kernels and b) average phase difference between base acceleration and tip velocity plotted against frequency for case 1 (blue) and case 3 (red).

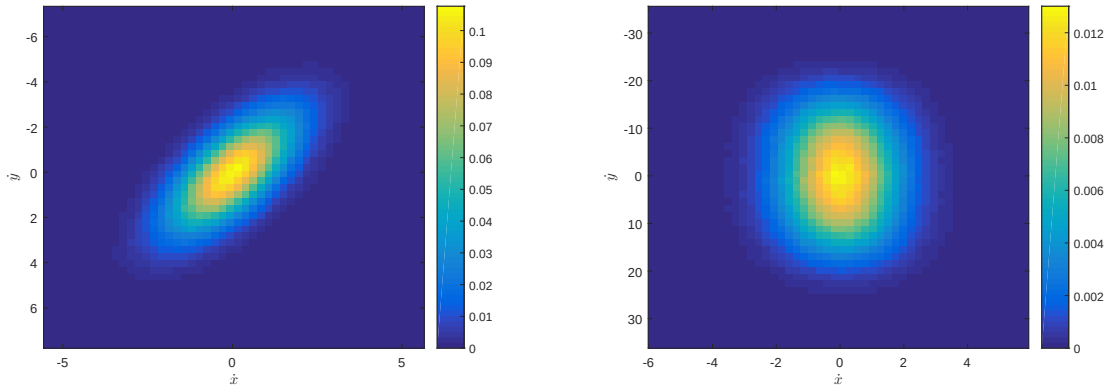

(a) (b)

Fig. 4.27 JPDF of base and tip velocity for a) 2DOF and b) SDOF cases.

of the response to just one input force frequency and then extending to all frequencies in the input spectrum is illustrative. In the 2DOF case, a single input frequency force oscillates the base at that frequency, which vibrates the tip mass at this frequency and three times this frequency due to the cubic stiffness. The tip velocity at the higher frequency in turn generates base motion at this frequency which in turn affects the tip motion. In the SDOF case, input base motion at a single frequency similarly produces a tip response at the input frequency and three times this frequency, but the higher frequency does not affect the base motion and the dynamics will therefore be different as seen in Figure 4.26.

Another way of observing this effect is looking at the correlation between the base and tip velocities for the two cases as shown in Figure 4.27 where the joint probability density functions of base and tip velocity are displayed. Here, different parameter values of $M = 0.01$kg, $m = 0.01$kg, $c_b = 1.0$kg/s, $k_b = 20$N/m, $c = 0.02$kg/s, $k = 50$N/m, $\varepsilon = 1 \times 10^6$N/m^3 and $F_0 = 5 \times 10^{-3}$N have been chosen to exaggerate the effect. It is clear that in the 2DOF case, the base and tip motion are strongly correlated, whereas in the SDOF case they are not; further emphasising the difference in dynamics between the two cases. Additionally, the magnitude of the tip velocity in the SDOF case is significantly higher.

Experimentally, the non-causal part of the first kernel and therefore the effect of the base mass is seen to reduce as damping is increased. In order to validate that the 2DOF system is modelling this effect correctly, Figure 4.28 shows the kernel with the same parameters as Figure 4.23 and $F_0 = 5 \times 10^{-3}$N^{2}s and compares it to the kernel when damping is increased to $c = 0.08$kg/s. Similar to the experiment, the simulations show that the kernel is causal as damping is increased suggesting the 2DOF system is modelling the experiment well.

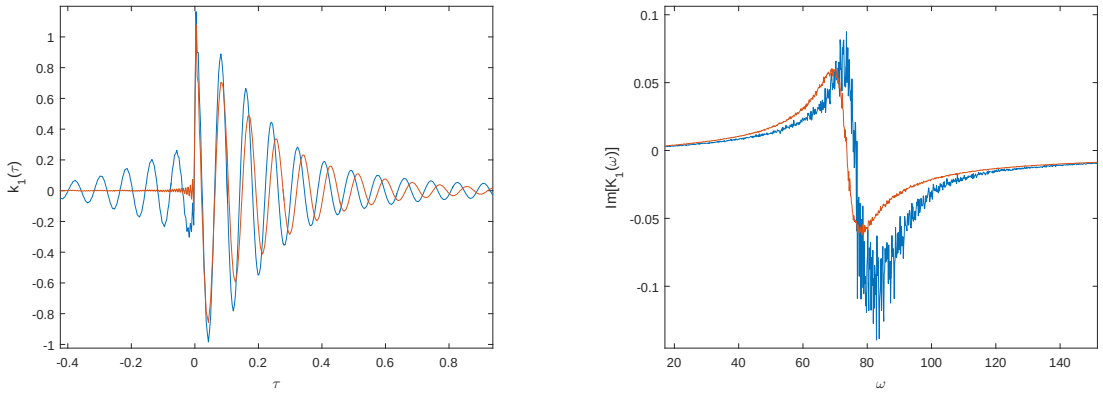

(a) (b)

Fig. 4.28 a) Time and b) frequency domain first kernels with $c = 0.02$kg/s (blue) and $c = 0.08$kg/s (red) for the 2DOF system.

4.4.1 Causality of the Kernel of the 2DOF System

The preceding numerical simulations illustrate the differing dynamics of the two systems of cases 1 and 3, but they do not describe why it is that a non-causal kernel arises in case 1. A more mathematical analysis of the first kernel between base acceleration and tip velocity for the 2DOF system of case 1 is investigated in what follows.

Taking the nonlinear system of Figure 4.19, two extended Wiener series can be calculated with the external force, F, as the input and the base acceleration, $\ddot{b}$, and tip velocity, $\dot{y}$, as outputs such that

$$\ddot{b}(t) = \int_{-\infty}^{\infty} k_{b1}(t-\tau)F(\tau)d\tau + \sum_{n=2}^{\infty} \mathbf{g}_n[k_{bn};F(t)] \tag{4.3}$$

$$\dot{y}(t) = \int_{-\infty}^{\infty} k_{y1}(t-\tau)F(\tau)d\tau + \sum_{n=2}^{\infty} \mathbf{g}_n[k_{yn};F(t)]. \tag{4.4}$$

For these series, the kernels are definitely causal because no displacement can be seen before a force is applied. The series can also be written in the frequency domain by taking a Fourier transform of both sides to yield

$$\ddot{B}(\omega) = K_{b1}(\omega)\hat{F}(\omega) + \sum_{n=2}^{\infty} \mathscr{F}\left(\mathbf{g}_n[k_{bn};F(t)]\right) \tag{4.5}$$

$$\dot{Y}(\omega) = K_{y1}(\omega)\hat{F}(\omega) + \sum_{n=2}^{\infty} \mathscr{F}\left(\mathbf{g}_n[k_{yn};F(t)]\right) \tag{4.6}$$

where $\mathscr{F}$ represents the Fourier transform and $\ddot{B}(\omega) = \mathscr{F}(\ddot{b}(t))$, $\dot{Y}(\omega) = \mathscr{F}(\dot{y}(t))$ and $\hat{F}(\omega) = \mathscr{F}(F(t))$.

The kernel of interest in this chapter, called $\lambda_1(\tau)$ here, has the base acceleration, $\ddot{b}$, as an input and tip velocity, $\dot{y}$, as an output such that

$$\dot{y}(t) = \int_{-\infty}^{\infty} \lambda_1(t-\tau)\ddot{b}(\tau)d\tau + \sum_{n=2}^{\infty} \mathbf{g}_n[\lambda_n; \ddot{b}(t)] \tag{4.7}$$

with its frequency domain equivalent

$$\dot{Y}(\omega) = \Lambda_1(\omega)\ddot{B}(\omega) + \sum_{n=2}^{\infty} \mathscr{F}\left(\mathbf{g}_n[\lambda_n; \ddot{b}(t)]\right) \tag{4.8}$$

where $\Lambda_1(\omega) = \mathscr{F}(\lambda(t))$. Substitution of Eq. (4.5) into Eq. (4.8) yields

$$\dot{Y}(\omega) = \Lambda_1(\omega)K_{b1}(\omega)\hat{F}(\omega) + \Lambda_1(\omega)\sum_{n=2}^{\infty} \mathscr{F}\left(\mathbf{g}_n[k_{bn}; F(t)]\right) + \sum_{n=2}^{\infty} \mathscr{F}\left(\mathbf{g}_n[\lambda_n; \ddot{b}(t)]\right). \tag{4.9}$$

The causality of the kernel $\lambda_1(\tau)$ is of interest here and can be investigated from Eq. (4.9). For the linear case, only the first kernels contribute so using Eq. (4.6), Eq. (4.9) becomes

$$K_{y1}(\omega)\hat{F}(\omega) = \Lambda_1(\omega)K_{b1}(\omega)\hat{F}(\omega) \tag{4.10}$$

and therefore

$$\Lambda_1(\omega) = \frac{K_{y1}(\omega)}{K_{b1}(\omega)}. \tag{4.11}$$

Here, for $\lambda_1(\tau)$ to be causal, $\Lambda_1(\omega)$ and therefore $\frac{K_{y1}(\omega)}{K_{b1}(\omega)}$ must contain no poles with negative imaginary components, or alternatively must be analytic in the lower half-plane. The kernels $K_{y1}(\omega)$ and $K_{b1}(\omega)$ are themselves causal so contain no poles in the lower half plane, although due to the division by $K_{b1}(\omega)$, any of its zeros would become poles of $\Lambda_1(\omega)$. Zeros of $K_{b1}(\omega)$ occur at any frequency that the base mass does not move and in a damped system, this requires the tip mass to also be stationary. Hence $K_{y1}(\omega)$ will also have a zero at this frequency accounting for the stationary tip mass. Any possible zeros in $K_{b1}(\omega)$ would therefore cancel with the zeros in $K_{y1}(\omega)$ such that $\Lambda_1(\omega)$ has no poles in the lower half plane and so is causal.

For a nonlinear system, however, there is no obvious reason from Eq. (4.9) why $\lambda_1(\tau)$ should be causal. In addition, both the numerical and experimental results suggest that it is not necessarily causal. The reason being that both $\ddot{b}$ and $\dot{y}$ are caused by the force, F, but can be correlated to each other. This means the kernel $\lambda_1(\tau)$ is not an extended Wiener kernel as

assumed because its input is dependent on its output. Since $\lambda_1(\tau)$ is not an extended Wiener kernel, there is no reason why it should be a causal kernel.

An alternative perspective is to view any realisation of the input, $\ddot{b}$, to the series of Eq. (4.7) as a negligibly small subset of all possible realisations from any prescribed spectrum $S_{\ddot{b}\ddot{b}}(\omega)$. This is because only realisations capable of being generated by the 2DOF system can provide the input. If all possible realisations from $S_{\ddot{b}\ddot{b}}(\omega)$ were included as inputs, the series of Eq. (4.7) would be an extended Wiener series and so all the kernels would be causal. Since only a subset of possible realisations are taken, $\lambda_1(\tau)$ is not an extended Wiener kernel and so is not required to be causal.

4.4.2 Validity of Results and Application of the Theory

With the discrepancy between the intended base-excited SDOF oscillator desired and the real 2DOF experimental system, it is important to understand under what conditions the experiment can validate the SDOF theory of Chapter 3 and additionally, when can the theory be reasonably applied to real systems. Importantly, the numerical simulations of Figure 4.24 and Chapter 3 strongly suggest the theory is true; the question is the relevance of the experimental results to the theory. The interaction between the tip mass and the base via a nonlinear spring is the critical concern. The experiment is thought to be valid when this effect is not strong therefore when nonlinearity is low and, as has been observed, when damping is not too low. Additionally, it is expected that the larger the tip mass compared to the base mass the less valid the SDOF assumption becomes since the tip will provide greater feedback to the base.

Usefully, the experimental deviation from the theory illuminates a concern with the application of the theory to real systems. A base motion independent of the oscillator motion is assumed in the theory, but is not observed in the experiment. Since, in a real application, the base motion is affected by the oscillator, the Wiener theory for calculating power, whilst still true, is inapplicable. This effect will be strong when the nonlinearity is strong and when the mass of the base and oscillator are comparable. Conversely, when the oscillator mass is small compared to the base mass, the motion of the base will be independent of the oscillator to a good approximation and therefore the extended Wiener theory of Chapter 3 can be reasonably applied. In many energy harvesting applications the harvester will be an unobtrusive device with a small mass, maybe even MEMS scale, on a significantly larger application and therefore the Wiener approach for power dissipation will generally be valid.

In addition, the spectrum of Figure 4.3 is evidently shaped by the dynamics of the tip mass. In circumstances where the oscillating mass affects the base, it is therefore important to

use the spectrum of the base calculated from the entire system including the mass as the input to the extended Wiener series rather than the base spectrum when no oscillator is attached.

In summary, whilst the theory of Chapter 3 has been validated numerically and experimentally for small nonlinearity, care should be used when applying it to cases where the damping is low and nonlinearity is strong such that oscillating mass can affect the base motion.

4.5 Conclusions

The aim of this chapter has been to experimentally validate Eq. (3.42) which states that when using the extended Wiener series approach of Chapter 3 the integral over the frequency domain of the first extended Wiener kernel is proportional to the triple product $\mathrm{E}\left[\mathbf{f}^{\mathrm{T}}\mathbf{M}^{-1}\mathbf{f}\right]$. A simple experiment involving a base-excited cantilever beam with magnets generating a nonlinear restoring force on a tip mass was analysed and produced strong results with a mean error of 1.3% for all monostable configurations when compared to the values predicted by theory.

Additionally, the experimental results exhibit very similar behaviour to the numerical simulations of Chapter 3. As expected, the first kernel of the beam in a nonlinearly stiffening configuration displays an increased resonant frequency when excited more strongly due to oscillating in a stiffer displacement range. In a bistable configuration the frequency of the main peak of the kernel was seen to reduce as excitation increased and jumps between potential wells became more frequent. Furthermore, as nonlinearity increases, the damping of the kernel increases due to the power being distributed from the first to the increasingly influential higher order kernels.

Despite the consistency with Eq. (3.42) for most cases, the experiment did not exactly realise the simple SDOF oscillator desired and therefore deviated somewhat from the theory. Non-Gaussian base excitation was observed and, importantly, the continuous nature of the beam results in higher order resonances that contribute a small amount to the integral over the kernel. Furthermore, the divergence from a SDOF system means the assumption that $k_1(0) = 0.5$ could be inaccurate.

An interesting phenomenon involving non-causal kernels for certain configurations such as high nonlinearity and low damping exposed a subtle deficiency in the experimental approach. Despite a SDOF model seeming reasonable, in reality the system is more appropriately modelled as a forced base mass connected via a nonlinear spring to the tip mass. The result is that the tip vibration feeds back to the input base excitation meaning for a nonlinear system, the kernel calculated is not strictly an extended Wiener kernel. This effect

is small for the levels of nonlinearity displayed in the monostable configurations of Section 4.3 therefore the results are considered to be unaffected. Crucially, this also illuminates that the Wiener approach will not be applicable to real systems unless the nonlinear feedback from the oscillatory mass to the base is small. Additionally, the spectrum of the base motion for the entire system including the oscillating mass must be used as the input to the extended Wiener series.

Extensions to the experiment could be made to further validate the theory. Harsh nonlinearities such as impact could be analysed although the effects discussed in Section 4.4 would be stronger and modifications such as increased damping may be required. Additionally, a MDOF system could be investigated such that the addition of more than one mass from the triple product $\mathrm{E}\left[\mathbf{f}^{\mathrm{T}}\mathbf{M}^{-1}\mathbf{f}\right]$ could be validated by coupling two cantilevers together with a magnetic force. Alternatively the effect on the first kernel of constraining the system such that the triple product becomes less than the total mass could be investigated although a new experimental design would be required.

Improvements to the experiment would include using a SDOF system rather than a continuous beam and minimising feedback from the oscillating mass to the base motion. The former condition could be met using a single oscillating mass connected to a base via nonlinear springs where the nonlinearity could be provided either geometrically using light, linear springs or again using magnets. Feedback from the oscillating mass to the base could be mitigated by using a smaller mass on a more massive base and providing a mechanism for greater damping such as including sliding friction between the mass and its supporting structure.

Chapter 5

Response of a Nonlinear Oscillator to Combined Random and Deterministic Excitation

5.1 Introduction

The methods described in Chapters 2 and 3 are suitable for purely stochastic and stationary excitation. There exist relatively few methods to model the response of nonlinear systems to a combination of deterministic and stochastic vibration despite the likelihood of harmonic oscillations containing noise in realistic applications. This chapter explores the probabilistic response of nonlinear systems excited by this type of excitation and investigates the applicability of an efficient class of method, the global weighted residual method, by comparing its computational speed and accuracy to other common methods.

The Duffing oscillator is used to illustrate the probabilistic response to white and harmonic excitation via the joint probability density function of the displacement and velocity. Monte-Carlo simulations were performed to generate the JPDF which was observed to spread around the attractor that would be seen if only deterministic excitation was present. In strongly nonlinear cases such as where under only harmonic excitation either chaos or more than one periodic solution can be found, the addition of noise excitation produces geometrically complex JPDFs.

Since Monte-Carlo and other methods such as finite element [46] and path integral [94] methods are computationally expensive, generally prohibiting application where more than a few degrees of freedom are present, this chapter investigates the ability of the less computationally demanding global weighted residual methods to produce the geometrically

complex JPDF responses observed. A technique using a JPDF in the form of a Gram-Charlier type C series is extended from [63] and found to produce accurate results, although the method fails due to ill-conditioning as the shape of the JPDF required by the dynamics becomes too complex.

In energy harvesting amongst other applications the calculation of power dissipated under harmonic and random excitation is of interest. In this case, knowledge of the entire JPDF is not required and a simpler method than the global weighted residual ones may be sufficient. Due to its simplicity, reliability and speed, methods using the equivalent linearisation technique are applied and compared for both speed and accuracy.

In what follows, the response of the Duffing oscillator to this form of excitation is presented using Monte-Carlo simulations to generate the JPDF of the response in Section 5.2. Two weighted residual methods are then described and their accuracy and limitations are investigated by comparing them to results from Monte-Carlo and path integration methods in Section 5.3. Finally, Section 5.4 describes and compares a number of equivalent linearisation methods for calculating the power dissipated by a nonlinear system under this form of excitation.

Sections 5.2 and 5.3 and Appendix A contain a revised version of [35].

5.2 Monte-Carlo simulations

This section aims to illustrate the dynamics of an oscillator under combined deterministic and random excitation by investigating the Duffing oscillator's response to sinusoidal and white noise excitation using Monte-Carlo simulations. Similar results have previously been shown using a variety of methods in [1, 6, 44, 64, 66, 93, 94] and agree with those presented here.

The equation describing a Duffing oscillator under harmonic and white noise forcing is

$$\ddot{x} + c\dot{x} + kx + \varepsilon x^3 = F\cos(\omega t) + \xi(t) \tag{5.1}$$

where as in previous chapters, $\xi(t)$ is a white noise process with autocorrelation function $\pi S_0 \delta(\tau)$.

The Monte-Carlo method is a simple but computationally expensive technique for generating the JPDF of the response. The oscillator of Eq. (5.1) is excited by a large number of realisations of the random forcing. The ensemble of responses is found using the ode45 time integration function in MATLAB and then the likelihood of the response displaying a given

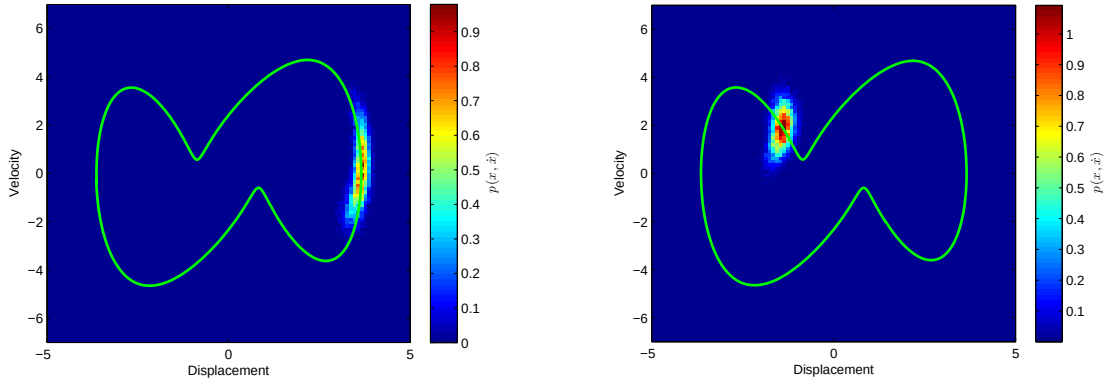

(a) (b)

Fig. 5.1 JPDFs from Monte-Carlo simulations of response to combined harmonic and random excitation at a) $t = 28.4$ and b) $t = 32.4$ when $c = 0.7$, $k = 0.5$, $\varepsilon = 0.5$, $F = 10$, $\omega = 1$ and $S_0 = 0.05$. The response over one cycle for purely harmonic forcing is superimposed.

displacement and velocity at a given time can be found from the proportion of realisations that display this displacement and velocity at each time step.

Figure 5.1 shows the Monte-Carlo JPDF in the phase plane for the Duffing oscillator of Eq. (5.1) at two times when $c = 0.7$, $k = 0.5$, $\varepsilon = 0.5$, $F = 10$, $\omega = 1$ and $S_0 = 0.05$ and an ensemble of 10000 realisations. The Monte-Carlo simulations presented in this paper have initial conditions $x(0) = \dot{x}(0) = 0$. However, the figures display the responses when the system is at steady-state at times that illustrate the characteristic dynamics. It can be seen that the response follows the deterministic trajectory superimposed onto the figure and the noise perturbs the response about the deterministic case.

The ensemble average of the response of the noisily forced oscillator, found from the steady-state JPDF over one cycle of the harmonic component of the forcing, is compared with the mean trajectory when only harmonic forcing is applied in Figure 5.2. The mean response is affected by the presence of the white noise, but still displays approximately the same path.

When subjected to harmonic excitation, nonlinear oscillators can produce complex responses such as exhibiting more than one steady-state response and chaotic solutions. It is interesting to investigate the response of such systems when noise is added to the excitation. A simple example of the former case is when a Duffing oscillator is excited harmonically such that it exhibits either a high or low magnitude orbit depending on the initial conditions. The JPDF of this case is displayed in Figure 5.3 at two times when $c = 0.5$, $k = 0.5$, $\varepsilon = 0.5$, $F = 10$, $\omega = 3.05$ and $S_0 = 0.8$ and 20000 realisations. Similar to the simple case of Figure

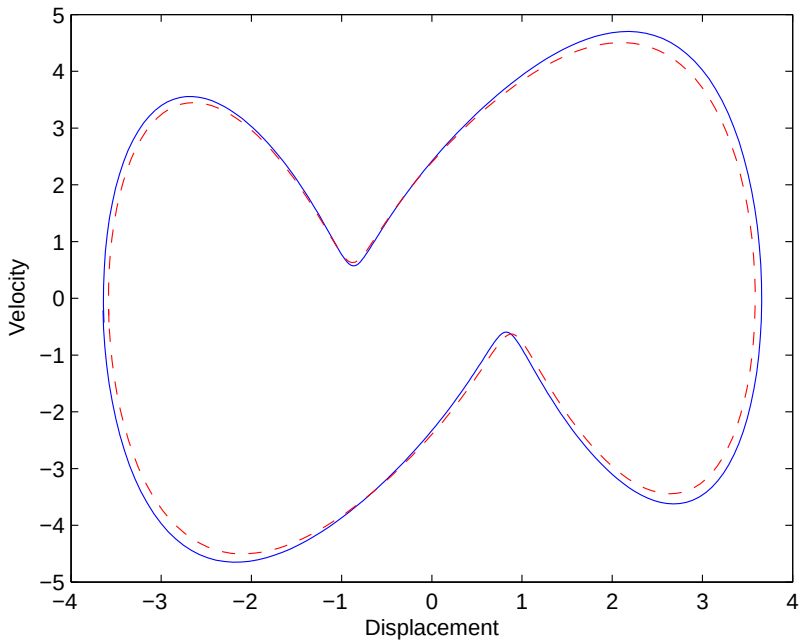

Fig. 5.2 Mean response of harmonically excited oscillator with (red dashed) and without (blue solid) noise.

5.1, the response spreads around one or other of the deterministic orbits and the noise can make the response jump from oscillations about one orbit to oscillations about the other.

When a nonlinear oscillator is harmonically excited, within some parameter ranges, a chaotic response can be observed that is both non-periodic and sensitive to its initial conditions. Chaotic systems contain an underlying fractal structure that can be uncovered by sampling the response at the frequency of the harmonic forcing in the phase plane to find a 'Strange Attractor'. In the periodic solutions above with noise and harmonic excitation, the JPDF spreads out around the periodic trajectory that would be observed if only harmonic excitation were applied. However, in the deterministic chaotic case there is no periodic trajectory for the response to spread around and the trajectory is extremely sensitive to small perturbations from noise. As can be seen from Monte-Carlo simulations of a chaotic system in Figure 5.4, when noise is added to the harmonic excitation the JPDF remains close to fractal, similar to a strange attractor, but it has diffused slightly due to the noise. With noise added to the harmonic excitation, the chaotic case is therefore similar to the periodic cases above in that the noise spreads the JPDF around the deterministic attractor although in the chaotic case, the individual realisations can differ dramatically.

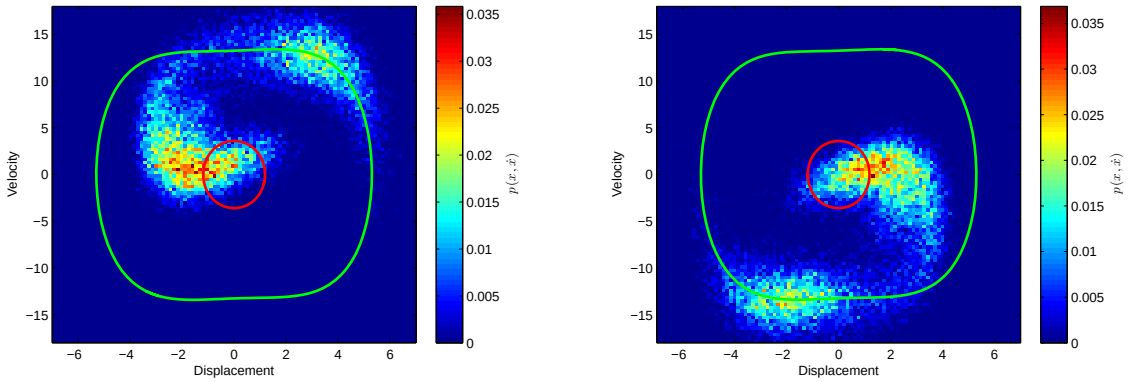

(a) (b)

Fig. 5.3 JPDF from Monte-Carlo simulations of Duffing oscillator excited in a configuration where, under harmonic excitation, two responses (solid lines) exist. $c = 0.5$, $k = 0.5$, $\varepsilon = 0.5$, $F = 10$, $\omega = 3.05$ and $S_0 = 0.8$, a) $t = 34$ and b) $t = 37$.

In [64] diffuse chaotic attractors from noisy and harmonic excitation have been simulated using the path integration method and the possibility of using a no-noise limiting case of stochastic methods to model deterministic chaos has also been discussed. The matrix continued fractions method has been applied in [44] to calculate a time-invariant PDF of a noisy chaotic response averaged over one forcing period assuming the PDF's response is periodic. The necessary periodicity of the response has been discussed and the effect of increasing noise is shown to generate a more diffuse attractor. The periodicity is illustrated here in Figure 5.5 by observing the mean square velocity of the Monte-Carlo results over time. The periodic nature at steady-state suggests that the JPDF's moments are periodic so it may be possible to obtain useful information about the chaotic response despite not being able to mathematically describe the complex shape of the JPDF.

5.3 Global weighted residual methods

In the light of the complexity of a noisy chaotic attractor and the computational expense of Monte-Carlo and path integration methods, it is interesting to investigate how the global minimisation properties of the weighted residual methods attempt to generate complex instantaneous attractor geometries. In this section two weighted residual methods are taken from the literature and extended to model the response to harmonic and white noise excitation then compared to Monte-Carlo and path integration results.

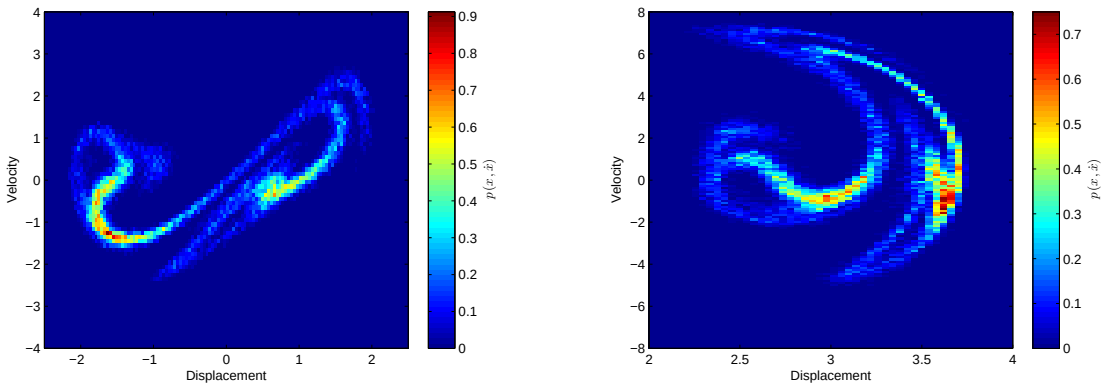

(a) (b)

Fig. 5.4 JPDFs at time a) $t = 141.1$ and b) $t = 142.8$ from Monte-Carlo simulations of a bi-stable Duffing oscillator with a noisy chaotic response. $c = 0.1$, $k = -0.5$, $\varepsilon = 1$, $F = 10$, $\omega = 1$ and $S_0 = 1 \times 10^{-3}$ and 20000 realisations.

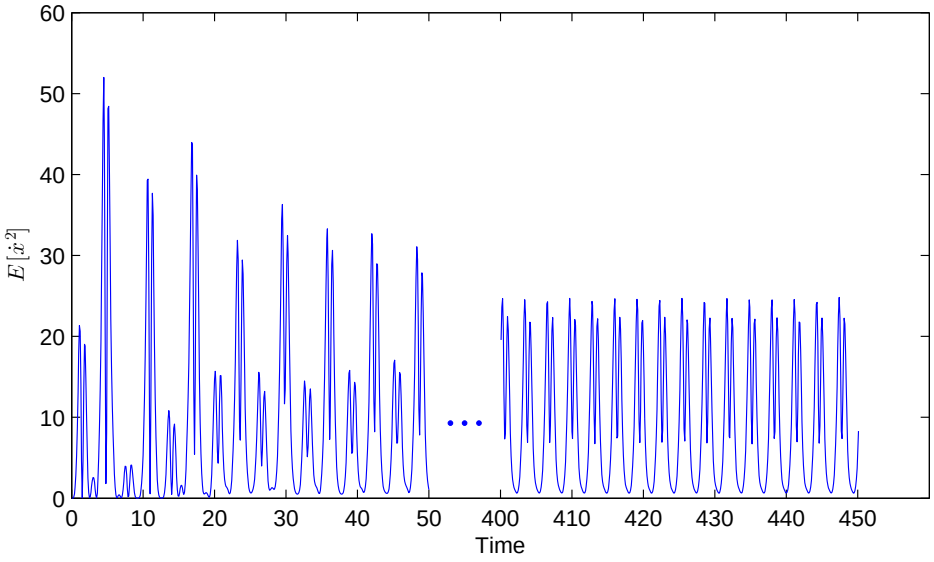

Fig. 5.5 Time history of mean squared velocity of chaotic response.

5.3.1 Theory

In a weighted residual method, the form of the proposed PDF is important as it dictates the range of possible shapes the PDF can display. Two different proposed PDFs, p_A and p_C, are compared in this section: the Gram-Charlier type A series, Eq. (5.2), and Gram-Charlier type C series, Eq. (5.3), and the relevant solution methods taken from [89] and [63] are used. These two methods were chosen because they can be solved similarly, are simple and elegant due to the use of Hermite polynomial orthogonality and should be representative of the majority of weighted residual methods.

$$p_A(z,\dot{z},t) = C\exp\left(-\frac{z^2}{2}-\frac{\dot{z}^2}{2}\right)\sum_{m=0}^{\infty}\sum_{n=0}^{\infty}a_{mn}(t)H_m(z)H_n(\dot{z}) \tag{5.2}$$

$$p_C(z,\dot{z},t) = C\exp\left[\sum_{m=0}^{\infty}\sum_{n=0}^{\infty}a_{mn}(t)H_m(z)H_n(\dot{z})\right] \tag{5.3}$$

In Eqs. (5.2) and (5.3), C is a normalisation constant such that $\int_{-\infty}^{\infty}\int_{-\infty}^{\infty} p\,dxd\dot{x} = 1$ and a_{mn} are time varying coefficients to be found. $H_n(z)$ is a nth order Hermite polynomial defined as

$$H_n(z) = (-1)^n e^{\frac{z^2}{2}}\frac{\mathrm{d}^n}{\mathrm{d}z^n}e^{-\frac{z^2}{2}} \tag{5.4}$$

and

$$z(t) = (x - x_m(t))/\sigma_x(t) \tag{5.5}$$

$$\dot{z}(t) = (\dot{x} - \dot{x}_m(t))/\sigma_{\dot{x}}(t) \tag{5.6}$$

where $x_m(t)$, $\dot{x}_m(t)$ and $\sigma_x(t)$, $\sigma_{\dot{x}}(t)$ are estimates of the mean and standard deviation of the displacement and velocity respectively found from an equivalent linearisation method for non-stationary excitation taken from [74] and described in more detail in Section 5.4.1. The transformation from x to z is used to ensure that the JPDF is defined around the deterministic response as suggested from the results of the Monte-Carlo simulations section and is scaled to an appropriate magnitude according to the noise present. This transformation is not appropriate for the chaotic case since it does not spread around the deterministic trajectory.

A proposed PDF is substituted into the Fokker-Planck equation

$$\mathscr{L}(p) = \frac{\partial p}{\partial t} + \dot{x}\frac{\partial p}{\partial x} - \frac{\partial p g(\dot{x},x,t)}{\partial \dot{x}} - \pi S_0\frac{\partial^2 p}{\partial \dot{x}^2} = 0 \tag{5.7}$$

where $g(x,\dot{x},t) = c\dot{x} + kx + \varepsilon x^3 - F\cos(\omega t)$. The Duffing nonlinearity is taken here as an example, but any integer power nonlinearity could be used.

The proposed PDFs from Eqs. (5.2) and (5.3) can be substituted into Eq. (5.7) using the known properties of the Hermite polynomials

$$\frac{dH_n(x)}{dx} = nH_{n-1}(x) \tag{5.8}$$

$$xH_n(x) = H_{n+1}(x) + nH_{n-1}(x). \tag{5.9}$$

However, regardless of the values of the a_{mn} coefficients the substitution will not be equal to zero in the nonlinear case with a finite Gram-Charlier series thus a residual error, Δ, remains such that $\Delta_A = \mathscr{L}(p_A)$ and $\Delta_C = \mathscr{L}(p_C)$. This residual can be multiplied by appropriate weighting functions and minimised by integrating over state space. The weighted integrals for the Gram-Charlier type A and C series are

$$\int_{-\infty}^{\infty}\int_{-\infty}^{\infty} H_r(z)H_s(\dot{z})\Delta_A \mathrm{d}\dot{z}\mathrm{d}z = 0 \tag{5.10}$$

$$\int_{-\infty}^{\infty}\int_{-\infty}^{\infty} H_r(z)H_s(\dot{z})e^{-\frac{z^2}{2}-\frac{\dot{z}^2}{2}}\frac{1}{p_C}\Delta_C \mathrm{d}\dot{z}\mathrm{d}z = 0. \tag{5.11}$$

The orthogonality properties of Hermite polynomials

$$\int_{-\infty}^{\infty} H_r(z)H_n(z)e^{-\frac{z^2}{2}}\mathrm{d}z = \sqrt{2\pi}n!\delta_{rn} \tag{5.12}$$

$$\int_{-\infty}^{\infty} H_r(z)H_m(z)H_n(z)e^{-\frac{z^2}{2}}\mathrm{d}z = \begin{cases} \frac{\sqrt{2\pi}r!m!n!}{(s-r)!(s-m)!(s-n)!} & r+m+n \text{ even} \\ 0 & r+m+n \text{ odd} \end{cases}, \tag{5.13}$$

where δ_{rn} is the Kronecker delta function and $2s = r+m+n$, have been exploited to greatly reduce the number of terms in the resulting equations.

It is clear that for computation of this method, the infinite Gram-Charlier series must be truncated in some way. A truncation method known to produce good results from [63] is adopted and involves removing terms above a chosen order, N, such that $m+n \leq N$. In the weighted integrals of Eqs. (5.10) and (5.11), r and s therefore vary from $0 \rightarrow N-s$ and $0 \rightarrow N-r$ respectively to produce a number of coupled differential equations of the form

$$\frac{\mathrm{d}a_{rs}}{\mathrm{d}t} = f_{rs}(a_{00}, a_{10}, a_{01}, a_{11}...) \tag{5.14}$$

that can be solved using a numerical ODE solver such as ode45 in MATLAB to yield the required a_{mn} coefficients.

5.3.2 Results

The results found from the weighted residual methods (abbreviated to WR-A and WR-C for type A and C respectively) will now be compared in terms of accuracy and speed to results from Monte-Carlo simulations (MC) and the path integration method (PI) of [94] that is described in Appendix A. Despite the noisy JPDFs, the MC simulations will be taken as the benchmark, since the method most realistically models the dynamics provided a large enough ensemble is taken.

A qualitative comparison of the results is shown for a strongly nonlinear, highly damped oscillator in Figure 5.6 where the JPDFs at two times are shown using each of the methods and Figure 5.7 provides a more quantitative comparison by comparing only the displacement PDFs. The WR-A method shows poor similarity to the MC simulations and regions of negative probability in Figure 5.7a whereas it provides a reasonable approximation in Figure 5.7b. The PI method does not appear to produce the complexity of the MC JPDF and its mean value is incorrect in Figure 5.7b.

The WR-C results provide a good approximation of the Monte-Carlo simulations, although the tail probability in Figure 5.7b is less accurate. This is due to the form of the Gram-Charlier type C series meaning that when the JPDF is constructed, it can produce regions of exponentially growing probability away from the mean response. To ensure these high probabilities do not affect the JPDF in the region of interest, only the probabilities in the vicinity of the mean are taken. This also increases the speed of the construction of the JPDF since calculations are only performed in regions of significant probability. The effect of this truncation is observed in Figure 5.7b where the displacement PDF does not drop smoothly to zero, but has been truncated abruptly. It appears the method is providing a good approximation to the true response in the vicinity of the mean motion, but worse results elsewhere. This is discussed further in the limitations section below.

In order to compare the statistical moments retrieved from each method, the variation of the mean square velocity has been plotted against time in Figure 5.8. The equivalent linearisation [74] and WR-C method show almost identical results and both closely resemble the MC solution. Negative mean square velocity values are displayed for the WR-A solution suggesting there are times when the JPDF is largely negative and therefore extremely inaccurate. The JPDF using the PI method is only solved for every quarter cycle, and generates results slightly worse than equivalent linearisation and WR-C.

For the solutions above, an ensemble of 10000 realisations was used and the weighted residual solutions were truncated at $N = 5$ and $N = 3$ for the type A and C respectively. For the type A solution, the value was selected since a smaller value shows little divergence from the Gaussian JPDFs of equivalent linearisation results whereas a larger value produces highly

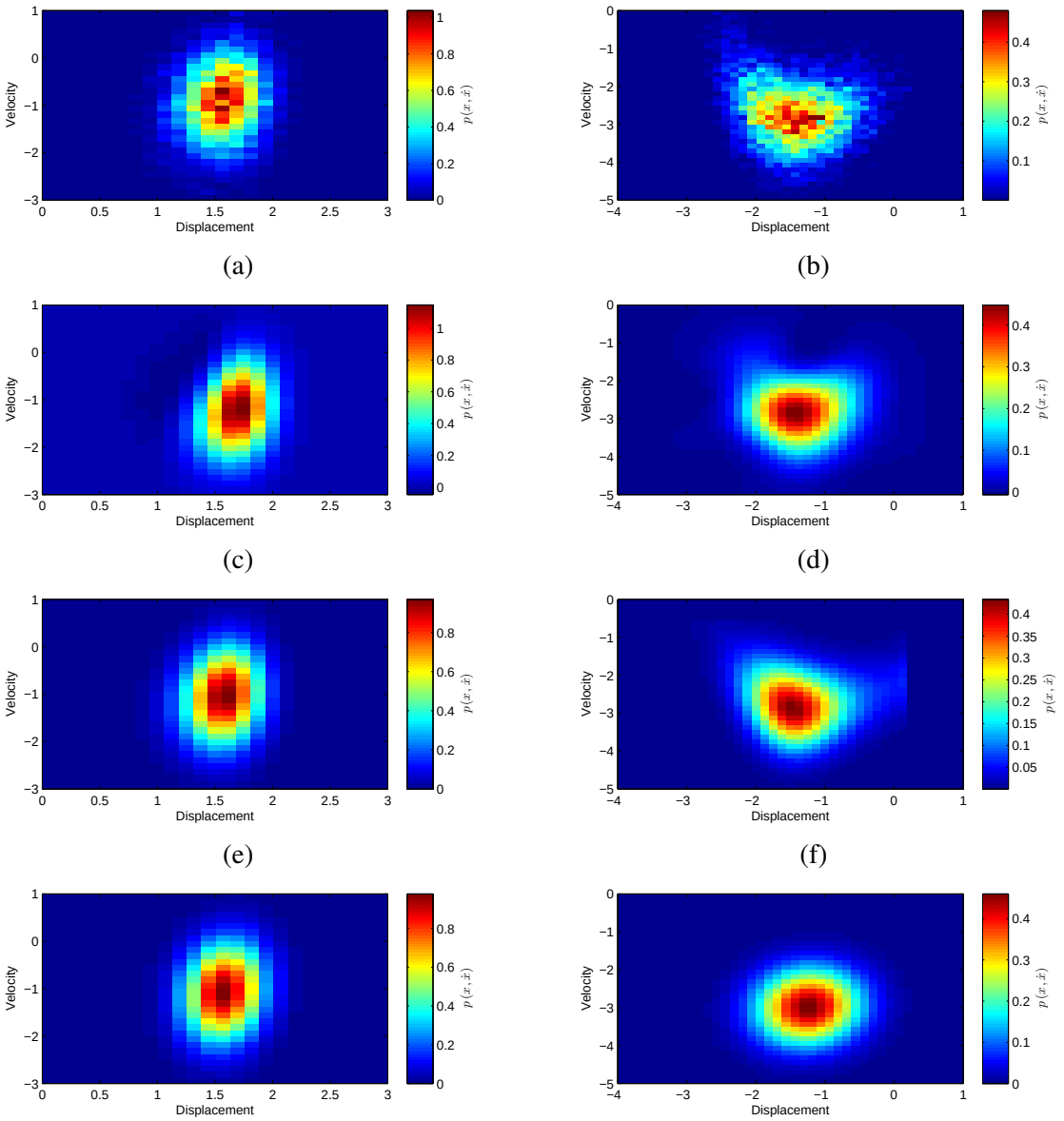

Fig. 5.6 JPDFs from MC a) and b), WR-A c) and d), WR-C e) and f) and PI g) and h) at times $t = 17.3$ a), c), e) and g) and $t = 18.8$ b), d), f) and h). $c = 3.0$, $k = -0.5$, $\varepsilon = 1$, $F = 10$, $\omega = 1$ and $S_0 = 0.5$.

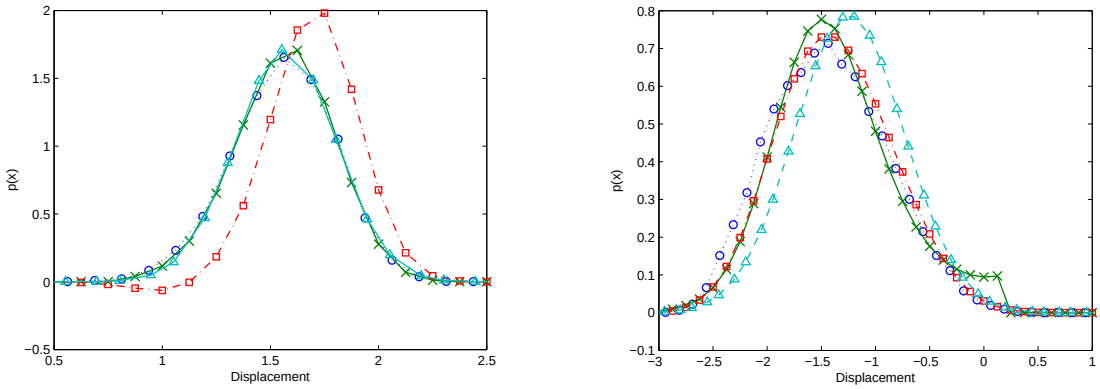

(a) (b)

Fig. 5.7 Probability density functions of displacement from MC (dark blue dotted line with circles), WR-A (red dash-dot line with squares), WR-C (green solid line with crosses) and PI (light blue dashed line with triangles) methods at times a) $t = 17.3$ and b) $t = 18.8$.

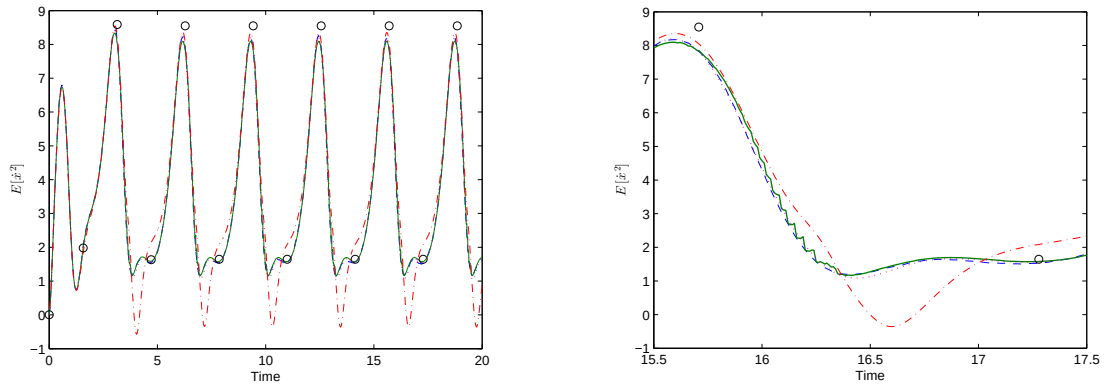

(a) (b)

Fig. 5.8 Mean square velocity against time from MC (blue dashed), WR-A (red dash dot), WR-C (green solid), PI (black circles) and equivalent linearisation (purple dotted). b) Shows an enlarged view of the time history in a).

inaccurate and negative JPDFs. For the type C solution, the value was chosen high enough to allow for a complex JPDF shape, but low enough to avoid ill-conditioning as discussed in the limitations section below.

For the case shown in Figures 5.6 to 5.8 the times taken to compute the response are displayed in Table 5.1, where the equations were solved from $t = 0$ to $t = 20$ with a time step, dt, of d$t = 0.01$ for the MC and weighted residual methods, and a time step of a quarter of the period of the harmonic excitation frequency, d$t = 1.6$, for the PI method. An 80×80 grid in the phase-plane has been used for each method.

Method	**Computation Time (s)**
Monte-Carlo	1.4×10^4
Weighted Residual type A	6.8
Weighted Residual type C	4.5
Path Integration	64
Equivalent linearisation	0.78

Table 5.1 Computation time for solution methods.

It is clear that the MC method is the slowest, although it strongly depends on the accuracy of the response desired and therefore the ensemble size used. The weighted residual methods solve rapidly and the accuracy of the JPDF from the type C solutions suggests it is an appropriate method to use for investigating this form of excitation if a fast method is required. However, depending on the desired information, the equivalent linearisation method may be sufficient.

The path integration method is known to be robust and able to produce complex JPDF shapes. In this case however, the results have shown worse accuracy than the WR-C solutions and taken longer to perform. Additionally, the solution is only found at each quarter cycle and using shorter time steps would require significantly more computational effort. It should be noted that only a simple PI method has been investigated and modifications such as those in [66] may improve the method significantly.

5.3.3 Limitations of the weighted residual type C method

The weighted residual type C method produces good results for the parameters chosen above, but has obvious limitations due to the possible shapes made available by the truncated Gram-Charlier type C series (e.g. the JPDF will never be fractal like the chaotic case). Additionally,

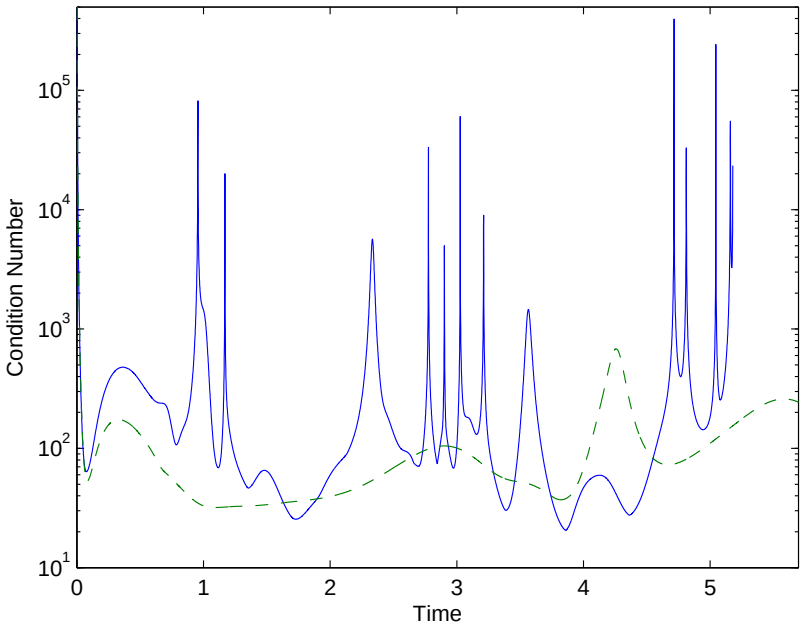

Fig. 5.9 Condition number against time with $c = 1$ (blued solid) and $c = 4$ (green dashed) and $k = -0.5$, $\varepsilon = 1$, $F = 10$, $\omega = 1$ and $S_0 = 0.5$.

it has been observed that when the parameters require a JPDF too complex for the shapes allowed by Eq. (5.3), the ODEs of Eq. (5.14) become unstable and fail to solve.

The coupled equations of Eq. (5.14) have been investigated to assess the cause of the instability. The dependence of the right hand side of each individual equation on each a_{mn} coefficient is found by differentiating every equation by every coefficient. A matrix, K_{ij}, is therefore formed where $K_{ij} = \partial f_i / \partial a_j$ if f_{rs} and a_{mn} are written as vectors f_i and a_j. The condition number of this matrix gives an indication of the conditioning of the equations and has been plotted against time in Figure 5.9 for a high damping case that provides a stable solution and a lower damping case that goes unstable at $t = 5.2$. The sharp peak in condition number at this point, along with the preceding peaks show that the equations are ill-conditioned therefore numerical errors grow with time leading to instability.

Observing the JPDF at the point of instability illuminates more physically what occurs in the unstable equations. The JPDF is projected by the Gaussian distribution in the weighting function of Eq. (5.11) into a region around the mean response. The weighted residual solutions will therefore model the response well in this region, but at the expense of accuracy further from the mean. This often results in areas of large probability far from the mean that are removed by truncating the JPDF as described in the Section 5.3.2. When the

dynamics requires a complex JPDF shape, in order to approximate it near the mean, the global minimisation of the weighted residuals allow the response just away from the mean to be less accurate. The equations have been seen to become unstable when the true JPDF becomes a complex shape and cannot be satisfactorily modelled by the truncated Gram-Charlier type C series. At this time, anomalous external regions of high probability are seen to move towards and merge with the JPDF around the mean.

A number of parameters affect the stability of the solution. In particular, the order of the truncated Gram-Charlier series affects the number of coupled equations and the number of terms in each equation. It is found that truncation at a lower value generates stable solutions that are less accurate whereas truncation at higher values produces ill-conditioned equations that show greater accuracy due to a greater range of JPDF shapes allowable. This effect is shown in Figure 5.10 where an error, e, is calculated from the difference between the mean square velocity of the MC and WR-C results such that

$$e = \frac{1}{T\sigma_{\dot{x}}^4}\int_0^T (\mathrm{E}[\dot{x}_{MC}^2] - \mathrm{E}[\dot{x}_{WR}^2])^2 \mathrm{d}t \tag{5.15}$$

where

$$\sigma_{\dot{x}}^2 = \frac{1}{T}\int_0^T \mathrm{E}[\dot{x}_{MC}^2]\mathrm{d}t \tag{5.16}$$

and T is the time period of the harmonic excitation. As nonlinearity increases, the JPDF increases in complexity so the equations fail to solve. The value of nonlinearity at which the equations fail to solve is lower the higher the order of truncation of the series due to higher order solutions having worse conditioning. As nonlinearity increases, the higher order solutions are slightly more accurate by this error measure, but may be significantly more accurate if an error measure involving the entire JPDF was used.

Improvements to this method could potentially be made by using a more suitable proposed JPDF and weighting function. Similar to [17] an adaptation could be made whereby the weighting functions depend on the JPDF calculated at the previous time-step. Most modifications would likely produce a significantly more computationally intensive solution since orthogonal functions may not exist or would take longer to compute or functions would have to be calculated at each time-step and numerical integration may be necessary for the weighted integrals. Additionally, it is difficult to envisage the form of a proposed JPDF that would give enough flexibility for more complex JPDF shapes.

In summary, the WR-C method produces good results if the JPDF varies only slightly from Gaussian. This occurs when nonlinearity is small, damping is large or the noise is small relative to the harmonic excitation such that the JPDF spreads out in an approximately linear region. The more complex JPDF shapes from certain parameter regions of the Duffing

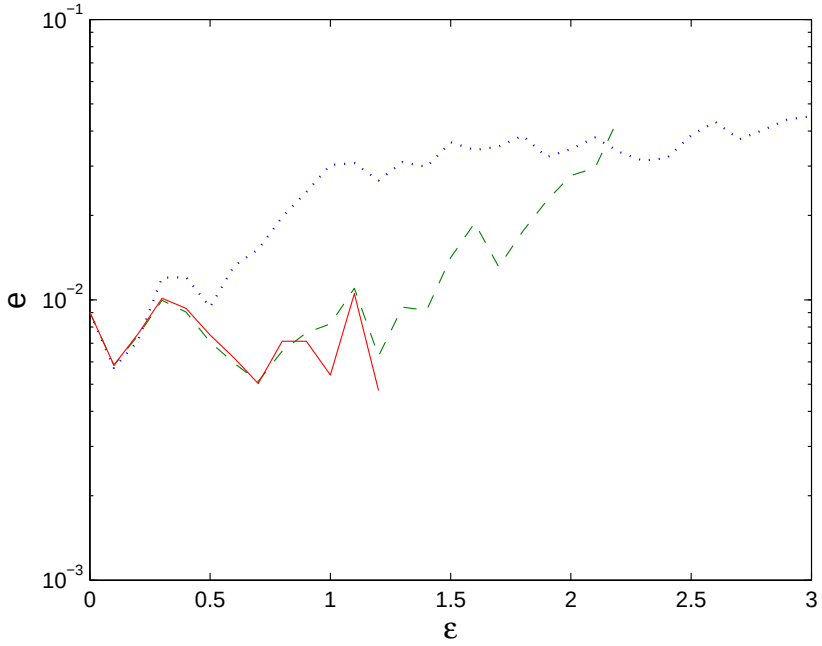

Fig. 5.10 Error, e, against nonlinearity, ε for varying truncation values: $N = 3$ (blue dotted), $N = 4$ (green dashed) and $N = 5$ (red solid) when $c = 0.5$, $k = 5$, $F = 10$, $\omega = 1$ and $S_0 = 0.5$. Where no error point is plotted, the solution has failed to solve.

oscillator such as the solution with a double response, Figure 5.3, or chaotic solution, Figure 5.4, will most likely require computation using a different method.

5.4 Equivalent Linearisation Methods for Calculating Power Dissipation

In energy harvesting and other applications the calculation of power from harmonic and random excitation will be of interest. Methods such as those in the previous section that involve calculation of the entire JPDF are useful, but excessive when only the power dissipated is of interest. Alternatively, equivalent linearisation [8] methods are appealing since they account well for nonlinearity whilst providing rapid solutions. In what follows, three methods involving equivalent linearisation are described and compared both to each other and to benchmark numerical time domain simulations over an ensemble of random excitation. In all following cases an oscillator of the form of Eq. (5.1) is used with $c = 0.5$, $k = 0.5$, $\varepsilon = 2$ and $F = 3$ and the power is investigated over a range of harmonic excitation frequencies around the resonant frequency of the oscillator and over a range of noise excitation magnitude.

The results from numerical time integration of the equations of motion are shown in Figure 5.11 over the range $0 < S_0 < 3$ and $0 < \omega < 4$. The power dissipated is seen to increase with noise and around the resonant frequency of the oscillator. However, with higher noise, the resonant frequency increases since the noise forces the oscillator further into higher displacement, stiffer, nonlinear region thus increasing the frequency of the response. Additionally, as the noise increases the resonant frequency becomes less pronounced probably because the harmonic excitation becomes less significant when compared to the noise.

5.4.1 Coupled ODEs

A simple equivalent linearisation method that splits the response into mean and noise terms then generates coupled ODEs that are solved numerically is described in [74]. This method is outlined briefly below for a Duffing oscillator and is the method used in Section 5.3 to provide an estimate of the mean and standard deviation of the response in Eqs. (5.5) and (5.6).

The response of an oscillator subject to harmonic and random excitation can be split into two parts; a zero mean noise term, x_0, and the mean variation, m_x. These can be substituted into the equation of motion Eq. (5.1) to yield

$$\ddot{x}_0 + \ddot{m}_x + c(\dot{x}_0 + \dot{m}_x) + k(x_0 + m_x) + \varepsilon(x_0 + m_x)^3 = F\cos(\omega t) + \xi(t). \tag{5.17}$$

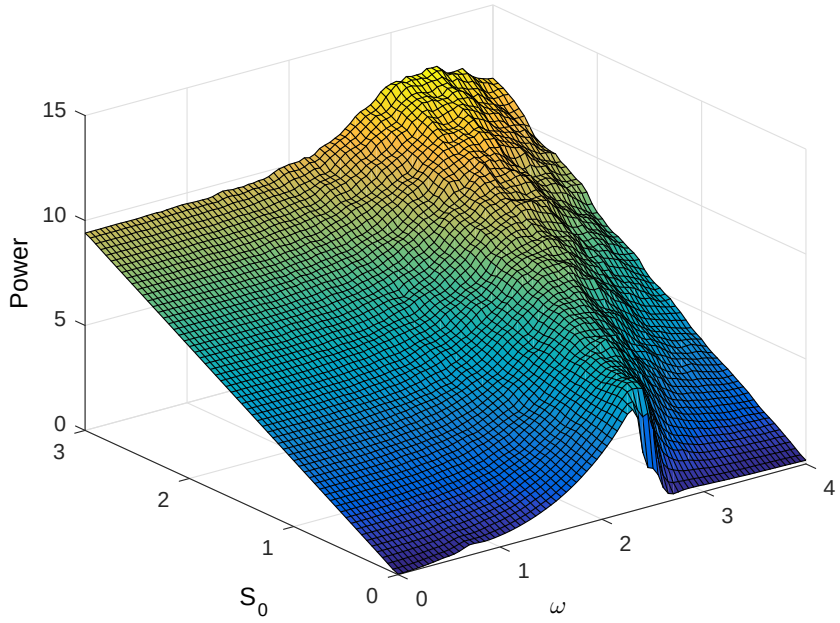

Fig. 5.11 Power dissipated by a nonlinear oscillator subjected to harmonic and white noise excitation calculated by numerical time integration.

The ensemble average of Eq. (5.17) is taken

$$\ddot{m}_x + c\dot{m}_x + km_x + \mathrm{E}\left[\varepsilon(x_0+m_x)^3\right] = F\cos(\omega t) \tag{5.18}$$

and subtracted from Eq. (5.17) yielding

$$\ddot{x}_0 + c\dot{x}_0 + kx_0 + \varepsilon(x_0+m_x)^3 - \mathrm{E}\left[\varepsilon(x_0+m_x)^3\right] = \xi(t). \tag{5.19}$$

From Eq. (5.19) the standard equivalent linearisation technique can be employed to find the equivalent linear stiffness, k_{Eq}, as

$$k_{Eq} = \mathrm{E}\left[\frac{\partial}{\partial x_0}\left[kx_0 + \varepsilon(x_0+m_x)^3 - \mathrm{E}\left[\varepsilon(x_0+m_x)^3\right]\right]\right] \tag{5.20}$$

$$= k + 3\varepsilon\mathrm{E}\left[x_0^2\right] + 3\varepsilon m_x^2. \tag{5.21}$$

Taking now the linear oscillator with equivalent linear stiffness, k_{Eq} and subjecting it to only the white noise excitation, it is known that the solution must satisfy the Lyapunov

equation

$$\dot{\mathbf{V}} = \mathbf{G}\mathbf{V}^{\mathrm{T}} + \mathbf{V}\mathbf{G}^{\mathrm{T}} + 2\pi S_0 \begin{pmatrix} 0 & 0 \\ 0 & 1 \end{pmatrix} \tag{5.22}$$

where

$$\mathbf{V}(t) = \mathrm{E}\left[\mathbf{z}\mathbf{z}^{T}\right] \tag{5.23}$$

$$\mathbf{z} = (x_0 \;\; \dot{x}_0)^{\mathrm{T}} \tag{5.24}$$

$$\mathbf{G} = \begin{pmatrix} 0 & 1 \\ -k_{Eq} & -c \end{pmatrix} \tag{5.25}$$

and can be found from the state-space representation of the equations of motion.

Eqs. (5.18) and (5.21)-(5.25) can be combined to generate the following five coupled ODEs for the mean and noise terms

$$\dot{X}_1 = X_2 \tag{5.26}$$

$$\dot{X}_2 = -cX_2 - k_{Eq}X_1 + F\cos(\omega t) \tag{5.27}$$

$$\dot{X}_3 = 2X_4 \tag{5.28}$$

$$\dot{X}_4 = X_5 - cX_4 - k_{Eq}X_3 \tag{5.29}$$

$$\dot{X}_5 = -2k_{Eq}X_4 - 2cX_5 + 2\pi S_0 \tag{5.30}$$

where $X_1 = m_x$, $X_2 = \dot{m}_x$, $X_3 = \mathrm{E}\left[x_0^2\right]$, $X_4 = \mathrm{E}\left[x_0\dot{x}_0\right] = \mathrm{E}\left[\dot{x}_0 x_0\right]$ and $X_5 = \mathrm{E}\left[\dot{x}_0^2\right]$. These five equations can then be solved by numerical time integration to find the mean motion and the statistical properties. The method can be extended to multiple degrees of freedom, but is only shown here for the single-degree-of-freedom Duffing equation. Inspection of Eq. (5.21) shows that the equivalent linear stiffness is increased by both mean and noise terms as required for a stiffening nonlinearity.

Figure 5.12 displays the power harvested as noise and excitation frequency vary for the equivalent linearisation method and compares them to the benchmark numerical time-integration results. Reasonable similarity is seen, but resonance effects are magnified with equivalent linearisation whereas the resonance peak of the simulated system is smoother with larger random excitation. These differences are most likely due to the equivalent linearisation approach being unable to find a sensible linear response when the system is oscillating with two orbits as in Figure 5.3.

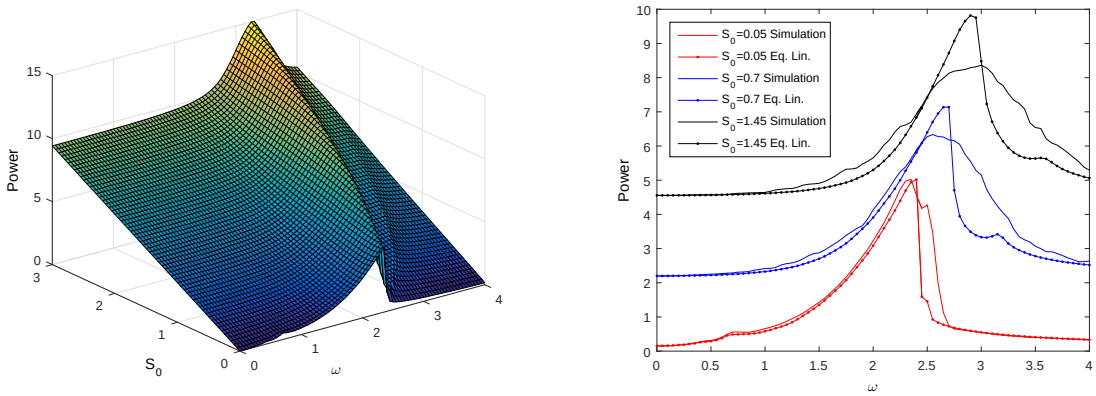

(a) (b)

Fig. 5.12 a) Power dissipated calculated with the equivalent linearisation technique of Eqs. (5.26)-(5.30) and b) comparison of equivalent linearisation to numerical time-integration simulations.

5.4.2 White Noise with Describing Function

Whilst compared to time-integrating the equations of motion this method is quick to solve, alterations to the method have been attempted to provide an approximate analytical solution. A simple approach is to use the equivalent stiffness of Eq. (5.21), but replace the time varying mean term, m_x, with an estimate of the mean motion provided by the describing function [92] for a harmonically forced oscillator. If the oscillator is found in a region with more than one deterministic response as in Figure 5.3, the mean response is estimated by taking the upper, middle (unstable) and lower orbit magnitudes, X_U, X_M and X_L respectively and finding the estimated response magnitude, X, such that

$$X = X_L + X_U - X_M \tag{5.31}$$

An estimate of the equivalent linear stiffness can made using the mean square displacement from the noise and harmonic terms giving

$$k_{Eq} = k + 3\varepsilon \mathrm{E}\left[x^2\right] + 3\varepsilon X^2/2 \tag{5.32}$$

where the mean square velocity from the noise can be calculated using the known [68] relationship

$$\mathrm{E}\left[x^2\right] = \frac{\pi S_0}{c k_{Eq}}. \tag{5.33}$$

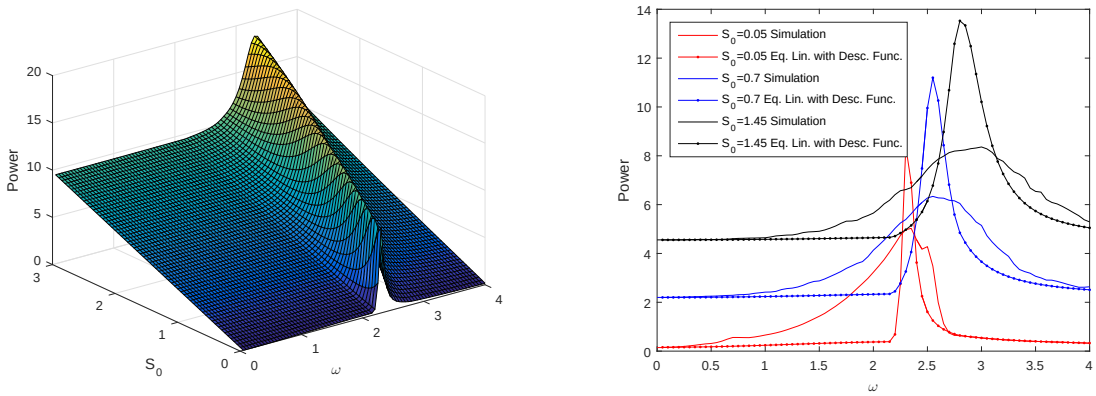

(a) (b)

Fig. 5.13 a) Power dissipated calculated with the equivalent linearisation combined with describing function technique and b) comparison of equivalent linearisation and describing function to numerical time-integration simulations.

The power dissipated by the linear system using k_{Eq} can then be calculated by summing the power from the white noise, $\pi S_0/2$, and the power from the harmonic excitation

$$P_{Harm} = \frac{cF^2\omega^2}{(k_{Eq} - \omega^2)^2 + (c\omega)^2}. \tag{5.34}$$

Figure 5.13 shows the power from this method is plotted as the frequency and noise magnitude are varied. It is clear that this method does not handle the response around resonance well. Whilst it calculates the resonant frequency correctly, the method generates a peak that is too sharp and too high when compared to the numerical simulations. The poor quality fit when there is low noise suggests that errors arise when the approximate displacement magnitude of the describing function is used in the equivalent linearisation procedure in Eq. (5.32).

5.4.3 White with Narrowband Noise

An improvement on the describing function approach is to approximate the harmonic excitation as narrowband noise meaning that the equivalent linear stiffness can be calculated from the mean squared displacement from the noise which is the area under the response spectrum. Supposing the noise spectrum, $S_{FF}(\omega')$, at frequency ω' is comprised of white noise and a delta function to represent the harmonic excitation such that

$$S_{FF}(\omega') = S_0 + \frac{F^2}{2}\delta(\omega' - \omega) \tag{5.35}$$

where the magnitude of the delta function is chosen to provide the same mean square displacement as the harmonic excitation.

The mean squared displacement of the response, $\mathrm{E}\left[x^2\right]$, is the integral over the magnitude of the oscillator frequency response squared multiplied by the excitation

$$\mathrm{E}\left[x^2\right] = \int_0^\infty \frac{1}{(\omega'^2 - k_{Eq})^2 + (c\omega')^2} \times \left(S_0 + \frac{F^2}{2}\delta(\omega' - \omega)\right) d\omega' \tag{5.36}$$

$$= \frac{\pi S_0}{c k_{Eq}} + \frac{F^2}{2}\frac{1}{(\omega^2 - k_{Eq})^2 + (c\omega)^2} \tag{5.37}$$

using Eq. (5.33). Eq. (5.37) and the standard linearisation result, $k_{Eq} = k + 3\varepsilon\mathrm{E}\left[x^2\right]$, from [74] can be combined to generate a fourth order polynomial for k_{Eq} that can be solved to yield the equivalent linear stiffness and hence the power can be found by addition of the power from the noise and harmonic term as in Eq. (5.34). For parameters where the system response has only one possible magnitude, the polynomial has only one real positive root and hence equivalent stiffness. For parameters where the system exhibits two possible magnitude responses, as in Figure 5.3, the polynomial has three real positive roots that provide three different power outputs.

The power dissipated in the equivalent linear system as the excitation frequency and noise magnitude are varied is shown in Figure 5.14a where if three power values exist they are plotted in different colours. Figure 5.14b displays the power where if it is in the three response regime, it is estimated from the upper, P_U, middle, P_M, and lower, P_L values as $P = P_L + P_U - P_M$.

Although the averaging of the three response region is an approximation, it works well when the noise is low and predicts the correct resonance peak at all noise levels. The fit becomes worse at higher noise levels where the three response region becomes narrower. A strong resonance peak is produced in this region and suggests once again that the equivalent linearisation technique is not a good tool for modelling the Duffing oscillator in the presence of noise when multiple deterministic responses are possible. The use of the delta function spectrum to represent harmonic excitation is an approximation that works only so far since a delta function spectrum represents an ensemble of harmonic excitations of varying magnitude, but with mean square displacement dictated by the magnitude of the delta function.

5.4.4 Comparison of Methods

The methods discussed above have been compared against each other for two criteria; speed and accuracy. The accuracy is measured by calculating the mean percentage error over the

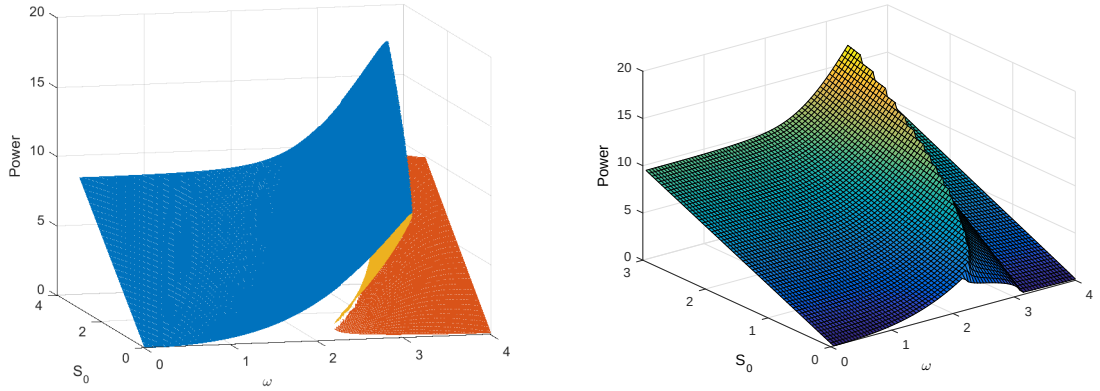

(a)

(b)

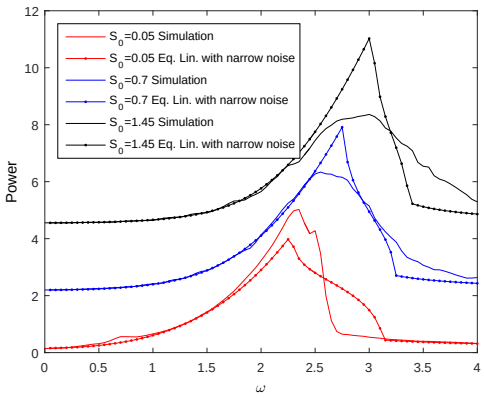

(c)

Fig. 5.14 Power dissipated calculated with the equivalent linearisation using white plus narrowband noise a) including all roots, b) averaging roots and c) comparison of equivalent linearisation using white plus narrowband noise to numerical time-integration simulations.

noise magnitude and harmonic frequency range where the error is the modulus of the power calculated from the method of interest minus the power from numerical time-integration simulations. Table 5.2 displays the comparison, although to conclude which method is optimal will depend on the accuracy required for the application. It is clear, however, that a successful method must correctly combine the random noise and the harmonic behaviours and that none of the above simplifying methods cope well in regions where more than one deterministic response is possible.

Method	**Mean Error (%)**	**Computation Time (s)**
Numerical time-integration	0	7.3×10^4
Coupled ODEs	6.5	200
Linearisation with describing function	15	0.33
Linearisation with narrowband noise	7.8	0.40

Table 5.2 Comparison of equivalent linearisation methods for calculating power.

5.5 Conclusions

The combination of harmonic and white noise vibrations is thought to be a useful approximation of some types of realistic excitation. Monte-Carlo simulations were used to illustrate the dynamics of a Duffing oscillator under such excitation, where the response was found to spread out around the trajectory that would be observed if only deterministic excitation was present. For the chaotic case, the noise was found to diffuse the JPDF from a chaotic attractor, although the attractor and therefore the moments were found to settle to a periodic state.

To investigate how the global weighted residual method models these complex responses, two methods from the literature have been extended and applied to this form of excitation. When the JPDF takes the form of a Gram-Charlier type A series, results were seen to become inaccurate and unphysical, even producing negative mean square velocity. However, a Gram-Charlier type C series was found to generate accurate and rapid results when compared to Monte-Carlo and path integration methods for weak nonlinearity.

Despite good solutions within certain parameter ranges, the WR-C method has limitations due to the conditioning of the governing equations. When the dynamics of the system requires a JPDF with a geometry far beyond what the Gram-Charlier type C series can produce, the equations become ill-conditioned and fail to solve. The method is therefore

useful for responses where the JPDF does not vary significantly from Gaussian such as weakly nonlinear or highly damped cases.

In many cases, response statistics such as moments that do not require complete knowledge of the JPDF will be desired meaning the global weighted residual technique is excessive. In energy harvesting the power dissipated is of interest, therefore the simpler equivalent linearisation technique has been extended in a number of ways to assess its ability to accurately provide the power estimates under harmonic and noise excitation. It was found that the best method depends on the relative magnitudes of the noise and harmonic excitation, the proximity to resonance of the harmonic excitation frequency and the desired accuracy and computational efficiency. A strongly performing method by all criteria is modelling the noise as a summation of narrow and white noise and then applying equivalent linearisation. This provides a rapid solution and high accuracy.

Chapter 6

Conclusions and Further Work

6.1 Conclusions

The primary aim of this thesis has been to develop new methods for understanding the response of nonlinear systems to random excitation, with a particular emphasis on energy harvesting. Three categories of random excitation were considered: white noise in Chapter 2, non-white noise (any random noise without a flat spectrum) in Chapters 3 and 4 and combined harmonic and white noise in Chapter 5. As the thesis progresses, the complexity of the excitation examined increases and as such different techniques were employed, generally with less capability the more complex the input.

6.1.1 White Noise Excitation

In Chapter 2, the power dissipated by systems under white noise base excitation was investigated. Building on the work of [47, 48] where power dissipated is known to be proportional to the magnitude of the excitation and total oscillating mass according to Eq. (1.1), an upper bound on electrical power harvested by a general SDOF energy harvester system was derived.

The harvester included a general stiffness and an electrical circuit with a general nonlinear resistor whereby the known white noise power input is split between mechanical and electrical damping. The upper bound on electrical power derived was found to be a simple function of the system parameters and, usefully, to be independent of the nonlinearities in the system.

Since the electrical circuitry acts like a low-pass filter, low frequency and therefore low stiffness devices were observed to perform closest to the upper bound. A zero stiffness device was the best of the stiffness profiles examined although practically it could not be implemented due to an infinite mean square displacement. A strongly performing realisable alternative is a bistable device which exhibits similar low stiffness properties whilst restraining

displacement. Unfortunately, one flaw of this design is that it must be tuned to the excitation level and if that changes, lower power output is observed.

Similar bounds for a harvester with nonlinear damping were derived although the method did not account for all possible damping nonlinearities. For maximum power, damping is to be minimised and so will generally be small compared to electrical damping. It is thought therefore that an upper bound using higher fidelity damping models would not provide a significantly more useful bound. In addition, the effect of combining white noise with either external or parametric harmonic excitation was assessed, concluding that no deterministic term has an impact on the power input by the noise given by Eq. (1.1).

The utility of deriving an upper bound on electrical power over and above analysing a number of specific harvesting systems is evident in the output of Chapter 2: illuminating features of a harvester that produce strong performance and guiding design towards a target. Additionally, the bound will be helpful as a measure of harvester efficiency when comparing devices to the physical upper limit of Eq. (2.43). Finally, the feasibility of vibration harvesting in a given operating environment can be quickly assessed by using the bound to estimate the power available to harvest and the approximate size and specification of a device required to do so.

6.1.2 Non-white Noise Excitation

White noise excitation is a good approximation of noise when its spectrum is flat or when the bandwidth of an oscillator is significantly narrower than that of the noise. However, in many situations, this will not be the case and the excitation spectrum may have one or more dominant frequencies. In these cases, the analysis of Chapter 2 would no longer be applicable and a new approach would be required.

The Wiener series, an orthogonal series expansion relating a white noise input to a nonlinear system to its output, was extended in Chapter 3 to account for inputs with non-white spectra. The random output is comprised of increasing order g-functionals, the form of which was derived in Section 3.2 by enforcing orthogonality between any g-functional and Volterra functional of a lower order.

When applied to power dissipation of a system, this approach is effective since only the kernel of the first g-functional and the input spectrum contribute according to Eq. (3.62). In addition, a useful property was derived for this kernel, namely that its integral over frequency is proportional to the total oscillating mass according to Eq. (3.42), and allows for simple analysis of power dissipation.

It is interesting to assess how the results for non-white noise compare with the power bounds for white noise derived in Chapter 2. Despite seemingly having more power available

in a white excitation compared to a non-white one with peak magnitude equal to that of the white noise, in fact the maximum power available for dissipation in both is the same. The reason being that an extremely narrow first kernel sees the input spectrum as white noise. This is, however, assuming the first kernel cannot be negative at some frequencies; an assumption that has only been proven for systems exhibiting detailed balance [48]. In some circumstances, where one or more generalised coordinate is constrained, the maximum power available is reduced due to the vector triple product term, $\mathrm{E}\left[\mathbf{f}^{\mathrm{T}}\mathbf{M}^{-1}\mathbf{f}\right]$, and therefore the integral over the kernel becomes less than the total oscillating mass.

The properties of the first kernel derived in Section 3.4.1 were validated both numerically and experimentally with a number of characteristic features of the kernel being observed. The integral over frequency of the first kernel was shown to relate to the total mass as expected and in addition, the kernels became more damped with increasing nonlinearity.

The experimental system was a base-excited beam with a tip mass where nonlinearity was introduced using magnets. Despite the accurate results (with a mean error of 1.3% for all monostable configurations), the system contained sources of error from the continuous nature of the beam along with a somewhat non-Gaussian input. Nevertheless, the largest deviation from the desired SDOF oscillator with base excitation came from the interaction between the tip with the base and shaker. For a nonlinear system, the tip provided feedback to the base so that the excitation was tuned to the oscillator. This meant that the kernel calculated was not actually an extended Wiener kernel and so exhibited different properties. Despite this effect, positive results were observed for systems where the nonlinearity was moderate and the damping was not too low.

The extension of the Wiener series to non-white noise significantly increases its applicability as it retains two of its important features: the series converges and the kernels can be easily calculated. There is no reason that the series should be restricted to calculating power dissipation, although the feature of the first kernel explored in Chapters 3 and 4 is particularly applicable for analysing power flows. Usefully, for any linearly damped system the power dissipated will be proportional to the mean square velocity, a property often of interest in random systems.

A considerable benefit of the extended Wiener series approach for energy harvesting is how it simply illustrates the characteristics of devices that will harvest effectively. Linear oscillators with low damping tuned to the peak excitation frequency are thought to be optimal and can perform close to the upper bound provided by white noise. The value of the simplicity of the approach was observed when comparing to the complexity of optimising any real harvester device. In Section 3.7.1 the simplest conceivable harvester model with linear stiffness and electrical and mechanical damping excited by filtered noise demonstrated how

complex power dissipation is from even a basic linear system and therefore the value of the simple conceptual understanding provided by the extended Wiener approach.

A crucial assumption in the extended Wiener theory approach for power dissipation that was illuminated by the experiment was the independence of the base motion from the motion of any oscillator vibrating on the base. In some circumstances, such as low oscillator mass compared to base mass, this assumption is valid; however, in other circumstances the assumption will invalidate the applicability of the extended Wiener approach and the power dissipated must be calculated via a different method. The results for white noise of Chapter 2 are equally subject to this limitation.

6.1.3 Combined Harmonic and White Noise Excitation

The technique of Chapter 3 for modelling systems under random excitation is applicable to a wide range of possible vibrations; however, it does not account for vibration containing both noise and harmonic components characteristic of many engineering applications. Chapter 5 therefore investigated the probabilistic response to excitation with both a harmonic component and white noise.

Monte-Carlo simulations were initially conducted to explore how the joint probability density function of displacement and velocity behaves. In general the response spreads around the trajectory that would be observed if no noise was present, or more specifically around the deterministic attractor if more than one trajectory or chaotic motion occurs.

An important concern when calculating the probabilistic response to randomly excited nonlinear systems is the computational expense since when extending to higher degrees of freedom, the scaling of any problem is such that it renders expensive methods unusable. Chapter 5 therefore described and compared a number of possible computationally efficient methods. Of particular interest were weighted residual techniques, where the form of a JPDF is proposed and substituted into the Fokker-Planck equation and the subsequent error is minimised using a weighted residual approach. This approach with a Gram-Charlier Type C series used as the proposed JPDF produced strong results for weak nonlinearity, but failed due to ill-conditioning when the JPDF required by the dynamics was too complicated for the Gram-Charlier series to recreate.

For energy harvesting applications where power dissipation is of interest, knowledge of the entire JPDF is unnecessary. A number of simpler approaches based on the equivalent linearisation technique were devised and compared in terms of accuracy of power calculation and speed. Two useful methods were found involving splitting the equations of motion into mean and noise terms then solving the resulting coupled equations and treating the excitation as random noise with a flat spectrum and a delta function accounting for the harmonic term.

In summary, energy harvesting from white noise excitation has been investigated in Chapter 2 where an upper bound on the power available to harvest was derived. For vibrations of non-white spectra, the Wiener series approach has been extended and the power dissipated by nonlinear systems with these inputs can be simply calculated. Where the excitation contains combined broadband and harmonic components, the JPDF of the response can be calculated using a weighted residual approach provided the nonlinearity is weak. Additionally, adapting the equivalent linearisation approach provides an accurate and fast method for calculating the power dissipation.

6.2 Suggestions for Further Work

A number of results in the thesis have revealed interesting opportunities for further work. One application of the power bound of Eq. (2.43) is to provide an estimate of the specification of a harvester given an operating environment. A database of vibration sources such as the one discussed in [72] could be used along with power requirements of a typical wireless sensor node and standard parameter values for a piezoelectric or electromagnetic harvester to estimate the size of the oscillating mass required. An assessment of the feasibility of harvesting from various applications in different environments could therefore be made.

Additionally, although numerical simulations are compared to the bounds in Chapter 3, a comparison of current real physical devices would also be useful. Observation of how close the current state-of-the-art harvesters come to the bound would illustrate whether or not further optimisation is of any value along with allowing an easy comparison of different devices to each other. Collection of the relevant data would most likely be an obstacle since few papers publish all of the required system parameters and many use non-white noise. The non-white noise data would also be useful to assess the first extended Wiener kernel and suggest whether improvements could be made by reducing the nonlinearity in order to narrow the kernel around the peak frequency of the excitation spectrum.

Random excitation with time varying statistics, either changing in magnitude or frequency content is highly probable in many environments where energy harvesting may be applied, although very little theoretical analysis exists. This is most likely due to the mathematical difficulty of excitation of this form and the many ways in which a signal could vary. Nevertheless, investigating how the extended Wiener approach could be modified to account for variations would be of value. Alternatively, a method solving the non-stationary Fokker-Planck equation similar to that of Chapter 5 could be investigated.

Whilst both the numerical and experimental validation of the properties of the first extended Wiener kernel were convincing, a number of improvements to the experiment could

be made to ensure its validity. Using a point mass would remove the effects created by the continuous nature of the beam and reducing the oscillating mass compared to the base mass, potentially even using a MEMS system, would significantly reduce the problematic feedback from the oscillating mass to the base.

The weighted residual method for calculating the response of nonlinear systems to combined harmonic and white noise excitation is limited by the complexity of the JPDF required by a system and the subsequent ill-conditioning of the equations. Its applicability is therefore limited to relatively weak stiffness nonlinearity; however, it may be that damping nonlinearities provide closer to Gaussian JPDFs and the method becomes attractive. This would be worth further consideration, particularly due to the prevalence of nonlinear damping mechanisms in reality.

This thesis has only considered vibration energy harvesting although a number of other forms of harvesting such as electromagnetic, wind, solar and thermal also exist. It would be interesting to explore the applicability of the white noise power bound or a similar approach to these cases, in particular electromagnetic harvesting.

References

[1] Anh, N. and Hieu, N. (2012). The Duffing oscillator under combined periodic and random excitations. *Probabilistic Engineering Mechanics*, 30:27–36.

[2] Beeby, S. and White, N. (2010). *Energy Harvesting for Autonomous Systems*. Artech House series smart materials, structures, and systems. Artech House.

[3] Beeby, S. P., Torah, R. N., Tudor, M. J., Glynne-Jones, P., O'Donnell, T., Saha, C. R., and Roy, S. (2007). A micro electromagnetic generator for vibration energy harvesting. *Journal of Micromechanics and Microengineering*, 17:1257–1265.

[4] Beeby, S. P., Tudor, M. J., and White, N. M. (2006). Energy harvesting vibration sources for microsystems applications. *Measurement Science and Technology*, 17(12):R175–R195.

[5] Bhandari, R. G. and Sherrer, R. E. (1968). Random Vibrations in Discrete Nonlinear Dynamic Systems. *Journal of Mechanical Engineering Science*, 10(2):168–174.

[6] Bontempi, F. and Faravelli, L. (1998). Lagrangian/Eulerian description of dynamic system. *Journal of Engineering Mechanics*, 124(1):901–911.

[7] Cai, G. and Lin, Y. (1994). Nonlinearly damped systems under simultaneous broad-band and harmonic excitations. *Nonlinear Dynamics*, 6:163–177.

[8] Caughey, T. K. (1963). Equivalent Linearization Techniques. *The Journal of the Acoustical Society of America*, 35(11):1706–1711.

[9] Cottone, F., Gammaitoni, L., Vocca, H., Ferrari, M., and Ferrari, V. (2012). Piezoelectric buckled beams for random vibration energy harvesting. *Smart Materials and Structures*, 21(3):035021.

[10] Cottone, F., Vocca, H., and Gammaitoni, L. (2009). Nonlinear Energy Harvesting. *Physical Review Letters*, 102(8):080601.

[11] Crandall, S. (1980). Non-Gaussian Closure for Random Vibration of Non-Linear Oscillators. *Journal of Non-Linear Mechanics*, 15:303–313.

[12] Cryns, J. W., Hatchell, B. K., Santiago-Rojas, E., and Silvers, K. L. (2013). Experimental Analysis of a Piezoelectric Energy Harvesting System for Harmonic, Random, and Sine on Random Vibration. *Advances in Acoustics and Vibration*, 2013.

[13] Daqaq, M. F. (2010). Response of uni-modal duffing-type harvesters to random forced excitations. *Journal of Sound and Vibration*, 329(18):3621–3631.

[14] Daqaq, M. F. (2011). Transduction of a bistable inductive generator driven by white and exponentially correlated Gaussian noise. *Journal of Sound and Vibration*, 330(11):2554–2564.

[15] Daqaq, M. F. (2012). On intentional introduction of stiffness nonlinearities for energy harvesting under white Gaussian excitations. *Nonlinear Dynamics*, 69(3):1063–1079.

[16] Daqaq, M. F., Masana, R., Erturk, A., and Dane Quinn, D. (2014). On the Role of Nonlinearities in Vibratory Energy Harvesting: A Critical Review and Discussion. *Applied Mechanics Reviews*, 66(4):040801.

[17] Di Paola, M. and Sofi, A. (2002). Approximate solution of the Fokker-Planck-Kolmogorov equation. *Probabilistic Engineering Mechanics*, 17(4):369–384.

[18] Er, G. (1998). Multi-Gaussian Closure Method for Randomly Excited Non-linear Systems. *International Journal of Non-Linear Mechanics*, 33(2):201–214.

[19] Er, G. (1999). A consistent method for the solution to reduced FPK equation in statistical mechanics. *Physica A: Statistical Mechanics and its Applications*, 262(1-2):118–128.

[20] Erturk, a. and Inman, D. (2008a). On Mechanical Modeling of Cantilevered Piezoelectric Vibration Energy Harvesters. *Journal of Intelligent Material Systems and Structures*, 19(11):1311–1325.

[21] Erturk, a. and Inman, D. (2011). Broadband piezoelectric power generation on high-energy orbits of the bistable Duffing oscillator with electromechanical coupling. *Journal of Sound and Vibration*, 330(10):2339–2353.

[22] Erturk, a. and Inman, D. J. (2008b). Issues in mathematical modeling of piezoelectric energy harvesters. *Smart Materials and Structures*, 17(6):065016.

[23] Friswell, M., Bilgen, O., Ali, S., Litak, G., and Adhikari, S. (2014). The effect of noise on the response of a vertical cantilever beam energy harvester. *Journal of Applied Mathematics and Mechanics*.

[24] Goldstein, H., Poole, C. P., and Safko, J. L. (2002). *Classical Mechanics*. Addison Wesley.

[25] Green, P., Worden, K., Atallah, K., and Sims, N. (2012). The benefits of Duffing-type nonlinearities and electrical optimisation of a mono-stable energy harvester under white Gaussian excitations. *Journal of Sound and Vibration*, 331(20):4504–4517.

[26] Green, P. L., Papatheou, E., and Sims, N. D. (2013). Energy harvesting from human motion and bridge vibrations: An evaluation of current nonlinear energy harvesting solutions. *Journal of Intelligent Material Systems and Structures*, 24(12):1494–1505.

[27] Haiwu, R., Guang, M., Xiangdong, W., Wei, X., and Tong, F. (2004). Response statistic of strongly non-linear oscillator to combined deterministic and random excitation. *International Journal of Non-Linear Mechanics*, 39(6):871–878.

[28] Halvorsen, E. (2008). Energy Harvesters Driven by Broadband Random Vibrations. *Journal of Microelectromechanical Systems*, 17(5):1061–1071.

[29] Halvorsen, E. (2013). Fundamental issues in nonlinear wideband-vibration energy harvesting. *Physical Review E*, 87(4):042129.

[30] Halvorsen, E., Le, C. P., Mitcheson, P. D., and Yeatman, E. M. (2013). Architecture-independent power bound for vibration energy harvesters. *Journal of Physics: Conference Series*, 476:012026.

[31] Harne, R. L., Sun, A., and Wang, K. W. (2015). An investigation on vibration energy harvesting using nonlinear dynamic principles inspired by trees. *Active and Passive Smart Structures and Integrated Systems*, 9431(94310L):1–14.

[32] Harne, R. L. and Wang, K. W. (2013). A review of the recent research on vibration energy harvesting via bistable systems. *Smart Materials and Structures*, 22(2):023001.

[33] Harne, R. L. and Wang, K. W. (2014). Prospects for Nonlinear Energy Harvesting Systems Designed Near the Elastic Stability Limit When Driven by Colored Noise. *Journal of Vibration and Acoustics*, 136(2):021009.

[34] Hatchell, B., Mauss, F., Amaya, I., Skorpik, J., Silvers, K., and Marotta, S. (2011). Missile captive carry monitoring and helicopter identification using a capacitive micro-electromechanical systems accelerometer. *Structural Health Monitoring*, 11(2):213–224.

[35] Hawes, D. H. and Langley, R. S. (2015). Numerical methods for calculating the response of a deterministic and stochastically excited Duffing oscillator. *Proceedings of the Institution of Mechanical Engineers, Part C: Journal of Mechanical Engineering Science*, 230(6):888–899.

[36] He, Q. and Daqaq, M. F. (2014). Influence of potential function asymmetries on the performance of nonlinear energy harvesters under white noise. *Journal of Sound and Vibration*, pages 1–11.

[37] He, Q. and Daqaq, M. F. (2015). New Insights Into Utilizing Bistability for Energy Harvesting Under White Noise. *Journal of Vibration and Acoustics*, 137(2):021009.

[38] Heit, J. and Roundy, S. (2014). A Framework for Determining the Maximum Theoretical Power Output for a Given Vibration Energy. *Journal of Physics: Conference Series*, 557:012020.

[39] Hosseinloo, A. H. and Turitsyn, K. (2015). Fundamental Limits to Nonlinear Energy Harvesting. *Physical Review Applied*, 4(6):064009.

[40] Hosseinloo, A. H. and Turitsyn, K. (2016). Non-resonant energy harvesting via an adaptive bistable potential. *Smart Materials and Structures*, 25(1):015010.

[41] Jin, X.-l., Huang, Z.-l., and Leung, Y. T. (2011). Nonstationary probability densities of system response of strongly nonlinear single-degree-of-freedom system subject to modulated white noise excitation. *Applied Mathematics and Mechanics*, 32(11):1389–1398.

[42] Joo, H. K. and Sapsis, T. P. (2014). Performance measures for single-degree-of-freedom energy harvesters under stochastic excitation. *Journal of Sound and Vibration*, 333(19):4695–4710.

[43] Jung, P. (1993). Periodically driven stochastic systems. *Physics Reports*, 234(4&5):175–295.

[44] Jung, P. and Hanggi, P. (1990). Invariant Measure of a Driven Nonlinear Oscillator with External Noise. *Physical Review Letters*, 65(27):3365–3368.

[45] Kumar, P. and Narayanan, S. (2006). Solution of Fokker-Planck equation by finite element and finite difference methods for nonlinear systems. *Sadhana*, 31(4):445–461.

[46] Langley, R. (1985). A finite element method for the statistics of non-linear random vibration. *Journal of Sound and Vibration*, 101(1):41–54.

[47] Langley, R. (2014). A general mass law for broadband energy harvesting. *Journal of Sound and Vibration*, 333(3):927–936.

[48] Langley, R. S. (2015). Bounds on the vibrational energy that can be harvested from random base motion. *Journal of Sound and Vibration*, 339:247–261.

[49] Lee, Y. W. and Schetzen, M. (1965). Measurement of the Wiener Kernels of a Non-linear System by Cross-correlation. *International Journal of Control*, 2(3):237–254.

[50] Li, H., Qin, W., Deng, W., and Tian, R. (2016). Improving energy harvesting by stochastic resonance in a laminated bistable beam. *The European Physical Journal Plus*, 131(3):60.

[51] Lin, Y. (1976). *Probabilistic Theory of Structural Dynamics*. R. E. Krieger Publishing Company.

[52] Lin, Y. and Cai, G. (2004). *Probabilistic Structural Dynamics: Advanced Theory and Applications*. Engineering Reference Series. McGraw-Hill.

[53] Marmarelis, P. Z. (1978). *Analysis of physiological systems : the white-noise approach*. Plenum Press.

[54] Martens, W., von Wagner, U., and Mehrmann, V. (2011). Calculation of high-dimensional probability density functions of stochastically excited nonlinear mechanical systems. *Nonlinear Dynamics*, 67(3):2089–2099.

[55] Martens, W., Wagner, U., and Litak, G. (2013). Stationary response of nonlinear magneto-piezoelectric energy harvester systems under stochastic excitation. *The European Physical Journal*, 222:1665–1673.

[56] Masana, R. and Daqaq, M. F. (2011). Relative performance of a vibratory energy harvester in mono- and bi-stable potentials. *Journal of Sound and Vibration*, 330(24):6036–6052.

[57] Masana, R. and Daqaq, M. F. (2013). Response of duffing-type harvesters to band-limited noise. *Journal of Sound and Vibration*, 332(25):6755–6767.

[58] McInnes, C., Gorman, D., and Cartmell, M. (2008). Enhanced vibrational energy harvesting using nonlinear stochastic resonance. *Journal of Sound and Vibration*, 318:655–662.

[59] Megerle, B., Rice, T., McBean, I., and Ott, P. (2013). Numerical and experimental investigation of the aerodynamic excitation of a model low-pressure steam turbine stage operating under low volume flow. *Journal of Engineering for Gas Turbines and Power*, 135(1):012602.

[60] Meimukhin, D., Cohen, N., and Bucher, I. (2013). On the advantage of a bistable energy harvesting oscillator under band-limited stochastic excitation. *Journal of Intelligent Material Systems and Structures*, 24(14):1736–1746.

[61] Méndez, V., Campos, D., and Horsthemke, W. (2013). Efficiency of harvesting energy from colored noise by linear oscillators. *Physical Review E*, 88(2):022124.

[62] Mitcheson, P., Yeatman, E., Rao, G., Holmes, A., and Green, T. (2008). Energy Harvesting From Human and Machine Motion for Wireless Electronic Devices. *Proceedings of the IEEE*, 96(9):1457–1486.

[63] Muscolino, G., Ricciardi, G., and Vasta, M. (1997). Stationary and Non-stationary Probability Density Function for Non-linear Oscillators. *International Journal of Non-Linear Mechanics*, 32(6):1051–1064.

[64] Naess, A. (2000). Chaos and nonlinear stochastic dynamics. *Probabilistic Engineering Mechanics*, 15:37–47.

[65] Nakano, K., Cartmell, M., Hu, H., and Zheng, R. (2014). Feasibility of Energy Harvesting Using Stochastic Resonance Caused by Axial Periodic Force. *Journal of Mechanical Engineering*, 60:314–320.

[66] Narayanan, S. and Kumar, P. (2012). Numerical solutions of Fokker-Planck equation of nonlinear systems subjected to random and harmonic excitations. *Probabilistic Engineering Mechanics*, 27:35–46.

[67] Nayfeh, A. and Serhan, S. (1990). Response statistics of non-linear systems to combined deterministic and random excitations. *International Journal of Non-Linear Mechanics*, 25(5):493–509.

[68] Newland, D. (2012). *An Introduction to Random Vibrations, Spectral & Wavelet Analysis: Third Edition*. Dover Civil and Mechanical Engineering. Dover Publications.

[69] Nguyen, S. D., Halvorsen, E., and Jensen, G. U. (2013). Wideband MEMS Energy Harvester Driven by Colored Noise. *Journal of Microelectromechanical Systems*, 22(4):892–900.

[70] Pellegrini, S. P., Tolou, N., Schenk, M., and Herder, J. L. (2013). Bistable vibration energy harvesters: A review. *Journal of Intelligent Material Systems and Structures*, 24(11):1303–1312.

[71] Ramlan, R., Brennan, M. J., Mace, B. R., and Kovacic, I. (2010). Potential benefits of a non-linear stiffness in an energy harvesting device. *Nonlinear Dynamics*, 59(4):545–558.

[72] Rantz, R. and Roundy, S. (2016). Characterization of real-world vibration sources with a view toward optimal energy harvesting architectures. *Proceedings of SPIE*, 9801:1–16.

[73] Risken, H. (2012). *The Fokker-Planck Equation: Methods of Solution and Applications*. Springer Series in Synergetics. Springer Berlin Heidelberg.

[74] Roberts, J. and Spanos, P. (2003). *Random Vibration and Statistical Linearization*. Dover Civil and Mechanical Engineering Series. Dover Publications.

[75] Roundy, S. and Wright, P. (2004). A piezoelectric vibration based generator for wireless electronics. *Smart Materials and Structures*, 13:1131–1142.

[76] Schetzen, M. (2006). *The Volterra and Wiener Theories of Nonlinear Systems*. Krieger Publishing Company.

[77] Scruggs, J. (2009). An optimal stochastic control theory for distributed energy harvesting networks. *Journal of Sound and Vibration*, 320:707–725.

[78] Spanos, P. D., Sofi, A., and Di Paola, M. (2007). Nonstationary Response Envelope Probability Densities of Nonlinear Oscillators. *Journal of Applied Mechanics*, 74(March 2007):315.

[79] Spencer, B. F. and Bergman, L. A. (1993). On the Numerical Solution of the Fokker-Planck Equation for Nonlinear Stochastic Systems. *Nonlinear Dynamics*, 4:357–372.

[80] Stephen, N. (2006). On energy harvesting from ambient vibration. *Journal of Sound and Vibration*, 293(1-2):409–425.

[81] Su, D., Zheng, R., Nakano, K., and Cartmell, M. P. (2014). On square-wave-driven stochastic resonance for energy harvesting in a bistable system. *AIP Advances*, 4(11):117140.

[82] Sun, J.-Q. and Hsu, C. (1988). First-passage time probability of non-linear stochastic systems by generalized cell mapping method. *Journal of Sound and Vibration*, 124(2):233–248.

[83] Tehrani, M. G. and Elliott, S. J. (2014). Extending the dynamic range of an energy harvester using nonlinear damping. *Journal of Sound and Vibration*, 333(3):623–629.

[84] van Drongelen, W. (2010). *Signal Processing for Neuroscientists, A Companion Volume: Advanced Topics, Nonlinear Techniques and Multi-Channel Analysis*. Elsevier insights. Elsevier Science.

[85] van Schaijk, R., Elfrink, R., Oudenhoven, J., Pop, V., Wang, Z., and Renaud, M. (2013). A MEMS vibration energy harvester for automotive applications. *Proceedings of SPIE*, 8763.

[86] Wagner, U. V. and Wedig, W. V. (2000). On the Calculation of Stationary Solutions of Multi-Dimensional Fokker-Planck Equations by Orthogonal Functions. *Nonlinear Dynamics*, 21:289–306.

[87] Wehner, M. F. and Wolfer, W. G. (1983). Numerical evaluation of path-integral solutions to Fokker-Planck equations. *Physical Review A*, 27(5):2663–2670.

[88] Wellens, T., Shatokhin, V., and Buchleitner, A. (2004). Stochastic resonance. *Reports on Progress in Physics*, 67(1):45–105.

[89] Wen, Y. (1975). Approximate Method for non-linear random vibration. *Journal of the Engineering Division*, 101(4):389–401.

[90] Westwick, D. and Kearney, R. (2003). *Identification of Nonlinear Physiological Systems*. Biomedical Engineering. Wiley.

[91] Wiener, N. (1958). *Nonlinear problems in random theory*. MIT Press, Cambridge, Mass.

[92] Worden, K. and Tomlinson, G. (2000). *Nonlinearity in Structural Dynamics: Detection, Identification and Modelling*. CRC Press.

[93] Xie, W., Xu, W., and Cai, L. (2006). Study of the Duffing-Rayleigh oscillator subject to harmonic and stochastic excitations by path integration. *Applied Mathematics and Computation*, 172(2):1212–1224.

[94] Yu, J. and Lin, Y. (2004). Numerical path integration of a non-homogeneous Markov process. *International Journal of Non-Linear Mechanics*, 39(9):1493–1500.

[95] Zhang, X., Zhang, Y., Pandey, M., and Zhao, Y. (2010). Probability density function for stochastic response of non-linear oscillation system under random excitation. *International Journal of Non-Linear Mechanics*, 45(8):800–808.

[96] Zhang, Y., Zheng, R., Kaizuka, T., Su, D., Nakano, K., and Cartmell, M. (2015). Broadband vibration energy harvesting by application of stochastic resonance from rotational environments. *The European Physical Journal Special Topics*, 224(14-15):2687–2701.

[97] Zhao, S. and Erturk, a. (2013). On the stochastic excitation of monostable and bistable electroelastic power generators: Relative advantages and tradeoffs in a physical system. *Applied Physics Letters*, 102(10):103902.

[98] Zheng, R., Nakano, K., Hu, H., Su, D., and Cartmell, M. P. (2014). An application of stochastic resonance for energy harvesting in a bistable vibrating system. *Journal of Sound and Vibration*, 333:2568–2587.

[99] Zhu, D., Tudor, M. J., and Beeby, S. P. (2010). Strategies for increasing the operating frequency range of vibration energy harvesters: a review. *Measurement Science and Technology*, 21.

[100] Zhu, H. T. (2015). Probabilistic Solution of a Duffing-Type Energy Harvester System Under Gaussian White Noise. *ASCE-ASME Journal of Risk and Uncertainty in Engineering Systems, Part B: Mechanical Engineering*, 1(1):011005.

Appendix A

Path Integration Method

The path integration method of [94] that is used in Chapter 5 is described in this appendix. For simplicity it is described for a system with a single random variable such as a first order system and can be extended easily to higher dimensions such as the Duffing oscillator. It is based on the principle that the long-term evolution of the PDF can be found by computing the evolution over small time-steps. The PDF at the ith time-step, $p(x^{(i)},t_i)$, can be found from the PDF at the previous time-step, $p(x^{(i-1)},t_{i-1})$, and the transition PDF, $q(x^{(i)},t_i|x^{(i-1)},t_{i-1})$ such that

$$p(x^{(i)},t_i) = \int_{R_s} q(x^{(i)},t_i|x^{(i-1)},t_{i-1})p(x^{(i-1)},t_{i-1})\mathrm{d}x^{(i-1)} \tag{A.1}$$

where R_s is a finite area of state-space that contains all significant probability and the transition PDF $q(x^{(i)},t_i|x^{(i-1)},t_{i-1})$ represents the probability of the response being at a position $x^{(i)}$ at one time-step given that it was at position $x^{(i-1)}$ at the previous time-step.

If a good approximation of the transition PDF can be found, the evolution of the PDF over time can be found from an initial distribution, $p(x^{(0)},0)$, with repeated use of Eq. (A.1). The equation can be discretised for numerical calculation by splitting state-space into K sub-intervals and each sub-interval into L Gauss-Legendre points such that Eq. (A.1) becomes

$$p(x_{mn}^{(i)},t_i) = \sum_{k=1}^{K} \frac{\delta_k}{2} \sum_{l=1}^{L} c_{kl} q(x_{mn}^{(i)},t_i|x_{kl}^{(i-1)},t_{i-1}) \times p(x_{kl}^{(i-1)},t_{i-1}) \tag{A.2}$$

where δ_k is the length of sub-interval k, c_{kl} is the weight of the klth Gauss point at location x_{kl}. The probability of the response being found at the mnth Gauss point at t_i is therefore found by summing the probability given by taking each Gauss point at the previous time-step and multiplying the probability that the response is at this point with the probability that the response travels from this point to the mnth point over a single time-step.

All that remains is to find a suitable transition PDF. For small enough time-steps, a Gaussian approximation is valid such that Gaussian closure can be used to find the mean, $m_1(t)$, and mean square, $m_2(t)$, response from the klth to the mnth Gauss point. The transition PDF becomes

$$q(x_{mn}^{(i)}, t_i | x_{kl}^{(i-1)}, t_{i-1}) = \frac{1}{\sqrt{2\pi}\sigma(t_i)} \times \exp\left(-\frac{(x_{mn} - m_1(t_i))^2}{2\sigma(t_i)^2}\right) \tag{A.3}$$

where $\sigma^2(t) = m_2(t) - (m_1(t))^2$. For the case of the Duffing oscillator (Eq. (5.1)) under combined harmonic and white noise excitation, the moment equations from Gaussian closure are

$$\dot{m}_{10} = m_{01} \tag{A.4}$$

$$\dot{m}_{01} = -cm_{01} - km_{10} - 3\varepsilon m_{10}m_{20} + 2\varepsilon m_{10}^3 + F\cos(\omega t) \tag{A.5}$$

$$\dot{m}_{20} = 2m_{11} \tag{A.6}$$

$$\dot{m}_{11} = m_{02} - cm_{11} - km_{20} - 3\varepsilon m_{20}^2 - 2\varepsilon m_{10}^4 + m_{10}F\cos(\omega t) \tag{A.7}$$

$$\dot{m}_{02} = -2cm_{02} - 2km_{11} - 6\varepsilon m_{20}m_{11} + 4\varepsilon m_{10}^3 m_{01} + \pi S_0 + 2m_{01}F\cos(\omega t) \tag{A.8}$$

where $m_{ij} = \mathrm{E}[x^i \dot{x}^j]$.

For stationary excitation the transition PDF will be the same at every time-step thus only requires calculation once and can be used repeatedly. For non-stationary excitation the transition PDF will change with time therefore under harmonic excitation, it will change over the period of the excitation. If the period is split into a suitable number of time-steps then that number of transition PDFs can be calculated and used repeatedly for every oscillation of the harmonic excitation. In the simulations of Chapter 5, the time-step is taken as a quarter of the period of the harmonic excitation.